Non-convalent functionalization of carbon nanotubes : From the organization of surfactants to the self-assembly ofporphyrins.

Géraud Delport

NNT : 2016SACLN075

THESE DE DOCTORAT

DE

L'UNIVERSITE PARIS-SACLAY

PREPAREE A

L'ECOLE NORMALE SUPERIEURE DE CACHAN

(ECOLE NORMALE SUPERIEURE DE PARIS SACLAY)

ECOLE DOCTORALE N° 572

Ondes et Matière

Spécialité de doctorat : Nanophysique

Par

M.Géraud DELPORT

Non-convalent functionalization of carbon nanotubes.

From the organization of surfactants to the self-assembly of porphyrins.

Thèse présentée et soutenue à Orsay, le 14 décembre 2016 :

Composition du Jury :

Mme Rachel MEALLET-RENAULT, Professeure, Présidente du Jury
M Stéphane BERCIAUD, Professeur, Rapporteur
M Tobias HERTEL, Professeur, Rapporteur
M Jean-Louis BANTIGNIES, Professeur, Examinateur
M Talal MALLAH, Professeur, Examinateur
M Jean-Sébastien LAURET, Professeur, Directeur de thèse
M Stéphane CAMPIDELLI, Chercheur, Invité
M Christophe VOISIN, Professeur, Invité

"Thermodynamics is a funny subject. The first time you go through it, you don't understand it at all. The second time you go through it, you think you understand it, except for one or two small points. The third time you go through it, you know you don't understand it, but by that time you are so used to it, so it doesn't bother you any more."

Arnold Sommerfeld

Contents

Remerciements

C'est pour moi une immense fierté de pouvoir terminer l'écriture de ce manuscrit. Cet énorme ouvrage, bien que non exhaustif, tente de résumer tous les travaux réalisés pendant ces trois années de thèse. Ce fut un travail de longue haleine, parfois solitaire mais souvent collectif. Je tenais dans ces quelques lignes à remercier toutes les personnes qui m'ont aidé et soutenu pendant ma thèse.

Tous d'abord, je souhaite remercier Tobias Hertel et Stéphane Berciaud de m'avoir fait l'honneur de rapporter mon travail, mais aussi Talal Mallah et Jean Louis Bantignies, qui ont été examinateurs dans mon jury de thèse. Enfin je voudrais remercier Rachel Méallet Renaud qui a accepté d'en être la présidente et qui a fait tout son possible pour me fournir les papiers à temps pour la qualification. Je remercie aussi Jean François Roch qui, en tant que directeur du laboratoire Aimé Cotton, a permis la réalisation de cette thèse.

Ensuite, je souhaite remercier Jean Sébastien, qui a été un encadrant extrêmement attentif au jour le jour. Je ne peux compter le nombre de fois où je suis venu te voir et où tu m'as accueilli dans ton bureau avec patience et pédagogie. J'ai particulièrement apprécié les discussions scientifiques que nous avons pu avoir. Je n'oublierais pas notre "road trip" en Bavière jusqu'au fin-fond d'un monastère pour discuter optique des nanotubes et jouer au bowling en buvant des bières à la pinte. J'ai aussi apprécié d'apprendre à enseigner la physique du solide à tes côtés.

Mon travail n'aurait pas signifié grand-chose sans les contributions de Stéphane Campidelli et de Christophe Voisin. Leur sens critique et leur expérience scientifique ont été d'une grande aide quand il a fallu discuter, comprendre et mettre en forme nos résultats. Je me souviendrais longtemps de nos longues réunions de travail. De même, je me dois de remercier Emmanuelle, Gaëlle et Damien, Anne Debarre, les autres chercheurs/ingénieurs permanents de l'équipe Nanophotonique qui m'ont apporté une aide précieuse.

Je me dois aussi de mentionner ici tous les étudiants et post-doctorants qui ont contribué à mon travail. Sans eux le travail au laboratoire aurait été morne et routinier. Ma reconnaissance va d'abord à Cyrielle Roquelet et Fabien Vialla, les

deux thésards qui m'ont précédé, mais aussi formé aux propriétés optiques et à la physico–chimie des nanotubes. Mon travail de thèse aurait été beaucoup moins abouti sans leur aide précieuse. Je remercie aussi Fabien Boitier, Silvia et Vincenzo, Guillaume Clavé, toujours prêts à discuter de science. J'ai beaucoup appris sur l'optique et la chimie des nano-objets grâce à eux.

J'ai une pensée particulière pour les deux thésards qui prennent la suite de mon travail : Shen et Lucile. J'ai beaucoup apprécié de travailler à leur côté et je suis sûr que leurs travaux vont porter leurs fruits et donner lieu à des articles intéressants. Ils m'ont beaucoup soutenu, en particulier quand la soutenance se rapprochait à grand pas. Je dois aussi remercier Yi, Gaëtan, Katia, Khaoula, Hiba, Paul et Ferdinand avec qui nous avons partagé des discussions scientifiques qui m'ont donné envie d'en apprendre plus sur les pérovskites hybrides. J'aurai beaucoup de plaisir à travailler avec ceux qui sont encore dans l'équipe. Je voulais aussi mentionner tous les stagiaires avec qui j'ai travaillé : Clément, Claire, Océane, Fong, Khamal, Rabah...

J'aimerais rendre hommage à tous les collaborateurs avec qui nous avons travaillé tout au long de ma thèse. Je pense à Salomé, Laurent Alvarez, Guillaume Cassabois, Rozenn Le Parc, Alain Pénicaud, Adrien et Yannick, Arianna, Philippe, Annick, Ahmed, Guillaume, Pham, Sylvie Rousset, Jérôme, Valérie, Gilles et j'en oublie sûrement d'autres.

Je voulais aussi remercier tous les autres membres des laboratoires Aimé Cotton et LPQM avec qui j'ai partagé des discussions amicales et/ou scientifiques. Je pense notamment à Thomas Hingant, Jean-Philippe, Loïc, François, Marie-Pierre, Ludovic, Clément Lafargue, Mélanie, Diep, Aliou, Nitin, Sophie, Simon, PierNicola, Margarita, Anaïs, Pierre, Timothée et le petit Loïc, Vincent, Soroush, Stefan, Qinggele, Isabell, Luis... J'en oublie certainement beaucoup.... Mes remerciements vont spécialement à Zina, Jean-Baptiste, Ginette, Christian, Isabelle Ledoux, Jean, Emmanuel, Luc, Joseph, Hervé, Colin, Monique, Sandra, Magali, Yasmine, Sylvie, Fabien, Fabienne, Jacques, Thierry, Anne...

Enfin, ces trois années n'auraient pas eu la même saveur sans la bonne humeur et l'humour douteux de mes copains de promo à l'ENS Cachan : Thomas, Eline, Pierre, Florian (et Marie), Guillaume F., Giovanni, Thibaut, Laura, Adrien, Alan, Léo, Tigrane, Mélanie...

Last but not least, je voulais remercier Céline qui me soutient depuis plus de dix ans maintenant. Elle a été à mes côtés pour m'encourager quand j'en avais besoin et pour me soutenir dans tous les moments difficiles. Je n'aurais pas été aussi loin sans elle. Lucette m'a aussi aidé par sa présence pendant ma rédaction (même si elle m'embêtait pendant mes répétitions de soutenance...).

J'ai été très ému de voir tant de membres de ma famille à ma soutenance, et en particulier mes deux grand-mères. Un grand merci à mes parents pour avoir organisé ce pot si délicieux et à mon petit frère qui a pu se libérer malgré son planning compliqué. Merci en outre à mon petit papa et la biquette pour avoir relu ce manuscrit, en anglais s'il vous plait et qui ont essayé d'en éradiquer les fautes. Enfin, je voulais remercier tous les gens qui m'ont envoyé un message de soutien à l'annonce de ma soutenance. Cela m'a donné beaucoup de courage.

Introduction

The topic of the current manuscript is included in the vast domain of nanosciences. This science is dedicated to understand, control and apply the properties of matter at a very small level. Emerged in the middle of the twentieth century, this research field has never cease to grow and diversify. Nanosciences are still very active nowadays, due to the common efforts of theoretical works, state of the art fabrication techniques and better microscope instrumentation.

In this year 2016, the Nobel committee has recognized twice the importance of mastering the structure of materials at a very small scale. The Nobel prize in Physics was attributed to David J. Thouless, F. Duncan M. Haldane and J. Michael Kosterlitz *"for theoretical discoveries of topological phase transitions and topological phases of matter"*. Among other topics, their work highlighted the influence of the topology (1D, 2D, holes...) of an object on its intrinsic physical properties. The next day, Jean-Pierre Sauvage, Sir J. Fraser Stoddart and Bernard L. Feringa received the Nobel prize in Chemistry for their work on designing and controlling organized molecular assemblies called *molecular machines*. Though these two research fields are very different, they both are meant to investigate on the properties and the potentialities of nanomaterials.

The research in nanosciences regroups many complementary disciplines, such as quantum physics, organic chemistry, nanofabrication, optoelectronics. It led to technological breakthroughs in several applied sciences such as mechanics, electronics or medicine. Among the applications of nanosciences, the design of next generation photovoltaic devices is a very active domain. A new type of photovoltaic devices has emerged, based on thin layers of nanomaterials: it is called the third generation photovoltaics. With the ongoing growth of the photovoltaic industry, such thin films solar cells could be employed to build cheap, light and adaptable solar panels that would be inserted in many surfaces (windows, cars roofs, everyday objects,...).

This new generation of solar cells require an intensive research on the light absorbent materials. Many research groups are working on the inclusion of organic dyes, that have the ability to efficiently absorb light and transfer it to their environment [1]. This concept of organic solar cell was created by Graëtzel, who designed

the first prototype in 1991 [2]. Among the many molecules tested in laboratories, the porphyrin molecule is a very popular choice [3]. Adapted from natural dyes, these porphyrins molecules will be at the center of the present work, for their remarkable optoelectronic properties and their adaptability.

Carbon nanomaterials are also very promising candidates as materials for the next generation of solar cells [4, 5]. Their limited cost, their carbon composition, and their remarkable electronic properties make them suitable to replace rare or expensive elements in such photoactive devices. Over the last thirty years, the carbon nanostructures have received a growing interest. This includes two nobel prizes for the discovery of fullerenes in 1996 [6] and more recently of graphene in 2010 [7]. These two nano-objects as well as carbon nanotubes share the same carbon sp^2 structure, but have different geometries and dimensions.

Among these materials, single walled carbon nanotubes and graphene are at the center of this manuscript. While the first of these objects is a unidimensional object, the latter has a perfect two dimensional structure. Both objects have very good intrinsic electric conductivities. This explains why both elements are already used in prototypes as electrodes or flexible conductive surfaces. However, this geometric difference induces drastic differences between the objects. In particular, only some nanotubes possess an electronic gap, that allows them to emit light or to be used in transistor devices.

Controlling nanomaterials at the smaller scale offers the possibility to combine them into hybrid nanostructures. This opportunity has led to many advances, such as the creation semiconducting quantum dots [8], Van der Waals heterostructures [9], or hybrid perovskites materials [10]. This mixing ability will be extensively employed in the present research work. Due to their carbon sp^2 thin structure, graphene and nanotubes are ideal candidates for such hybrid assemblies.

In this work, the porphyrins will be stacked at the surface of the carbon materials (nanotube/graphene). One major objective is to preserve the exceptional properties of these two complementary materials. The other one is to generate new effects in these hybrid structures. Between these two objects, an energy transfer process has been reported with a 100 % efficiency [11]. These effects are particularly valuable for photovoltaics research, as they allow to transfer the energy from one material to another in a thin film solar cell. Yet, the mixing of the porphyrins and the nanotubes, called a *functionalization process* requires many improvements.

The first chapter of this thesis will describe the main physical, electronic and optical properties of the carbon nanotubes and the porphyrins molecules. Then, an introduction of the experimental techniques employed in this work will be done. Finally, the main aspects of the creation of such hybrids nanotubes/porphyrins compounds will be detailed.

In this thesis, the creation of the nanotube/porphyrin assemblies is performed in a water/surfactant environment. This surfactant materials have the ability to self-organize in water, to form micelles. These encapsulating structures are suitable to isolate and protect hydrophobic carbon nano-objects such as molecules or nanotubes. In the second chapter, the role of the surfactant environment inside the nanotube/porphyrin hybrid objects will be monitored. A comprehensive kinetic study of the functionnalization process will be performed, in connection with the stability properties of this surfactant medium. The different steps of this complex mechanism will be described and studied. The creation of assemblies of porphyrin with graphene nanosheets will also be discussed, exhibiting significant differences with the nanotube samples.

In complement to this kinetic study, the third chapter will focus on the equilibrium state of the nanotube/porphyrin compounds. The process of coverage of the nanotube surface will be described, thanks to a thermodynamic Hill model that is adapted to the adsorption processes. The ability of porphyrins to cooperate during their stacking on the nanotube will be highlighted. The presence of multilayers of porphyrins at the carbon surface will also be discussed. The thermodynamic parameters of the reaction will be extracted in various surfactant environments or for various types of nanotubes. It will be shown that the π-stacking reaction is more favored on large diameter nanotubes than on small diameters. This effect will be discussed in relation with binding energies effects. Finally, the coverage of graphene nanosheets with porphyrin molecules will also be studied thanks to this thermodynamics formalism.

Finally, an important challenge is to determine how the porphyrins are oriented on the carbon surface. They could be either totally ordered or randomly positioned. This organization is very important because it fixes the number of molecules that can stack onto the nanotube. It may also have an influence on the efficiency of the energy transfer. The last chapter of this thesis will use optical spectroscopy to demonstrate such porphyrins organization. A dipole coupling model will be developed to predict the spectroscopic effects of such molecular ordering. Different geometries of porphyrins assemblies will be analyzed, in connection with examples in literature. These results will be confronted to the experimental results, both in absorption and in polarized photoluminescence experiments.

Chapter I

Theoretical and experimental physics of carbon nanotubes and porphyrin molecules

Single-walled carbon nanotubes (SWNTs) and porphyrin molecules are outstanding nanoobjects of great interest for the scientific community. The main purpose of this chapter is to describe the theoretical and spectroscopic elements at the origin of remarkable optoelectronic properties. This will be the object of the two first sections dedicated to theoretical and optical properties of single-walled carbon nanotubes and porphyrin molecules. Then, we will see how such these objects can form nanohybrid compounds, leading to an ultraefficient energy transfer phenomenon. To understand this effect, the two last parts will describe the experimental techniques that allow the fine control and monitoring of the interaction in such assemblies: one detailing the required spectroscopy experiments and the other insisting on the physicochemistry conditions to create these effects.

1 Physical properties of single-walled carbon nanotubes

The discovery of graphite dates back from the sixteenth century [12]. Since then, the importance of carbon materials in science and industry never ceased to grow. The scientific knowledge on graphite increased all along the twentieth century, especially along the development of new experimental techniques to study nanomaterials (electron microscopy, X-ray diffractions,....). Working on graphite synthesis, researchers discovered the presence of new allotropic form of carbon: the fullerenes [13], the carbon nanotubes [14] ... However, carbon nanotubes may have been accidentally produced for centuries, as researchers unveiled the presence of nanotubes inside ancient damascus swords from the 17^{th} century [15].

1.1 Basic properties of carbon nanotubes

In 1991, Ijima and coworkers were the first to perfom an extensive scientific characterisation of carbon nanotubes, starting a new reseach field [14, 15]. As they showed on transmission electron microscope images (TEM, figure I.1 left), SWNTs are made of one to several layers of carbon rolled to form concentric tubes. The diameter of carbon nanotubes ranges between 0.4 and 30 nm, while their lengths ranges from nanometers to millimeters [16, 17]. With their large aspect ratio, carbon nanotubes are almost ideal 1D physical objects. Among other techniques, scanning tunneling microscopy techniques (STM) on carbon nanotubes (see figure I.1 right) were useful to reveal the honeycomb carbon structure in such tubes, proving their similarity with graphite. With their remarkable nanostructure, carbon nanotubes have been intensely studied in many research field, such as mechanics [18], electronics [19], thermal exchanges [20], optoelectronics [21].

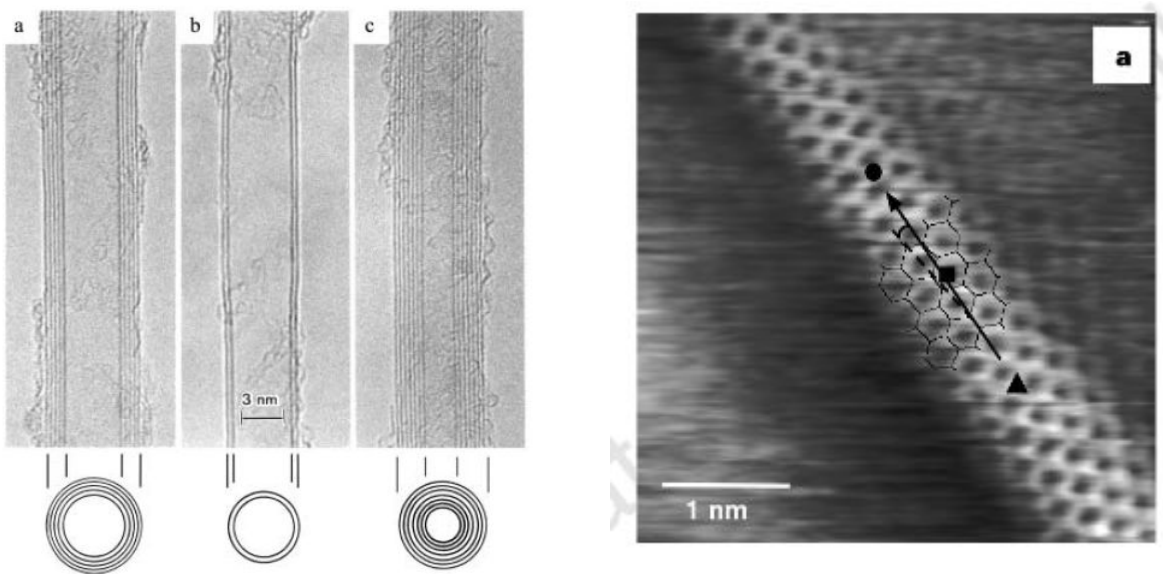

Figure I.1: Examples among of the first observations of the carbon nanotubes structure; Left: The observation by TEM of multi-wall coaxial nanotubes with various diameters, and numbers of shells N reported by Iijima in 1991 [14]; Right: Atomic structure and spectroscopy of a isolated SWNT on a gold substrate in 1998 [22].

1.2 Geometrical description

Description in the direct space

Each of the carbon nanotubes shell is a rolled carbon layer called graphene (monolayer graphite, [23]). The carbon nanotubes electronic characteristics are often derived from graphene properties, under a *zone folding approximation* [24]. This model

uses boundary conditions to respect the continuity of the carbon lattice upon folding. Hence, the preliminary study of graphene structure is essential to understand the properties of carbon nanotubes.

Graphene is a one atom thick two dimensional honeycomb carbon lattice. The unit cell of graphene is made of two different sites A and B (see figure I.2). The network of the A atoms (respectively the B atoms) forms a hexagonal lattice, with base vectors $\vec{a_1}$ and $\vec{a_2}$ (defined as the connection between an A atom and its two identical neighbors). In a $(\vec{e_x}, \vec{e_y})$ orthogonal base, these vectors are expressed as:

$$\vec{a_1} = \frac{\sqrt{3}}{2} b \ \vec{e_x} - \frac{1}{2} b \ \vec{e_y} \quad ; \quad \vec{a_2} = \frac{\sqrt{3}}{2} b \ \vec{e_x} + \frac{1}{2} b \ \vec{e_y} \tag{I.1}$$

where $b = \sqrt{3}a = 246$ pm, where a is the carbon-carbon distance.

The are only a limited number of manners to create a carbon nanotube out of a graphene sheet, as both edges of the sheet have to connect and superimpose to ensure the continuity of the the sp^2 carbon lattice. To predict every allowed carbon nanotube, a formalism has been developped [25, 26]. As explained on figure I.2, a set of coordinates (n,m) is enough to define one carbon nanotube. These numbers are called the chiral indices of the tube, as they describe the symmetry of the tube. Hence, an ensemble of nanotubes having the same indices are said to belong to a common *chirality* (for instance the (6,5) chirality). Nanotubes are said to be achiral if they can be reproduced by a mirror symmetry. They can be classified under two forms (see figure I.2: armchair tubes with m=n and zigzag tubes with m=0. Any other (n,m) couple will create a chiral tube, that will exist in two distincts forms, called enantiomers [27, 28].

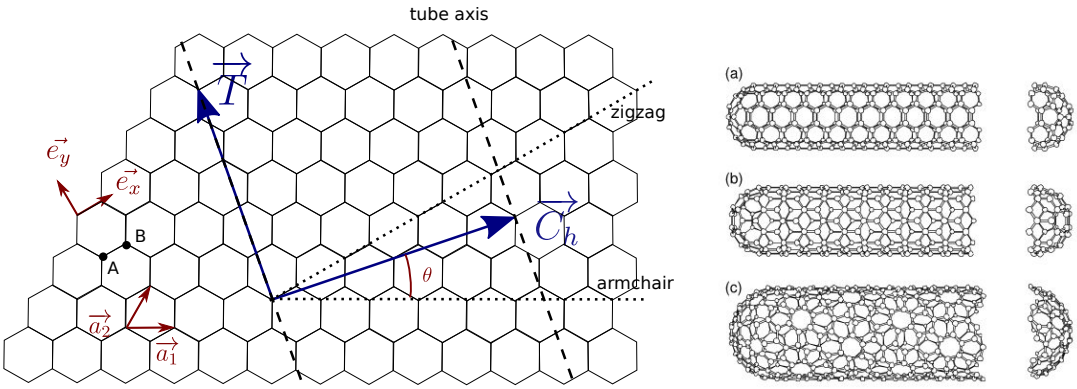

Figure I.2: Geometrical construction of a (n,m) = (4,2) nanotube using the edge matching rule. A given chiral vector $\vec{C_h}$ is enough to single out a chirality, right armchair zigzag, chiral [17].

Using those two coordinates, we can build two primitive vectors $\vec{T}$ and $\vec{C_h}$ that describe entirely the geometry of any tube. The translation vector $\vec{T}$ is parallel to the nanotube axis and joins the two first equivalent carbon atoms (see figure I.2). Its expression in the $(\vec{a_1}, \vec{a_2})$ base is:

$$\vec{T} = t_1\vec{a_1} + t_2\vec{a_2} = \frac{2m+n}{d_R}\vec{a_1} - \frac{n+2m}{d_R}\vec{a_2} \tag{I.2}$$

where d_R is the least common denominator of $2m+n$ and $n+2m$. The vector that is orthogonal to $\vec{T}$ and follows the circumference of the carbon nanotube is called the chiral vector $\vec{C_h}$.

$$\vec{C_h} = n\vec{a_1} + m\vec{a_2} \tag{I.3}$$

On the corresponding graphene sheet, it connects the two carbon atoms that become identical once the tube is rolled. The perimeter of the tube is equal to the norm C_h of the chiral vector. Thus, the diameter of the tube d_{Nt} can be expressed as a function of n and m:

$$d_{Nt} = \frac{C_h}{\pi} = \frac{b}{\pi}\sqrt{n^2+m^2+nm} \tag{I.4}$$

One can define the chiral angle θ of the tube as the angle between the two vectors $\vec{C_h}$ and $\vec{a_1}$ (it is comprised between 0° and 30°):

$$\cos(\theta) = \frac{2n+m}{2\sqrt{n^2+m^2+nm}} \tag{I.5}$$

Finally, we may quantify the number of hexagons per unit cell:

$$N = \frac{|\vec{C_h} \wedge \vec{T}|}{|\vec{a_1} \wedge \vec{a_2}|} = \frac{2(n^2+nm+m^2)}{d_R} \tag{I.6}$$

Description in the reciprocal space

The reciprocal lattice of graphene is hexagonal with the following primitive vectors:

$$\vec{a_1}^\star = \frac{2\pi}{\sqrt{3}b}(\vec{e_x} - \sqrt{3}\vec{e_y}) \quad ; \quad \vec{a_2}^\star = \frac{2\pi}{\sqrt{3}b}(\vec{e_x} + \sqrt{3}\vec{e_y}) \tag{I.7}$$

In the first Brillouin zone, the center is called Γ, while the two remarkable extremities of the hexagon are called K and K' (see figure I.3). As for the direct lattice, we may adapt the reciprocal lattice of graphene for carbon nanotubes. We then define the reciprocal base vectors of the nanotube as $\vec{K_1}$ and $\vec{K_2}$, as a function of $\vec{T}$ and $\vec{C_h}$:

$$\vec{K_1}.\vec{C_h} = 2\pi \;\; ; \;\; \vec{K_1}.\vec{T} = 0 \;\; ; \;\; \vec{K_2}.\vec{C_h} = 0 \;\; ; \;\; \vec{K_2}.\vec{T} = 2\pi \tag{I.8}$$

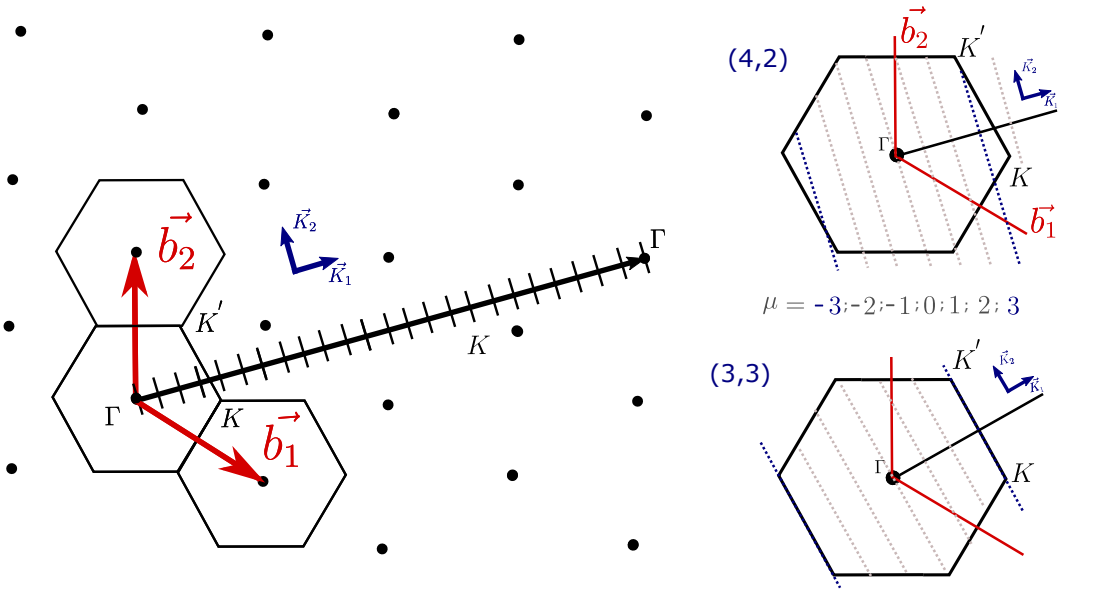

Figure I.3: Left: Hexagonal reciprocal lattice of Graphene in the k space along with the quantization lines of a (4,2) carbon nanotube; Right: Representation of the quantization lines for a (4,2) and a (3,3) carbon nanotubes. We observe that they intersect the K point for the (3,3) while they do not for the (4,2).

It yields:

$$\vec{K_1} = \frac{1}{N}(-t_2\vec{a_1}^\star + t_1\vec{a_2}^\star) \quad ; \quad \vec{K_2} = \frac{1}{N}(-m\vec{a_1}^\star + n\vec{a_2}^\star) \tag{I.9}$$

Since $\vec{T}$ and $\vec{C_h}$ are orthogonal, so do $\vec{K_1}$ and $\vec{K_2}$. $\vec{K_1}$ turns to be parallel to the axis of the tube while $\vec{K_2}$ is perpendicular. Finally, any vector of the reciprocal space can expressed as:

$$\vec{k} = k_\perp \frac{\vec{K_1}}{K_1} + k_\parallel \frac{\vec{K_2}}{K_2} \tag{I.10}$$

For an infinitely long nanotube, the $k_\parallel$ coordinate is quasi-continuous and ranges between $-\pi/T$ and π/T, where T is the norm of the translational vector. However, in the diameter direction, the continuity of the tube imposes a periodic boundary condition for $k_\perp$:

$$k_\perp C_h = \mu \times 2\pi \quad ; \quad \mu = -\frac{N}{2} + 1, ..., 0, ..., \frac{N}{2} \tag{I.11}$$

1.3 Electronic properties

Band structure of graphene

We are now going to extend the zone folding approximation to model the electronic properties of carbon nanotubes. In a quantum chemistry model, the n=2 subshell of carbon atoms includes four electrons placed into four atomic orbitals: $2s$,$2p_x$, $2p_y$ and $2p_z$. In the two dimensional graphene lattice, carbon atoms undergo a sp^2 hybridization. As a carbon atom interacts with its three first neighbors, their $2s$ are mixed with their $2p_x$ and $2p_y$ orbitals to create three in plane σ levels. A last π_z orbital, lies perpendicularly to the carbon plane. Three electrons are included in this σ levels, while one additional electron occupies the π_z one. These π_z electrons will form the π double bonds, that are highly delocalized over the carbon networks. Moreover, the π electrons are of great importance as they will drive the noncovalent interaction with organic molecules.

Graphene (as for carbon nanotubes) electronic structure is commonly modeled through a one electron tight binding approach [29, 30]. In such a model, we neglect any electron-electron interaction as well as any curvature effect on the electrons. As we are dealing with low energy electronic properties (close to the 1-2 eV gap of a nanotube for instance), we may also consider that the σ levels are far enough in energy ($>$ 10 eV at the Γ point) to be neglected in the calculation [31]. Hence, we may focus on one π_z electron per atom, which is an easier assumption to treat with a tight binding model. Under these hypotheses, we use the Bloch formalism to express the global π wavefunction ψ_k as a linear combination (LCAO) of each π_z atomic orbital function Φ_π [32]:

$$\psi_k(\vec{r}) = \frac{1}{N}\sum_{j=1}^{N} e^{i\vec{k}.\vec{r_j}} \left(\Phi^a_{\pi_z-j}(\vec{r}) + e^{i\vec{k}.\vec{AB}}\Phi^b_{\pi_z-j}(\vec{r})\right) \tag{I.12}$$

where $\vec{r}$ is the position in the crystal and $\vec{k}$ is the Bloch eigenvector associated to the wavefunction. Here, j represents each unit cell, while a and b stands for the two differents type of position in the lattice. If we restrict the coupling to nearest neighbors and neglect the atomic wavefunction overlap, the energy dispersion of the π band can be written as [24]:

$$E(k) = \pm\gamma_0\sqrt{1 + 4\cos\frac{\sqrt{3}k_x a}{2}\cos\frac{k_y a}{2} + 4\cos^2\frac{k_y a}{2}} \tag{I.13}$$

in which $\gamma_0 \simeq$ 2.7 eV is the transfer integral between first neighbors. This complex formula provides the band structure represented on figure I.4, showing a six-fold symmetry with valleys around the K and K' points. The positive and negative values of energies correspond respectively to the conduction and the valence band. The two bands connect at each K/K' points, at a position called the Fermi level, in

which the energy is equal to $E_F = 0$. As a consequence, graphene has a zero gap: it is called a semi-metal. Around these positions, we can develop the energy dispersion for values of $\vec{k}$ close to $\vec{k_F}$:

$$E(\vec{k_F} + \delta\vec{k}) \simeq \pm\gamma_0 \frac{\sqrt{3}a}{2}|\delta\vec{k}| \tag{I.14}$$

We see that this dispersion is linear with $|\delta\vec{k}|$ around the Fermi level, whereas a parabolic behavior is commonly expected for a classical solid. This effect leads to remarkable electronic properties such as very high electrons mobility [31, 33] or quantum fermions properties [34, 35].

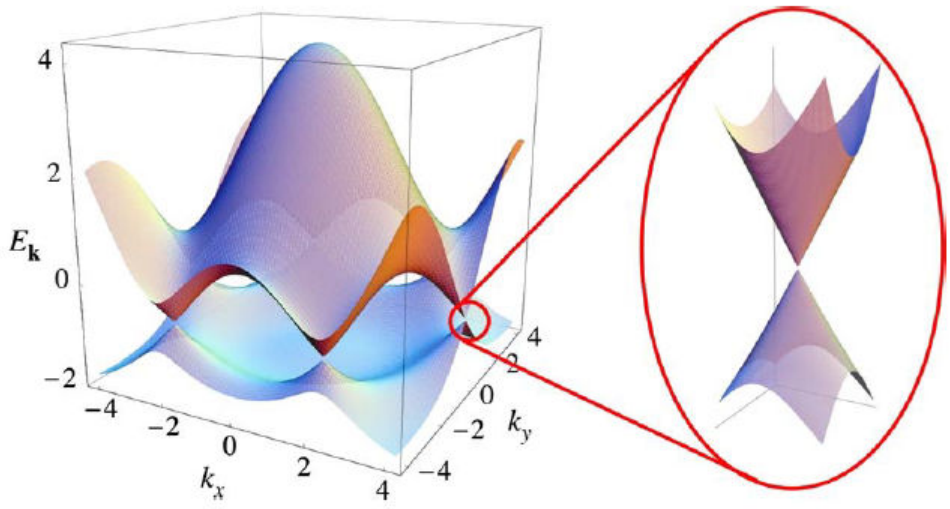

Figure I.4: Left: Tridimensional band structure of graphene as a fonction of the coordinates (k_x, k_y) with a $\pi/3$ rotation with respect to the formula I.13; Right: Zoom around the K point that shows the linear dispersion at the Dirac points [36].

Developing the zone folding approximation

For infinite size graphene, the vector $\vec{k}$ can vary continuously in the first Brillouin zone. For carbon nanotubes, we previously saw that the wavevectors were quantized perpendicularly to the tube. In the zone folding approximation, we will use the graphene band structure and restrict it to the values of $\vec{k} = \vec{k_\parallel} + \vec{k_\perp}$ that respect the nanotube boundary conditions. This simple method neglects the effects of curvature on electrons confinement [24], or changes in shape of the dispersion diagram called trigonal warping [37]. These effects will be studied in next sections. The dispersion relation for carbon nanotubes is expressed as a function of the μ quantification number:

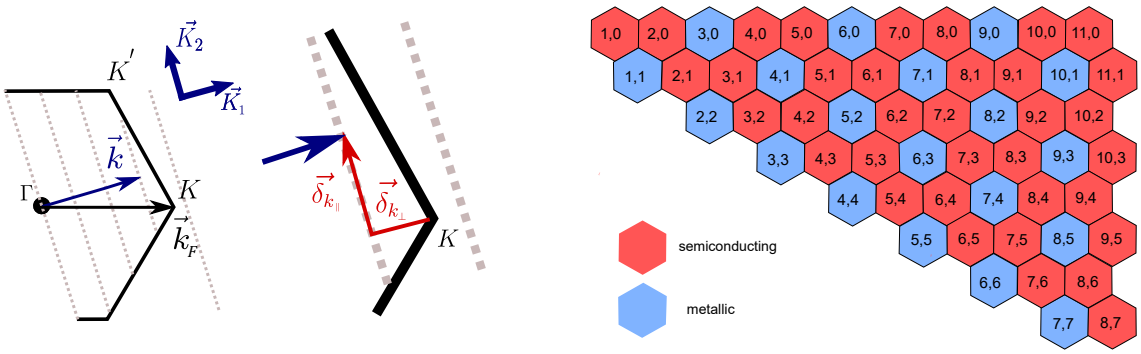

Figure I.5: Left: Geometrical determination of the allowed k states for a (4,2) nanotube under the zone folding approximation; Right: Labelling of the metallic and semiconducting families of carbon nanotubes according to their chiral numbers.

$$E_\mu = E_{graphene}\left(k_\parallel \frac{\vec{K_1}}{K_1} + \mu\vec{K_2}\right) \quad ; \quad \mu = -\frac{N}{2}+1, ..., 0, ..., \frac{N}{2} \tag{I.15}$$

On figure I.5 left, we see the sectioning of the first Brillouin zone for a (4,2) nanotube. We see a succession of lines, each corresponding to a value of μ. Interestingly, no one of them intersect with the K point of the Brillouin zone. This tells us that the energy dispersion of the (4,2) nanotube does not include any K or K' points, that are located at the graphene Fermi level. As a consequence, (4,2) nanotubes present an energy gap: they are semiconducting. However, on the equivalent diagram for the (3,3) nanotube (figure I.3 right), one quantization line crosses the K point. This chirality, as any armchair tube, is metallic.

In fact, this zone folding method is a good tool to predict the presence of a gap for a given chirality of nanotube. As seen on figure I.5 right, a majority of carbon nanotubes are semiconducting. This proportion can be calculated by considering the norm of the vector $\vec{k}$, close to the Fermi wavevector $\vec{k_F}$. We can decompose it according to figure I.5: $\vec{k} = \vec{k_F} + \delta\vec{k}_\parallel + \delta\vec{k}_\perp$. One can derive that the quantification of $\delta\vec{k}_\perp$ has to verify [38]:

$$|\delta\vec{k}_\perp| = \frac{2}{3d_{Nt}}|3\mu - n + m| \tag{I.16}$$

From this formula, we see that nearly one third of the chiralities of nanotubes are metallic (see figure I.5), since one of their allowed $\vec{k}$ vectors points to a K/K' point. Their chiral indices verify $\mathrm{mod}(n-m, 3) = 0$. For any other combination, the nanotubes are semiconducting. The energy dispersion close to the K points can be developed into:

$$E(\delta k_\parallel, \delta k_\perp) = \pm\sqrt{E_\parallel^2 + E_\perp^2} \tag{I.17}$$

where $E_{\parallel} = \frac{\gamma_0\sqrt{3}a}{2}\delta k_{\parallel}$ varies continously with $\delta k_{\parallel}$, while $E_{\perp}$ is quantified with μ:

$$E_{\perp} = \frac{\gamma_0\sqrt{3}a}{3d_{Nt}}|3\mu - n + m| \quad ; \quad \mu = -\frac{N}{2} + 1, ..., 0, ..., \frac{N}{2} \tag{I.18}$$

This formula can also be used to evaluate the energy width of the gap. We see that the minimum of energy in the conduction band is reached when $\delta k_{\parallel} = \vec{0}$ and μ is chosen to minimize the value of $|3\mu - n + m|$. Doing the same in the valence band, one can extract the value of the energy gap: $\Delta E = E_{\perp}(\mu) - E_{\perp}(-\mu)$. From formula I.18, one can see that this value is inversely proportional to the diameter of the tube.

Electronic density of states

In the quasi-continuous limit, the electronic density of states is generally expressed as an integral over the reciprocal space [38]:

$$n(k) = \frac{g}{l_{BZ}} \int \mathrm{d}k \delta(k - k_i) \frac{\partial \epsilon}{\partial k_i} \tag{I.19}$$

where l_{BZ} is the length of the 1D Brillouin zone in the reciprocal space and g is the degree of degeneracy. In our case, it is here equal to 2 due to the K-K' intervalley equivalence, or 4 if the spin degeneracy is included. The k_i are the roots of the equation $E - \epsilon(k) = 0$. For an infinitely long carbon nanotube, we can integrate easily this expression over the $\vec{K}_2$ translational direction. Due to the quantization of μ, this leaves us with a discrete sum over the $\vec{K}_1$ perpendicular direction:

$$n(E) = \frac{2a}{\pi^2\gamma_0 d_{Nt}} \sum_{\mu} f(E, E_{\mu}) \tag{I.20}$$

with:

$$f(E, E_{\mu}) = \begin{cases} |E|/\sqrt{E^2 - E_{\mu}^2} & , \text{ if } |E| > E_{\mu} \\ 0 & , \text{ if } |E| < E_{\mu} \end{cases} \tag{I.21}$$

This density of states diverges when E gets close to any E_{μ} value. This is a classical behaviour for electrons in unidimensional solids, that usually have a density of states in $1/\sqrt{\Delta E}$. These divergences are called Van Hove singularities [39]. Due to the two-fold degeneracy, the density of states is symmetrical with respect to the Fermi level. From equation I.18, the position of the pth singularity corresponds to:

$$E = pE_0 \quad ; \quad p \in \mathbb{Z}^*; \quad E_0 = (\gamma_0\sqrt{3}a)/(3d_{Nt}) \tag{I.22}$$

This model predicts that the splitting between singularities is fixed by the diameter of the tube. The value of p are restricted by the nature of the tube. For metallic nanotubes: $\mathrm{mod}(p, 3) = 0$, while for semiconductiong ones: $\mathrm{mod}(p, 3) = 1$ or 2.

Taking advantage of their accessible sp^2 surface structure, the density of states of carbon nanotubes has been widely studied by scanning tunnelling experiments [32,36,40]. This is one the most efficient tool to study the density of states of carbon nanotube or graphene [41,42]. Figure I.6 shows one example among them, performed by Lin *et al.* [32].

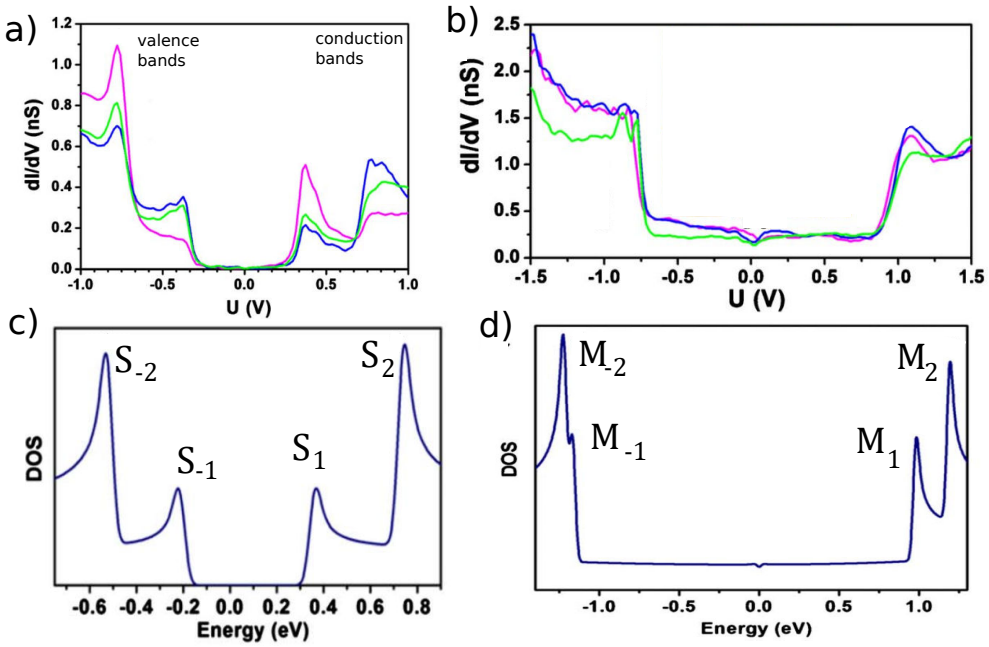

Figure I.6: Density of states evaluation of carbon nanotubes measured by scanning tunneling spectroscopy, adapted from [32]: a) Experimental data for a semiconducting tube; b) Experimental data for a metallic tube; c) Model of density of states for a semiconducting tube; d) Model of density of states for a metallic tube.

They measured the derivative dI/dV of the tunneling current with respect to voltage. Under certain hypotheses, this conductance can be regarded as an indirect evaluation of the density of states [43]. For one metallic and one semiconducting nanotube shown in figure I.6 a) and b), these diagrams exhibit a series of resonances, for which the conductance signal increases dramatically. These divergences are found at relatively regular positions, both for positive and negative voltages. These peaks correspond to the predicted Van Hove singularities that can be found in the valence and the conduction bands. Between the two first singularities, the signal goes to zero for the semiconducting nanotube, proving the absence of available states. This allows to measure the gap of 0.5 eV for the studied nanotube. At the opposite, the conductance signal is always positive for the metallic tube. Finally, they performed a tight-binding calculation of the density of states that matches with the spectroscopy

data. These experiments prove that the tight binding model is relevant to provide a good insight into the electronic properties of carbon nanotubes.

1.4 Optical properties

Knowing the density of states, we may predict the basic interactions between photons and carbon nanotubes. We will mainly focus on the absorption and the emission of photons by semiconducting nanotubes. In general, the optical properties of a solid are linked to its electronic dispersion and density of states. To absorb a photon of energy $\hbar\omega$, an electron has to be promoted from a filled state of the valence band to an empty state of the conduction band. In a semi-quantum formalism, the probability Γ of the photon absorption (or the symmetric emission) can be evaluated through the Fermi golden rule:

$$\Gamma(\omega) = \frac{2\pi}{\hbar} \sum_{\vec{k},\vec{k'}} |M(\vec{k},\vec{k'})|^2 \delta\left(E' - E - \hbar\omega\right)\left(f_v(E) - f_c(E')\right) \tag{I.23}$$

where $f_v(E)$ (respectively $f_c(E')$) is the Fermi-Dirac occupation probability in the valence band (respectively the conduction band):

$$f(E) = \frac{1}{1 + e^{\frac{E-E_F}{k_B T}}} \tag{I.24}$$

The (E',$\vec{k'}$) values are assigned to the final state while the bare ones correspond to the initial state. The probability Γ is a sum over all the combinations of wavevectors: it will strongly depend on the joint density of states in the valence and in the conduction band. This is the reason why the optical properties of carbon nanotubes are governed by the multiple Van Hove singularities.

The matrix elements $|M(\vec{k},\vec{k'})|^2 = |\langle v| H_{dip} |c\rangle|^2$ take into account the light-matter interaction. This dipolar matrix includes the optical selection rules, as it only couples a restricted number of quantum states [44]. In particular, such transitions have to respect the conservation of energy, $E' = \hbar\omega + E$ and of momentum, $\hbar\vec{k'} \simeq \hbar\vec{k}$. Here, we have neglected the wavevector of photons ($\sim 10^7$ m^{-1}) with respect to the one of involved electrons ($\sim \pi/a \sim 10^{10}$ m^{-1}): we call such event a vertical transition. In the following experiments, the light-matter interaction will be treated with the dipole approximation [45, 46].

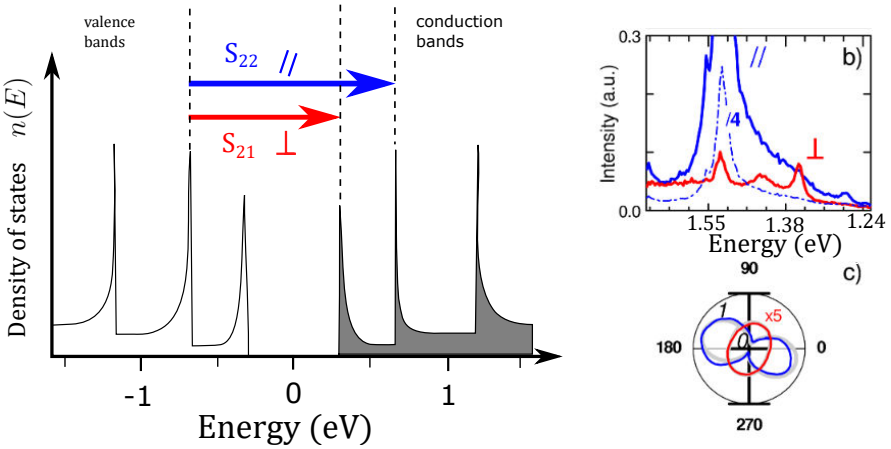

Figure I.7: Left: Density of states from a (15,2) nanotube according to [47]; Right top: Photoluminescence excitation plot for a (15,2) nanotube when the incident light has a parallel or perpendicular polarization with respect to tube axis; Right bottom: PL intensity versus polarization angle of the laser excitation. Data taken at S_{22} (blue) and S_{12} (red) transitions. The gray lines are $\cos^2(\theta)$ functional form. Top and bottom figures are adapted from the reference [48].

However, the dipolar interaction strongly depends on the polarisation of the light electric field. For a polarization along the tube axis, the electronic transition can only take place between symmetrical singularities, having the same μ quantum number: $\mu' - \mu = 0$. The strongest transition will occur when the electric field is parallel to the nanotube axis [48]. However, for a perpendicular polarization, the transition must involve non symmetrical bands: $\mu' - \mu = \pm 1$. The optical transitions are called $S_{ii'}$ for semiconducting nanotubes and $M_{ii'}$ for metallic ones, where i refers to the i^{th} Van hove singularity in the valence band, while i' corresponds to the conduction band.

All of these opto-electronic properties can be assessed by several experimental techniques including absorption or photoluminescence experiments [45, 48]. The photoluminescence of a (15,2) nanotube has been studied by Lefebvre and coworkers in figure I.7 right. These experimental techniques will be broadly detailed in the following sections. When they modify the excitation energy, they exhibit different luminescence resonances that correspond to the allowed transitions between the nanotube's Van Hove singularities (see figure I.7 left). Moreover, when they use a polarized excitation beam, they can selectively activate some of these transitions. The symmetrical transitions S_{ii} can be triggered by a light parallel to the tube axis, while the crossed ones $S_{ii\pm1}$ require a perpendicular polarization. This is a direct consequence of selection rules. Furthermore, one may easily notice that the intensity of the parrallel transition S_{22} is one order of magnitude larger that the perpendicular

one S_{12} [48, 49].

According to the precedent discussion, the electronic transitions that can be triggered by photons can be sorted as:

$$S_{ii} = \frac{6\gamma_0 a}{\sqrt{3}d_{Nt}} p \quad ; \quad i \in \mathbb{N}^* \quad ; \quad p(i) = \{1, 2, 4, 5, 7, ...\} \tag{I.25}$$

for semiconducting tubes, while for metallic:

$$M_{ii} = \frac{18\gamma_0 a}{\sqrt{3}d_{Nt}} i \quad ; \quad i \in \mathbb{Z}^* \tag{I.26}$$

In consequence, this model predicts that the energy of the optical transitions should vary in $1/d_{Nt}$. In addition, the energies of the transitions for a metallic tube are three times larger than for a semiconducting one with a similar diameter. A plot of the accessible optical transitions as a function of diameter has been first established by Kataura *et al.* (see figure I.8 left, [50]), and tends to verify roughly those predictions.

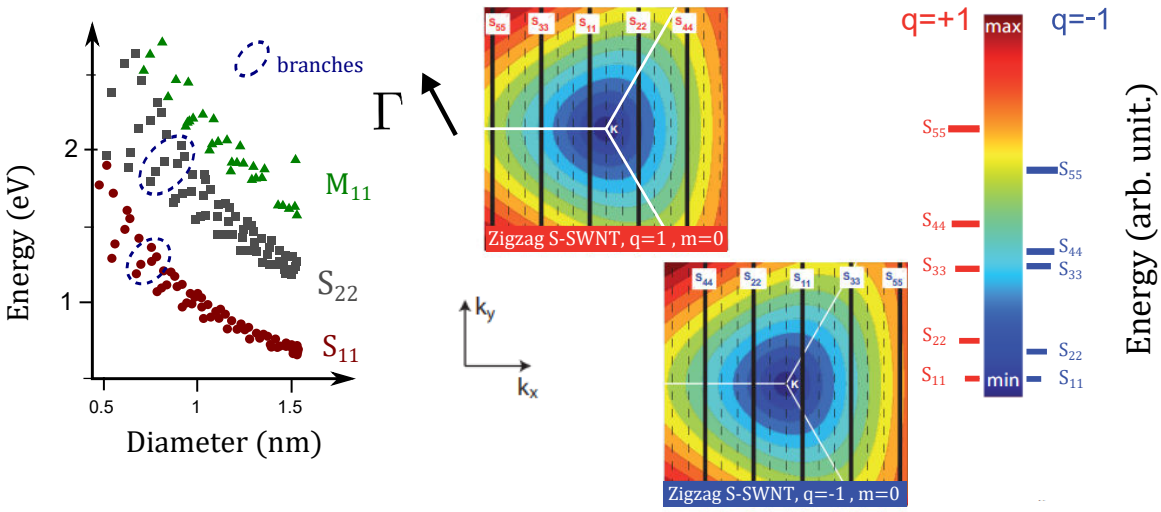

Figure I.8: Left: Kataura plot of the transitions as a function of diameter for semiconducting and metallic nanotubes, from [50]; Right: Effect of the trigonal warping on the position of transition energies for two nanotubes of similar diameters but with different values of $q = \mathrm{mod}(n - m, 3)$; freely adapted from [51].

Beyond the zone folding approximation

In a closer look on the figure I.8 left, the Kataura plot exhibits significant deviations from the $1/d_{Nt}$ master curve, with the presence of branches of chiralities. More

precisely, semiconducting nanotubes can be sorted in two categories, according to the value $+1$ or -1 of their number $q = \mathrm{mod}(n - m, 3)$. To study this phenomenon, one should take into account the trigonal shape of the dispersion curve around K points, instead of the circular symmetry that we have assumed implicitely [37, 51]. As seen on figure I.8 right, this effect will shift the S_{ii} transitions of a nanotube in different directions and proportions.

Excitons and self-energy

Another point that we have neglected until now is the electron-electron interaction. Indeed, the tight-binding formalism is based on the hypothesis of independent electrons. Due to the one dimensional structure of a nanotube, the electrons are strongly confined [52, 53], and this will amplify the correlation between them. Even if we cannot detail the many body quantum effects in such manuscript, we can single out the two main types of electronic interactions that will influence the optical properties of carbon nanotubes. They can be easily explained using a simple Coulomb interaction picture.

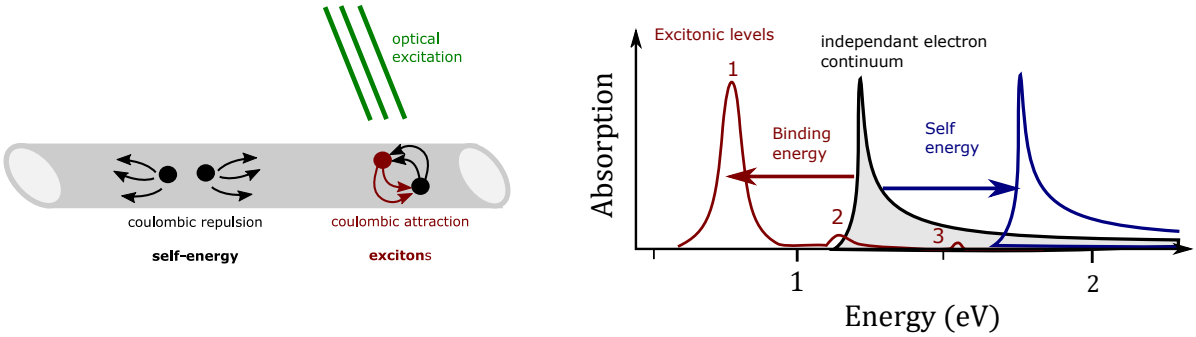

Figure I.9: Left: Artistic view of the effect of the two examples of correlations between electrons; Right: Representation of the opposite effects of excitonic binding energy and self-energy on the position of the Van Hove singularities.

The first effect is due to the electrostatic repulsion between electrons, which is called Coulombic self-energy [53, 54]. This phenomenon tends to destabilize the global system and thus increase the required optical transitions energies of around 1 eV for small diameter nanotubes. The second dynamic effect takes place upon photonic excitation of the material. When one electron is promoted into the conduction band, it leaves a vacancy, called a hole, into its initial quantum state. The promoted electron and the remaining hole can be treated as pair of opposite charge quasiparticles that will attract each other. Such a hydrogen-like couple of quasiparticles is called an exciton [55]. In small carbon nanotubes this charged pair has a binding energy of around 400 meV, that is around 100 times larger than in usual inorganic semiconductors [56]. This excitonic energy contribution is of the same order of

magnitude as the calculated gap for independent electrons, that is around 1.5 eV. Thus, the exciton behavior is dominant, and the optical properties of nanotubes have to be understood as transitions between excitonic levels. As a consequence of this attractive interaction, the excitonic states are located below (respectively above) the continuum of states in the conduction band (respectively the valence band). In conclusion, self-energy and excitonic effects are large but contribute in opposite directions (see figure I.9) to the global transitions energies. This is a reason why the tight binding model provides relatively accurate transitions energies despite the importance of the correlation effects [57].

1.5 Thermodynamical growth conditions

The first batch of nanotubes discovered by Ijima [14] was produced through arc discharges onto graphite electrodes in both high pressure and high temperature conditions. Their relatively uncontrolled method gave birth to a variety of carbon structures, including amorphous carbon. As the interest for carbon grew over the years, numerous research groups put a lot of effort into improving and diversifying the synthesis techniques. One can cite the work of Thess *et al.* that first managed in 1996 to create ropes of aligned single walled carbon nanotubes, with a small diameter distribution, through a LASER vaporization technique [58].

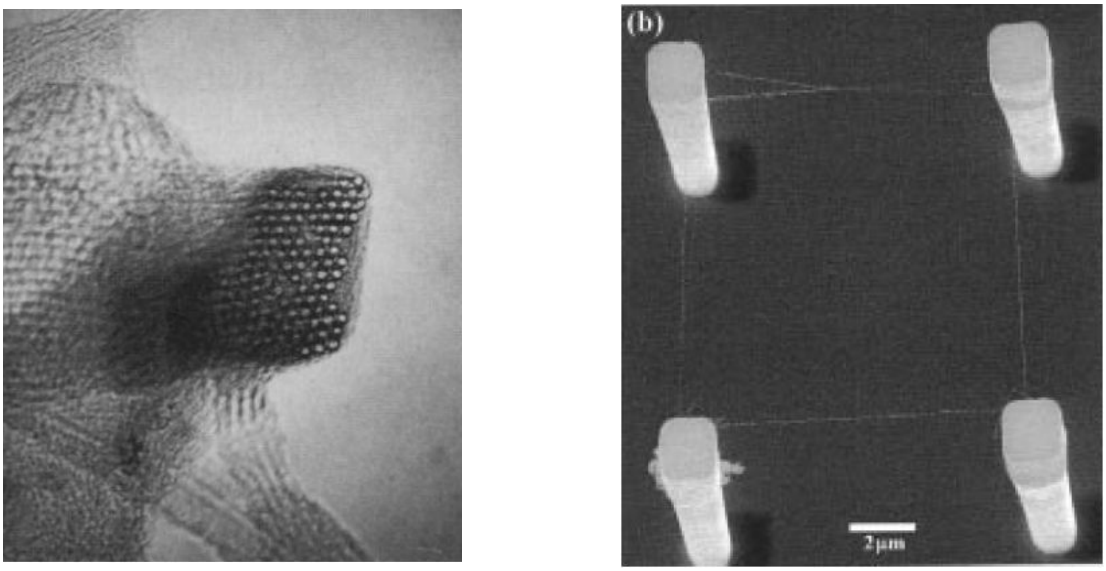

Figure I.10: Left: SEM image of a rope containing around 100 single walled nanotubes from the LASER ablation technique [58]; Right: SEM image of a square of suspended SWNT bridges produced by CVD [59]

Similarly to other carbon materials, the synthesis of carbon nanotubes requires three things: a source of carbon atoms, favorable thermodynamics conditions [60],

and a catalyst particle (at least for single walled carbon nanotubes). Here, the catalyst has to be of nanometric size, as its very structure has a great influence on the final material geometry. As for the thermodynamics conditions, they consist in bringing the adequate pressure and temperature to turn the carbon source into carbon nanotubes. These required thermodynamics conditions may be reached by physical or chemical growth process. The two examples presented above are physical routes: an electric (Arc discharge) or a powerful light source (LASER radiations) is used to vaporize graphite. Those high energy sources are able to reach very high local temperatures (3000 °C for at the surface of the arc electrode [61]) that provide a very good crystallinity [62]. However, they are only able to synthesize large diameter nanotubes, with a bandgap below 0.9 eV.

Then, chemical methods based on classical Chemical Vapor Depostions techniques (CVD) have been developed [63]. In CVD, transition metal catalysts nanoparticles are exposed to a carbon-rich gas phase under the proper pressure and temperature conditions. The gaseous carbon-rich molecules will then turn into nanotubes at the surface of catalyst particles. Along with nanotubes bundles, CVD allows the direct fabrication of single nanotubes that can be readily used for optoelectronics studies [64]. This technique offers great promises in industry, as it is easily scalable and could provide large quantity of low-cost nanotubes materials.

The two most developed CVD techniques are called HiPCo and CoMoCAT. HiPCo stands for High Pressure catalytic decomposition of Carbon monoxide catalyst [65]. This methods is particular, as both the iron pentacarbonyl catalyst $Fe(Co)_5$ and carbon monoxide are under gaseous form. This inexpensive technique reaches nowadays a 70 % yield of single walled nanotube production, with very small diameters between 0.7 and 1.1 nm. Moreover, the produced tubes can be several micrometers long and can be readily used without any purification step. CoMoCAT is for Cobalt Molybdenum catalyst [66]. Here, the catalysts are cobalt solid nanoparticles. This sample will be mostly used in this thesis, as it produces quasi monochiral samples, with a majority of 0.8 nm (6,5) nanotubes and very few other chiralities with close diameters.

However, these techniques still provide several chiralities in the same batch. This problem has been adressed by postprocessing techniques, to sort out nanotubes in liquid phases, extracting one chirality at a time [67–69]. Some of these techniques are now advanced enough to be used at the preindustrial stage. However, they are still consuming too much time and money to offer low cost monochiral material for optoelectronics. Indeed, several groups are still working on selecting the good catalyst alloys in order to produce monochiral samples. In 2014, two groups [70, 71] independently achieved that goal for two chiralities of nanotubes.

2 Quantum and optical properties of tetraphenylporphyrin molecules

Tetraphenyl porphyrin molecules are widely used artificial dyes that have been inspired by nature. Due to its very efficient light absorption and emission, it has been massively used in this Phd. In a very similar manner to the previous section, this one starts with a general introduction of the general chlorophyll class of molecules. Then, a progressive description of the structural, electronic and optical properties of tetraphenyl porphyrin will be done in order to understand the origin of such remarkable optoelectronic characteristics.

2.1 Generalities on natural dyes and chlorophyll derivatives

The name porphyrin comes from the Greek word *porphura* which means purple, as a reference for their intense colour. In fact, porphyrin and similar molecules are very common in living organisms. These molecules belong to the large class of dye molecules or fluorophores, that have the ability to efficiently harvest the visible light energy and turns it into usable electronic energy. The first parent of porphyrin to be isolated was the chlorophyll in 1817 by Caventou and Pelletier that were looking for the origin of colour in vegetal organisms. The first research interests in the porphyrins date back from the nineteeth century [72, 73].

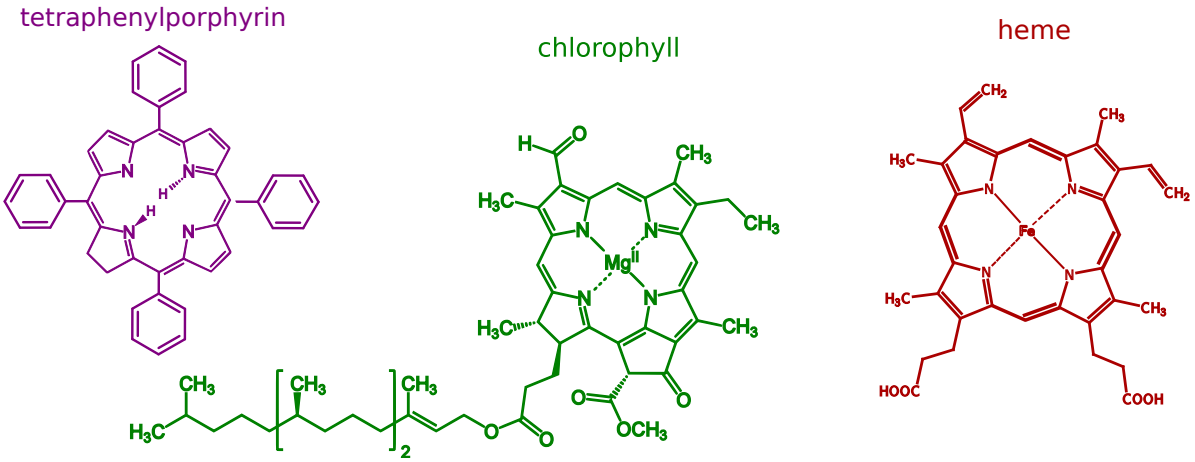

Figure I.11: Chemical representation of the structure of the tetraphenylporphyrin , the chlorophyll and the heme molecules.

Among other occurences, porphyrins derivatives were discovered as a pigment in Turaco bird feathers [74] or in human's blood (as heme, a component of red hemoglobin) [75]. One can notice that chlorophyll gives its green colour to leaves (*chloro* in Greek), that hemoglobin is red, while porphyrin is purple. Despite their similarities (seen in figure I.11), these molecules present a large chemical tunability,

that makes them very interesting for research and applications. Even now, the chemical research on porphyrins is still very active, in subject such as photodynamical therapy [76] and organic solar cells [77].

In vegetal organisms, the chlorophyll derivatives play an important role in the photosynthetic process. The figure I.12 displays the example of photosynthetic subunit LH_2, present in the *Rhodopseudomonas acidophilia* bacteria. This large molecular cluster is composed of two types of chlorophylls derivatives B800 and B850 along with another classical dye called caroten. Each of these molecules is designed to collect specific wavelenghts [78], turning light energy into electronic excitation. By ultrafast experiments, Herek and others researchers evidenced a complex energy pathway [79]. Every chromophore absorbs a part of the incident photons, generating excited electrons. These electrons are then transferred from the host molecule to its neighbor within a few picoseconds, to be eventually extracted from the LH_2 structure (see figure I.12). At the end of the cycle, the LH_2 is ready to absorb new incident photons. One can observe the very precise ordering of the different dye molecules in order to optimize the energy transfer cascade. After a series complex steps, this electronic energy reaches the biochemical reaction center where it will be stored for later bacteria's development.

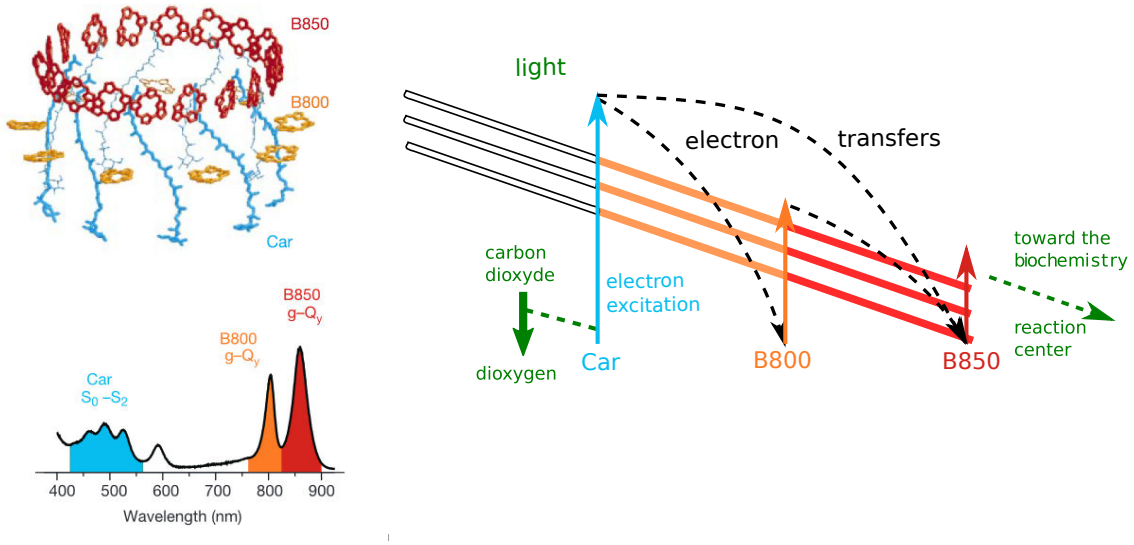

Figure I.12: Left: Chemical structure and absorption spectrum of the LH_2 photosystem; Right: Artistic view of the complex charge transfer mechanism in LH_2 that turn light into chemical energy during photosynthesis, adapted from [79] and [80].

The complexity of this mechanism along with the wide tunability of the chlorophylls properties inspired numerous researchers [80–82]. Furthermore, it demonstrates the natural ability of porphyrins to efficiently harvest light and transfer its

energy to its neighboring environment. This justifies the choice of tetraphenyl porphyrin to create organized nanoassemblies with carbon nanotubes.

2.2 Structural and geometrical properties of porphyrins

The base element of the tetraphenylporphyrin (TPP), called the porphine core, is made of four symmetric pyrrol subunits that are linked by methyne bridges. As its derivatives presented above, the tetraphenylporphyrin has the ability to form a chelate complex by including a large metal atom (zinc, platinum, iron...) inside its macrocycle (see figure I.11). In absence of a metal, the porphyrin is called free-base porphyrin as it macrocycle only includes two hydrogens atoms. The porphyrin does not exist in the tetraphenyl form in nature: it is an artificial compound designed for chemical purposes. The first synthesis of meso-tetraphenylporphyrin was reported in 1941 [83], where the authors mixed the required pyrrols with benzaldehydes in order to get the phenyl substituents. The centre macrocycle is a conjugated structure, with delocalized π bonds. This conjugation forces the porphyrin structure to be planar.

In principle, the phenyls groups should also be included in the molecules plan in order to participate in the conjugation stabilization. However, phenyls are quite large substituents and their hydrogens are likely to be sterically repulsed by the pyrroles neighboring hydrogens [84]. Hence, the phenyls groups tend to oscillate very rapidly, forming an angle between 40 and 70° with respect to the macrocycle (as represented on figure I.14 a). This combination of a rigid electron-rich macrocycle and of flexible phenyls groups gives some adaptability to the TPP molecule. As a consequence, it is an ideal candidate for stacking on all kind of surfaces. Over the past forty years, researchers have studied the interaction of porphyrins with metal layers [85,86], DNA branches [87], liquid- liquid interface [88,89], carbon materials ...

2.3 Electronic properties of porphyrins

Simplified Hückel model

Similarly to graphene, a simple Hückel model, using a Linear Combination of Atomic Orbitals (LCAO) [90], is quite convenient to get a first insight into the porphyrin energy levels. As early as 1950, reseachers employed such a molecular orbital LCAO formalism to develop an extensive model of the porphyrin electronic structure [91,92]. The porphyrin macrocycle possesses 20 carbons, 2 nitrogens and 22 $2p_z$ electrons. However, only 18 of these electrons participate to the conjugation, as the nitrogens double bonds correspond to a cross-conjugation [93]. If we set aside the influence of the nitrogen atoms and the coupling with the phenyls, the porphyrin structure can be modeled as a cycle of 20 carbon atoms with 18 delocalized electrons (see figure I.13 below).

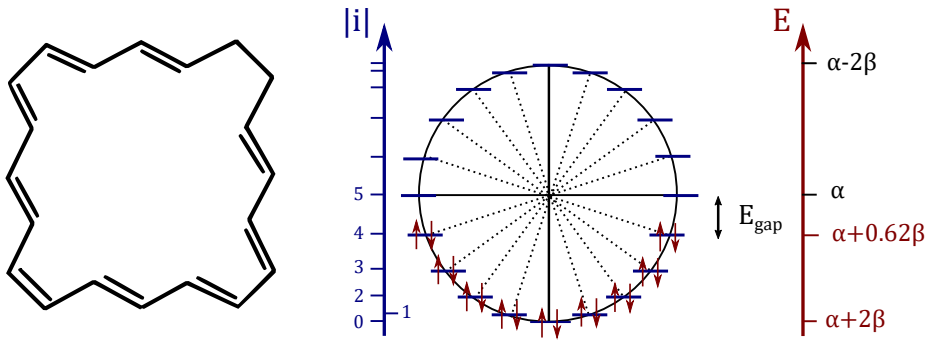

Figure I.13: Left: Model of the TPP as a 20 carbon atoms macrocycle with 18 π electrons; Right: Electronic diagram according to Hückel theory [94] representing the occupied and the empty states as a function of their quantum number absolute value $|i|$ and their energy.

According to Hückel theory, the ith level of such cyclic system has an energy of:

$$E_i = \alpha + 2\beta \cos\left(\frac{2\pi i}{N}\right) \quad ; \quad i = 0, 1, ..., N-1 \quad ; \quad \beta = -2.62 \ \text{eV} \tag{I.27}$$

with N the number of involved carbon atoms and β the electron exchange integral associated to a carbon-carbon bond. The number i can be regarded as the quantum number associated to the corresponding level. As seen on figure I.13, this allows to set up the porphyrin energy diagram and to place the 18 available π_z electrons. Particularly, this determines the Highest Occupied (HOMO) and the Lowest Unoccupied (LUMO) Molecular Orbitals. The gap between these two states can be estimated with the formula [94]:

$$\Delta E = 2\beta \left[\cos\left(\frac{2\pi|i|_{LUMO}}{N}\right) - \cos\left(\frac{2\pi|i|_{HOMO}}{N}\right)\right] \tag{I.28}$$

where $|i|$ is the norm of the corresponding level number. This formula indicates that the gap gets smaller as N increases, with the HOMO and the LUMO levels getting closer. This general behavior explains why the most efficient dye molecules commonly have a large chemical structure with many delocalized π bonds (as for the carotene on figure I.11). Indeed, as the the HOMO and the LUMO levels get closer, the allowed optical transitions move to lower energies and the molecule starts to absorb light in the visible region. For the N=20 carbon atoms and the 18 electrons to be placed, this simple model provides $|i|_{HOMO} = 4$ and a gap value of 1.62 eV, which is not so far from the real TPP optical bandgap of around 1.95 eV.

Extensive independent electron calculation

However, this Hückel calculation is too simplified to explain the complex electronic density of states and absorption properties (position, amplitude and width of the energy bands) of TPP. Among other considerations, the influence of the nitrogen atoms and of the phenyls groups should be considered. Over the years, many attemps to calculate the porphyrin electronic levels have been performed [91, 95–98]. On figure I.14 c), we can see one example from Palumno *et al.* [99] of a more extensive model. Instead of Hückel LCAO model, they used an independent electron Density Functional Theory (DFT) to find the energy levels. We see on I.14 c) inset, that their level diagram presents a degenerate LUMO / LUMO +1 level and two separated HOMO and HOMO -1 levels. From these levels, the evaluated TPP bandgap is of 1.7 eV. However, there is still a debate on the value of the independent electron TPP bandgap, as other models recently predicted much higher values (up to 4 eV) [99].

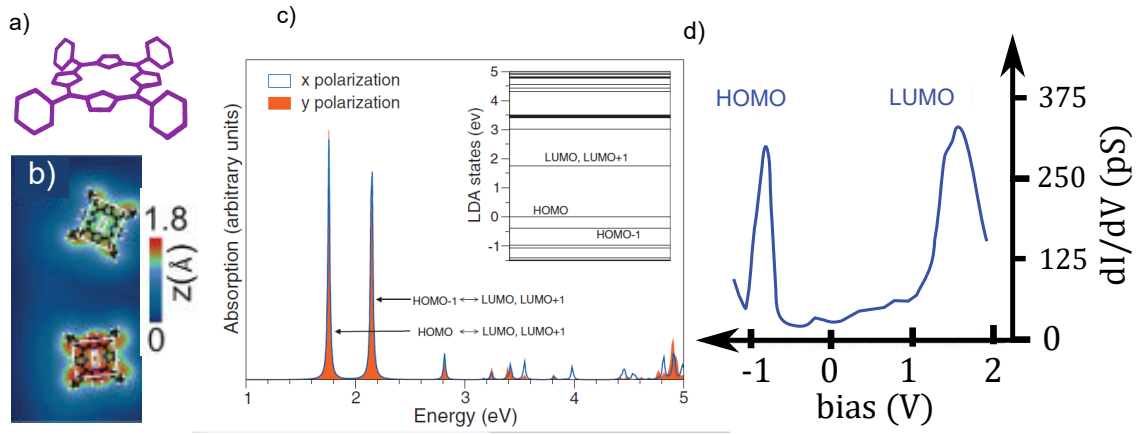

Figure I.14: a: Geometrical representation of the porphyrin with its four phenyl-groups tilted; b: STM topological image of two porphyrins on a gold surface [100]; c: Calculated absorption spectrum of tetraphenylporphyrin within the independant electron DFT calculation; Inset: The energy levels, from [99]; d: Scanning tunneling spectroscopy over a porphyrin on a gold surface, adapted from [100].

In a Fermi golden rule description, the authors of the article [99] calculated the interaction matrix elements to determine the allowed optical transition. As seen on figure I.14 c), their calculated absorption spectrum of TPP exhibits two main optical transitions in the visible region: the HOMO→ LUMO/LUMO+1 at 1.75 eV and the HOMO-1→ LUMO/LUMO+1 at 2.2 eV. These large bands lying just above the gap are very similar to the experimental ones, presented on the spectra of functionalized porphyrins (such as chlorophyll, see figure I.12). However, we will see that tetraphenylporphyrin spectrum exhibits large deviations from this independent electron absorption diagram.

Finally, as for carbon nanotubes, the independent electron energy levels description can be confronted with the experimental data from scanning tunelling spectroscopy. On I.14 b) and d), we see the work from Pham *et al.* [100], where the authors scanned over a single tetraphenylporphyrin on a gold surface. The density of states extracted from tunneling conductance measurement shows a large LUMO band and a sharp HOMO band that present similarities with the previous DFT predictions.

2.4 Importance of the electron correlation and its optoelectronic consequences

Absorption spectra of porphyrins

On figure I.15 left is represented the absorption spectrum of the free base TPP (H_2TPP) and of its complex (ZnTPP). H_2TPP exhibits four weak transitions in the visible part, while the ZnTPP presents only two bands. Those bands are very common in chlorophyll derivatives and are called the Q bands [101]. In 1956, Platt remarked that the geometry of H_2TPP has a two-fold symmetry while the metallic porphyrin has a four-fold one. Using a semi-empirical model, he demonstrated that the symmetry breaking could explain the splitting of the Q bands in H_2TPP. Thus, he called the two lowest ones $Q_x(0,0)$ and $Q_x(1,0)$, and the upper $Q_y(0,0)$, $Q_y(1,0)$ [102] (more details on figure I.16). This set of numbers (α,β) represents the different vibronic levels [103] associated to each transition. For H_2TPP, in dichloromethane, the respective energy position of these four bands are 1.91, 2.09, 2.25 and 2.40 eV.

Yet the main optical transition, called the Soret (or B) band occurs in the near UV region at 2.95 eV. The Soret band of TPP has a molar extinction coefficient of 4.10^5 $cm^{-1}mol^{-1}L$, which is very large. It is higher than the value for most classical dye molecules, that usually ranges between 10^3 and 10^5 $cm^{-1}mol^{-1}L$. For example, anthracene has a value of 9000 while phthalocyanine reaches $1.6.10^5$ $cm^{-1}mol^{-1}L$ (among others, [104]). As for the Q bands, this transition is splitted in two contributions, B_x and B_y [99], but they are nearly degenerate.

Historical four orbital's model

We can see that the precedent independent electron models could not explain the amplitude and the position of such optical transitions, especially in the UV range. In 1969, Gouterman suggested a semi-empirical model to reproduce the absorption spectrum of porphyrins [105]. Based on the symmetry of the porphyrin molecule, he suggested to mix the four main orbitals (HOMO-1 , HOMO , LUMO and LUMO+1) to create four new states b_1, b_2, c_1, c_2. Studying the selection rules between such states, he predicted the existence of two allowed transitions in the UV region, B_x and B_y, and two nearly forbidden ones in the visible region, Q_x and Q_y (see figure I.15 right).

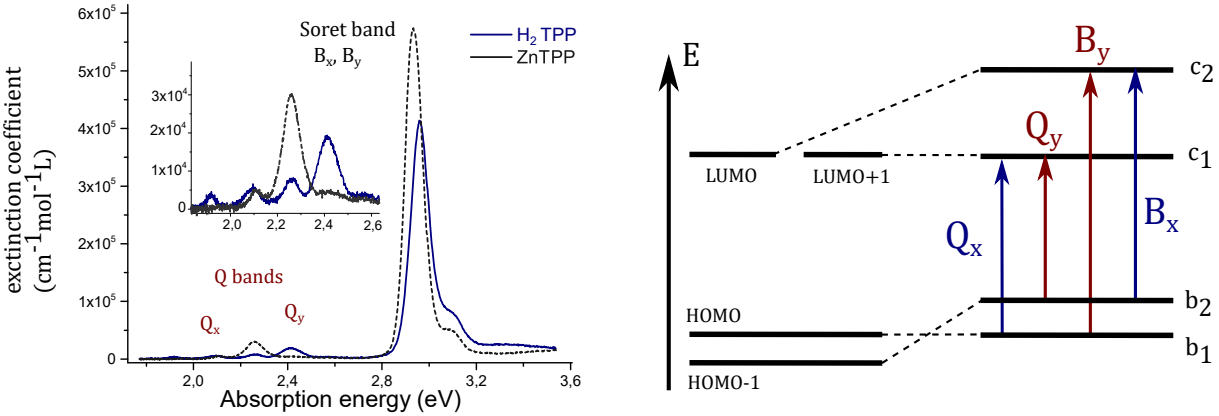

Figure I.15: Left: Optical absorption spectrum of the free base (blue) Zn (black dots) tetraphenylporphyrin in dichloromethane; Right: Transition from the LCAO molecular orbitals to the Gouterman's mixed electronic levels and the four allowed optical transitions, adapted from [105] and [106].

However, Gouterman stated that his model was not able to predict the relative position of B_x (and Q_x) with respect to B_y (and Q_y) [105]. In 1957, Weigl demonstrated by polarization spectroscopy [107] that the actual energy positions of the bands verify Platt's attributions [102]: Q_x, Q_y, B_x, B_y (in the ascending order).

Full model including of electron correlations

A few decades later, Palumno and coworkers explained the success of such semi-empirical theory by an extensive complex calculation [99]. By including the electron correlations effects into a DFT calculation, they managed to reproduce the symmetry considerations from Gouterman and explain the tetraphenylporphyrin excitation spectrum. As for carbon nanotubes, the consideration of electron-electron and electron-hole interactions are essential to understand the interaction between light and tetraphenyl porphyrin molecules.

2.5 Excited states relaxation of tetraphenylporphyrin

Photoluminescence properties

Upon high energy optical excitation, the TPP has the ability to re-emit light at a lower energy. This process is called photoluminescence. On figure I.16, we detail the photoluminescence (PL) spectrum of the TPP, superimposed with its absorption spectrum. The PL diagram presents two broad lines at 1.72 and 1.90 eV, that correspond to the $Q_x(0,1)$ and the $Q_x(0,0)$ bands. No sensible PL signal originates from the Q_y or the B band, at higher energies. Upon light excitation, the PL diagram of a molecule is deeply connected to the electronic relaxation kinetics.

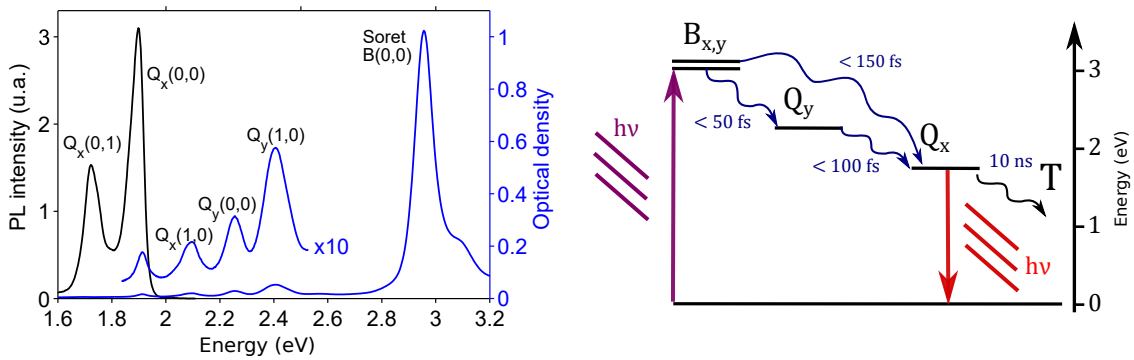

Figure I.16: Left: Optical absorption spectrum (blue) and photoluminescence spectrum (black) of the tetraphenylporphyrin in micelles, adapted from [108]; Right: Electronic relaxation diagram of the TPP upon excitation on the Soret band, adapted from [109].

In 2002, Baskin and coworkers performed an extensive time resolved study of the TPP electronical dynamics [109]. They established the diagram presented on figure I.16 right. Upon excitation on the B state at 3.1 eV, they showed that the system relaxes to the Q_y levels in less than 50 fs and in the Q_x band within 150 fs. At the end of the relaxation, the return to the ground state can be done by two competitive processes. The first one is the direct emission of a photon (fluorescence) from the Q_x states, while the second is a nonradiative decay through the triplet (T) states. Time resolved photoluminescent experiments allowed to show an exponential luminescence decay of around 10 ns [110, 111], limited by the competition with the triplet pathway. For TPP in organic solvents, the fluorescence yield Φ_f has a value around [112]:

$$\Phi_f = \frac{N_{\text{photon-emitted}}}{N_{\text{photon-absorbed}}} \simeq 10\ \% \tag{I.29}$$

2.6 Polarized response of TPP

As we mentioned above, the TPP has a two-fold rotational symmetry, due to the presence of two hydrogen atoms on the pyrrole groups, at the center of the macrocycle. The two directions, Ox and Oy, are defined as shown on figure I.17 left. They are respectively parralel and perdicular to the hydrogen axis. This symmetry is the reason of the coexistence of the x and y states for the B and the Q bands. Indeed, we can see on figure I.17 left that Palumno's many-body DFT calculations [99] managed to reproduce the symmetry discrimination of each state.

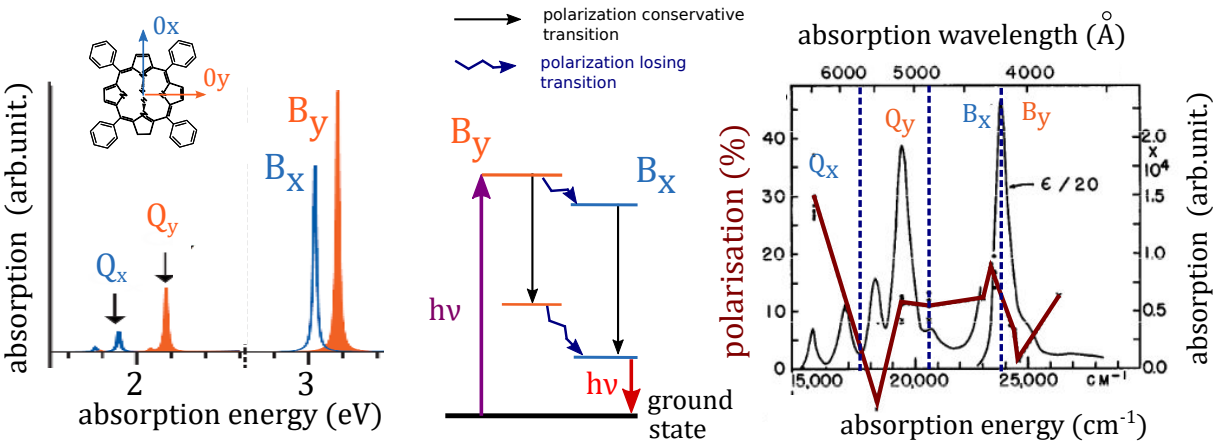

Figure I.17: Left: Representation of the polarized Soret and Q bands from the TPP as calculated in [99]; Center: Exciton photoluminescence diagram illustrating the effect of relaxation on the polarization memory; Right: Absorption and polarization photoluminescence diagram of the TPP, from [107].

Experimentally, this orientation splitting has consequences on the polarization resolved absorption and photoluminescence properties of TPP. On figure I.17 center, one can see the excitation diagram of TPP expressed as excitonic transitions, instead of electron levels. According to the selection rules of the dipolar interaction, there is a strict correspondence between the optical polarization and the allowed excitons transition. Whatever the excitation level, it was shown before that the TPP emission was essentially done on the Q_x energy levels. Hence, if TPP is excited using Oy polarized photon at 2.91 eV, the B_y created exciton would have to lose its symmetry before collapsing and emitting a Ox polarized photon [113].

This effect has been evidenced as early as 1957 by Weigl, using polarized photoluminescence spectroscopy [107] (see I.17 right, the details of such experiments will be discussed in the next section). When TPP was excited on a B_x or Q_x transition, he observed that the polarization of light was partially conserved through the process (*i.e.* the value of polarization is positive). However, when exciting on Oy transitions, the orientation was lost (the value of polarization was close to zero). These results contributed to understand the symmetry and the energies of the different optical transitions of TPP. These effects will be extensively discussed in the chapter 4.

3 Employed experimental techniques

3.1 Optical absorption spectroscopy

The absorption spectroscopy is a very common technique in material physics and analytical chemistry. As explained before, it gives a rapid access to the allowed optical transitions and consequently to the energy levels of the studied materials. The experiment consists in directing a monochromatic light beam onto the sample and measuring the intensity of light I that passes through the sample. This intensity is then compared to the initial intensity I_0, to measure the proportion of photons that were absorbed by the material. The physical quantity that is studied is called the Optical Density (O.D.):

$$\text{O.D.} = -\log(T) = -\log\left(\frac{I}{I_0}\right) \tag{I.30}$$

Repeating the procedure over a set of different wavelengths allows to obtain the spectroscopic response of the sample. One may as well repeat the absorption experiment over times to obtain kinetic information during a chemical reaction.

In our laboratory, we use a Lambda 950 spectrometer from Perkin-Elmer that is equipped with two opical lines. As seen on figure I.18, it allows a parallel measurement of I, on the line containing the real sample and I_0, measured after passing across the reference line (see figure I.18). This spectrometer possess several lamp sources and several photodetectors to scan from the UV (300 nm) to the near infrared (1600 nm) region. In most of this work, we use $L = 1$ mm suprasil quartz cuvettes (see I.18 right) that are designed to have a minimum absorption. This material is also quite useful for luminescence experiments as its purity guarantees that it does not emit light.

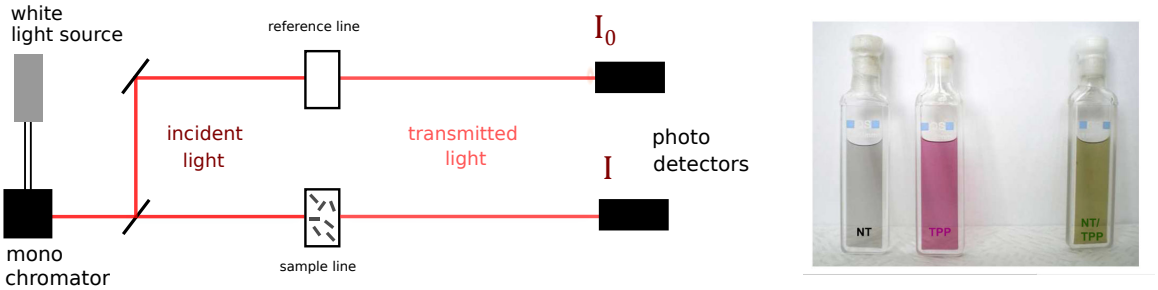

Figure I.18: Left: Schematic representation of a double beam absorption spectrometer that is used in this work; Right: Suprasil optical cuvette containing nanotubes and porphyrins molecules and hybrid samples in surfactants.

According to the classical electromagnetism laws, when an electromagnetic wave propagates through a dielectric medium its intensity is decreases exponentially with the optical path L:

$$\mathrm{I} = \mathrm{I}_0 \exp\left(\frac{-4\pi\kappa L}{\lambda}\right) \quad ; \quad \mathrm{O.D.} = \frac{4\pi\kappa L}{\lambda} \tag{I.31}$$

where κ is the imaginary part of the medium refractive index. For a dilute solution (*i.e.*for optical densities smaller than 1), the refractive index is proportional to the concentration c of the studied nanoobjects, and the optical density follows the Beer-Lambert's law:

$$\mathrm{O.D.} = \varepsilon_0 L c \tag{I.32}$$

where $\varepsilon_0(\lambda)$ is the molar extinction coefficient (expressed in $\mathrm{cm}^{-1}\mu\mathrm{mol.L}^{-1}$). Thus, the amplitude of the absorption peaks is a indirect measurement of the nano-objects concentration. As we will see later, the position and the width of the peaks also provide valuable information: on the environment of the objects and their possible aggregation.

3.2 Photoluminescence spectroscopy

The photoluminescence (PL) is a powerful technique that is widely employed in semiconductor physics, even for bulk opaque samples for which any absorption measurement is prevented. It is also a common tool in analytical chemistry. As already mentioned before, the process of photoluminescence is deeply connected to the electron dynamics of the photomaterials. It starts with the absorption of a high energy photon and ends with the emission of a low energy photon. In between, the absorbed photon promotes the electron (or the exciton) to a an empty state. Then, this electron loses energy and falls into the bottom of the conduction band. As for absorption, it provides a useful insight into the electronic properties of a material and its environment. However, it is more restrictive than absorption, as it is limted to ligth emitting materials. As described for carbon nanotubes, PL signal is very sensitive to aggregation, that usually modifies the relaxations pathways and decreases (quenching) or increases (enhancement) the photoluminescence quantum yield [114].

Figure I.19 left details the homebuilt setup that is used to study photoluminescence. In order to excite resonantly different nanoobjects, several lasers sources can be used (at 405, 532, 635 and 905 nm). If an extensive spectral response of a material is required, we may also use a 1000 W white xenon lamp coupled to a monochromator (spectrapro 2150i , Roper Scientific). This configuration allows to pump the sample with a continuous set of wavelentghs between 350 and 800 nmn, with a resolution of 3-5 nm and a spectral power density of 50 μW/nm (against several mW for a LASER source). Monitoring PL signal as a function of the pumping wavelength is

called photoluminescence excitation (PLE) spectroscopy. To collect the light emission from the sample, we use a spectrometer that combines a monochromator and a photodetector. If we want to monitor light in the visible region (such as TPP emission), a Peltier cooled CCD camera is employed (Pixis, Roper scientific). When an infrared signal is studied (such as nanotubes luminescence), we use a liquid nitrogen cooled InGaAs photodetector (Oma V, Roper scientific).

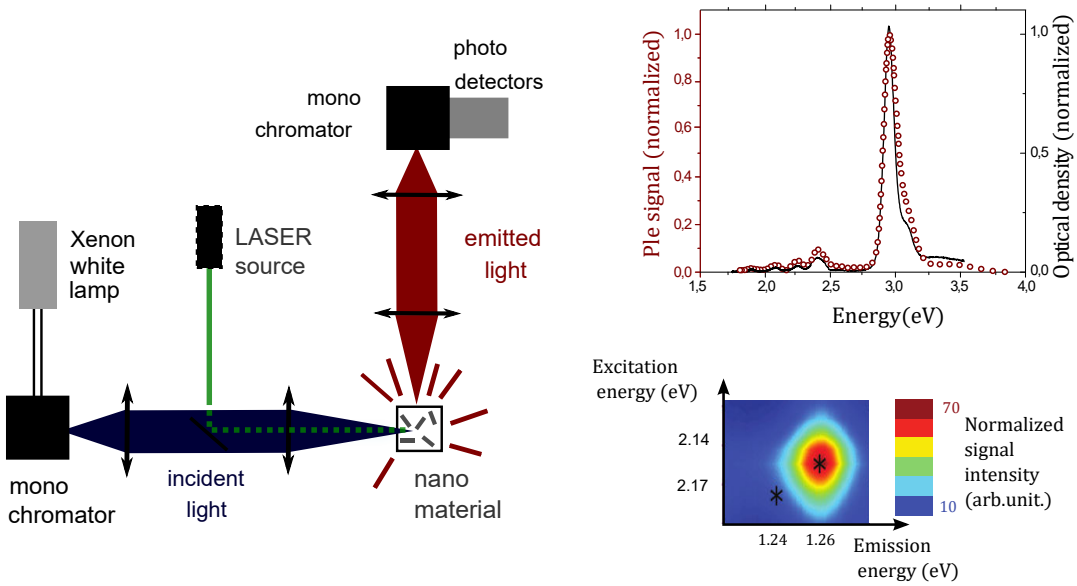

Figure I.19: Left: Schematic representation of the photoluminescence excitation setup; Right top: Absorption and PLE response of a micelle suspended TPP sample; Right bottom: Example of a 2D resonance on a PLE Map.

On figure I.19 top right, one can see the superimposition of the absorption spectrum (black) of a TPP solution in sodium cholate and its PLE signal recorded on the $Q_x(0,1)$ band emission at 1.72 eV. On a PLE spectrum, the intensity measured by the photodetector is normalized by the incident light power (or number of photons) at each excitation wavelength. We see that the PLE signal exhibits the same resonances as the absorption response, at corresponding energies. Being able to confront both signals on the same sample is important to control the sample quality and its evolution (over time or upon functionalization). Finally, one can display the PL and the PLE response of a sample on the same graph (see figure I.19 bottom right). This is called a photoluminescence excitation map, and presents itself as a 2D contour plot. The colour scale corresponds to the normalized number of photons, while the x and y axes are respectively the emission and excitation energies. This tool turns to be very practical to study the correlation between the absorption and emission properties of a sample. We will see in the next section that is is commonly used to

single out the different chiralities of nanotubes.

3.3 Time resolved Photoluminescence

In this work, we also studied the dynamics of light emission, especially from porphyrins. This technique is particularly sensitive to the aggregation behavior of molecules. Due to the proximity of aggregated molecules, the electronic excitation may relax through different relaxation pathways (either radiative or non radiative). As a consequence, the quantum yield and the luminescent dynamics of the dye will be modified. Such processes are monitored through a time resolved photoluminescence experiment (TR-PL, detailed on figure I.19 right). It consists in an adaptation of the PL setup to work on pulsed synchronisation regime. A supercontinuum picosecond laser (Fianium), coupled to a monochromator is used to excite the sample. The photodetector is replaced by a fast avalanche photodetector that will monitor the delay between the trigger pulse the emitted photon. An acquisition card (picoquant) is then used to create the statistical diagram of photon impacts as a function of time delay (see figure I.20 right). In the present case, the experiments has a temporal resolution of 70 ps.

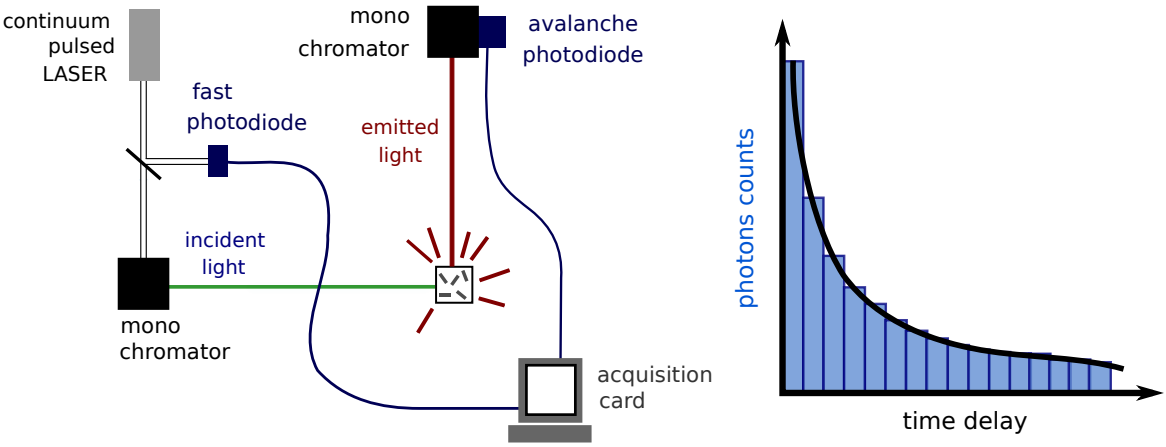

Figure I.20: Schematic representation of the photoluminescence excitation(left) and Time resolved photoluminescence (right) experiments.

For organic fluorescent dyes, the TR-PL response often exhibits an exponential behaviour, with a lifetime between one and a few tens of nanoseconds [115]. This monoexponential behaviour is indicative of single radiative pathway. Hence, the measurement of multiexponential components gives information on the aggregation state of the sample [116].

3.4 Anisotropy measurement

As mentionned ealier, the optical selection rules may induce a direct connection between the polarization of light and the electronic absorption spectrum of a nanobject. If this correlation is lost during the electron relaxation, the final emitted photon may have each polarization with equal probability: this is called an isotropic emission. However, if the correlation is maintained through the process, it will induce an anisotropic emission diagram (such as in figure I.7). Hence, measuring the correspondence between the absorption and emission polarization gives information on the relaxation mechanism.

The measure of anisotropy is performed with a polarization resolved photoluminescence experiment (detailed in figure I.21 from [113]). Starting from the classical PL setup, one should add two polarizers, one before and one after the sample. Each of them is set up to have a vertical (V) and horizontal (H) position (i.e. 0 and 90°) with respect to the plane of the experiment. The anisotropy is the normalized difference between the parallel ($I_{\parallel}$) and the perpendicular ($I_{\perp}$) polarized intensities. However, these two quantities are inaccessible with a simple experiments.

Instead, we actually measure the four PL intensities, corresponding to every possible configuration of the two polarizers: VV, VH, HH, HV. The two last components are measured to evaluate the parasite polarization contribution induced by the optical components (lenses, cuvette, diffraction gratings, optical filters, photodetectors...). Thus, the anisotropy has to include a correction factor $G = I_{HV}/I_{HH}$. We can then evaluate the experimental anisotropy r:

$$r = \frac{I_{VV} - GI_{VH}}{I_{VV} + 2GI_{VH}} \quad ; \quad p = \frac{3r}{2+r} \tag{I.33}$$

This measure can be repeated for a series of excitation (PLE) or emission (PL) wavelengths. The total emitted intensity is expressed as $I_T = I_{VV} + 2GI_{VH}$. The polarization P is a physical value equivalent to the anisotropy (only used in figure I.17 right).

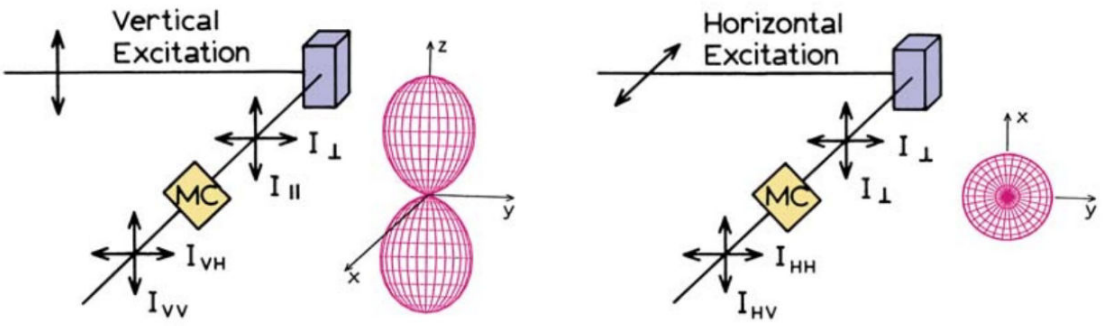

Figure I.21: Principle of polarization resolved photoluminescence to extract anisotropy , from [113].

This experimental anisotropy is not exactly the intrinsic value of each monitored nanoobjects. Indeed, when such experiment is performed on a bulk liquid sample, we need to take into account all of the orientations of the studied objects in their 3D environment. If the absorption and emission dipoles are fully parallel, it yields only $r_{\parallel}$=0.4, due to the isotropic distribution of angles. If they are fully orthogonal, the anisotropy will be $r_{\perp}$=-0.2. In a general case, the value lies between those extremities. From the value of r, one can have an indirect access to the intrinsic anisotropy and to the parallel and perpendicular intensity $I_{\parallel}$ and $I_{\perp}$. They can be extracted from the formulae [117]:

$$I_{\parallel}(\lambda) = \frac{r(\lambda) - r_{\perp}}{r_{\parallel} - r_{\perp}} I_T \quad ; \quad I_{\perp} = \frac{r_{\parallel} - r(\lambda)}{r_{\parallel} - r_{\perp}} I_T \tag{I.34}$$

Many interesting effects can influence the value of anisotropy, such as optical diffusion, near field effects [118], aggregation [119], radiative or non radiative energy transfer, and finally rotation of the nanoobjects. Particularly, the Brownian rotation of the studied objects can be an important source of depolarization for nanometric size objects. For a spherical objects of radius r in a medium of viscosity η, the rotational time is estimated to [120]:

$$\tau_r = \frac{4\pi\eta r^3}{3kT} \tag{I.35}$$

For a porphyrin of $r \simeq 1.4$ nm in dichloromethane (of $\eta = 4.1\ 10^{-4}$Pa.s) at 20 °C, the rotational time is estimated to $\tau_r \simeq 1$ ns. It follows that a TPP molecule can revolve 10 times around itself during its fluorescence lifetime (10 ns), losing the anisotropy information. To deal with this issue, one may use a very viscous solvent: the historical polarization experiments on TPP were performed in castor oil ($\eta = 0.65$ Pa.s) [107]. As we will see in chapter 4, another solution is to perform time-resolved polarization measurements and to look at the initial value of the anisotropy.

For carbon nanotubes, the high aspect ratio (length of around 500 nm) and the very short luminescence lifetimes (100 ps) allow to neglect the rotational depolarization. Hence, the polarization results that are shown on single carbon nanotube on figure I.7 right can also be performed on a bulk sample of nanotubes, as shown first by Miyauchi [117]. On figure I.22, we see the polarization resolved PLE spectrum of an ensemble of (6,5) carbon nanotubes, where we can clearly single out the parallel and perpendicular polarized transitions. Similar studies on nanotube/porphyrins complexes will be detailed in the chapter 4.

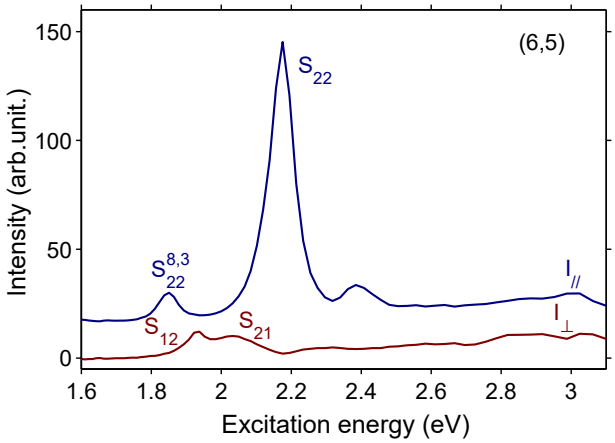

Figure I.22: Polarization resolved PLE spectrum of an ensemble of (6,5) carbon nanotubes (monitored on an emission energy of 1.26 eV), from [108].

4 Fabrication of porphyrin/nanotube hybrid objects with energy transfer properties

4.1 Functionalization of carbon nanotubes

Adsorption on carbon materials

We already showed that graphene and carbon nanotubes have very remarkable structural and electronic properties. As many forms of carbon, they are also interesting for their ability to adsorb physical or chemical elements. The research on adsorbtion abilities of carbon materials dates back from more than three centuries [121, 122]. More recently, people started to massively study the storage of gases and liquid into active carbon and coal derivatives [123] around 1920. Among the many topics studying the physicochemistry of carbon surfaces, one can also cite the removal of organic pollutants from waste water [124–127].

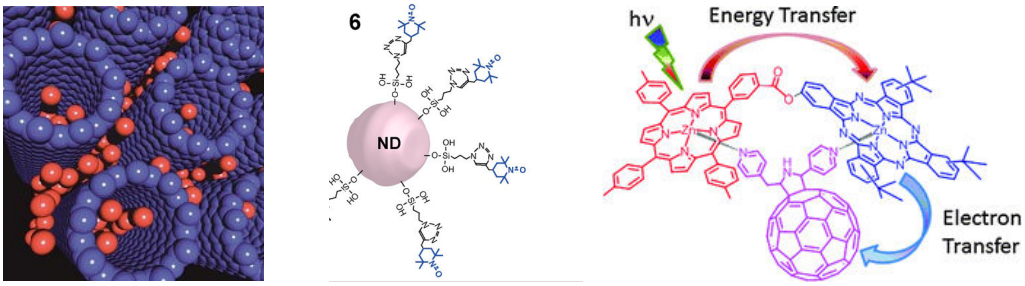

Figure I.23: Three example of adsorption on nanocarbon allotropes; Left: Hydrogen storage in a carbon nanotube from [128]; Center: Biocompatible functionalized nano diamond from [129]; Right: Electron transfer triad based on a modified fullerene. [130]

Bringing new functionalities to carbon nanoobjects

Covering carbon surfaces with molecules to bring new chemical functionnalities is a very developped research field. The functionalisation techniques can be based upon two phenomen: the physisorption or the chemisorption process. The first one is Van Der Waals interaction between the adsorbate and the carbon surface, with an energy below 1 eV. The second consists in a creation of a chemical bond between the two reactants, with an energy above 5 eV.

These techniques offer wide possibilities of material improvement. It may enhance their isolation (as surfactant for carbon nanotubes [131]) or favor their biocompatibility (as for nanodiamond [132] and fullerenes nano-onions [133]). Finally, numerous researchers have used functionnalization to modify the electronic properties of sp^2 carbon materials (as for fullerenes [134] or graphene quantum dots [135]). For instance, it can amplify the electron transfer properties of fullerenes in organic solar cells (see figure I.23 right, [130]). All of these historical adsorption techniques have inspired the recent physical and chemical research of functionalization of carbon nanotubes and graphene.

Covalent functionalization

Covalent functionalization is the most intuitive way to modify carbon surface properties. Indeed, it is based upon the classic organic chemistry reactions: ozonation, hydrogenation, alkylation, halogenation.... SWNTs have a large sp^2 carbon surface that is an ideal platform for molecules to adsorb and interact. [136]. Most of the reactions consist in breaking some of the double bonds to replace them by another chemical function (see figure I.24 left). This covalent technique has been employed very early to increase the solubility of nanotubes in solvents [137, 138].

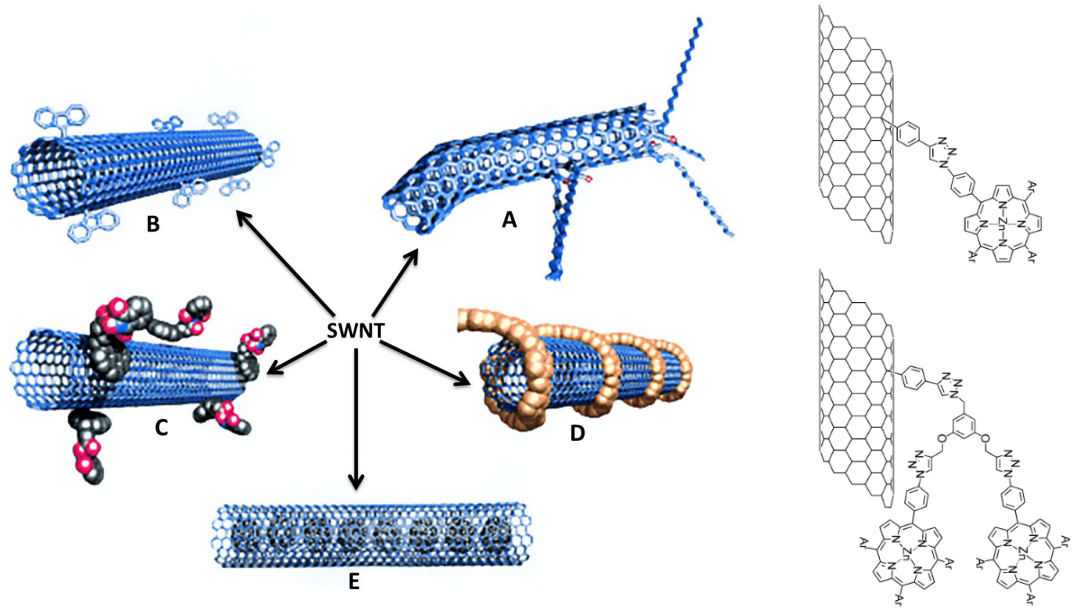

Figure I.24: Left: Covalent and noncovalent examples of SWNTs functionalization: A) Defect-group functionalization, B) Covalent sidewall functionalization, C) Noncovalent exohedral functionalization with surfactants, D) Noncovalent exohedral functionalization with polymers, and E) Endohedral functionalization from [139]; Right: Example of click chemistry that allows a minimal defects creation, from [140]

However, this technique induces the replacement of the sp^2 double bonds by sp^3 carbons bonds, destroying the periodicity of the carbon lattice and the electronic properties of carbon nanotubes or graphene. This provokes a fall of the electron mobility and of the electronic absorption transitions. Thus, this technique cannot be used whenever the intrinsic properties of electrons are required. It remains of great interest for composite materials, for heat conduction or mechanical purposes.

For optoelectronics applications, one way to cope with this problem is to keep the number of sp^3 defects to the minimum. Techniques such as click chemistry [140] are studied to reach a large covering with a very low number of binding anchors. Finally, researchers have learned to play on the funcionalization extent to control the number of defects and modify the carbon nanotubes electronic properties [141]. Instead of killing their excitonic properties, a low level of defects may enhance their luminescence properties [142] of modify their quantum emission properties [143].

Noncovalent functionalization

The noncovalent fonctionnalization is based upon a weak Van der Waals electromagnetic interaction. It consists in a dipole-dipole interaction between the electrons

of the two objects. This explains why surfactant molecules with long hydrocarbon chains couple easily to the surface of carbon nanotubes. Among candidates for non covalent fonctionalization, the large conjugated molecules (such as porphyrins) are very popular. They easily couple to the sp^2 carbon surface due to their large number of available π electrons. This process is called π-stacking [144], as it involves an overlap between the π orbitals of the two materials, at the surface of contact.

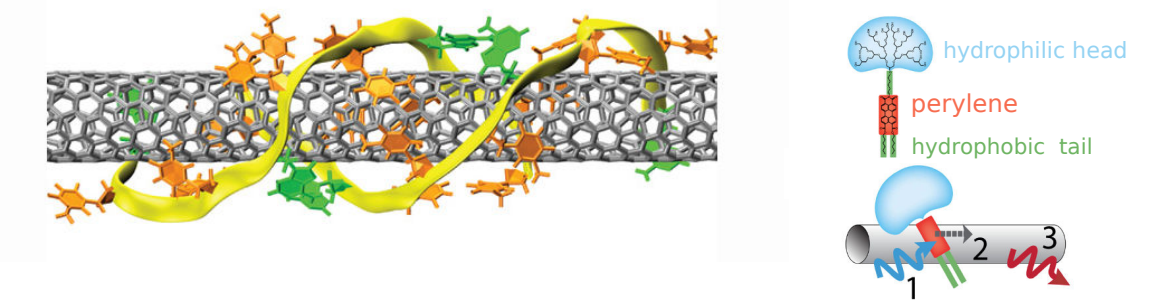

Figure I.25: Left: Representation of DNA wrapped SWNT [145]; Right: Interaction of perylene based surfactant with a carbon nanotube [146].

To stack molecules onto nanotubes, the weakness of this interaction is a drawback. Indeed, other effects such as nanotube-surfactant encapsulation, molecule-molecule stacking or nanotubes self aggregation will always compete with the desired noncovalent functionalization. As we will see later in this manuscript, this may limit the reaction yield. For the same reasons, the molecules-nanotubes compounds may also exhibit a poor stability over time.

On the other hand, this weak interaction has the advantage of preserving the structural and electronic properties of the nanotube. This the reason why the wrapping of nanotubes with polymers (such as PFO [147]) or with surfactants are the two best options to disperse them into a liquid sample, while preserving their absorption and luminescence properties. Among the many examples of noncovalent fonctionalization, the wrapping of nanotubes with DNA branches is an interesting alternative [148]. Indeed, DNA is a biocompatible, chiral and highly tunable molecule that can be used to isolate different nanotubes chiralities [145] and to include them as luminescence bioprobes [149].

As for the covalent functions, a noncovalent coating may bring new photoactive functionalities. For instance, the excitation of a surfactant on its UV absorption may induce a photodoping effect leading to a midgap luminescence of the nanotube [150]. In addition, PFO [147] or porphyrin [151] polymers can absorb light and non radiatively transfer their energy to the nanotubes. We can also cite the work from Ernst and coworkers that modified the structure of a surfactant to include a perylene dye inside. This molecule will also transfer its energy to the nanotube ([146], see figure I.25 right).

Endohedral functionnalization

Finally, a last technique to functionalize a nanotube is the endohedral insertion. As shown on figure I.24, it consists in integrating small molecules [152] or fullerenes [153] inside a nanotube. Endohedral functionnalization is a simple technique: it happens naturally when a liquid is brought in contact with a nanotube powder [152]. One major drawback of the endohedral technique is the limitation to small molecules and to a low coverage concentration due to the diameter of carbon nanotubes.

The inclusion of solvent molecules will modify the electronic properties of the host. Thus, the absorption resonances of the nanotube will broaden and the luminescence yield will decrease [154]. However the filling of nanotubes with hydrocarbon molecules prevents this effect and result in an intense luminescence signal from the nanotube [152]. Recently reasearchers have used the large aspect ratio of nanotube to create linear aggregates of molecules and obtain giant scattering [155] or non linear optical properties [156].

4.2 Micellar suspension of SWNTS

Necessity of a noncovalent protecting layer around nanotubes

Whatever the synthesis technique, the commercial nanotubes samples are gathered into a powder. In this structure, the nanotubes are attracted to each other through Van Der Waals forces between their adjacent surfaces (see figure I.10). This attractive interaction can reach 150 eV for two tubes of around 300 nm while the thermal agitation energy is only a few tens of meV. After Ijima's discovery [14], researchers put a lot of efforts to break apart bundles and to solubilize nanotubes, using in organic solvent and matrix polymers [137, 157, 158]. As seen on figure I.26, it was enough to monitor the absorption resonances predicted by tight binding calculation.

However, the first true isolation of nanotubes was achieved in water suspensions of micelles by Bachilo and coworkers [131, 159]. They sonicated a powder of nanotubes in presence of sodium dodecyl sulfate micelles (SDS). SDS molecules are amphilic, which means that they have one hydrocarbon tail that will interact with the surface of the nanotube and one ionic head that will connect with water molecules. Upon strong sonication, they form a protective shell that efficiently compete with self bundling effects. This non covalent technique was essential to monitor the PL signal from carbon nanotubes (as seen on figure I.26 right).

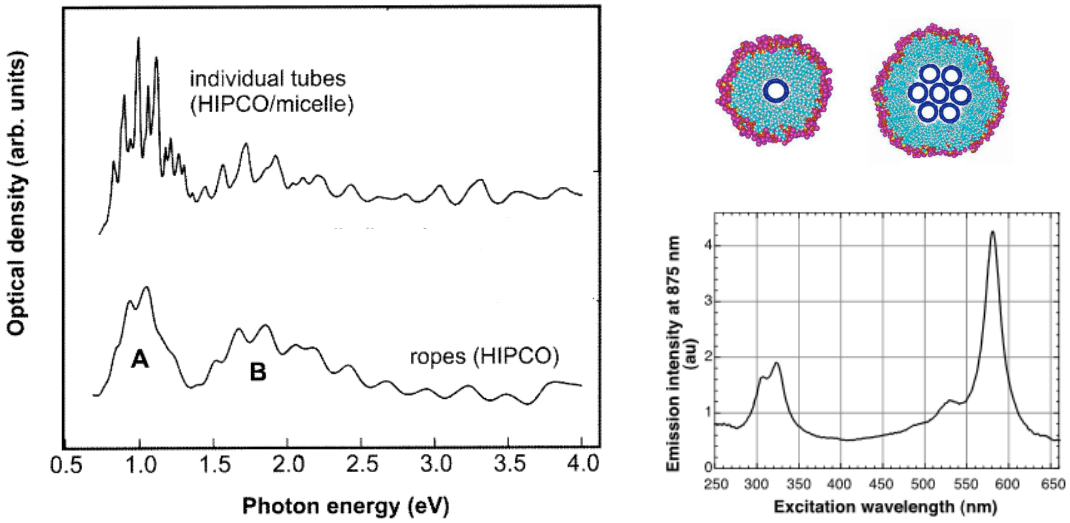

Figure I.26: Left: Optical absorption spectra of ropes of carbon nanotubes versus micelle suspended ones, adapted from I.26; Right top: Artistic view of the micelle shell around a single nanotube and around a bundle, adapted from [131]; Right bottom: first photoluminescence excitation spectrum of a nanotubes sample after encapsulation in SDS, from [131]

4.3 Sample fabrication technique

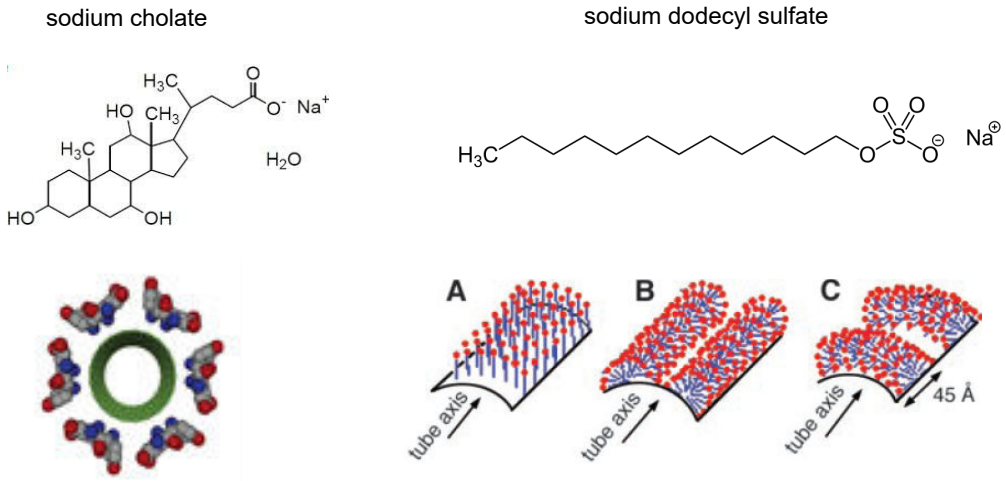

Figure I.27: Representation of the two surfactants used in this work: sodium cholate (left) and sodium dodecyl sulfate (right), chemical structure and organization around a nanotube, adapted from [160, 161].

In our work, suspending carbon nanotubes in micelles is always the first step of the sample preparation. We either use sodium cholate (SC) or sodium dodecyl sulfate (SDS) as surfactant agents (Sigma-Aldrich). The different suspension capacities of SC and SDS have been evidenced and used very early, for instance to sort out nanotubes chiralities [67]. This difference can be explained by their drastically different structures (as seen on figure I.27). SC is a bile salt, designed to carry and digest very large lipid stucture inside human's intestine. It has a flat structure that will stand parallely to the carbon surface. SDS has a classical surfactant structure and is likely to form spherical or hemispherical micelles (B or C in figure I.27 right).

Our sample protocol starts with the preparation of a 2 w.t.% suspension of surfactant into a Ph=8 borate buffer (10^{-2} mol.L^{-1}). We add a small amount of nanotube powder, generally to reach a 0.15 mg.mL^{-1} concentration. Placing the sample into a 2° C thermostat, a strong tip sonication is applied for 1h30. This timescale is usually enough to suspend the nanotubes inside the surfactant micelles. Yet, this intense sonication breaks the long nanotubes into smaller portions of around 300 nm, due to the presence of defects in the lattice structure [162]. At this stage, the suspension contains a mixture of isolated nanotubes, bundles and amorphous carbon. An ultracenfugation of 1h at 120 000 g is required to select the isolated nanotubes only. We obtain a grey solution that is stable from a few days (for SDS) to a few weeks (for SC suspensions).

Optical characterization of samples

After the preparation step, our samples are controlled with absorption and photoluminescence spectroscopy, to ensure that the suspension occurred correctly. On figure I.28 is displayed the absorption spectrum of two suspensions made with the previous protocol: one from a CoMoCAT batch (blue) and the other from a HiPCo (black) batch. On each spectrum, one can see the presence of numerous peaks that can be attributed to different chiralities, using the Kataura assignement [50]. We may also single out the S_{22} transitions (between 2.5 and 1.5 eV) from the S_{11} (below 1.5 eV). Between the two samples, one can see the difference of amplitude at the same absorption energy. Indeed, the two growth techniques do not produce the same chiralities in the same proportion. Among other techniques, absorption spectroscopy can provide an estimation of the concentration of each chiral species.

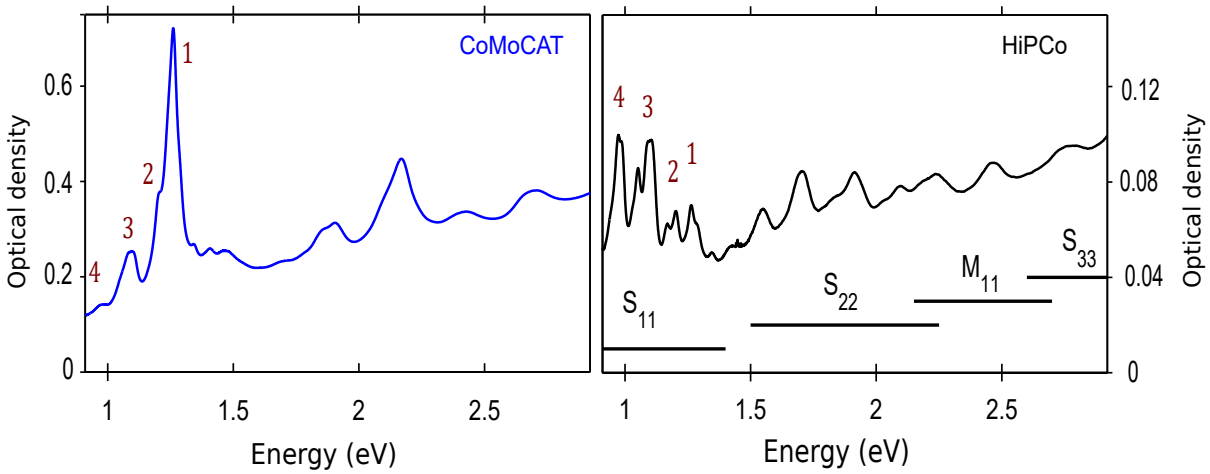

Figure I.28: Absorption spectra of two samples of carbon nanotubes grown with the CoMoCAT (blue) and the HiPCo techniques (black), adapted from [108]

The second characterization employed is the photoluminescence excitation map. On figure I.29 is presented the PLE response of the CoMoCAT and HiPCo samples. As for absorbance, PLE allows to assign a $S_{22} \rightarrow S_{11}$ relaxation pathway to a given chirality [159]. The resolution is even finer, as we are looking at 2D resonant processes. We can clearly see that the CoMoCAT batch includes mainly (6,5) nanotubes while the HiPCo contains numerous species with diameter around $0.8 - 1$ nm.

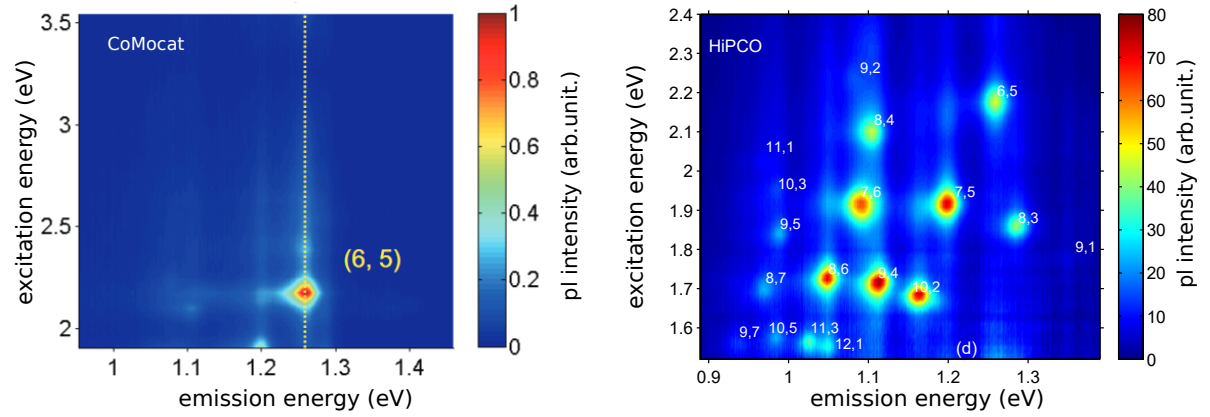

Figure I.29: PLE maps of two samples of carbon nanotubes grown with the CoMoCAT (left) and the HiPCo techniques (right), adapted from [108, 163]

Description of the swelling method technique

Many groups have worked on the noncovalent functionalization of nanotubes with porphyrin molecules [164, 165]. However, if many of them look at the porphyrin properties, they did not study the nanotubes luminescence. Among them two groups evidenced luminescent energy transfer from the porphyrin to the nanotubes in 2008: our team (Magadur *et al.*, [166]) and Casey *et al.* [167]. In the first article hydrosoluble porphyrins were used to suspend nanotubes: it led to a quite poor quality of samples (low luminescence signal) due to the imperfect behavior of porphyrins as surfactant.

In the second study, the authors chose to work in a suspension of a non-ionic surfactant called Triton. However their nanotubes suspension exhibited poor stability due the incompatibility of Triton with nanotubes. They performed the functionalization by a simple mixing of the porphyrin and the nanotubes suspensions. Upon functionalization, both groups evidenced the creation of a new excitation resonance on the nanotubes luminescence. They attributed these results to an energy transfer from the molecule to the nanotube, that required a further investigation to understand its nature. However, both methods provide quite unstable samples, as TPP and nanotubes have different affinities with their environment and in particular with surfactants. These effects will be detailed in the next chapter. This proved the necessity to find an optimized micellar environment, that is at the same time suitable for the molecules and for the nanotubes.

To achieve such goal, the former student Cyrielle Roquelet in our group designed a controlled method of non covalent functionalization with higher chemical yields and better sample stability [168]. The control of the functionnalization process is achieved using the sodium cholate micelle as nano-reactor. This allows to benefit from the stability of SC micelles. The porphyrin molecules are carried into the nanotube's micelle by an organic solvent. Indeed Wang *et al.* have shown that organic solvent could penetrate into nanotubes micelles by a mild sonication process [169]. Hence, our functionnalization method, represented on figure I.30 is called the micelle swelling method. It starts with the preparation of solution of TPP in dichloromethane (DCM). This solution is added to the cholate nanotube's suspension in order to respect a 10% DCM/water volume ratio. For 3 h, a mild tip sonication is applied to mix the two phases. This sonication will provide a sufficient amount of energy for the organic phase to successively get inside the micelles and evaporates. The swelling time has been chosen to be long enough for the molecule to stack onto the tube without disturbing the nanotubes suspension. Once the reaction is complete, the cholate suspension of nanohybrid compounds is stable for weeks.

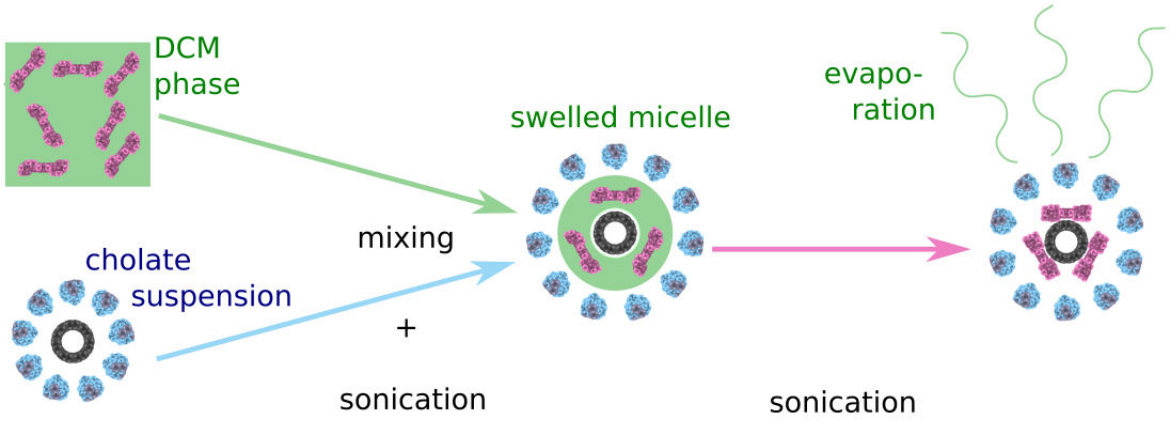

Figure I.30: Principle of the swelling method, adapted from [108].

4.4 Spectroscopic monitoring of the non-covalent coupling

There are many spectroscopic evidences of the strong interaction between the porphyrin and the nanotubes. The most trivial one can be seen with bare eyes, as the color of the hybrid sample is different from the one of the TPP or the nanotubes samples. This naive signature indicates an absorption change that can be quantified on an absorption spectrum of a functionalized HiPCO sample (figure I.31). Upon functionalization, every nanotube transition is shifted a around 20 to 30 meV in the low energy direction (it is called a red-shift effect).

This is indicative of a modification of the close dielectric environment of the nanotubes inside the micelles (solvatochromic effect, [170]). Such effects were also present in the swelling experiments of Wang [169], however they disappeared upon solvent evaporation while they are permanent in our samples. We can then conclude that these shifts are created by the presence of TPP molecules at a very short distance, inside nanotubes micelles. As both S_{22} and S_{11} are shifted, we can see on figure I.32, that the $S_{22} \rightarrow S_{11}$ transition of each chirality undergo a 2D displacement. The molecules bands are also red shifted in a large proportion. The effect is more visible on the Soret band that is splitted in two: an unchanged and a 130 meV redshifted components. The fact that two band coexist is the signature of an incomplete chemical reaction, in which some porphyrins do not stack onto the tubes. This larger redshift is too large to be explained by a mere solvatochromic effect. However, the reasons of such effects are still under investigation and will be discussed in the chapter 4.

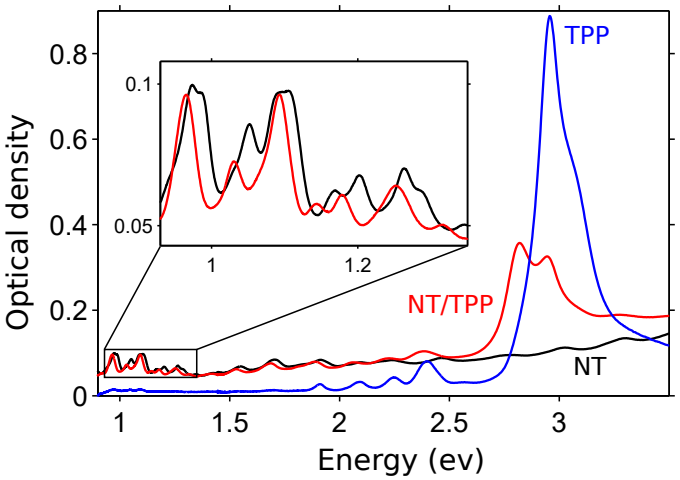

Figure I.31: Absorption spectra of an HiPCo nanotubes suspension in absence (black) and in presence of TPP (red) and of TPP alone in SC micelles (blue), adapted from [108].

Energy transfer effect

To go further in the investigation of the molecules nanotube coupling a photoluminescence study has to be performed. On figure I.32 is displayed the PLE map of pristine and porphyrin functionalized suspension of HiPCo nanotubes.

Every nanotube resonance is present after molecules attachment, which proves that the non covalent coupling did not disturb the π electrons structure of carbon nanotubes. Moreover, we observe a 2D redshift of each of these bands, as both S_{11} and S_{22} transitions are displaced.

Aside from the classical peaks, a new series of resonances appears on the same horizontal line corresponding to a 2.82 eV excitation energy. This is exactly the energy of the shifted component of the Soret Band. However, the emission energy of these new peaks is deeply inside the porphyrin bandgap, and every one of them matches the S_{11} energy of a chirality of nanotube. As seen on the diagram of the figure I.32 left, they correspond to a complex phenomenon that starts with the absorption of a photon by the molecule and ends with emission a photon from the nanotube. This is an energy transfer mechanism in which the TPP is the donor and the nanotube the acceptor. With a closer look on the photoluminescence excitation line on figure I.32 c), one can see a similar effect upon excitation on the Qy(1,0) porphyrin band.

The fact that this energy transfer phenomenon leads to an increase of the nanotube luminescence tells us that an electron hole pair is exchanged between the donor and the acceptor.

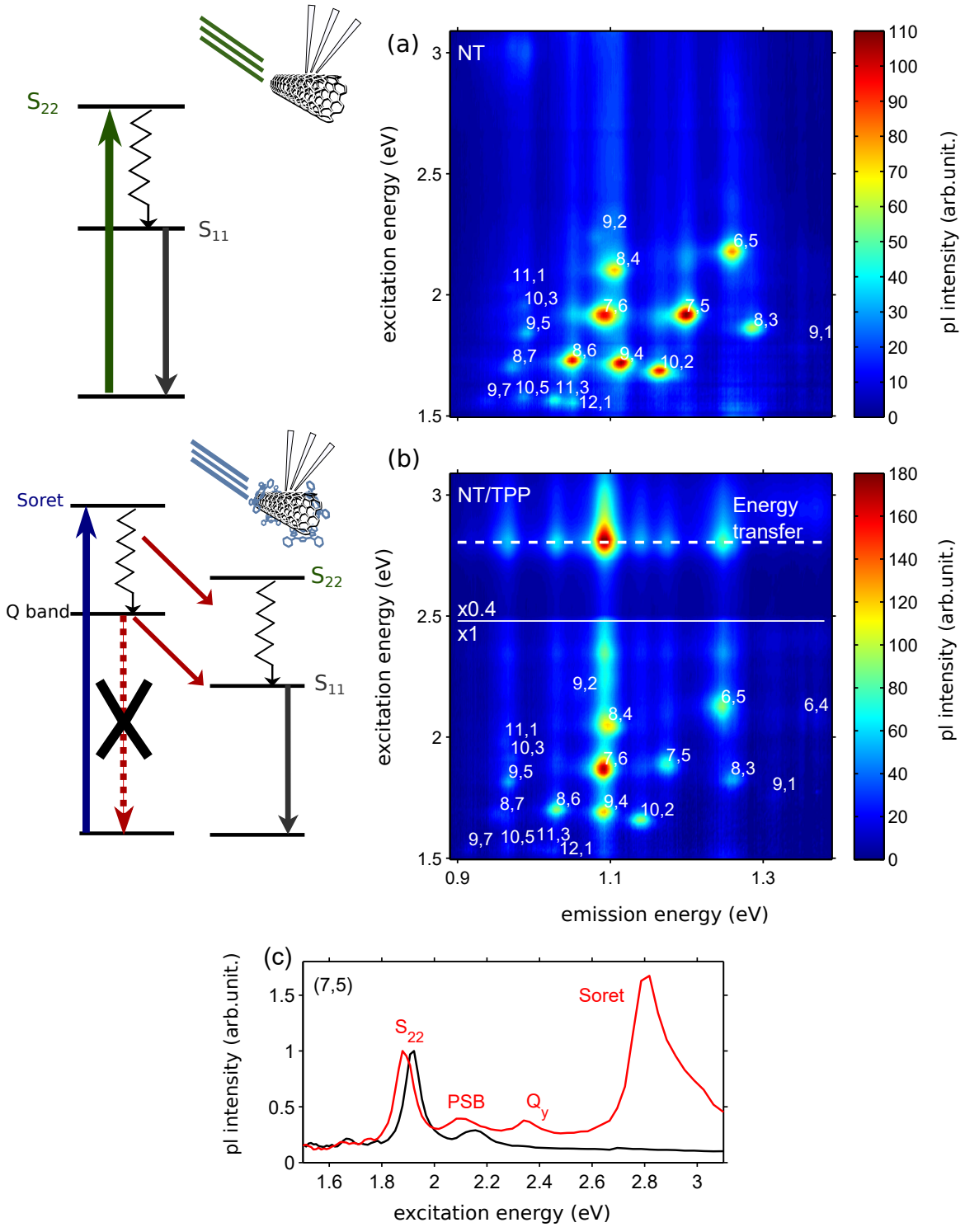

Figure I.32: Photoluminescence excitation maps of an HiPCo nanotubes suspension in sodium cholate micelles, in absence (a) and in presence (b) of TPP. (c): Excitation spectrum of the (7,5) chiral species at a 1.20 eV emission energy, adapted from [108].

Measurement of the strong transfer efficiency

A quantitative evaluation of the transfer efficiency has been published by Roquelet *et al.* in 2010 [11]. Upon donor excitation, the new transfer pathway competes with the classical relaxation behaviour presented in previous sections. As a consequence, the quantity of created excitons will be splitted into the two relaxation pathways. In the article, Roquelet *et al.* used three different methods to measure the amplitude of this new energy transfer with respect to the classical luminescence porphyrin behaviour.

The first technique is based upon the new resonance, Soret $\rightarrow S_{11}$, on the PLE maps presented on figure I.32. We can quantify the proportion of the transfer process through the R ratio of the transfer transition intensity over the intrinsic transition $S_{22} \rightarrow S_{11}$ one:

$$R = \frac{I_{Soret}}{I_{S_{22}}} \tag{I.36}$$

The value of such ratio can be linked to intrinsic and external parameters. The $I_{S_{22}}$ intensity is proportional to the concentration of monitored tubes, to the nanotube absorption cross section $\sigma_{S_{22}}$ and to the luminescence quantum yield of the tubes ϕ_{pl}. On the other hand, the I_{Soret} transfer peak is also proportional to the stacked porphyrin concentration, to the Soret porphyrin absorption cross section σ_{Soret} and to the intrinsic relaxation efficiency relative to the nanotube ϕ_{rel}. Finally I_{Soret} is also proportional to the transfer efficiency between the two objects η that we want to evaluate. Under the hypothesis that the relaxation in the tube has the same efficiency in the both cases (i.e. $\phi_{pl} \simeq \phi_{relax}$), we can express the transfer ratio R as:

$$R = \frac{N \times \eta \times \sigma_{Soret}}{\sigma_{S_{22}}} \tag{I.37}$$

where N is the number of molecules around the nanotube. For a maximal molecule coverage on (6,5) enriched nanotubes sample, they showed that the measured value of $R \simeq 1.1$ implied that the transfer efficiency was close to 99 %. Indeed, the classical porphyrin luminescence pathway is totally quenched and every created exciton is transferred to the nanotube. Moreover, we see that this ratio R strongly depends on the quantity of molecules coupled with the nanotube. In the following work, we will monitor the intensity of this transfer peak to evaluate the capacity of molecules to stack onto the tube in various conditions.

The second method is the reference technique that reasearchers used in the first papers on nanotube/ molecules nanohybrids [164, 165]. It is based on the molecules fluorescence evaluation, presented on figure I.33 left. We compare the PL intensity of TPP alone in micelles and TPP in presence of nanotubes upon excitation on their respective Soret resonance energy (2.95 and 2.82 eV). In presence of nanotubes, the

porphyrin luminescence decreases of more than 3 orders of magnitude with respect to the molecules alone. This gives a quantitative evaluation of the quenching efficiency:

$$\eta_q = 1 - \frac{I_{d/a}}{I_d} \; > \; 99.999\ \% \tag{I.38}$$

where $I_{d/a}$ and I_d is the donor luminescence intensity in presence and in absence of the acceptor. However, we mentioned earlier that the hybrid NT/TPP samples always contain free molecules that do no interact with nanotubes. In fact, they showed in the article that the PLE spectrum of the TPP in presence of NTs only exhibits an unshifted resonance at 2.95 eV (instead of the expected shifted energy of 2.82 eV). In conclusion, the remaining porphyrin signal on the NT/TPP totally comes from the free porphyrins and the previous evaluation of 99.999 % is an underestimate of the actual transfer efficiency.

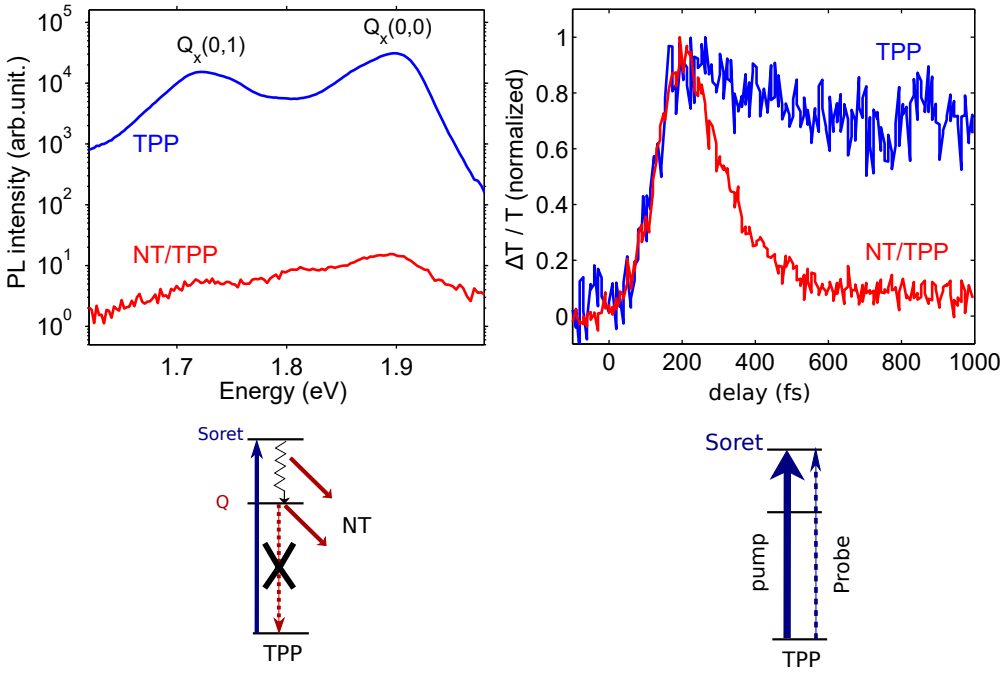

Figure I.33: Two methods to evaluate the energy transfer. Left: Comparing PL intensity of TPP in micelles (blue, excited at 2.95 eV) and TPP in presence of nanotube (red, excited at 2.82 eV); right: Monitoring the relaxation time of Soret with a degenerate pump/probe experiments for TPP in micelles (blue, excited at 2.95 eV) and TPP in presence of nanotube (red, excited at 2.82 eV), adapted from [108].

The third techniques is based on a homemade femtosecond pump/probe setup, to monitor the ultrafast relaxation behavior of the porphyrins. In a degenerate

configuration, the pump and the probe beams are set at the same energy, to excite the TPP and TPP/NT samples on their respective Soret transitions (either 2.95 or 2.82 eV). By monitoring the transient absorption of the samples, one can have an access on the excitation lifetime of the Soret → ground state transition. On figure I.33 right, the lifetime of such transitions is measured to 150 fs for the NT/TPP sample, while it is five order of magnitudes larger in absence of acceptor (10 ns , [111]). This is due to the influence of the energy transfer pathway that drain the Soret excitons on a very short timescale. According to a simple kinetic formula, this technique provides the finest evaluation of the transfer yield:

$$\eta_T = 1 - \frac{\tau_{d/a}}{\tau_d} = 1 - 10^{-5} \tag{I.39}$$

All of these measurements proved that the vincinity of the nanotube surface has a great influence on the porphyrin excitation dynamics, leading to an ultraefficient energy transfer in such hybrid systems. These results are quite unexpected in regard to the weak noncovalent interaction between the molecules and the nanotubes. A few theoretical papers looked into this phenomena to understand the nature of such ultraefficient energy transfer. According to Malic and coworkers [171], we are dealing with a Förster nonradiative energy transfer, between nanoobjects on a very short distance (0.3 nm).

5 Conclusion

Both single walled carbon nanotubes and porphyrin molecules are hydrocarbon nanoobjects that are inspired by nature and widely studied in optoelectronics. They have remarkable quantum light absorption and excitonic properties that lead to intense luminescence abilities. Under a polarized excitation beam, they both have the capacity to emit photons with a maintained polarization. Interestingly, their flat and electron rich structures favor their coupling, through a noncovalent π-stacking interaction. A simple, controlled chemical reaction called micelle swelling has been designed using the cholate micelle as a nano-reactor. Finally, their interaction can be easily monitored, thanks to several classical spectroscopic techniques, showing an intense photoinduced energy transfer from the stacked porphyrin to the nanotubes.

In the last ten years, several groups have performed a functionalization of carbon nanotubes within a micellar environment [172–174]. The surfactant coverage has to be considered carefully, as it protects the nanotube surface as much as it limits the desired chemical reaction. Many papers show very slow reactions (several hours), that only take place in certain, carefully chosen, surfactant media [175, 176]. In this context, the following chapters will investigate on the interplay between the micellar environment and the reactants during the π-stacking reaction. We will see that the surfactant has a large influence on the kinetic and thermodynamic parameters of the stacking process.

Chapter II

Investigation into the kinetics of the reaction and the role of the surfactant environment

In order to gain control and maximize the yield of the reaction, we need a fine understanding of every effect involved in the process. In this chapter, we will try to develop our knowledge on the physical and chemical effects that favor the reaction as well as those that prevent it. One of the challenges of the functionalization in a micellar environment is to find a balance between the stabilization of the surfactant shell around reactants and their ability to couple with each other. In this context, the micelle swelling method presented above suffers from several limitations. The reaction is poorly tunable and reproducible, for instance due to the difficulty to control the intensity of the ultrasound waves. Furthermore, the presence of DCM inside the nanotubes micelles blurs the samples, preventing any in situ spectroscopy to monitor the progression of the reaction.

The first part of this chapter will detail the replacement of the swelling method by a two-steps method. Such controlled functionnalization was performed by mixing two surfactants suspensions, containing either the porphyrin or the nanotubes. Each elements of this reaction scheme will be carefully controlled (surfactant environment, porphyrins isolation,....). Surprisingly, this controlled techniques resulted in very long reaction timescales. The second part of this chapter is dedicated to understand the underlying reasons of such slow kinetics. A comprehensive characterization of the reaction kinetics will be performed, respectively for single surfactant and for mixed surfactant samples. The main effects that explain the observed timescale will be detailed. In the third part, the reaction mechanism will be detailed. In particular, the influence of the carbon surface characteristics (diameter, size, ...) will complete this chapter, with a comparison between carbon nanotubes and graphene nanosheets.

1 Control of the different stages of the micelle swelling

1.1 Generalities on the organization and the dynamics timescales in surfactants

Micellar equilibrium

To finely understand the reaction mechanism, one should take a great care of the physics of the surfactant environment (equilibrium, energetic paramaters, dynamics, ...). Surfactants are partially hydrophilic molecules that are only merely soluble in water. At low concentrations, the monomers are far enough from each other to be stable (see figure II.1). When the proportion of surfactant molecules reaches a certain concentration, they instantaneously form micelles. This organization is due to complex electromagnetic interactions between surfactant monomers, water molecules and other ions in solution. This dramatic change can be modelled as a physical phase transition, or an extremely cooperative chemical reaction [177], corresponding to the global equation:

$$\underbrace{\mathrm{Mo} + \mathrm{Mo} + ... + \mathrm{Mo}}_{N_a} = \mathrm{Micelle} \quad ; \quad K_{micellization} = \frac{[\mathrm{Micelle}]}{[\mathrm{Mo}]^{\mathrm{N}_a}} \tag{II.1}$$

where N_a is the aggregation number of monomers (Mo) inside a micelle. The larger is N_a, the more cooperative is the micellization process. This equilibrium is dynamic: surfactant molecules constantly enter and leave the micelle. The monomer/ micelle equilibrium is ruled by the the equilibrium constant $K_{micellization}$ and the micellization Gibbs energy $\Delta rG = -RT\ln(K_{micellization})$. This correspond to the amount of energy that is required to break the micellar structure. For SDS, this energy is around 20 kJ.mol^{-1} at 300 K [178].

The transition threshold is called the critical micellar concentration (cmc) and depends on the properties of the surfactant. For instance, SC is relatively flat and has several hydrophilic groups spread over its structure, while SDS with has a long hydrophobic tail. Consequently, SC is more stable in water than SDS, and its cmc is higher (15 mmol.L^{-1}) than the one of SDS (8 mmol.L^{-1}). It also explains why the SDS molecules have to gather into large aggregates to minimize their interaction with water (N_a=60), while SC can form small clusters (N_a=4). SDS is often regarded as a classical surfactant. Its behavior around the cmc is presented on figure II.1 left. In a few words, the monomer concentration progresses linearly below the cmc and is constant above it. It is exactly the opposite behavior for the concentration of micelles. Being null under the cmc, it progresses linearly above the cmc according to the formula:

$$c_{micelle} = \frac{c_{surfactant} - cmc}{N_a} \tag{II.2}$$

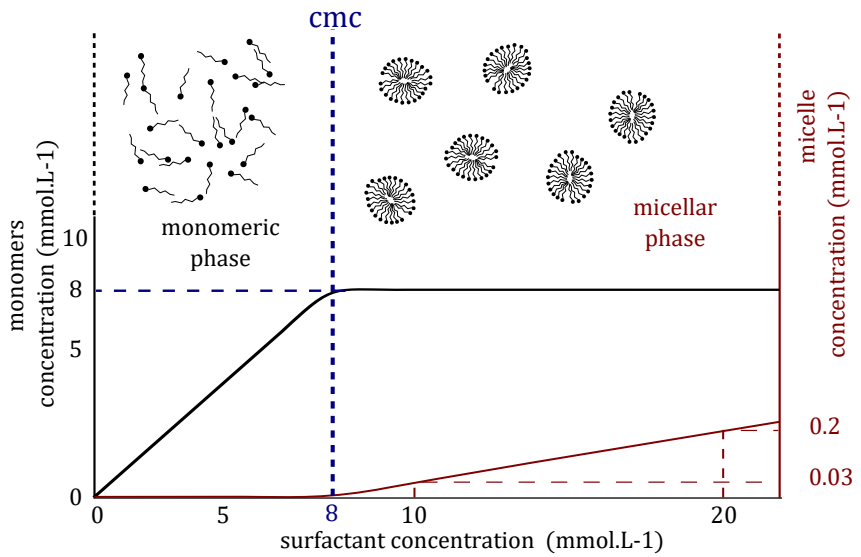

Figure II.1: Phase diagram of the SDS micellization process as a function of the surfactant concentration.

On figure II.2, one can see that many physical properties of the surfactant medium undergo a steep transition around the cmc, including the capacity to solubilize molecules.

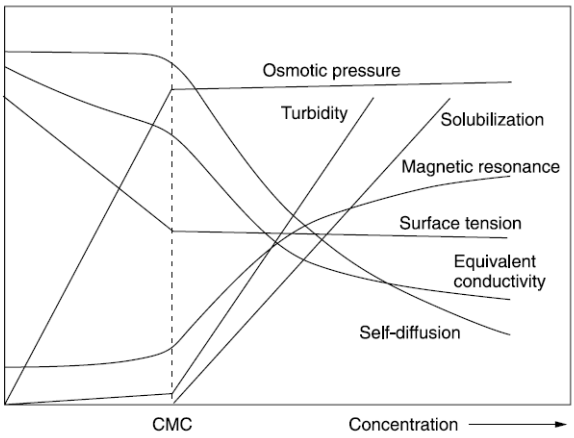

Figure II.2: Evolution of some important physical properties of a surfactant medium around the critical micellar concentration, from [179].

In the following work, we are going to use mainly 2 w.t. % suspension of SC and SDS surfactants. On table II.1, one can find the principal characteristics of such suspensions of SC and SDS. Each of them is far above the cmc. Due to the smaller

molar mass of SDS, the 2 w.t. % samples of SDS contain more monomers than the SC suspensions. However, the large SDS aggregation number N_a leads to a smaller micelles concentration.

	Molar mass ($g.mol^{-1}$)	**cmc** ($mmol.L^{-1}$)	$\mathbf{N}_a$ number	$\mathbf{c}_{surfactant}$ at 2 w.t. % ($mmol.L^{-1}$)	$\mathbf{c}_{micelle}$ at 2 w.t. % ($mmol.L^{-1}$)
SC	430.55	15	3-4	46	10
SDS	289	8	60	69	1

Table II.1: Main characteristics of SC and SDS.

Dynamic evolution of micelles

Finally, we will investigate on the interplay between the speed of the functionalization reaction and the dynamics of the micellar environment. In this chapter, we will also use different techniques (sonication, dilution, heating, ...) to influence the surfactant organization and the reaction kinetics. Hence, the dynamical properties of micelles have to be studied carefully. From this point of view, the literature states that surfactants equilibrium dynamics occur on very short timescales. As seen on figure II.3, the transition from isolated monomers to a spherical micelle occurs within a few nanoseconds.

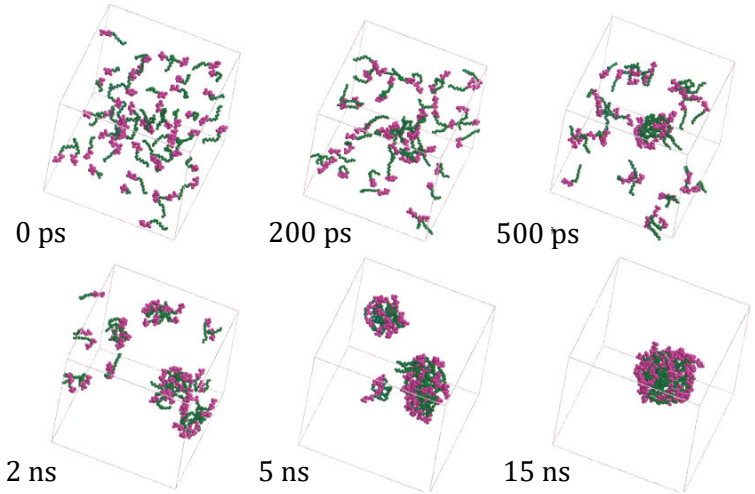

Figure II.3: Molecular Dynamics simulation of the spontaneous aggregation of dodecylphosphocholine (a molecule similar to SDS) into a spherical micelle over 15 ns, adapted from [180].

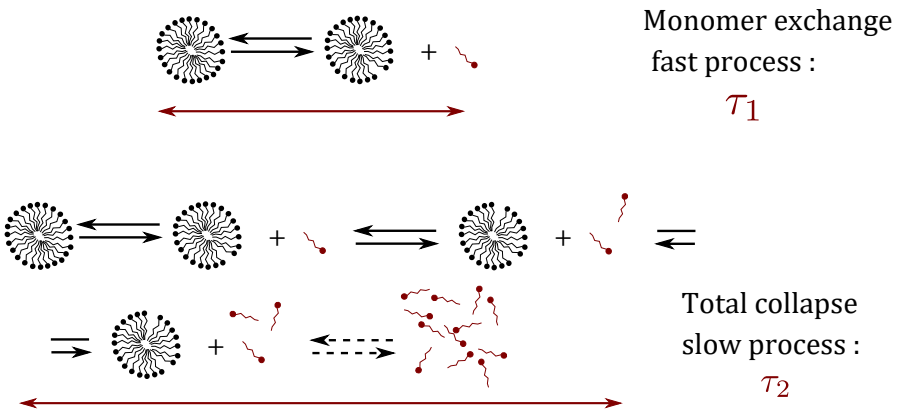

Figure II.4: Representation of the evolution over the two characteristic times τ_1 and τ_2, adapted from [181].

In fact, experimental investigations revealed the existence of two relaxation processes involved in micellar equilibria, with different characteristic times [179]. The movement of a single surfactant molecule, entering and leaving the micelle, occurs on a short timescale τ_1: from the nanosecond to the microsecond scale (see figure II.4). On longer times, micelle may totally collapse and reform themselves [181,182]. Lang *et al.* [183] stated that τ_2 was at least three orders of magnitude bigger than τ_1 (around 1 millisecond). Both τ_1 and τ_2 are extremely dependent of the nature of the micellar medium. For instance, the presence of ionic elements, such as the counterions inside the solution, will modify the micelle lifetime [184]. The chemical structure of the surfactant is also known to influence the micellar relaxation dynamics. The size of hydrophobic tail or the nature the hydrophilic head (such as the sulfate function of SDS) can bring additional stability to the micellar environment.

For ionic surfactants, this stability is enhanced by coulombic repulsion between adjacent monomers or even between different micelles. Due to these electrostatic forces, the monomer exhange is limited, and the collapse of the micelles is prevented. Hence, coulombic effects may both increase simultaneously the τ_1 and τ_2 relaxation times. As shown on figure II.5 left, such coulombic effects induce an exponential increase of the relaxation time τ_2 with the SDS concentration [185]. Indeed, Oh *et al.* proved that the proximity between adjacent micelles rises parallely to the micelle concentration, making them more stable.

The stability of a micelle is also influenced by the degree of hydrophobicity of its hydrocarbon core [186]. Moreover, the encapsulation of an hydrophobic dye could modify this stability [187]. Indeed, this dye would have a very unfavorable interaction with the aqueous polar environment. This will prevent the entry of water molecules and considerably slow down the collapse of the micelle. This may increase the τ_2

characteristic time by several orders of magnitudes. Bohne *et al.* studied the kinetics of release of hydrophobic pyrene aggregates (excimers) into empty SDS micelles and found several hours timescales, with first order dynamics (see figure II.5 right, [188]).

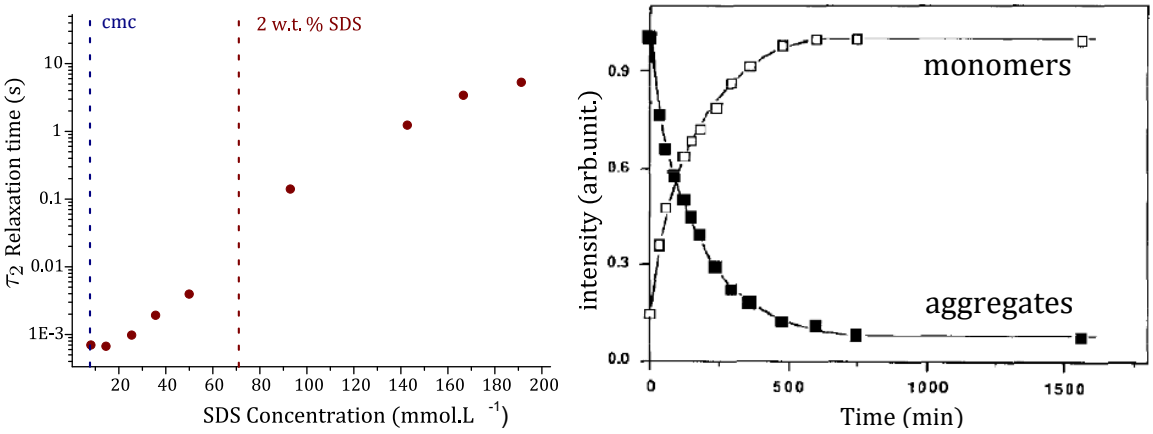

Figure II.5: Left: Evolution of the slow relaxation time τ_2, of SDS micelles as a function of surfactant concentration, measured by the frequency of bubble formation, adapted from [185]; Right: Redistribution kinetics of pyrene aggregates measured as the growth of the monomer fluorescence intensity and the decay of the aggregate (excimer) emission, along with their first order exponential fittings, adapted from [188].

Finally, the dye/micelle stability is influenced by the position of the molecule inside the micelle. If it is located at the center, the micelle will be very stable. However, Maiti and coworkers [120] showed that molecules such as porphyrins were residing at a close distance from the micelle surface. This structure will influence the micelle collapse, in which the porphyrin will remain attached to a few monomers. This unstable structure called a submicelle will be evoked in the next sections.

1.2 Design of a step by step reaction

One of the challenges of functionalization in a micellar environment is to find a balance between the stabilization of the surfactant shell around reactants and their ability to couple with each other. In this context, the micelle swelling method allows the creation of stable nanohybrid compounds leading to an intense photoinduced energy transfer. Such method is based upon the ability of sonication to break the solvent equilibrium. With the previous Phd student Fabien Vialla [108], we decided to separate the two main parts of the reaction: the suspension of the molecules in micelles and the stacking on the nanotubes. In this chapter, we will refer to this separate method as the *two steps swelling method*, in opposition to the *direct swelling method* presented in chapter 1.

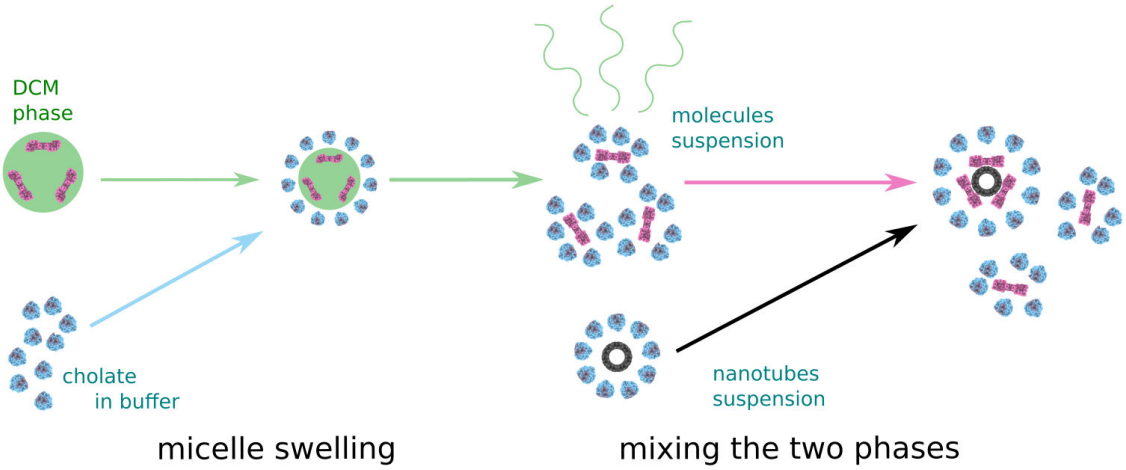

Figure II.6: Schematic of the two steps swelling method, adapted from [189].

This new reaction scheme is done by dispersing separately the NTs and the TPP monomers in a Ph=8 borate buffer 2% w.t. surfactant suspension. The method for NTs is the one explained in the previous chapter. For the molecule, it consists in a micelle swelling method without the presence of the tubes. A DCM solution of porphyrin is mixed with the surfactant suspension in a 10% DCM/water volume ratio, and tip sonicated for 1.5 hour at 12°C, until complete evaporation of the organic phase.

1.3 Control of the molecule suspension in surfactants

In order to maximize the yield of the reaction, the first step is to control the quality of the molecules suspensions. Indeed, if molecules are not correctly integrated in micelles, they may not be able to diffuse properly into the medium and never reach nanotubes. From previous studies from Maiti *et al.* [116,120], we know that porphyrin molecules have the tendency to self aggregate in surfactant. They can form different kinds of geometry of aggregates, with sizes ranging from a few to dozens of monomers. The surfactant has to be chosen carefully, as it may be actively involved in such aggregation, in a process called *surfactant assisted aggregation* [190, 191]. From the chemical point of view, this aggregation will compete with the noncovalent reaction with Nts, limiting the reaction yield. After suspending the molecules in micelles, optical spectroscopy is performed to ensure that the molecule suspension does not include aggregates of porphyrins.

As presented on figure II.7, a combination of absorption spectroscopy and time resolved PL is employed. This figure displays the results of two samples from the swelling method, made with an overconcentrated solution of porphyrins.

On the absorption spectrum, the most visible difference between the two samples is located on the Soret band region. For the red curve, one can see a symmetric, sharp band at 2.95 eV (420 nm), with a small shoulder at 3.1 eV (420 nm), very similarly to the absorption response of monomers in DCM. It is characteristic of an isolated porphyrins sample. In aggregated samples such as the black one, this Soret band can undergo several changes from one sample to another: broadening, decrease of its amplitude, creation of a low energy shoulder at 2.88-2.85 eV (430-440 nm), increase of the high energy shoulder,.... The two last effects are particularly visible on the absorption spectrum (black) of the aggregate on figure II.7 left.

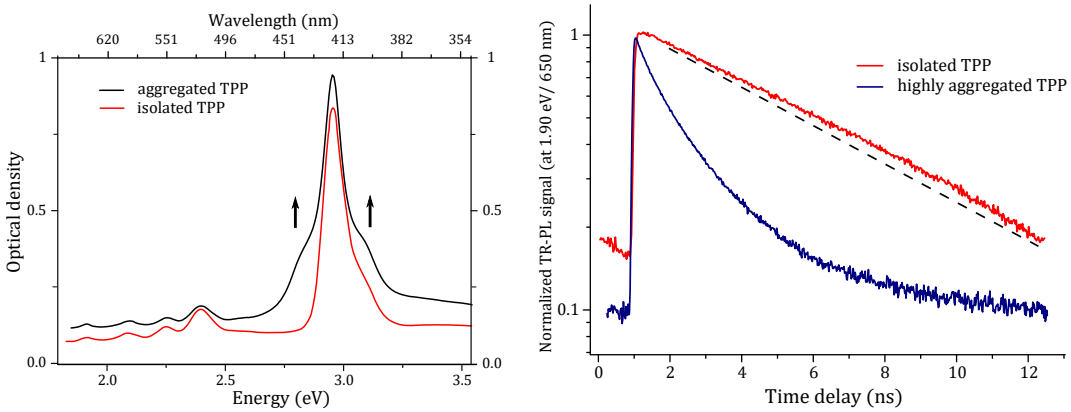

Figure II.7: Spectroscopic tools to measure aggregation; Left: Absorption spectrum of a properly isolated and an aggregated sample of TPP in sodium cholate; Right: Time resolved photoluminescence diagram upon excitation at 2.95 eV (420 nm) and collection at 1.90 eV (650 nm) of a sample containing isolated TPP and one including a high proportion of aggregates. The experiment is not performed at the magic angle.

According to Kasha theory on molecular aggregates, all of these spectroscopic variations are related to a dipole-dipole interaction within the aggregates [192]. This model, and its consequences, will be detailed in the fourth chapter. In particular, it explains why the changes are more visible on the Soret band than on the Q bands: such interaction only produces important effects for optical transitions with a high absorption coefficient.

The TR-PL spectra represented on figure II.7 right provide additional information on the occurrence of aggregation. The response from the isolated TPP (red curve) presents a quasi monoexponential behavior with a characteristic time of $\tau = 12$ ns. On the contrary, the signal from a highly aggregated sample (blue curve) presents a multiexponential behavior, including a shorter component with a timescale around 1 ns.

As explained in the previous chapter, such a variation of the PL lifetimes proves that the exciton can follow different relaxation pathways before collapsing. This

multiexponential behavior indicates a dispersion of aggregate sizes inside the TPP suspension [120]. As a conclusion the optical absorption and the TR-PL are two suitable experimental methods to discriminate between a suspension of monomers and a suspension of aggregates of porphyrins.

1.4 Comparison of the solubilization of porphyrins in sodium cholate and sodium dodecyl sulfate

Finally, we want to study the isolation capacity of the two main surfactants used in this work: sodium cholate and sodium dodecyl sulfate. In 1995, Maiti [120] showed that the ability of a surfactant to suspend isolated porphyrins increases with the size of their micelles. This size depends on the dimension of the surfactant molecules as well as on the aggregation number N_a.

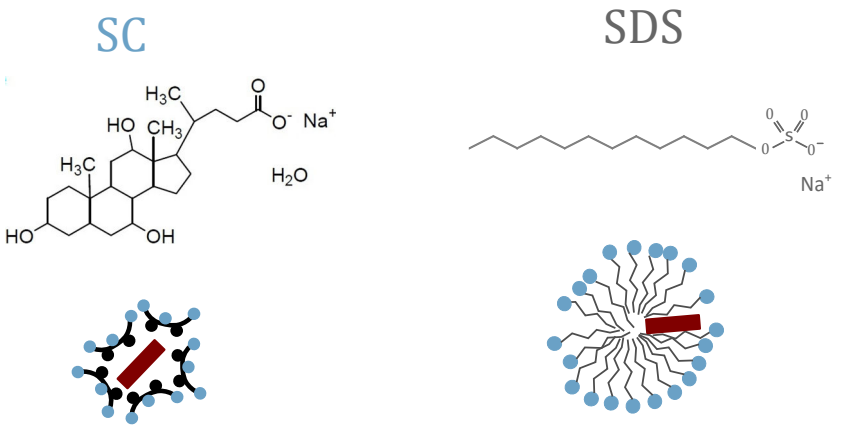

Figure II.8: Artistic view of the geometric differences between a micelle of SC and SDS surrounding a porphyrin.

For such comparison, we monitor the ability of molecules to pass from the organic phase to the aqueous phase. The swelling suspension of TPP into 2 wt% SC and SDS suspensions has been performed, using a 10 % DCM/water ratio and a soft tip sonication for 90 minutes. The reaction was repeated, starting with different concentrations of TPP in DCM, to vary the maximal concentration injected inside the micelles. Here, we define the maximal concentration as the theoretical concentration that could pass into the micelle suspension if the transfer from the DCM phase was 100% efficient. After the sonication, a slight centrifugation of 10 minutes at 6300 g is applied to remove the eventual aggregates.

The quantity of molecules in the micellar suspension is measured by monitoring the Q bands optical density. For a maximal concentration of 392 μmol.L^{-1}, figure II.9 left displays the absorption in SC (red) and in SDS (black). The amplitude of the

bands is at least seven times higher in SDS than in SC. This indicates that SDS has a higher capacity to incorporate porphyrins than SC.

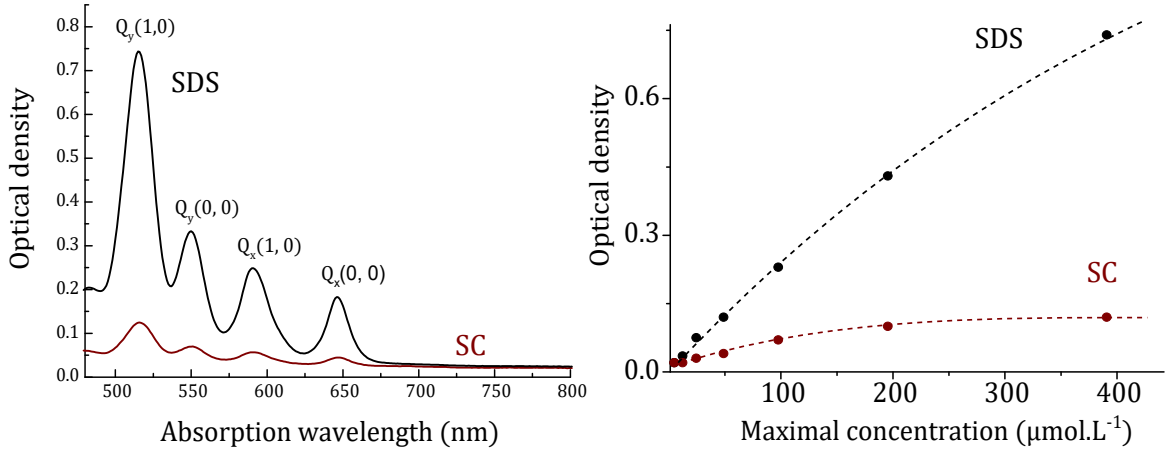

Figure II.9: Comparison of the suspension capacity of TPP in SDS and SC; Left: Optical absorption spectra of TPP for a maximal concentration of 392 μmol.L^{-1} in SC (red) and in SDS (black); Right: Optical density of TPP at the Q$_y$(1,0) band in SC (red) and in SDS (black), as a function of the maximal concentration.

In a second time, the intensity of the Q$_y$(1,0) band of TPP has been measured as a function of the maximal concentration for each surfactant (see figure II.9 right). For SC (red curve), the optical density reaches a threshold value for maximal concentrations above 100 μmol.L^{-1}. This behavior is very similar to the solubilization of a molecule in a classical solvent [116,193]. At low enough concentration, the molecules are surrounded by the solvent (surfactant, water) and have a very small probability to interact with each other: this the solvation stage. When the concentration increases, the self interaction of molecules starts to be predominant: this is the precipitation (or aggregation). The concentration threshold between those two effects depends on the environment and on the structure and geometry of the molecules.

For the SDS samples, the intensity of the Q$_y$(1,0) band of TPP evolves quite linearly. The estimated final concentration in the c_{max} = 392 μmol.L^{-1} sample was around $c_{final} \simeq 300$ μmol.L^{-1}, which is close to the maximal value. This experiment proved that the SDS has the capacity to suspend a large amount of porphyrins. With a larger quantity of inserted porphyrins and with a longer sonication time, final concentrations of isolated porphyrins as high as c_{final}=2000 μmol.L^{-1} were obtained. In comparison, direct inclusion of porphyrin powders in micelles by a simple stirring method enables to reach concentration of $\simeq 1\mu$mol.L^{-1} [120]. This proves the efficiency of the swelling method to force a large quantity of molecules into a micellar environment.

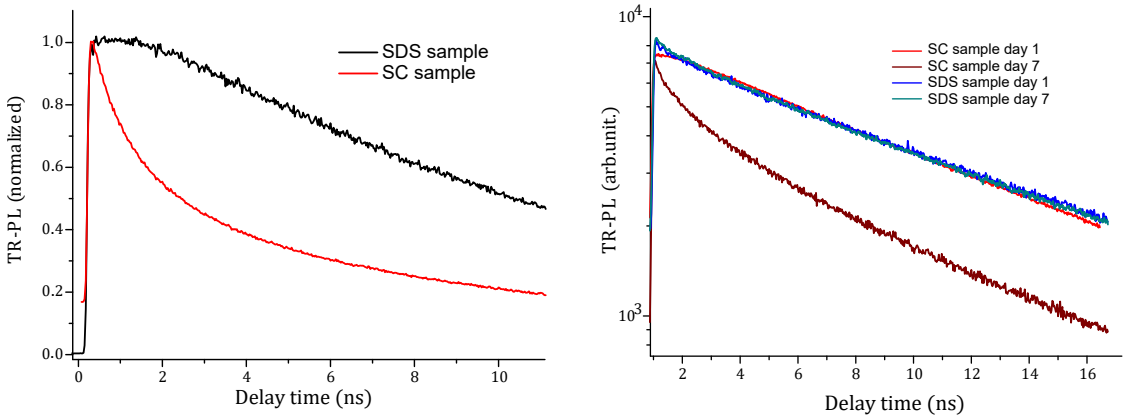

Figure II.10: Left: Time-resolved photoluminescence of 108 μmol.L^{-1} of TPP in SDS and 95 μmol.L^{-1} in SC, just after preparation; Right: Evolution over one week of a SDS and SC suspension of $c_{TPP} = 40$ μmol.L^{-1}. The experiments are not performed at the magic angle.

On figure II.10, the TR-PL response of porphyrins is measured, both in SC and in SDS, for concentration of respectively 95 μmol.L^{-1} and 108 μmol.L^{-1}. On SDS, the curve is mainly exponential, while the SC/TPP TR-PL decay is non-exponential, with the appearance of a short component. Thus, the SDS sample is made of properly solubilized TPP, while the SC sample contains a large amount of porphyrin aggregates.

A second important point is the stability of the suspension over time. The figure II.10 right exhibits the TR-PL experiments performed both on SC/TPP and SDS/TPP suspension for $c_{TPP} = 40$ μmol.L^{-1}. Within seven days, the SC/TPP decay becomes non-exponential, while no major change is observed in SDS. Thus, the structure of the SDS/TPP micelles is also more stable over time.

In conclusion, the stability of the TPP/surfactant structure strongly depends on the nature of the surfactant: its value in SDS is much larger than in SC. This allows to suspend more TPP inside a SDS suspension, and these molecules will remain isolated for a longer time. The exact opposite situation occurs for the nanotube/surfactant compounds: they are properly isolated inside SC micelles while they floculate within a few days in SDS. As presented before, this opposition can be explained by the small size of the TPP, that requires to be surrounded by a spherical micelle for a maximal isolation [194]. At the opposite, the relatively flat structure of the nanotube is more stabilized by a layer of cholate molecules. As we will see in the next parts, this stability will influence the stacking reaction on nanotubes.

1.5 Study of the reaction extent using the spectroscopic evolutions

Classical steps of an adsorption reaction

Until now, the stacking reaction was referred as the π-stacking of porphyrin molecules onto the sp^2 surface of the nanotube. In the last sections, it was shown that the surrounding medium has a quite complex independent equilibrium, that should be not neglected in order to model properly the global reaction. The theoretical reaction of stacking of TPP onto nanotubes can be symbolized through the global equation:

$$TPP \; + \; NT = TPP/NT \tag{II.3}$$

However, the actual adsorption reaction may include different substeps. In the literature, classical adsorption reactions are often treated as a succession of different stages [195, 196]. We may try to adapt such scheme to the stacking reaction. The first step is always the diffusion of the adsorbate from its bulk isolated state to the adsorbent remote environment: it is called the external diffusion. In the present case, it can be seen as the movement of the porphyrin from its separate micelle to the outside of the nanotube micelle (see figure II.11 left). Then the adsorbate has to transfer from the outside environment to the adsorbent surface: it is called the internal diffusion. In our case, it consists in passing through the surfactant palisade surrounding the nanotube (see figure II.11 right). If the reaction is very complex, such steps can subdivided into several steps. In our case, we may consider separately the collision of the TPP micelle with the NT micelle, and the adsorption of the TPP into an empty space on the nanotube surface.

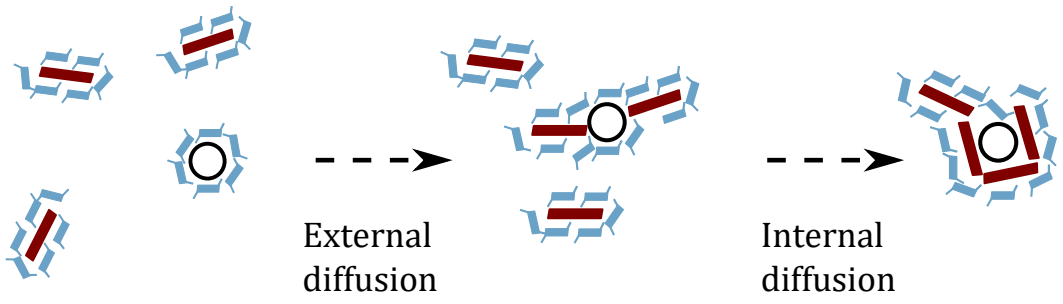

Figure II.11: Artistic view of the classical steps included into an adsorption mechanism.

All of these steps have their own timescale. In many reactions, at least one of these steps is much faster than the others. If the slowest one is the external diffusion step, it is called a diffusion limited (or mass transfer) reaction [196]. If this first step is rapid, it may be neglected. This is for instance the case for the adsorption of gases, as gases evolve rapidly in a 3D environment [197]. The reaction scheme can

then be simplified to a simple statistical adsorption process, where adsorbents have to encounter available adsorption sites.

In the present reaction configuration, these steps are likely to be ruled by the micelle environment. At this point, one has to keep in mind that the studied samples contain mostly empty micelles. It is possible to estimate the concentration of each elements in the medium. As seen before, the 2 w.t. % surfactant suspensions contain one to several millimoles of micelles, while the injected concentration of porphyrin is around 20 to 100 μmol.L^{-1}.

The concentration of micelles containing nanotubes is more difficult to calculate. The optical density on the S_{22} resonance at 570 nm in the samples used in this chapter is approximately of 0.033. To simplify the evaluation one can assume that every nanotube is a (6,5) one with a length of 500 nm (average length after sonication [198]). The (6,5) absorption cross-section on the S_{22} transition is known to be of approximately $\sigma_{S_{22}}$= 3.2×10^{-17} cm^2/atom [199, 200]. This value can be converted into an extinction coefficient for 500 nm long (6,5) nanotubes: $\varepsilon_{S_{22}}$= 1.2×10^8 L.mol^{-1}.cm^{-1}. This yields a very small concentration of micelles containing nanotubes of $c_{NT} \simeq$ 2.7×10^{-3} μmol.L^{-1}.

Hence, it is certain that the micellar environment contains a large proportion of empty micelles and a small part of filled ones, either with nanotubes or porphyrins. Knowing this, we can assume that a TPP micelle has a higher probability to shock with an empty micelle than with a nanotube.

2 Kinetic monitoring of the reaction

2.1 Samples in full sodium cholate

After obtaining a properly characterized suspension of isolated TPP, the second step of the reaction consists in a mix of the two suspensions: molecules and nanotubes. The first experiments were done by mixing and letting evolve two suspensions of porphyrins and HiPCo nanotubes in a 2 % w.t. SC environment. Even if it has been proved before that SDS was a better surfactant for molecules, this choice was made to be fully comparable with the one-step swelling method samples. It also ensures a maximal protection and isolation of the nanotube. To monitor the kinetics of the functionalization reaction, the shift of the S_{11} nanotubes transition and the amplitude of the Soret bands have been used. On figure II.12, one can see the progressive redshift of such bands, on a week timescale. The equilibrium is reached within 5 days (120 hours).

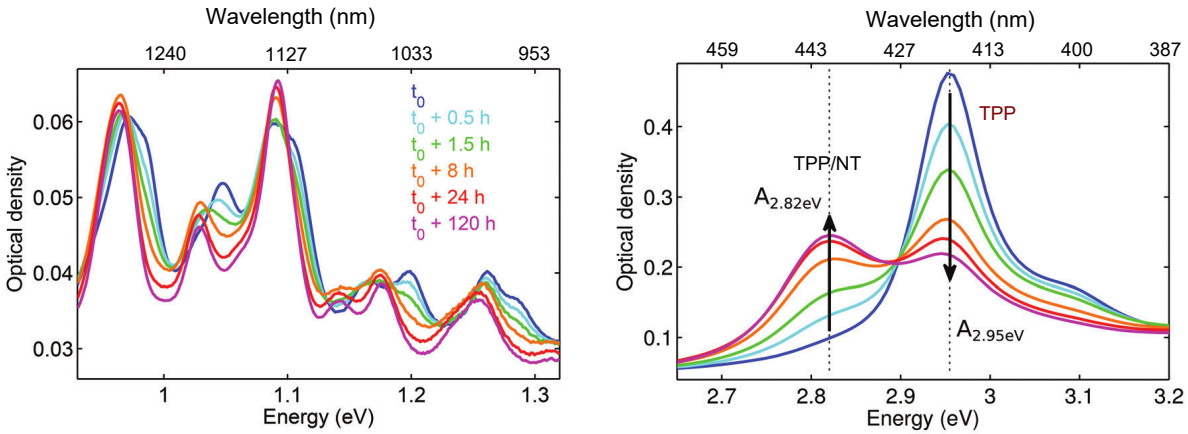

Figure II.12: Left: Evolution over time of the absorption of the nanotubes S_{11} transitions from the chiralities of a HiPCO batch after mixing with the porphyrin; Right: Evolution of the π-stacked and free porphyrin Soret absorption bands of the porphyrin over time.

The evolution of the Soret band is displayed on figure II.12 right. The peak of the free TPP at 2.95 eV (420 nm) decreases, while the one of the stacked TPP at 2.82 eV (440 nm) increases, according to the same dynamics. The timescale of this evolution is similar to the one of the nanotubes S_{11} transitions. It should be noted that this Soret band splitting exhibits an isosbestic point around 2.9 eV (428 nm), in which the absorption intensity is constant over time. This particular effect indicates the presence of an exchange between two distinctive molecular populations: the free porphyrins and the ones stacked at the surface of the tube. Finally, both contributions stabilize on the fifth day. The evolution of the optical density at 2.82 eV (440 nm) over time is plotted on figure II.13. Its increase is relatively well fitted with an exponential behavior, according to the formula:

$$A_{2.82}(t) = A_0 + (A_\infty - A_0)\left(1 - e^{-\frac{t}{\tau}}\right) \tag{II.4}$$

Such result evidenced a very slow kinetic, with a characteristic time τ of 8 hours. This is quite practical, as it gives enough times to collect every required spectroscopic data. However, this timescale is quite unexpected, as it is several order of magnitude larger than for the classical surfactant relaxation dynamics (according to section 1.1). At this point, the experimentalist does not have any leverage to control the efficiency or the timescale of the reaction. In particular, it is difficult to tune the concentration of isolated porphyrins due the poor solubility of the TPP in SC. Thus, there is a necessity to modify the surfactant environment.

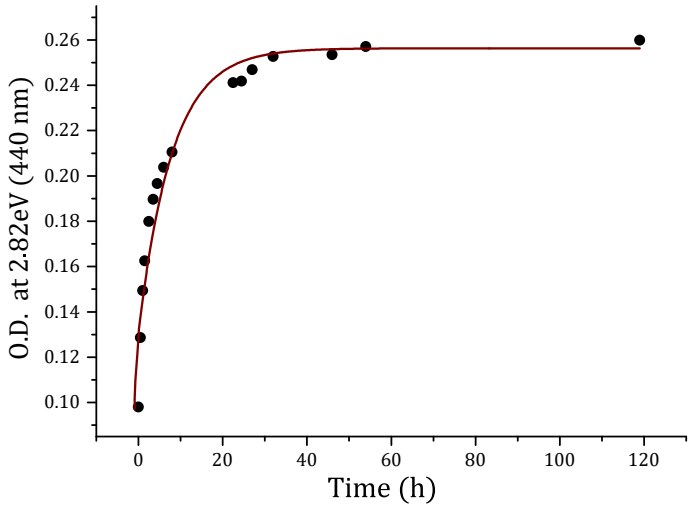

Figure II.13: Evolution over time of the amplitude of the Soret peak from the stacked porphyrins.

2.2 Effect of mixing of SC and SDS on a nanotube suspension

The next logical step was to mix SDS and SC solutions, to benefit from the qualities of both surfactants. SDS and SC mixes have been extensively employed to suspend carbon nanotubes.

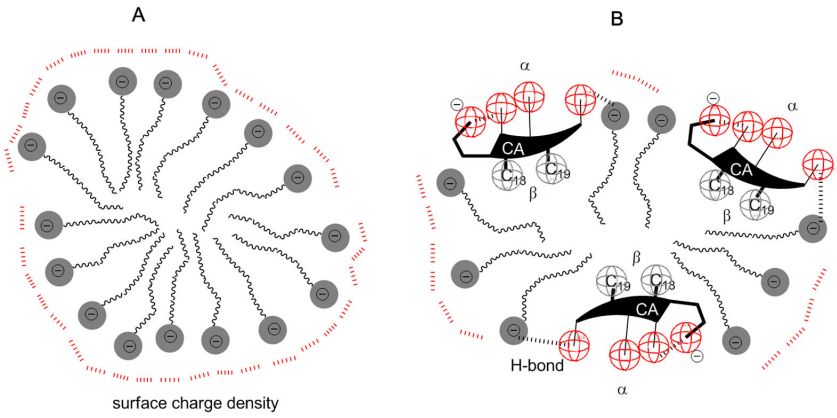

Figure II.14: Artistic view of a SDS (left) and a SDS/SC comicelle (right) alternating monomers of each types. The SDS monomers are represented in grey, while the SC ones (here called CA) are in black (hydrophobic part) and red (hydrophilic head), from [201].

As seen on figure II.14, these surfactants are known to mix remarkably well, forming hybrid micelles of around 40 monomers [201]. For a 1:1 SDS/SC proportion

ratio, Jojart and coworkers calculated a cmc of 4 mmol.L^{-1} [201]. This value is smaller than the value of both separate surfactants (see table II.1 earlier), proving the favorable interaction between them. Figure II.14 displays the modeled structure of the mixed micelle, where the SDS monomers are filling the empty spaces between the large cholate molecules.

On figure II.15, one can see the results of a molecular dynamics simulation from the same study [201]. It shows that the transition from separated monomers to hybrid SC/SDS micelles occurs within 10 microseconds. Such timescale is very similar to the one presented in section 1.1 for single surfactant reorganization.

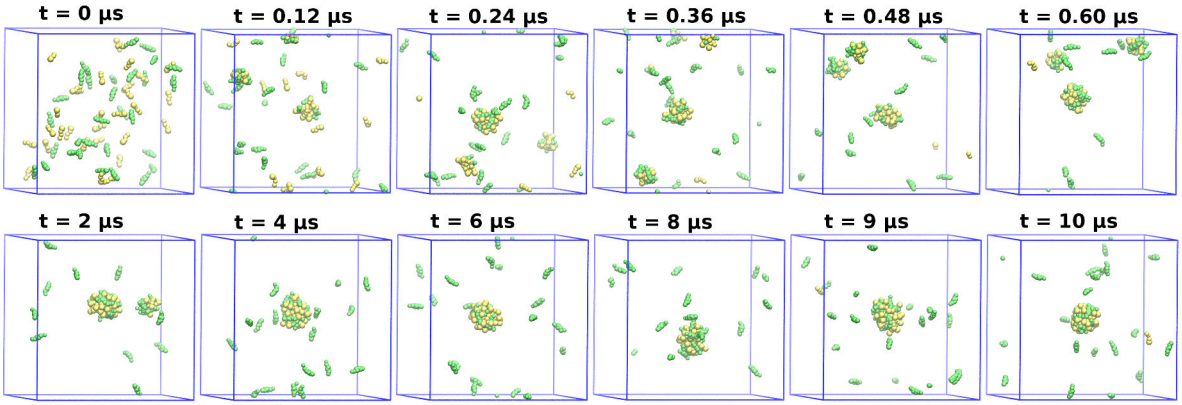

Figure II.15: Molecular dynamics of the formation of a mixed micelle of SC and SDS monomer within 10 μs; adapted from [201].

Before mixing with porphyrins, we have tested the behavior of a 2 %$w.t.$ SC CoMoCat nanotubes suspension upon dilution with a 2 %$w.t.$ SDS suspension. In the following work, the quasi monochiral CoMoCat nanotubes have been chosen to avoid any disturbance of the kinetic data coming from differences between chiralities. Upon a 50:50 volume dilution, the figure II.16 displays the evolution of the S_{11} maximum wavelength as a function of time. From the 982 nm initial value, the transition undergo a very fast shift to 995 nm. Then, the position is stable over time. This evolution occurs on a smaller timescale than the experiment resolution (of around 30 seconds).

This redshift has already been reported by several researchers, including an article from Maruyama and coworkers [202]. The SC micelle around surrounding the tube covers only 70 % of the tube surface [203]. This redshift may be interpreted as an ability of the SDS to enter inside the SC/nanotube micelle. The larger solvatochromism effect for SC/SDS mixes than for SC alone could indicate that SDS

is able to fill the available spaces inside the SC micelles, increasing the global surfactant coverage around the nanotube. Such effect proves that the mixing of the two surfactant phases occur very rapidly, in agreement with the τ_1 (respectively τ_2) relaxation model that predicts that SDS micelles release monomers (and eventually collapse) within less than a second in such conditions [185].

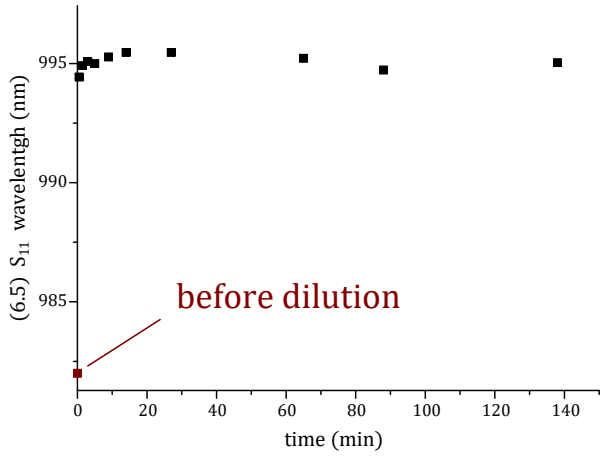

Figure II.16: Evolution of the (6,5) S_{11} transition wavelength of a full SC sample after mixing at t =0 with SDS in a 50:50 volume proportion.

Finally, we may study this effect at different proportion of SDS. This is quantified thanks to the volume ratio: $r_{sds} = V_{sds}/(V_{sds} + V_{sc})$. As seen on figure II.17, this effect appears progressively above a threshold ratio around $r_{sds} \simeq 20\%$:

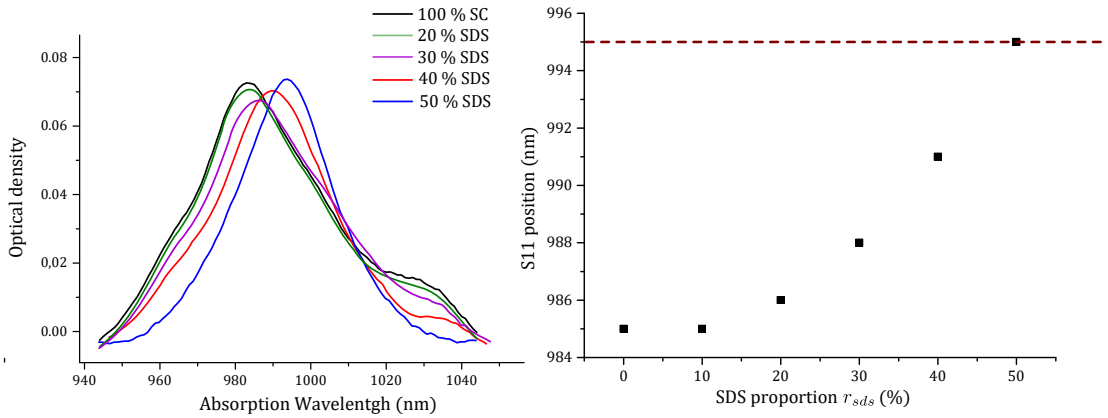

Figure II.17: Left: Optical absorption spectrum in the (6,5) S_{11} transition region as a function of the SDS volume proportion; Right: Variation of the (6,5) S_{11} absorption peak in mixed SC/SDS samples, as a function of the bulk SDS proportion.

For each volume proportion, SDS monomers are always available in the suspension and should in principle be able to enter the SC/NT micelle. It proves that there is a constant equilibrium between the bulk concentration and the micelle concentration of each surfactant. At low SDS concentration, SDS monomers cannot enter the SC nanotubes micelle in a significant proportion. When the concentration of SDS monomers is high enough, they are able to pass through the SC layer and interact with the nanotube.

2.3 Chemical reaction in mixed environment

After preparing a solution of porphyrins in a 2 %$w.t$. SDS suspension, we mixed it with a 2 %$w.t$. SC CoMoCat nanotubes suspension at $r_{sds} = 50$ % for a final TPP concentration of 20 μmoL.L^{-1}. The figure II.18 displays the spectroscopic responses of the sample once the equilibrium is reached. The results are very similar to the one for samples in single surfactants: shifted Soret band at 2.82 eV (440 nm), shifted nanotube transitions and energy transfer resonance. Thus, the presence of the SDS did not prevent the functionalization.

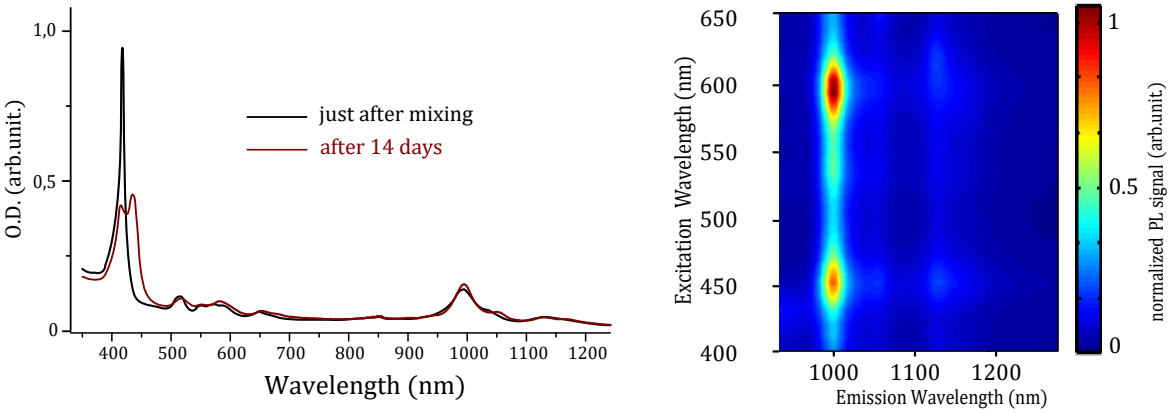

Figure II.18: Left: Optical absorption spectrum of the NT/TPP sample in mix SC/SDS environment, just after mixing (black) and after 14 days (red); Right: PLE map of the corresponding sample after 14 days.

The evolution of these features as a function of time has been monitored (see figure II.19). One can follow the amplitude of the free and stacked porphyrin Soret band, as well as the transfer ratio R. We see these characteristics evolve slowly to reach an equilibrium point within two weeks. This timescale is longer than the value in full SC samples.

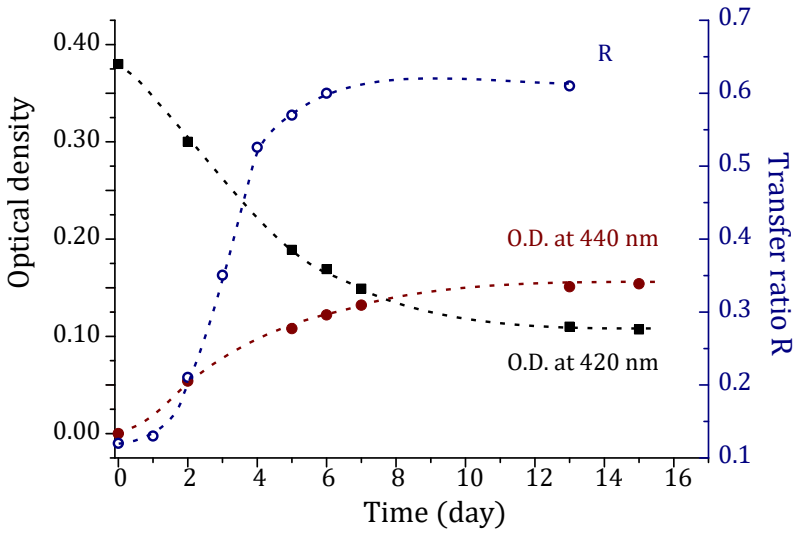

Figure II.19: Evolution of the optical density at 420 (black) and 440 nm (red) and of the transfer ratio R (blue) for the c_{tpp}=10 μmol.L^{-1} sample.

As a conclusion, these experiments highlight the presence of two characteristic times. A short one corresponding to the filling of the nanotube micelle with SDS monomers is quasi-instantaneous. This timescale is in agreement with the literature on micellar dynamics. Then, a longer timescale is evidenced, corresponding to the entering of the TPP inside the nanotube vicinity, visible in figure II.19. This very slow evolution remains to be explained.

2.4 Influence of the SDS micelles stability

Diffusion of dyes in micellar environment

The exchange of nanoobjects between micelles has been widely investigated [188, 204, 205]. For instance, Y. Rharbi *et al.* reported on the exchange of pyrene dyes in diverse micellar environment [204]. According to such studies, three kinds of micellar processes allow the exchange of hydrophobic molecules between micelles (figure II.20).

The first one is an exit-reentry pathway where the solute (the dye) spends a significant time in close contact with water molecules. This route is highly improbable for the hydrophobic porphyrin. The second one is a simple collision between two micelles, leading to a final larger micelle. It is called the collision-fusion mechanism (that may end up with a fission of the larger micelle, see figure II.20). The third one consists in the fission of the molecule's micelle into an unstable submicelle, that will merge with another micelle. We may assume that these three pathways occur simultaneously upon dilution, but that their relative proportion may vary along with the

stability of the micellar environment. All of these processes can be extremely slow in certain surfactants. For exchanges of dyes in SDS, Rharbi *et al.* have evidenced a reaction time longer than one day [205], which is similar to the present timescale for the Nt/TPP mixing process.

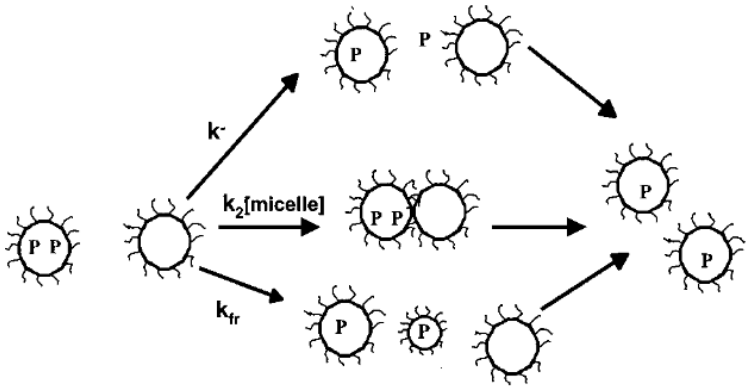

Figure II.20: Three different solute exchange mechanisms of pyrene derivatives (P) solubilized by Triton X-100, a nonionic surfactant. (a) Exchange via water mechanism. (b) Collision-fusion-fission mechanism. (c) fission-growth mechanism. The circles refer to the micelle core, and the letter P refers to the solute, from [204].

It is possible to adapt these two last processes to the Nt/TPP coupling process (see figure II.21). One of the empty micelle has to be replaced by a Nt/SC micelle, while the solute micelle corresponds to the TPP/SDS one:

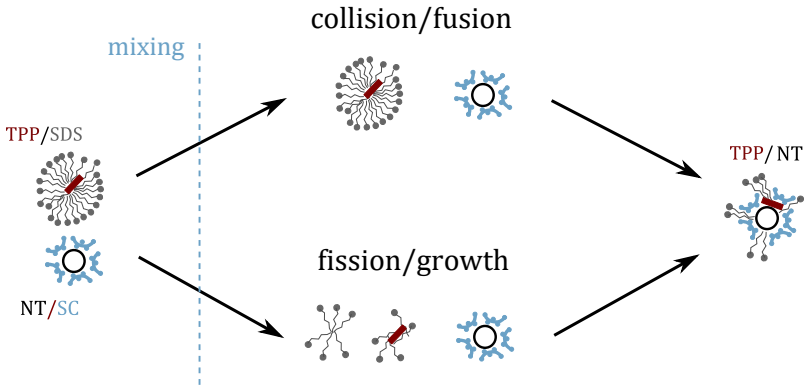

Figure II.21: Two probable micellar processes that would lead to the interaction between TPP and nanotubes, inspired from Rharbi 's work [204].

While the first one occurs between two stable micelles, the second one requires the destabilization of the molecule's SDS micelle. Moreover, large micelles have a slow diffusion dynamics, while monomers or small submicelles have larger diffusion

coefficients [206]. When the TPP are only surrounded by a submicelle, we see that they will rapidly diffuse and merge with the nanotube environment. At the opposite, they may remain isolated for a longer time if they are included in a stable SDS complete micelle. For these reasons, favoring the creation of submicelles is likely to speed up the reaction.

Evolution of the reaction timescale with SDS proportion

From the previous results, one may assume that the reaction velocity is limited by the extra stability of the TPP/SDS micelle. The simplest way to modify the organization of a surfactant phase is to create a dilution that will force a rearrangement. As a consequence, it has been decided to perform the stacking reaction using different proportions of the SDS phase (with different ratios $r_{sds} = V_{sds}/(V_{sds} + V_{sc})$). The final concentration of porphyrins will be maintained to 20 μmol.L^{-1} and the (6,5) nanotubes concentration will be controlled via the S_{11} optical density (of O.D.=0.15 after mixing).

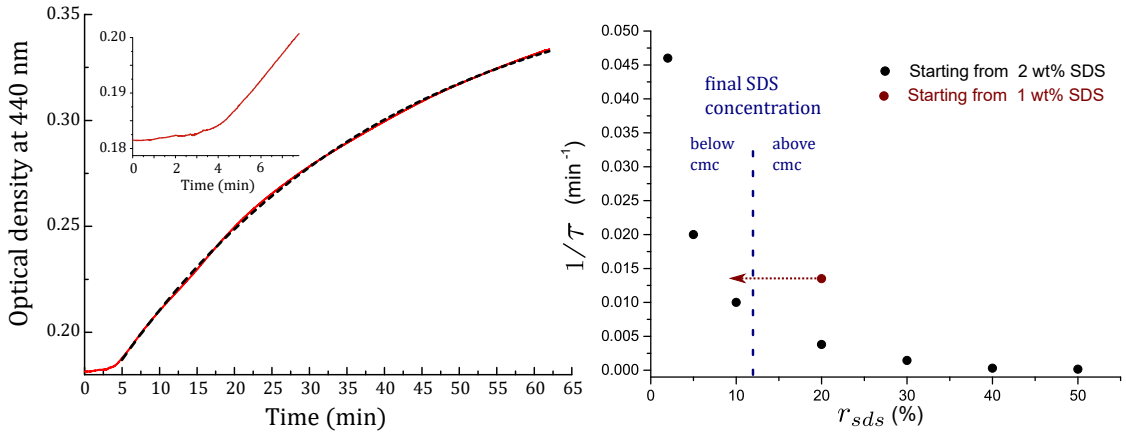

Figure II.22: Left: Optical density (Red) at 440 nm corresponding to the absorption of stacked porphyrins on nanotubes as a function of time for a SDS/SC ratio of 10% and its exponential fitting (black); (inset) zoom on the incubation stage; Right: Evolution of the reaction rate with SDS ratio for a final TPP concentration of 20 μmol.L^{-1}.

To study the influence of the micellar environment on the reaction speed, experiments as a function of the dilution ratio r_{sds} have been performed. As r_{sds} varies from 2 to 50 %, an exponential kinetic behavior is always observed. The variation of $1/\tau$ as a function of r_{sds} is displayed on figure II.22 right. An increase of the time constant is evidenced when the SDS ratio increases. From r_{sds} = 2% to 50%, its value is tuned from 20 minutes to approximately 3 days and 6 hours. It corresponds to a variation of the reaction rate $k = 1/\tau$ from 4.5×10^{-2} min^{-1} to 1.5×10^{-4}min^{-1}.

A progressive decrease of the functionalization characteristic time is observed as the proportion of the SDS phase decreases. With this decrease of the SDS concentration, it has been shown in section 1.1 that the concentration of SDS micelles is reduced, to eventually become unstable and relax into monomers. As a consequence, this decrease of the reaction timescale may be correlated with the stability of the TPP/SDS micelles, that can be overcome by a large dilution.

For $r_{sds} = 10\%$, the evolution of the optical density of the π-stacked porphyrins as a function of time is displayed in figure II.22. A sigmoid shape is observed characteristic of auto-catalytic reactions [87, 207]. These processes can be divided in two parts. The first part consists in a incubation process, where the reaction does not really start, as it is limited by another phenomenon [87, 207]. Here, for a $r_{sds} = 10\%$, the incubation time is of the order of 5 minutes, with a large variability from one sample to another. A possible explanation of this behavior will be discussed in the next chapter.

The second part of the kinetics corresponds to the functionalization reaction itself. The exponential fitted time constant is $\tau \simeq 60$ minutes which is two orders of magnitude faster than for $r_{sds} = 50\%$.

Beyond the information provided on the functionalization mechanisms, this proves the versatility of the method. At a r_{sds} ratio of 2%, the time constant of 20 minutes represents an important gain of time. In addition, we already proved that SDS is able to suspend a large quantity of isolated dye molecules. Hence, we are able to perform the functionalization in a fast, controlled and reproducible manner. Such reaction is simple enough to be performed as a basic titration. Adding very small amounts of TPP/SDS, one could control very precisely the reaction extent. Such precision was impossible with the direct swelling method.

Changes in the SDS organization upon dilution

In this part, the stability of the SDS micelles will be quantitatively discussed. The initial suspension of TPP is made at 2 w.t.% of SDS, corresponding to approximately 9 times the cmc of SDS ($cmc_{SDS} = 8$ mmol.L^{-1}) [208]. In this situation, the concentration of SDS micelles before dilution is around 1 mmol.L^{-1}. Then at a $r_{sds} = 50\%$, the final concentration of SDS is about 4 times the cmc, while $r_{sds} = 20\%$ leads to a concentration just above the cmc. As seen in figure II.23, the concentration of stable SDS micelles in these two configuration are respectively of 500 and 100 μmol.L^{-1}. Then, for lower ratios, the final SDS concentration falls below the cmc, which means that SDS micelles are no longer stable and will break into small submicellar structures. It is noteworthy that the speed of the reaction greatly increases for final SDS concentrations below the cmc.

As mentioned earlier, the value of the cmc changes when SDS is mixed with SC. This creates an uncertainty on the actual cmc value, that is likely to change with the

ratio of each surfactant [209]. Nevertheless, the value of 4 mmol.L^{-1} caculated by Jojart *et al.* [201] is not so far from the pristine SDS value of 8 mmol.L^{-1}. Therefore, the main interpretation of the dilution effects remain valid: a given proportion of SDS micelles are no longer stable and have to merge with the SC micelles. Thus, the pristine SDS cmc value will be used in the present discussion.

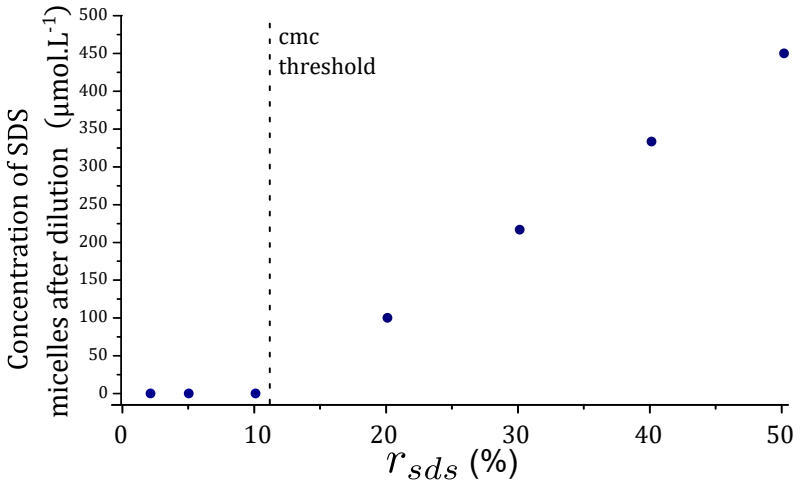

Figure II.23: Concentration of SDS stable micelles after dilution as a function of the r_{sds} ratio.

To test the influence of the SDS concentration on the reaction speed, a suspension of TPP of c_{final} = 20 μmol.L^{-1} in a 1 w.t.% of SDS has been prepared in the same conditions. Then, a r_{sds} = 20% suspension has been made. The final SDS concentration after dilution is 7 mmol.L^{-1}, below the cmc, and the corresponding reaction speed (red dot in figure II.22 right) is approximately four times higher than for the 2 w.t.% initial suspension with the same ratio. It is actually close to the 2 wt% experiment for a 10% SDS/SC ratio, confirming the role played by the concentration of micelles before the dilution. This is consistent with the fact that these two samples provide the same quantity of SDS to the final sample.

These results show that the c_{sds}/cmc ratio after mixing is an important parameter to understand the kinetics of such reaction. These results can be explained by considering the SDS micellar stability: as c_{sds}/cmc varies, the quantity of stable micelles evolves, modifying the reaction speed.

Passing the cmc threshold

Additionally to this equilibrium picture, we need to consider the disintegration dynamics of the SDS micelles. In particular, one has to remember that an important

proportion of micelles are empty. For each sample, the final TPP concentration after dilution is of $c_{final} = 20$ μmol.L^{-1}. Consequently, the concentration of TPP in the SDS phase before dilution ($c_{TPP-SDS}$) is different for each sample: between 40 and 1000 μmol.L^{-1} (see table II.2). However, the SDS micelle concentration before dilution is maintained to $c_{micelle-SDS}$=1000 μmol.L^{-1}. For the higher r_{sds} values, the TPP concentration before dilution is very small in comparison with the global proportion of SDS micelles. Yet, when r_{sds} decreases, the TPP concentration becomes important and a large proportion of micelles are filled with a dye. Thus, there may be a correlation between the proportion of occupied micelles before the dilution and the rate of the functionalization process.

r_{sds}(%)	$c_{micelle-SDS}$ (mmol.L^{-1})	$c_{TPP-SDS}$ (mmol.L^{-1})	x	p(0) (%)	p(1) (%)	p($x > 0$) (%)
50	1000	40	0.04	0.96	0.04	0.04
20	1000	100	0.1	0.91	0.09	0.09
10	1000	200	0.2	0.82	0.16	0.18
5	1000	400	0.4	0.67	0.27	0.34
2	1000	1000	1	0.37	0.37	0.64

Table II.2: Characteristics of the filled and empty SDS micelles before dilution for different ration r_{sds}: concentration of SDS micelle before dilution, concentration of TPP before dilution, ratio x of these two values, Poissonian probability for a micelle to be empty and to be filled. These numbers are calculated in order to get a 20 μmol.L^{-1} concentration of TPP in the final sample after dilution.

To quantify such effect, the number of molecules per micelles in the SDS phase (before dilution) can be calculated. Maiti *et al.* [210] suggested to evaluate the proportion p of micelles containing n molecules by a poissonian law:

$$p(n) = \frac{x^n e^{-x}}{n!} \tag{II.5}$$

where $x = c_{tpp}/c_{micelles}$. This method and the data from table II.2 can be used to evaluate the proportion of empty and filled micelles in the SDS phase before mixing with the nanotubes. On table II.2, one can observe that the probability of having one or several molecules per micelle (p($x > 0$)) is large below $r_{sds} = 10$ %.

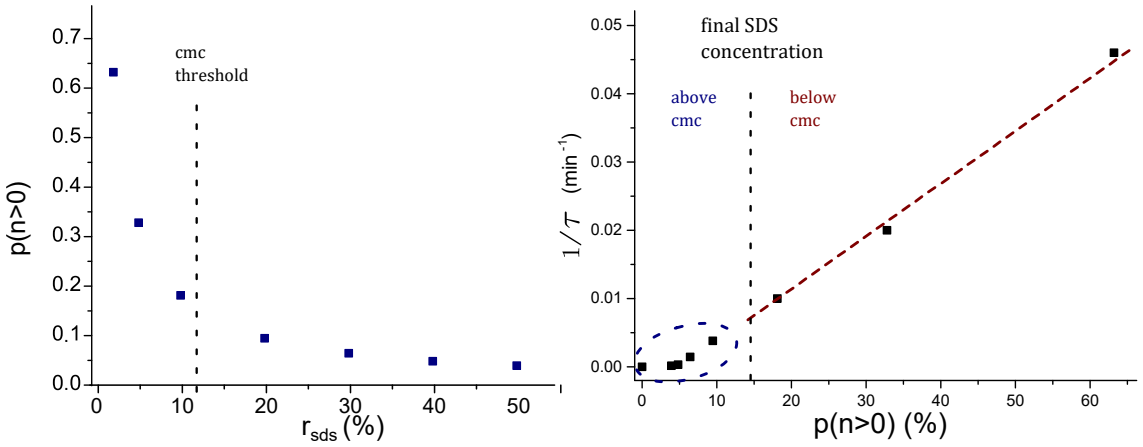

Figure II.24: Left: Evolution of the occupation probability of each micelle in the initial SDS phase as a function of r_{SDS} for a final TPP concentration of 20 μmol.L^{-1}; Right: Evolution of $1/\tau$ in regard of the proportion of micelles containing porphyrin in the SDS phase before dilution.

For the other ratios, the proportion of empty micelles is predominant, with an increasing importance as r_{sds} grows from 10 to 50 %. On figure II.24 left, one sees that the proportion of filled micelles decreases exponentially with r_{sds}, due to the Poisson formula. The characteristic time as a function of the proportion of filled micelles $p(n > 0)$ is plotted in figure II.24 right. For samples that pass below the SDS cmc (with high initial occupation probability) a linear tendency is observed. This proves the correspondence between the evolution of the two parameters. Hence, the proportion of empty micelles can be regarded as a limiting factor at low r_{SDS}, that should be kept to a minimum to ensure a fast stacking process.

However, at lower porphyrin occupation probability, the reaction timescale moves away from the linear behavior (see figure II.24 right). In this area, the competition between filled and empty micelles is not the relevant parameter. In this region, the porphyrin/SDS micelles remain stable, and the TPP diffusion occur through a slow micellar exchange process, involving fission growth or collision fusion events (as in figure II.21).

These effects may explain why the functionalization timescale is very long for large SDS ratios, while it decreases dramatically for $r_{sds} < 10\%$ (see figure II.22 right). At the moment of dilution, a competition between the reorganization of empty and filled micelles will occur. If the majority of SDS micelles is empty, these ones will rapidly fill the blank spaces inside the nanotube's coverage, limiting the rate of insertion of the TPP/SDS submicelles. Additionally, a collapsing TPP/SDS micelle may shock with other empty SDS micelles, instead of merging the nanotubes

SC micelles. On the other hand, if a large proportion of SDS micelles are filled, the functionalization timescale should be reduced, as the TPP/SDS will rapidly enter the nanotubes environment. This study of the filled/empty micelles competition has brought a finer insight into the evolution of the functionalization timescale when the SDS proportion is changed.

Evidence of a large activation Gibbs energy

The previous discussion showed that the stability of the surfactant environment was involved in the mechanism of functionalization. To understand this stability, a study of the reaction timescale as a function of temperature would also be valuable. In the theory of chemical kinetics, the rate k of a given reaction is fixed by the difference of energy between the initial state and the transition (or activated) state:

$$k_{\text{reaction}} = k_0 \exp\left(-\frac{E_a}{RT}\right) \tag{II.6}$$

where E_a is called the activation energy. A very small reaction rate is indicative of a very large activation energy E_a. When a simple exponential behavior is measured, the reaction rate is the inverse of the exponential time constant $k = 1/\tau$. On the microscopic scale, a chemical reaction only happens if the necessary reactants collide with sufficient energy. Hence, the activation energy can be pictured as a barrier to be overcome for the reaction to happen (see figure II.25). Indeed, the Arrhenius law (equation II.6) expresses the statistical rate of successful reactants collisions through a Boltzmann factor [211].

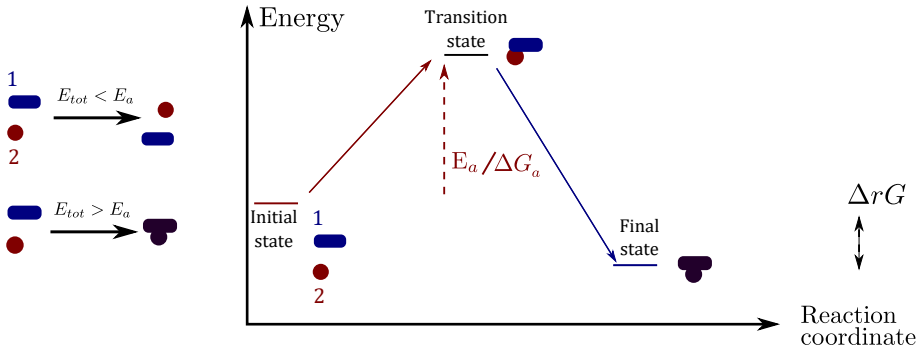

Figure II.25: Left: Artistic view of the influence of the activation energy; Right: Naive representation of the energy levels involved in a chemical reaction.

However, the reactants involved in the present reaction are not elementary molecules, but rather hybrid elements (NT+surfactants vs TPP+surfactants) including several monomers. As a consequence, these complex objects have a microscopic organization and a corresponding entropy contribution. For instance the ordering of the micellar

structure may evolve during the reaction. For such cases, Bruckener and coworkers suggested an adaptation of the Arrhenius model [212], where the activation energy is replaced by an activation Gibbs energy ΔG_a, that includes the entropy evolution:

$$k_{\text{reaction}} = k_0 \exp\left(-\frac{\Delta G_a}{RT}\right) \tag{II.7}$$

The possibility to evaluate a Gibbs energy of activation for the present reaction would bring valuable information on the kinetic mechanism. Thus, it has been decided to perform the stacking reaction as a function of temperature, for r_{sds}=10%. On figure II.26, an exponential decrease of the characteristic time is observed between 10 and 65°C. Once again, this brings additional tunability to the reaction, as it becomes possible to accelerate or stop the reaction by controlling the temperature. This evolution also proves that we are facing a thermally activated physico-chemical reaction, that follows Arrhenius law $k = 1/\tau \propto \exp(\frac{-\Delta G_a}{RT})$. A Gibbs energy of activation of 80 ± 10 kJ.mol^{-1} is extracted from the fit.

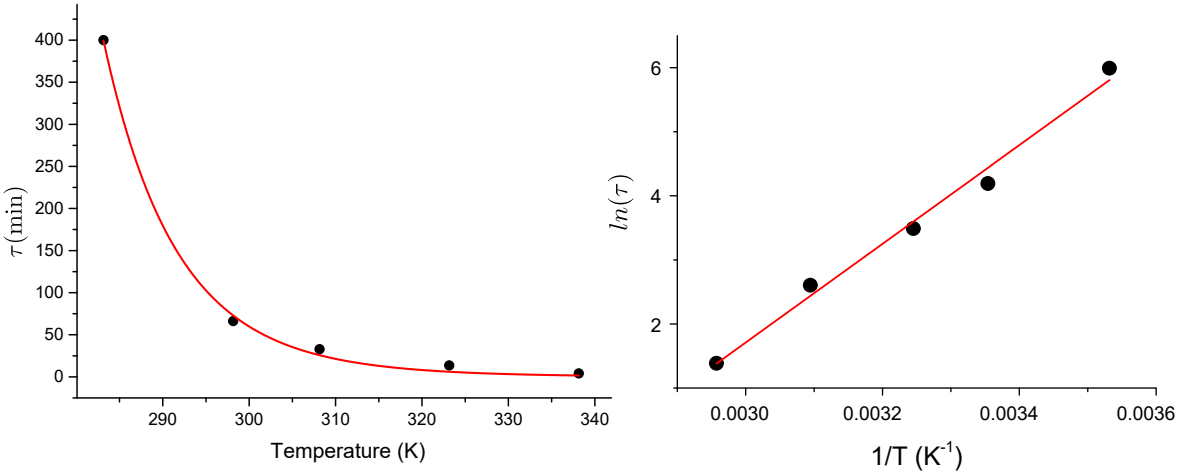

Figure II.26: Left: Evolution of the reaction time constant with temperature for $c_{tpp} = 20$ μmol.L^{-1} an $r_{sds} = 10$ %; Right: semi-logarithmic plot to extract the activation Gibbs energy.

Several other exponential evolutions, with similar timescales have been evidenced for reactions involving micelles suspended nanotubes [176, 213]. Among them, Mcdonald and coworkers [214,215] studied the dynamics of nanotubes flocculation upon dilution. They showed that it was a first order kinetics, driven by the surfactant desorption from the nanotube's surface. Upon a variation of the temperature, they found a large activation energy of the order of 50 kJ.mol^{-1}. In the present case, it is difficult to determine whether the activation energy corresponds to the stability of

the nanotubes micelles, of the molecules micelles, or to an interplay between both effects. This activation energy is also similar to the one found for the exchange of pyrene into TX-100 micelles [204]. Such similarities confirm that our reaction kinetic is limited by the diffusion of the TPP inside the surfactant environment.

Influence of the electrostatic repulsion effect

Above the cmc, several elements indicate that the TPP diffusion to the nanotube takes place by collision/fusion or fission/ growth pathways. For ionic compounds, these process have been proved to be extremely slow, due to the extreme stability of the micelles. As explained in the section 1.1, a main factor of stability for ionic micelles is the presence of charged functions. Through the interaction of these ionic centers, the micelle will be tightly organized to minimize the global electrostatic energy. These Coulomb interactions will significantly hinder the fast exit/entry dynamics of the monomers, blocking the fusion or fission of the whole micelles. Rharbi and coworkers compared the dynamical exchange of pyrene molecules between micelles of various surfactants [204, 205]. For non ionic surfactants (such as Triton X100), the timescale of such processes is close to a second, while they are drastically longer for ionic surfactant. For SDS, the authors showed that the pyrene exchange occurred on an day scale (see figure II.5 right), similarly to the dynamics observed for the Nt/TPP samples above the cmc.

surfactant	**M** ($g.mol^{-1}$)	**cmc** ($mmol.L^{-1}$)	$\mathbf{N}_a$ number	$\mathbf{c}_{surfactant}$ at 2 w.t. % ($mmol.L^{-1}$)	$\mathbf{c}_{micelle}$ at 2 w.t. % ($mmol.L^{-1}$)
SDS	289	8	60	69	1
Triton TX-100	625	0.5	155	32	0.2
CTAB	365	1	139	55	0.4

Table II.3: Principal characteristics of the micelles formed by the three compared surfactants, SDS, Triton and CTAB.

A protocol has been designed to test the presence of such Coulombic effects on the Nt/TPP reaction. The SDS (anionic) surfactant has been replaced by the non ionic Triton TX-100, or by the cationic CTAB. For each prepared sample, the final surfactant (Triton or CTAB) concentration was set to remain above the cmc.

Figure II.27 shows the kinetics for each surfactant of the reaction at a 50% ratio. In this situation, the concentration of Triton (or of CTAB) after dilution is much larger than the cmc. Consequently, this dilution ratio does not destabilize the TritonX100 nor the CTAB micelles. The micelles characteristics for each surfactant are presented in the table II.3. The characteristic time of the kinetics in Triton is of 8 minutes, which is three orders of magnitudes faster than the same experiments performed with SDS micelles at $r_{SDS} = 50\%$. Thus, the Triton micelles collapse with a much

faster dynamic than SDS ones. This is consistent with the absence of electrostatic micelle metastability in a nonionic surfactant. The mixture CTAB/SC represents an intermediary situation, with a characteristic time of 40 minutes. Here, the decrease of the timescale with respect to SDS/SC samples can be explained by the presence of attractive forces between the TPP/CTAB micelles and the Nt/SC ones. Yet, the repulsive electrostatic interactions within the CTAB micelles may explain why the timescale is five time larger than for Triton.

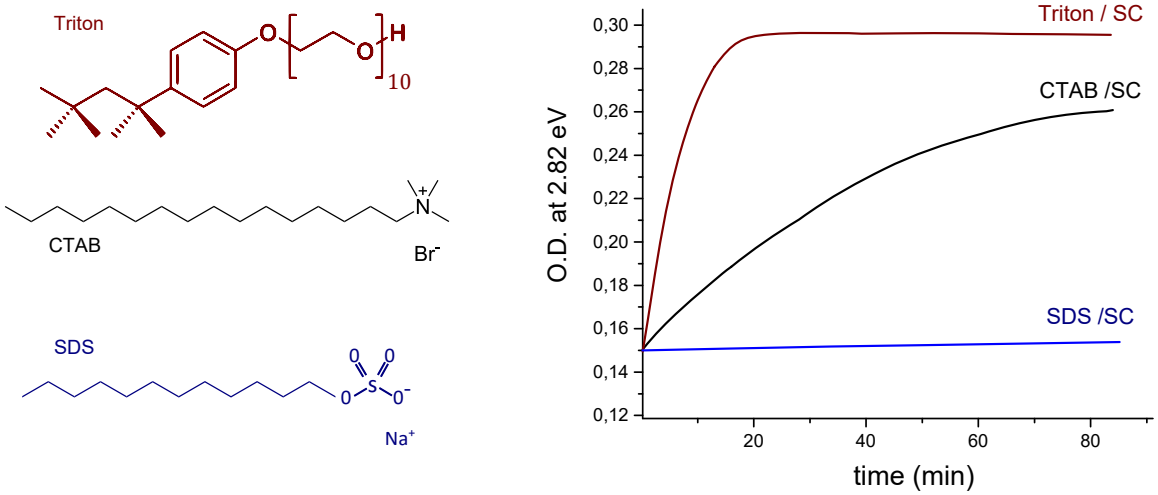

Figure II.27: Left: Chemical structure of the three compared surfactant with their different hydrophilic head; Right: Evolution of the optical density at 440 nm as a function of time for the three mixing configurations at $r = 50\%$.

On the fundamental point of view, this result strongly supports that internal and external coulombic repulsion is a limiting factor of the kinetics when anionic micelles are used. Above the cmc, these experiments confirm that the Nt/TPP interaction occurs via fusion/fission mechanisms. Additionally, this proves the versatility of such co-surfactant functionalization technique, that can be adapted to various surfactants according to the desired chemical reaction.

2.5 Summary of the microscopic reaction mechanism

The elements presented above indicate the presence of a slow, first order reaction, that is drastically influenced by a modification of the surfactant environment. This has been evidenced by the presence of a very large activation Gibbs energy. The corresponding reaction scheme is summarized in figure II.28.

The different stages of the reaction can be understood as follows. TPP are sol-

ubilized in SDS micelles and then diluted in a nanotubes suspension in cholate micelles. Then, the external diffusion of the TPP through the mixed surfactant medium starts. However, empty micelles will collapse first, limiting the diffusion rate of TPP molecules. In a second time, the SDS/TPP structure will meet with the SC/nanotube one. This is the internal diffusion step. The kinetics of the π-stacking reaction is slow, varying from days to tenths of minutes as a function of the chosen surfactant environment. Consequently, one can affirm that the external diffusion of the TPP is ruled by the high stability of SDS micelles, that limits the reaction rate.

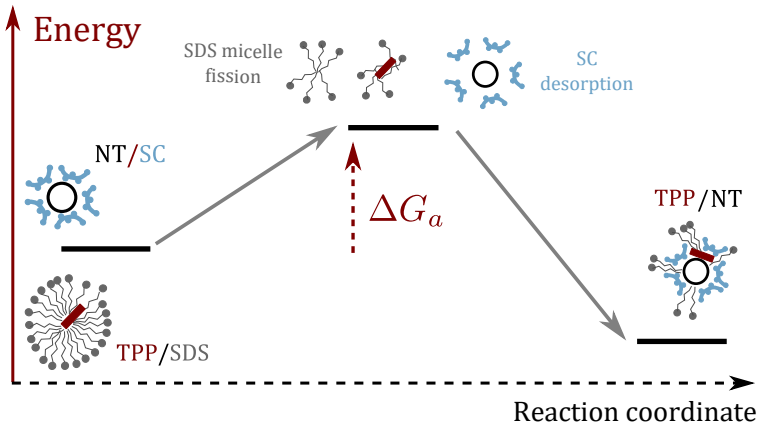

Figure II.28: Possible energy levels diagram according to the observed kinetic evolution.

Additionally, this stability can be tuned by changing the ratio r_{SDS}. Above the SDS cmc, this stability is driven by the electrostatic forces between SDS monomers. The porphyrins diffusion occur through very slow fusion/fission events. Below the SDS cmc, the interaction between adjacent micelles decreases and SDS micelles collapse. In this situation, the porphyrin can only be exchanged through fast fission/growth processes. Consequently, the SDS/TPP complexes are forced to merge with cholate micelles to be stabilized, speeding-up the π-stacking reaction. For these slow ratios, it has been shown that the proportion of empty micelles was the limiting kinetic factor. Despite the high binding energy of the TPP with its SDS micelle, a simple, controlled dilution can drastically raise the reaction speed. Changing the nature of the surfactant can also be a valuable alternative.

3 External and internal diffusion step

3.1 Hypotheses on the reaction kinetics theory

In the previous chapter, the interaction of the porphyrins with the nanotubes was presented through the equation:

$$TPP_{micelle} \; + \; NT_{micelle} = NT_{micelle}/TPP \tag{II.8}$$

This equation, symbolizing the π-stacking process, involves two different reactants. According to the kinetics theory this simple equation would not lead to first order kinetics [216]. A priori, this vision is totally different from the kinetic discussion developed in the previous sections, that focused on the exchange of the porphyrins between different micelles. Therefore, there are two different visions of the studied mechanism that seem to be incompatible.

These two steps can only coexist inside a more complex reaction mechanism. This mechanism can be seen as two successive steps: the external diffusion and the internal diffusion (π-stacking), accordingly to the discussion from the section 1.5. If the first step is only connected to the dynamics of micelle/TPP structures, the second will involve the nanotube and its micellar environment.

If the first step is regarded as the slowest step, the exponential behavior from the previous kinetics can be explained by a simple a diffusion model [217]. In such situation the reaction velocity can be expressed as $V \simeq k \times [TPP]$, where k is proportional to the diffusion coefficient of the TPP inside its environment. Through a simple calculation, this first order mechanism consistently leads to an exponential evolution of the reaction extent:

$$\frac{\mathrm{d}[TPP]}{\mathrm{d}t} = k \times [TPP] \;\; ; \;\; [TPP](t) = [TPP]_\infty + ([TPP]_0 - [TPP]_\infty)\left[1 - e^{-kt}\right] \tag{II.9}$$

However, this simple models completely neglects the influence of the internal diffusion. In reality, the internal diffusion process may not be totally neglected. This section will investigate on the relative influence of the two successive steps on the reaction kinetics.

3.2 Evolution of the velocity with reactants concentrations

To look for a possible contribution of the internal diffusion step, one can study the kinetics at different reactant concentrations. In principle, the velocity of this internal step should depend both on the porphyrin and on the nanotube concentration. In this section, the proportion of SDS will be maintained to $r_{sds} = 10\%$. Such a small ratio ensures that the external diffusion step is fast. This can help to observe a contribution from the second internal step.

Under this two steps hypothesis, the variation of the initial stacking velocity has been measured as a function of the concentrations of either the TPP or the nanotubes. This initial velocity is a simple and classical tool to find the partial reaction orders [218] relative to each reactant. To measure this velocity, the slope

ν_0 of the optical density at 440 nm was extracted, just after the incubation phase (see figure II.29). This quantity ν_0 is directly proportional to the theoretical initial velocity $\nu_0 = V_0 \times \epsilon_{440}$, where ϵ_{440} is the molar extinction coefficient of the stacked porphyrins.

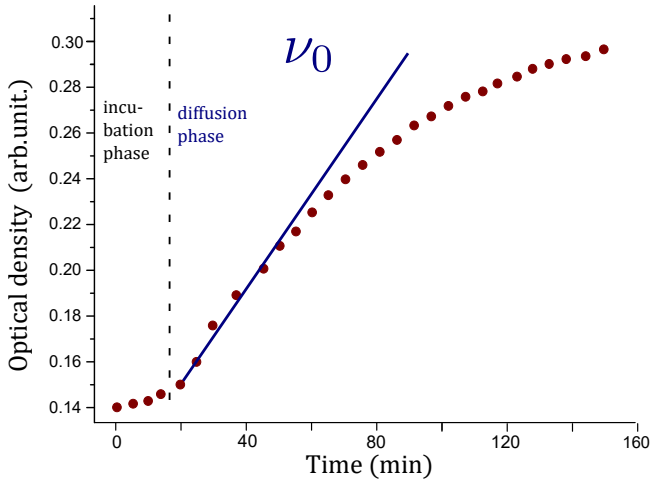

Figure II.29: Example of the linear fitting method to obtain the value of ν_0 from the evolution of the optical density at 440 nm after mixing for a given sample.

Influence of the adsorbate concentration

Figure II.32 displays the evolution of the reaction speed as a function of the final TPP concentration:

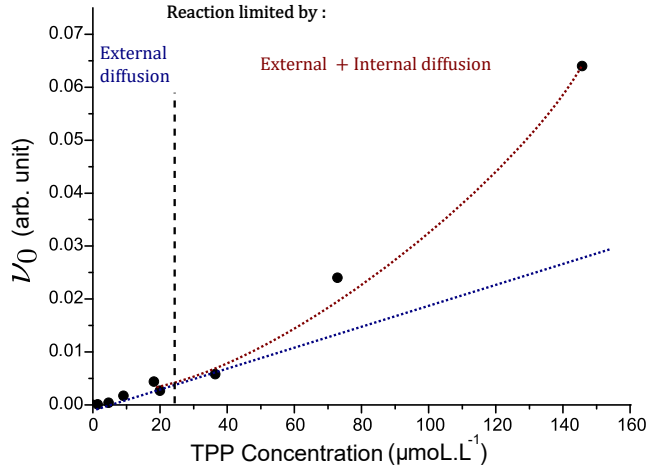

Figure II.30: Evolution of the initial velocity with the final porphyrin concentration for a r_{sds} ratio of 10 %.

We see that ν_0 increases with molecular concentration. On the first part of the curve, the evolution is quasi linear. At low concentration, the rate of destabilization/ diffusion of the SDS/TPP micelles is small and there are very few diffusing porphyrins. This behavior is consistent with the limitation of the kinetics by the external diffusion stage only.

However at high TPP concentration, the slope of the curve increases. Thus, the dependence of the velocity with the porphyrin concentration has changed. The fact that this second step is surlinear is an important result. It proves that the partial order relative to the TPP is here larger than one. Another technique to verify such result is to monitor the time evolution of a very concentrated sample ($c_{final-TPP} = 140\ \mu mol.L^{-1}$):

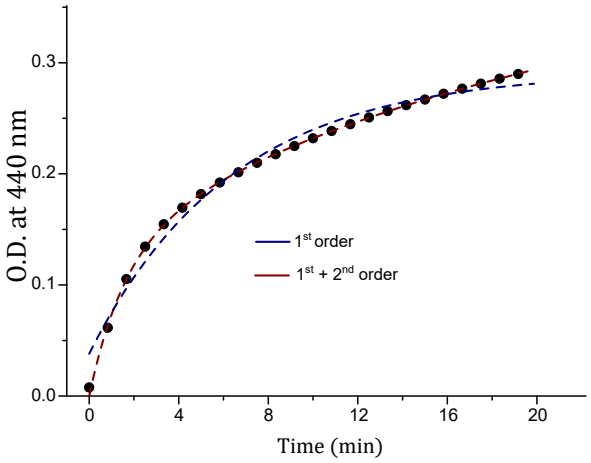

Figure II.31: Evolution of the optical density at 440 nm with time for a r_{sds} ratio of 10 % and $c_{final-TPP} = 140\ \mu mol.L^{-1}$.

On figure II.31, the characteristic timescale of the absorption variation at 440 nm is very short: around six minutes. However, such evolution does not follow an exponential behavior (blue dotted line). It may be fitted by the combination of a first and a second order fitting function (red dotted line):

$$A_{440}(t) = A_0 + \underbrace{A_1 e^{-k_1 t}}_{\text{first order}} + \underbrace{A_2 \frac{k_2 t}{1 + k_2 t}}_{\text{second order}} \tag{II.10}$$

Thus, these experiments are a clear evidence of two different reaction regimes with respect to the porphyrin concentration. As it will be detailed in the next sections, the π-stacking step implies the cooperation of several porphyrins that will bind to the tube simultaneously:

$$hTPP_{micelle} \; + \; NT_{micelle} = NT_{micelle}/TPP_h \;\; ; \;\; h > 1 \qquad \text{(II.11)}$$

From these results and the previous discussion on the mechanism, the observed cooperative regime can be attributed to the internal diffusion of the TPP inside the nanotube's micelle. At low concentration, this cooperative effect is too fast and has no impact on the initial velocity. In the high concentration region, the external diffusing rate of porphyrins becomes important. This explains why the effects of both the external and the internal diffusion are observable.

Influence of the adsorbent concentration

Following this internal diffusion hypothesis, one can postulate that the velocity should also depend on the nanotubes concentrations. Thus the final molecular concentration was fixed to 20 μmol.L^{-1} and several samples were prepared at different nanotubes S_{11} optical densities (i.e. different concentrations). On figure II.32, the velocity diagram can also be splitted in two parts. When the nanotube concentration is high enough, velocity tends to saturate. It may eventually become constant, even if the saturation threshold seems to be at a very high concentration. This result corresponds to a regime where the adsorption site concentration is high enough, and the velocity is only limited by the TPP/SDS diffusion. Consequently, the velocity do not depend on the nanotube concentration. Unfortunately, the higher concentrations that would bring additional information cannot be reached, due to the complexity of the nanotube dispersion procedure.

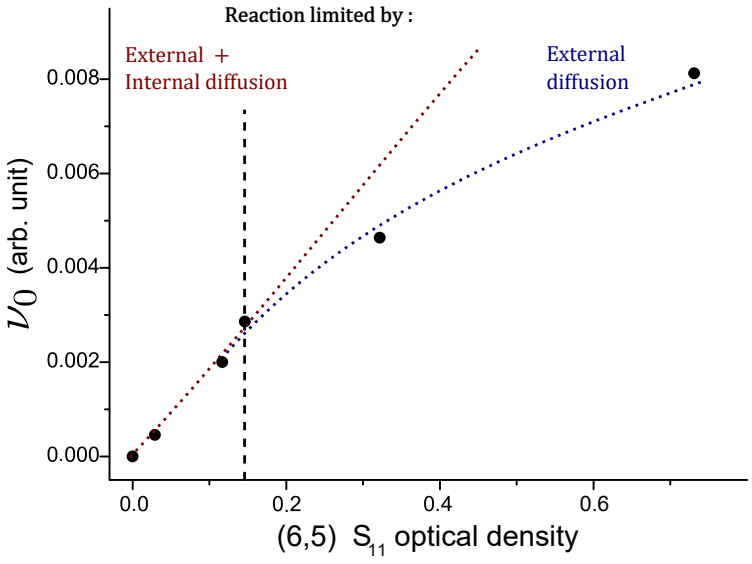

Figure II.32: Evolution of the initial velocity with nanotube optical density (after dilution) for a r_{sds} ratio of 10 % for a final molecular concentration of 20 μmol.L^{-1}.

At low concentration however, the velocity increases quite linearly. Hence, this part corresponds to a partial order of one with respect to the nanotube. In this part of the curve, the velocity is likely to be limited by the probability for the TPP to interact with the nanotube. The separation between external and internal regions seems to be inverted with respect to the TPP concentration evolution. The global behavior may be fitted with sublinear power law of 0.7.

As a conclusion, studying the initial velocity proved to be useful to gain insight on the global mechanism. It has been proved that the nanotube concentration plays an important role into the global mechanism. Until now, the reaction velocity was assumed to be entirely ruled by the stability of the TPP inside its micellar environment. This study has highlighted that the nanotubes play also a role. It is now clear that the internal and the external diffusion steps can both influence the reaction velocity, in different regimes of concentrations. The reasons of such dependence on the reactant concentrations will be detailed in the following chapter, in regard of the thermodynamics data and of a comprehensive model.

3.3 Velocity differences among a HiPCO sample

Since the nanotubes characteristics influence the kinetics, it can be valuable to look for differences of dynamics between nanotubes chiralities. During the internal diffusion stage, the porphyrin will have to enter the SC coverage of the nanotube, force the SC to desorb from the nanotube, and eventually adsorb at the nanotube surface. One can see that such steps will be deeply connected to the ordering of the cholate around the tube. It is commonly known that energetics and the organization characteristics of the SC/Nt binding varies from one chirality to another [67, 219].

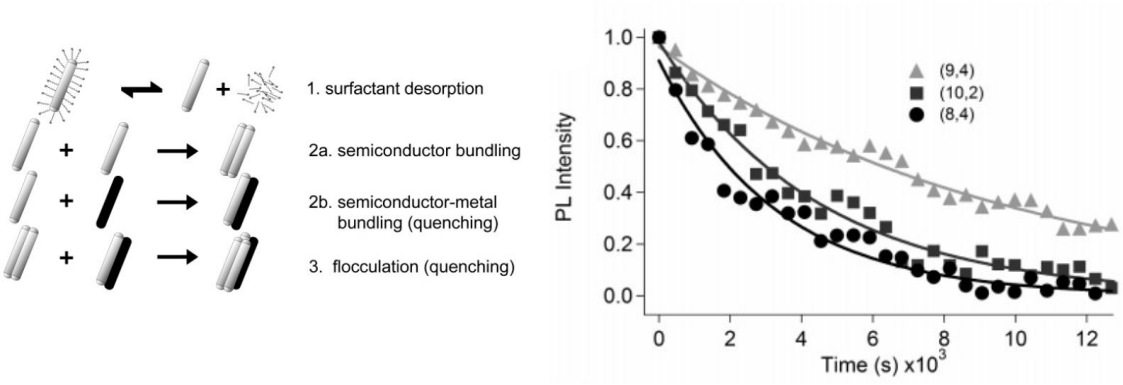

Figure II.33: Left: Simplified schematic of steps in nanotube rebundling and flocculation; Right: Photoluminescence intensity maximum versus time, showing progressive aggregation, for three different nanotube species, from [214].

Blackburn and coworkers [214] looked at similar effects by studying the flocculation (bundling) of nanotubes upon strong dilution. They found that the velocity of this process was limited by the desorption of the surfactant from the nanotubes surface (see figure II.33).

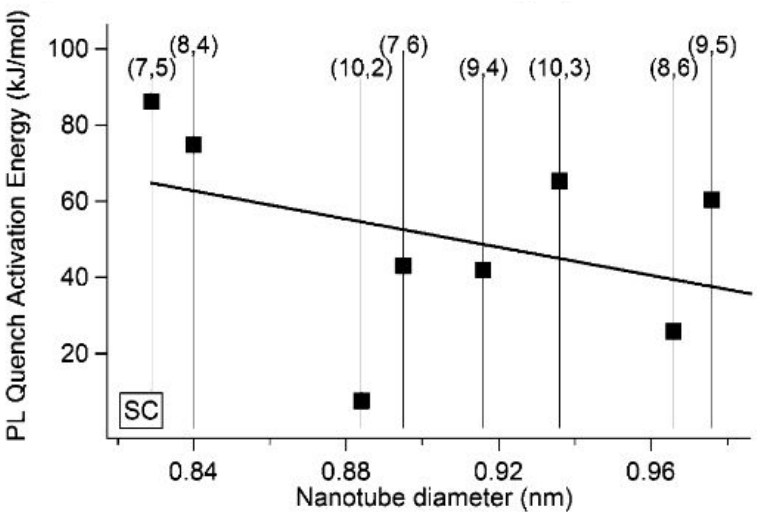

Figure II.34: Measured PL quench activation energy versus nanotube diameter for SC suspension surfactants, from [214].

Performing PLE maps, they monitored the bundling velocity for several chiralities of nanotube. They showed that some chiralities reacted faster than others. Repeating the experiments at various temperatures, they found a decrease of the activation energy with the nanotube diameter (see figure II.34). Thus, they proved that the cholate removal was more favored on larger nanotubes, leading to faster desorption dynamics.

Even if the NT/TPP interaction is more complex than a mere cholate desorption, one may wonder if similar diameter effects are present. To answer to this question, the interaction between TPP and HiPCo nanotubes has been monitored, in r_{sds} = 10% SDS/SC samples. Figure II.35 left displays the nanotubes absorption spectra (2 w.t. % SC sample), upon mixing with a TPP/SDS sample (to reach a final concentration of $c_{TPP} = 50\mu\text{mol.L}^{-1}$) for various time delays. As a function of time, the S_{11} transitions progressively redshifts. Despite the difficulty to point out the maximum position of each chirality, figure II.35 right shows the kinetic evolution of the reaction extent for (6,5), (7,6) and (8,6) nanotubes populations. The reaction extent has been extracted from the energy position of each transition: $X = (E_0 - E)/(E_0 - E_\infty)$. Upon an exponential fitting, different characteristic times

are obtained for the three chiralities: $\tau_{(7,6)} = 7$ min, $\tau_{(8,6)} = 16$ min and $\tau_{(6,5)} = 29$ min.

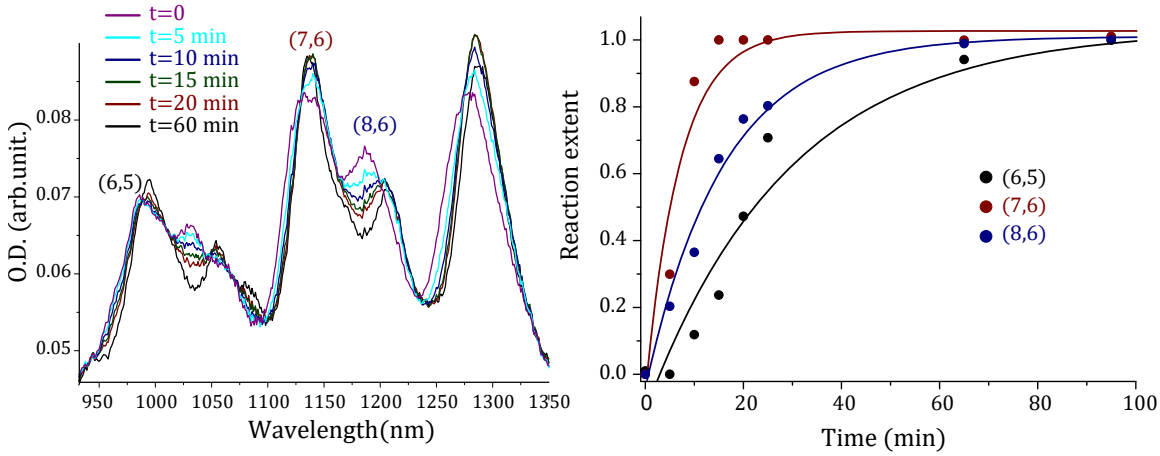

Figure II.35: Left: Evolution of the absorption of the S_{11} transitions from a SC/HiPCo sample after mixing with a TPP SDS suspension (final concentration $c_{TPP} = 50\mu$mol.L^{-1}); Right: Evolution of the reaction extent for three chiralities calculated from the shift of the S_{11} transition in energy along with their exponential fits.

Hence, this experiment evidences a variation of the reaction rate as a function of the nanotube chirality. In other words, the energy required for the TPP molecules to replace the nanotubes surfactant layer changes as a function of the nanotube species. This variation of velocity may correspond to differences in activation Gibbs energy :

$$\Delta G_2 - \Delta G_1 \simeq RT \ln\left(\frac{\tau_2}{\tau_1}\right) \quad ; \quad RT \simeq 2.5 \text{ kJ.mol}^{-1} \tag{II.12}$$

This estimation leads to variation of 2 to 3 kJ.mol^{-1} around the value of 80 kJ.mol^{-1} value for (6,5) nanotubes. Thus, this results present similarities with the nanotube flocculation experiment. However, the variation of the activation energy with diameter is one order of magnitude smaller than the data from Blackburn and coworkers ([214], $\simeq 20$ kJ.mol^{-1} between (7,6) and (8,6)). In our case, it is difficult to be quantitative, as an effect from the nanotubes concentration cannot be totally excluded. Indeed, a larger velocity may also come from a larger nanotubes concentration for a given chirality. A PLE experiment, or the use of chirality sorted samples would help to quantify the speed for each species of nanotube.

3.4 Stacking reaction of porphyrin on graphene nanosheets

To go further, the results on HiPCO nanotubes will be compared with the stacking reaction on graphene nanosheets. Indeed, if there is a diameter dependence of the

reaction velocity, the graphene could represent the infinitely large diameter limit (larger lateral size and larger radius of curvature).

The graphene nanosheets were purchased as a 2 wt% sodium cholate (SC) suspension [220] from NanoIntegris (PureSheet MONO [221], see figure II.36 left). The samples contain one to few layers graphene flakes in the proportion written below in Tab.(II.4). The graphene concentration is 0.05 mg.mL^{-1}, with an average flake area of 10^4 nm^2 and a large statistical dispersion in size [221].

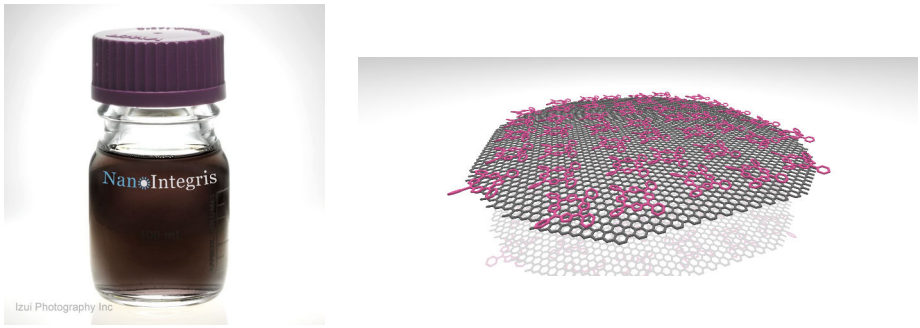

Figure II.36: Left: Suspension of PureSheets ™ Graphene Nanoplatelets from Nanointegris [221]; Right: Side view of a graphene nanosheet covered with porphyrins.

	1 layer	2-layers	3-layers	4-layers or more
Proportions in the graphene suspension (%)	27	48	20	5

Table II.4: Proportions of layers among the graphene sheets.

The functionalization reaction has been performed with the two step reaction method presented above, in a $50\% - 50\%$ volume proportion with both reactants in 2 w.t.% sodium cholate. After mixing the separated suspensions, the functionalization process was monitored by optical absorption spectroscopy (OAS) in the Soret porphyrin region. As graphene has a 2D semi-metallic electronic structure, it does not present any absorption band: its absorption is flat in the visible region. Nevertheless, it contributes to the scattering background on the absorption spectra (see figure II.37). The figure II.37 displays the optical density evolution of a sample including 8 $\mu mol.L^{-1}$ of TPP.

At the initial time, the absorption spectrum solely displays the free porphyrins response, with its main Soret band peak at 2.95 eV (420 nm). After a few minutes, an additional 2.79 eV (444 nm) resonance grows spontaneously and reaches a saturation

within 5 hours. In every sample, the final absorption shows an equilibrium, in which both shifted and unshifted populations are present.

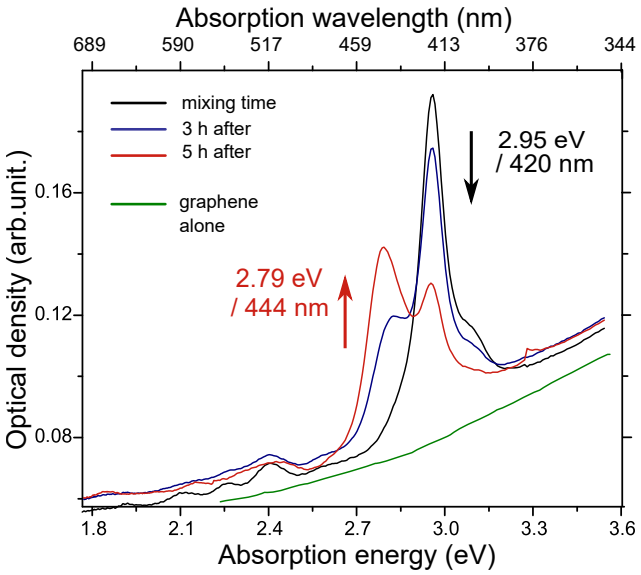

Figure II.37: Absorption spectra of the sample for a concentration of 8 $\mu mol.L^{-1}$ (*arrows symbolise evolution over time*).

It may be assumed that the adsorption process of TPP molecules on sp^2 graphene produces similar results to the one on nanotubes. Thus, the 2.95 eV (420 nm) and the 2.79 eV (444 nm) lines can be assigned respectively to the free and π-stacked porphyrin populations. In the following, the dynamics of the regular and the redshifted TPP absorption peaks will be followed.

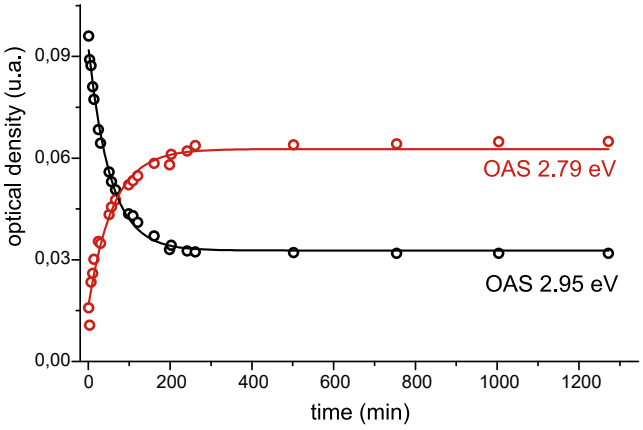

Figure II.38: Kinetic monitoring of the two main absorption peaks.

The absorption kinetics on figure II.38, of both free and π-stacked porphyrins peaks are properly fitted according to single exponential models, with characteristic times of around 60 minutes. Such exponential timescales are quantitatively faster than the previous results on HiPCO nanotubes from section 2.1, in which similar reaction conditions resulted in a timescale of around 120 hours. Since we have approximately the same carbon concentration (0.07 mg.mL^{-1} for HiPCO Nanotubes), we may quantitatively compare the two timescales. This would correspond to a difference in activation Gibbs energy of:

$$\Delta G_{a-\mathrm{Nt}} - \Delta G_{a-\mathrm{graphene}} \simeq 10 \text{ kJ.mol}^{-1}. \tag{II.13}$$

This represents a 10 to 15 % variation of the Gibbs activation energy, compared to the previously discussed activation energies for carbon nanotubes. From the discussion of the kinetic mechanism from the previous sections, one may try to explain such variation. Between graphene and carbon nanotubes, two physical parameters are changing. The first one is the size of each carbon nanoobjects: the graphene flakes have average width of 100 nm while the HiPCo nanotube's diameter is close to one nanometer. Consequently, the curvature of the carbon surface is also very different. These two parameters are likely to influence the adsorption dyanmics of both the surfactant and the TPP molecules. Indeed adsorption mechanism may strongly depend on dimensionality as well as on available adsorbent surface [222].

On the other hand, such effects could also be induced by the micelle environment itself. As it was shown in section 2.5, the reaction kinetics is influenced by the ability of the TPP to be exchanged and diffuse within the micellar environment. The fission/growth and collision fission pathways that were discussed earlier are still valid for graphene. As the dimension of the carbon surface increases, we may think that these two TPP exchange mechanisms may evolved, and probably be drastically accelerated. For instance, we may speculate that the large size of the graphene sheets has a higher capacity to break and absorb the TPP micelles. In a nutshell, a variation of the kinetics as a function of the size and curvature of the carbon surface has been evidenced. From one nanotube chirality to another or in comparison with graphene nanosheets, the reaction rate was shown to be different. Such differences are obviously linked to the microscopic functionalization mechanism. A proper model (diffusion in an electrostatic gradient) and simulation (molecular dynamics, DFT, ...) would bring an finer insight into the physical effects involved.

4 Conclusion

This chapter studied the organization of surfactants (and particularly SDS and SC) into micelles and their ability to drive the Nt/TPP interaction. It has been evidenced that the ability to suspend TPP is much higher into SDS, due to its large spherical structure with a protective hydrophobic center and a hydrophilic outer part. In a second time, a two step functionalization technique has been designed to control the reaction. The reaction timescale was shown to be limited by the stability of the surfactant medium. Such reaction is very slow in single surfactant media, but can be more controlled and accelerated in a surfactant mixes.

The versatility of such surfactant mixing allowed to performed an extensive study of the TPP exchange mechanism. Driven by a large activation Gibbs energy, the reaction timescale is ruled by the stability of the TPP/SDS micellar sructure. This metastability is due to the hydrophobicity of the TPP molecule, as well as to the coulombic interaction between anionic surfactants heads. Such stability could be easily overcome by a large dilution, as the SDS micelle is forced to break.

Then, the internal diffusion was shown to play an important role into the functionalization timescale. As the reactants concentration was changed, the presence of two concentration regimes was evidenced, in which external and internal diffusion have a different influence on the reaction velocity. In addition, the diffusion speed was proved to depend on the dimensionnality (length, curvature) of the carbon surface. For complex reasons, the TPP exchange mechanism is drastically accelerated for large and flat graphene nanosheets.

Finally, this chapter has highlighted the importance of controlling the organization of the micellar environment. During a functionalization process such as the present one, it can limit or favor the interaction between the reactants. This limitation may be kinetic, but it can also impact the final state of the reaction. In complement to this kinetic study, one may wonder if the surfactant environment has an impact on the thermodynamical characteristics of this adsorption reaction.

Chapter III

Thermodynamics of the functionalization process

The previous chapter was the first step to gain a wider perspective on the noncovalent functionalization mechanism. The essential message was that the diffusion of the nanoobjects through the micellar environment was responsible for the main characteristics of the reaction dynamics. Additionally, the kinetic role of the internal diffusion step has been highlighted. Since this step occurs after the external diffusion, it is difficult to study its energetic characteristics through a kinetic study.

The following chapter will attempt to collect important information on such internal diffusion by monitoring the equilibrium state of the reaction. The associated thermodynamic parameters will be assessed by sampling a wide range of porphyrin concentrations. This will provide a fine insight into the mechanisms that lead to the full coverage of the carbon nanotube surface.

After a short introduction of the adsorption thermodynamics, the study will first focus on monochiral (6,5) nanotubes samples. The monitoring of various spectroscopic features of both the nanotubes and the porphyrins will be used to carefully study the reaction equilibrium state. Then, the impact of a surfactant mixing on these thermodynamics results will be studied. A great care will be taken to find the link between these equilibrium considerations and the kinetic results from the previous chapter. For this purpose, a simulation of the reaction process will be presented in order to understand the relative contributions of the external and the internal diffusions into the global mechanism.

As a second step, the competition of the stacking process between different nanotube species will be studied using a polychiral HiPCO nanotube sample. Energetic and ordering considerations will be detailed, and a connection of such effects with thermodynamics considerations and DFT calculations will be discussed. As the infinite diameter limit, the stacking equilibrium on graphene nanosheets will also be studied.

Finally, this chapter will discuss the ability of molecules to present a cooperative

behavior during the π-stacking process. Porphyrins with slightly modified structures will be used to try to modulate this cooperative effect. Kinetic and thermodynamic studies of these samples will be performed to understand the actual impact of these structural modifications.

1 Thermodynamics equilibrium study on (6,5) nanotubes

1.1 Description of the formalism to study the reaction equilibrium

Any adsorption reaction consists in forcing a small component (the adsorbate) to leave its bulk equilibrium state to attach onto a surface (the adsorbent). Like many chemical or physical processes, such a reaction is often equilibrated [223]. In other words, the adsorbate has to be present in a large excess in order to fully cover the reacting surface. As any equilibrated reaction, such process has a characteristic reaction constant K, and a corresponding Gibbs energy ΔrG. Studying this equilibrium allows to understand which phenomena favor or limit the reaction extent.

In this chapter, we will elaborate a thermodynamic model to assess such values for the functionalization process. The previous kinetic discussion already proved that the reaction extent can be optically monitored as a function of time. This method will be adapted here to study the evolution of the nanotube coverage with TPP as a function of the porphyrin concentration. First, a proper formalism is required to describe the adsorption process. As presented in the previous chapter, every nanotube can be artificially cut into a series of adsorption sites, with an initial concentration c_{site}. Then the adsorption reaction can be simplified into a simple equation:

$$\text{site} + \text{TPP} = \text{site/TPP} \tag{III.1}$$

which symbolizes the attachment of a porphyrin molecule onto a carbon site. As in chapter II, the initial concentration of porphyrin is c_{TPP}. Since this process is equilibrated any sample eventually contains interacting and non-interacting porphyrins in significant proportions. The reaction constant K associated to such a reaction can be expressed as:

$$K = \frac{[\text{site/TPP}]_{eq}}{[\text{site}]_{eq}\,[\text{TPP}]_{eq}} \tag{III.2}$$

The brackets define the concentrations values, while the *eq* index indicates the equilibrium values. Here, every concentration is divided by 1 mol.L^{-1}, to form an adimensionalized K number. This constant rules the reaction equilibrium, as the reaction extent moves forward when the K value increases. The value of K is directly connected to the reaction Gibbs energy:

$$\Delta rG = -RT\ln(K) \tag{III.3}$$

The thermodynamics of an adsorption reaction is often studied through the Langmuir isotherm formalism [197, 224]. It consists in plotting the reaction extent X as a function of the available adsorbate concentration (see figure III.1 left). As the concentration increases, the adsorbent surface is progressively covered. At high available concentration, the extent saturates indicating a monolayer full coverage of the adsorbent. According to the theory, the reaction extent X is supposed to follow a saturation formula:

$$X = \frac{K\,[\mathrm{TPP}]_{eq}}{1 + K\,[\mathrm{TPP}]_{eq}} \tag{III.4}$$

Through this simple plot called the Langmuir isotherm, one can extract the equilibrium constant K, and the corresponding reaction Gibbs energy. One may study the evolution of such Langmuir curve as a function of different parameters to understand the reaction mechanism. For instance, varying temperature (see figure III.1 left) allows to single out the enthalpy and the entropy contributions:

$$\Delta rG = \Delta rH - T\Delta rS \tag{III.5}$$

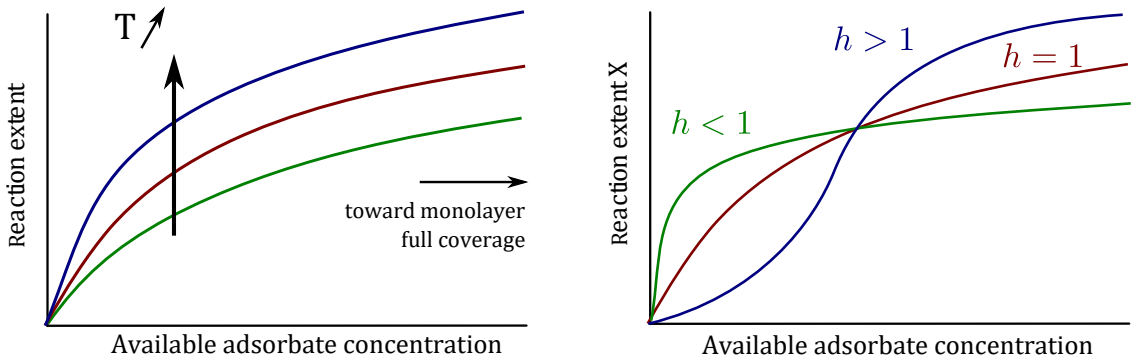

Figure III.1: Left: Example of three Langmuir isotherms for an exothermic reaction; Right: Three Hill isotherms for different Hill cooperativity parameter.

In the previous chapter, the preliminary study of this internal diffusion step showed some cooperative features. Such effects are very common in adsorption processes [225], particularly in biochemistry [226]. They can be taken into account by modifying the TPP partial order in the reaction equation:

$$\mathrm{site} + h\mathrm{TPP} = \mathrm{site/TPP_h} \tag{III.6}$$

where h corresponds to the TPP partial order: it is also called the cooperativity. The Langmuir formalism can be slightly modified to account for such cooperative (or

anti-cooperative) behavior. This is the Hill model [227, 228]. A simple calculation shows that the reaction extent can be now written as:

$$X = \frac{\left(K\left[\mathrm{TPP}\right]_{eq}\right)^{h}}{1+\left(K\left[\mathrm{TPP}\right]_{eq}\right)^{h}} \tag{III.7}$$

Mathematically, a new degree of freedom has been inserted into the model: the Hill coefficient called h. As seen on figure III.1 right, this coefficient influences the shape of the saturation curve. From the microscopic point of view, a h>1 value indicates that the adsorption of one element on a given site of the surface favors the adsorption of other elements on the same area. This is called a cooperative behavior. On the contrary, a h<1 value means that the presence of one adsorbate on the surface will prevent the attachment of others elements: the reaction is anticooperative.

Two different microscopic models may explain such cooperative behavior [229]: the simultaneous and the successive mechanisms. The most trivial one, based on the global equation III.6, corresponds to the simultaneous interaction of one adsorbent site (A) and h adsorbate (B):

$$A + hB \underset{K}{=} AB_h \tag{III.8}$$

Though it is simple, this model suffers from several limitations. Since h is directly related to a number of molecules, the model cannot account for the non-integer values of h that are evidenced in many cases [230, 231]. Secondly, this mechanism is statistically unfavorable, as it requires the gathering of h+1 reactants in the same area. In the theory of kinetic chemistry, only elementary reactions involving one or two reactants are considered probable [232]. In the alternative mechanism, a Hill coefficient greater than one is interpreted as a successive binding reaction:

$$A + B \underset{K_1}{=} AB + B \underset{K_2}{=} AB_2 + B \underset{K_3}{=} AB_3 ..... \underset{K_n}{=} AB_n. \tag{III.9}$$

Here, the K_i constant gets larger as i increases. This is a form of cooperativity, as the adsorption of the first B element onto a A site will favor other adsorptions onto the adjacent sites. In this picture, the Hill coefficient h can differ from the total number of molecules n involved, as its value is an averaged consequence of the successive steps (see equation III.9). Indeed, the experimentalist has usually access to the global X extent and not to the relative contributions of each step.

For the reaction studied in this work, both simultaneous or successive scenarii have to be explored. Indeed, the first kinetic step is an external diffusion of the porphyrins, that will bring a large amount of molecules at the vicinity of the nanotube micelle. Then, the simultaneous scenario cannot be totally rejected, as TPP molecules may

interact together at the moment of their adsorption. As it will be detailed in this chapter, the reality may be a compromise between these two hypotheses.

1.2 Evidences of a cooperative stacking

The following section details the study of the nanotube coverage as a function of the TPP concentration. Here, a monochiral sample has been chosen, to avoid the disturbance of chirality dependence effects. The first study was made on (6,5) sorted nanotubes in a 2 w.t. % cholate suspension (purchased from Nanointegris). Several samples were prepared by mixing two SC suspensions containing the nanotubes or the porphyrins. Based on the thermodynamics theory explained before, one may want to study the evolution of the nanotube coverage as a function of the quantity of injected molecules. Thus, several samples were prepared with different final TPP concentrations, ranging between 0.5 and 15 μmol.L^{-1}. Note that these values are much lower than the one used in the previous chapter. This is due to the fact that the NT concentration in such sorted samples is relatively low (optical density of 0.05 on the S_{11} line of (6,5)).

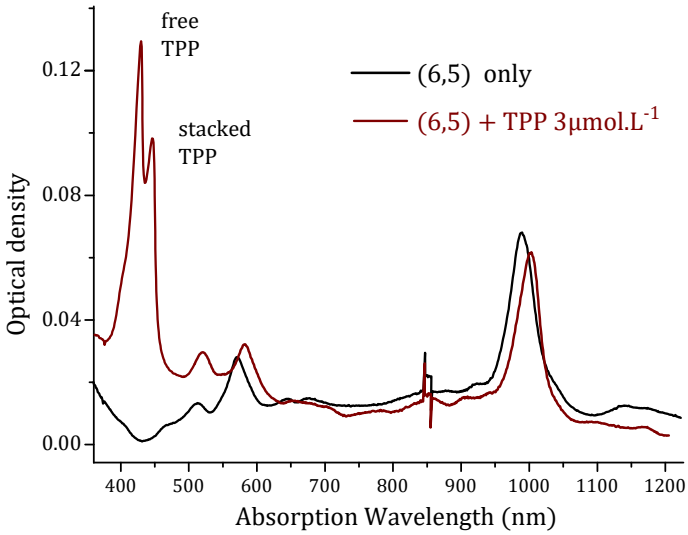

Figure III.2: Absorption spectrum of a (6,5) sorted nanotube suspension, left alone (black) or mixed with TPP (red) to reach a final TPP concentration of 3.5 μmol.L^{-1}.

The figure III.2 displays the absorption spectrum of the sample containing a final TPP concentration of 3.5 μmol.L^{-1} (red line). One can observe the usual spectroscopic evidences of the coupling of the porphyrins with the nanotubes: the shift of the S_{11} line to 1000 nm and the 440 nm Soret component, coming from the π-stacked porphyrins. One can observe the presence of the unshifted Soret band at 420 nm, which proves that the reaction is equilibrated (some non-interacting porphyrins are

still present).

In order to extract the thermodynamics parameters of such adsorption reaction, one may apply the Hill model formalism. Once the equilibrium is reached in each sample, the remaining free TPP concentration and the final reaction extent have to be quantified. As explained before, there are several manners to evaluate each of them. For instance, one may choose to assess the free porphyrin concentration by visible photoluminescence experiments. Indeed, the stacked porphyrin are known to be totally quenched by the nanotube [163]. In addition to the TPP/ NT samples, a series of reference samples were prepared without nanotubes, using exactly the same protocol. Monitoring the TPP luminescence, one may compare the PL value with and without nanotubes. On figure III.3 left is displayed the two PL spectra corresponding to a global TPP concentration of 5.5 μmol.L^{-1}. The presence of the nanotube (black curve) leads to a significant decrease ($\simeq 75\%$) of the PL signal.

On figure III.3 right is displayed the integrated PL value (between 600 and 800 nm) for each global porphyrin concentration, with (red) and without (black) nanotubes. The PL signal of TPP molecules in the absence of nanotubes grows linearly with concentration, indicating that an increasing number of monomers are solubilized. The slope of this curve allows us to extract the coefficient of proportionality γ_0 :

$$I_{PL_{TPP}} = \gamma_0 \times c_{tpp} \tag{III.10}$$

In the presence of nanotubes, the PL signal also rises with c_{tpp} but with a threshold behavior. For $c_{tpp} < 8$ μmol.L^{-1}, the PL signal increases with a very moderate slope, smaller than for the lone TPP samples. This indicates that an important fraction of monomers are quenched by their interaction with the nanotubes. However, for concentrations above 8 μmol.L^{-1}, the slope of the PL signal eventually recovers the value measured for the free TPP sample.

This behavior is typical of a total chemical reaction, where the number of adsorbed TPP eventually saturates once every adsorption site is occupied. From the difference of the two asymptotes (black and red dotted lines) in figure III.3 right), one can evaluate the concentration of porphyrins that are involved in the stacking process: $[TPP]_{stacked} \simeq 8$ μmol.L^{-1}. As the interacting porphyrin are totally quenched, the equilibrium concentration $[TPP]_{eq}$ of remaining free porphyrins can be evaluated through the formula:

$$[TPP]_{eq} \simeq \frac{I_{PL_{TPP-NT}}}{\gamma_0} \tag{III.11}$$

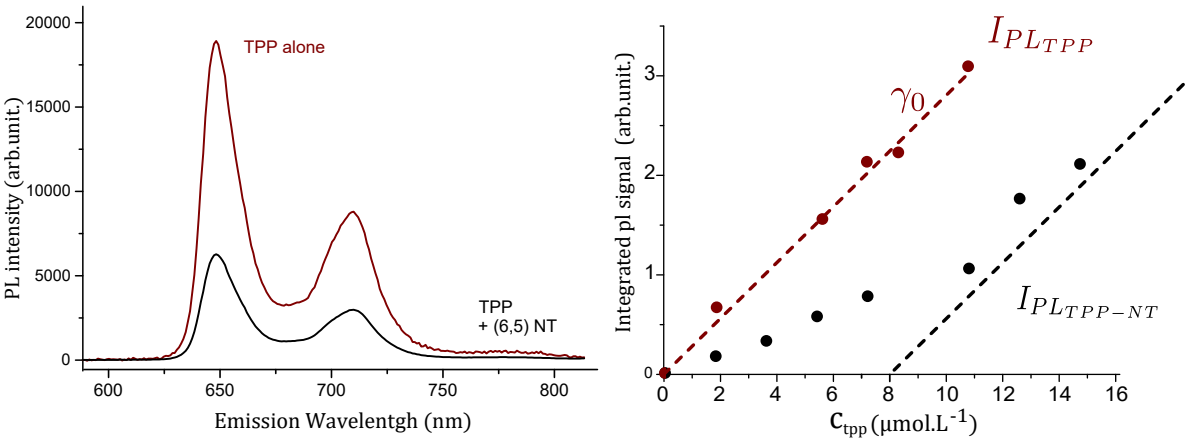

Figure III.3: Left: TPP PL signal under an excitation at 420 nm for a c_{tpp}=5.5 μmol.L^{-1} sample with (black) and without nanotubes (red); Right: Integrated PL signal vs concentration with and without nanotubes, the two dotted line highlight the linear asymptotic behavior at high concentrations.

To evaluate the reaction extent, the energy transfer ratio can be monitored in different samples. On figure III.4 left, the evolution of this energy transfer ratio is displayed as a function of the global porphyrin concentration c_{tpp}. It increases along with the TPP concentration, to reach a final value of 1.3. The curve undergoes a steep transition around a concentration threshold located at $c_{tpp}^{th} = 4 \pm 0.5$ μmol.L^{-1} (see figure III.4 left).

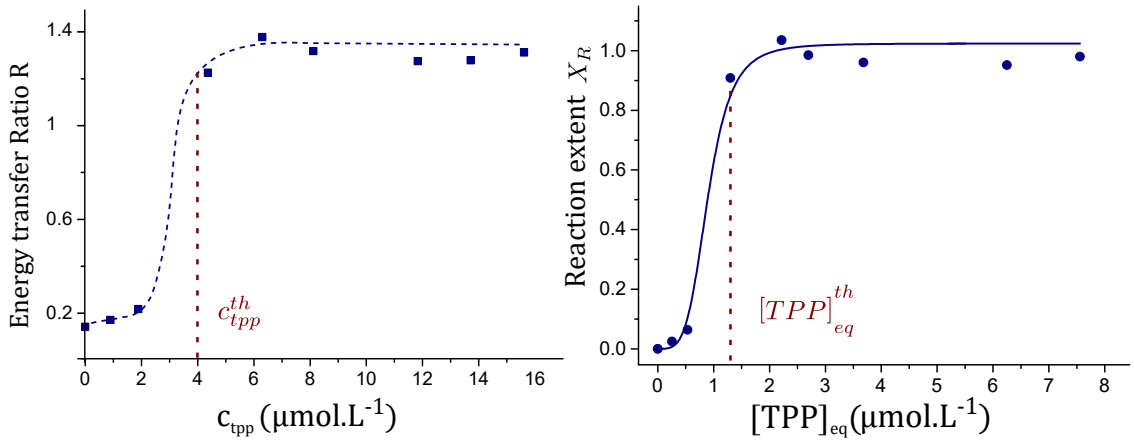

Figure III.4: Left: Evolution of the energy transfer ratio R on the (6,5) nanotubes as a function of the global porphyrin concentration; Right: Corresponding Hill diagram along with the corresponding saturation fitting function.

From the evolution of the energy transfer ratio R, one can extract an evaluation of the normalized reaction extent X_R:

$$X_R(c_{tpp}) = \frac{R(c_{tpp}) - R(c=0)}{R(c_\infty) - R(c=0)} \tag{III.12}$$

This parameter will be null at very small porphyrins concentrations and equal to 1 when the concentration is high enough. Following the previous thermodynamic discussion, one can plot X_R as a function of the equilibrium TPP concentration $[TPP]_{eq}$, calculated earlier. The corresponding Hill diagram is shown in figure III.4 right. As expected, the reaction extent increases along with the equilibrium porphyrins concentration. As in figure III.4 left, a steep evolution is observed. Indeed, a saturation of the reaction extent occurs above a concentration threshold of $[TPP]_{eq}^{th}$=1 μmol.L^{-1}. At this precise point, the total porphyrins concentration was of $c_{tpp} = 4 \pm 0.5$ μmol.L^{-1} (see figure III.4 left). The difference between these two threshold concentrations allows to calculate the quantity of quenched porphyrins:

$$c_{tpp}^{th} - [TPP]_{eq}^{th} \simeq 0.75 \times c_{tpp}^{th} \tag{III.13}$$

At this point of the curve, this result indicates that 75% of the porphyrins are π-stacked on the nanotubes.

To go further in the thermodynamics study, the Hill fitting model has been applied to the evolution of X_R (blue line in figure III.4 right). From this fit, a reaction constant of K=1.0 $\times$ 10^6 is obtained, corresponding to a free Gibbs energy of ΔrG=$-$34 kJ.mol^{-1}. The absolute value of this Gibbs energy will be commented in a next section. The Hill coefficient is found to be of h=4. From the previous discussion, this proves that the π-stacking of the porphyrins around the nanotubes is highly cooperative.

Similar cooperative effects were studied by DFT calculations by Orellana [233, 234]. As shown in figure III.5 left, he first modeled a system made of one (6,5) nanotube and one porphyrin. He calculated the most favorable position of the porphyrin around the nanotube. Consequently, the corresponding binding energy and binding distance were evaluated. Then, the same model was applied for 2,3,4 and 8 porphyrins, to investigate on an associative effect during the binding.

For every configuration, he found a similar TPP/nanotube distance of $\simeq$ 3 Å. For a single TPP, a TPP/NT binding energy of 1.36 eV (131 kJ.mol^{-1}) was evidenced. For two and three molecules, the molecules are stacking in a quite independent fashion, with a similar binding energy (per TPP molecule) of around 1.40 eV. However, there is a threshold when the nanotube is covered with 4 TPP. At this point, the molecules are very close and they start to organize, with their phenyl groups parallel to each

other. In this organized structure, the binding energy has almost doubled: 2.45 eV per molecule (236 kJ.mol^{-1}).

This is a form of cooperative behavior during the TPP π-stacking, that the author explained by the creation of 4-TPP ring structures (see figure III.5 left). They also show that two adjacent rings of porphyrins could attract each other, forming a 8 TPP structure, with a slightly increased binding energy 2.85 eV. This effect could be the starting point of the coverage of the nanotube surface by an organized layer of porphyrin molecules.

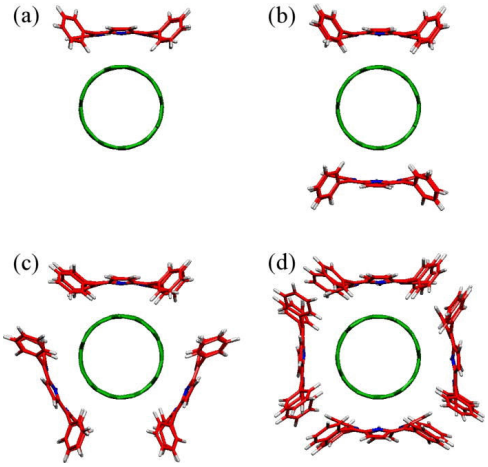

Complex	d (Å)	E_b (eV/TPP)
(6,5)-1TPP	3.16	1.36
(6,5)-2TPP	3.12	1.45
(6,5)-3TPP	3.12	1.40
(6,5)-4TPP	3.12	2.45
(6,5)-8TPP	3.12	2.67

Figure III.5: Left: Front view of tetraphenylporphyrin molecules π-stacked on the (6,5) CNT surface in the equilibrium geometry. (a) (6,5)-1TPP, (b) (6,5)-2TPP, (c) (6,5)-3TPP, and (d) (6,5)-4TPP; Right: TPP adsorption distance (d) and binding energy (E_b) per TPP monomer for the (6,5)-TPP complexes as a function of TPP coverage, from [233].

One can note the nice agreement between this 4-TPP ring structure and the Hill coefficient extracted from our previous thermodynamics results. Beyond this correspondence, these calculations cannot be directly compared to the thermodynamics results. This DFT model evaluates the binding energy of a few porphyrins onto a single nanotube, in a vacuum environment. On the other hand, the thermodynamic experiments study the replacement of the surfactant coverage by a porphyrin layer at the surface of the tubes. If these two processes present similarities, the latter is much more complex, with multiple processes involved (TPP/SC binding, SC/NT binding ...), including a variation of the collective order (entropy). These effects will be discussed in a next section.

1.3 Evaluation of the molecular coverage of the nanotube surface

From the monitoring of the porphyrin and the nanotube equilibrium state, one is able to quantitatively evaluate the number of binding sites. This will help to assess the maximum TPP coverage N on the nanotubes, that will be expressed as a quantity of molecules per unit length of nanotube. First, one may quantify the concentration of the NT suspensions. On the (6,5) highly sorted solution presented above, the NT concentration is evaluated by measuring the optical density on the S_{22} resonance. The (6,5) absorption cross-section on this transition has been measured experimentally [199, 200] to approximately $\sigma_{S_{22}}$= 3.2 $\times 10^{-17}$ cm^2/atom. This value corresponds to an extinction coefficient of $\varepsilon_{S_{22}}$= 2.5 $\times 10^8$ L.mol^{-1}.cm^{-1}.μm^{-1} (expressed per unit length of nanotube). From the optical density value on the figure III.2, one can find a concentration of available micrometers of nanotube of c_{NT}=1.3 $\pm$0.3 $\times$ 10^{-9} μm.mol.L^{-1}.

From the evaluation of the adsorption isotherm in figure III.7, one can observe that the saturation occurs for c_{tpp}=4 μmol.L^{-1}, corresponding to an equilibrium concentration of noninteracting porphyrins of $[TPP]_{eq}$=1 μmol.L^{-1}. At this point of the Hill curve, one can assume that a compact monolayer of TPP surrounds the nanotube. Hence, the concentration of adsorption sites c_{site} on the carbon layer can be expressed as the quantity of stacked porphyrin:

$$c_{site} = [TPP]_{stacked} = c_{tpp} - [TPP]_{eq} = 3\ \mu\text{mol.L}^{-1} \tag{III.14}$$

This value is significantly smaller than the concentration of stacked porphyrins obtained earlier from the TPP photoluminescence signal: $[TPP]_{stacked} \simeq 8\ \mu$mol.L^{-1}. This effect will be discussed in the next section. The coverage N can then be quantified as the quantity of porphyrin per unit of nanotube length:

$$N = \frac{c_{site}}{c_{NT}} = 2300\ \pm 900\ \text{porphyrins}/\mu m \tag{III.15}$$

This experimental value can be compared to a geometrical one derived from a simple calculation. A monolayer of TPP molecules can be regarded as a series of squares of lateral size L=1.25 nm, separated by a given Van der Waals distance D_{WDV}. STM measured from Pham and coworkers [100] of a TPP lattice on graphene found a value of L+D_{WDV}=1.4 nm. This value can be extrapolated to a monolayer of TPP around (6,5) nanotubes. If one assumes that TPP assemble into 4 monomers rings over the tube, this leads to a theoretical molecules density of:

$$N_{theo} = \frac{4}{L + D_{WDV}} \simeq 2860\ \text{porphyrins}/\mu m \tag{III.16}$$

This predicted value is consistent with the experimental coverage calculated above. This proves that a very dense network of porphyrins is achieved around the nanotubes.

1.4 Differences between the nanotube and the porphyrin spectroscopic features

Methods to assess the porphyrins concentration

Finally, this section will determine if all the methods to calculate the reaction extent and the equilibrium porphyrin concentration are equivalent. This discussion can start with the evaluation of $[\mathrm{TPP}]_{eq}$. In the previous discussion, it has been extracted from the TPP PL signal. Another possibility to probe the concentration of free TPP is to measure the optical density of a sample at 420 nm. The value of the equilibrium porphyrin concentration can be expressed as a function of the optical density $O.D._{420}$ as:

$$[TPP]_{eq} = \frac{O.D._{420}}{\varepsilon_{420} \times l} \tag{III.17}$$

where ε_{420} is the molar extinction coefficient of the porphyrin and l is the optical path within the sample cuvette. Figure III.6 displays the equilibrated porphyrin concentration calculated from this new method (red, $[\mathrm{TPP}]_{eq-O.D.}$) as well as the results from the previous method (black, $[\mathrm{TPP}]_{eq-I_{PL}}$). These two methods provide very similar porphyrin concentrations for each sample. As a conclusion these two methods are equivalent to measure the value of the equilibrium porphyrin concentration.

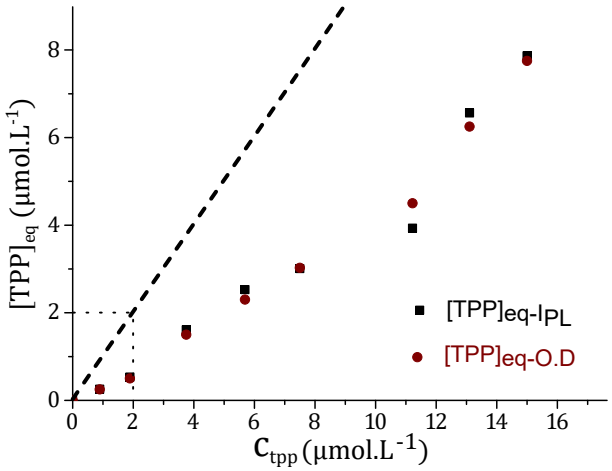

Figure III.6: The two methods to calculate the equilibrium porphyrin concentration for each prepared samples. The dotted black line accounts for the total concentration of porphyrins.

The reaction extent from the nanotube spectroscopy

The reaction extent can also by evaluated using many different spectroscopic features. First, many aspects of the nanotube spectroscopy can be used, such as the

evolution of the energy transfer ratio (used in the previous reactions), or the energy redshift of the nanotube's S_{11} and S_{22} transitions. On figure III.7 left, the evolution of such calculated physical values is plotted as a function of the global porphyrin concentration c_{tpp}. The energy position of the S_{11} and S_{22} transitions are shifted to lower energy values when the porphyrin concentration increases. The energy shift of the S_{22} is always larger than the one for the S_{11}. The final energy shift are respectively of -47 meV for the S_{22} and -20 meV for the S_{11}. This is consistent with the values found in a previous work [168]. Globally, these two features follow the same steep tendency as the energy transfer ratio, with a threshold located around $c_{tpp} = 4 \pm 0.5$ μmol.L^{-1} and similar slopes. This proves that these three features originate from a common microscopic phenomenon.

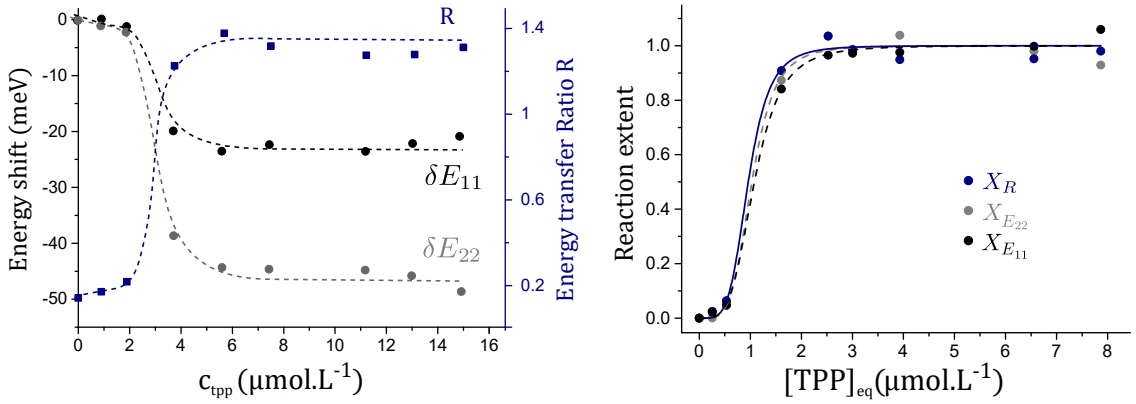

Figure III.7: Left: Evolution of the energy transfer ratio R and of the redshift of the S_{11} and S_{22} transition of the (6,5) nanotubes as a function of the global porphyrin concentration; Right: Corresponding Hill diagrams along with the corresponding saturation fitting functions.

The next logical step is to plot these extents as a function of the equilibrium TPP concentration $[TPP]_{eq}$. Such Hill diagrams are represented in figure III.7 right. One can see that these three evaluations of the reaction extent increase with the equilibrium TPP concentration. The three curves practically follow the same tendency, with a threshold around $[TPP]_{eq}$=1 μmol.L^{-1}. This supports the fact that these spectroscopic effects originate from the same microscopic phenomenon. Table III.1 shows the values of h, K and ΔrG extracted from the fit of the reaction extent from these three methods. The value in each case are very similar. A reaction constant around 10^6 is derived, that corresponds to a free Gibbs energy of -34 kJ.mol^{-1}.

	h	**K**	**ΔrG** (kJ.mol^{-1})
X_R	4.5 ±1	1.0×10^6	- 34.4
$X_{E_{22}}$	4.0 ±1	0.9×10^6	-34.2
$X_{E_{11}}$	4.5 ±1	1.0×10^6	-34.4

Table III.1: Thermodynamics parameters issued from the Hill fitting functions from the transfer ratio and the energy redshift from the (6,5) nanotube's transitions.

The porphyrins and the nanotubes reaction extents

In a second time, it would be interesting to measure the reaction extent from the molecule's point of view and to compare it to the nanotubes spectroscopy results. The simplest way to do this is to extract X from the porphyrin luminescence in figure III.3 right. For each concentration, the value of the PL intensity is already known in absence and in presence of nanotubes (respectively $I_{PL_{TPP}}$ and $I_{PL_{TPP-NT}}$). These two values are proportional to the noninteracting porphyrin concentration in each sample:

$$I_{PL_{TPP}} = \gamma_0 c_{tpp} \quad ; \quad I_{PL_{TPP-NT}} = \gamma_0 [TPP]_{eq} \tag{III.18}$$

The reaction extent $X_{PL_{TPP}}$ can then be assessed as:

$$X_{PL_{TPP}} = \frac{I_{PL_{TPP}} - I_{PL_{TPP-NT}}}{\Delta I_\infty} \tag{III.19}$$

where ΔI_∞ is the gap between the $I_{PL_{TPP}}$ and the $I_{PL_{TPP-NT}}$ at large porphyrins concentration, symbolized by the two dotted asymptotic lines.

On figure III.8, the two extents X_R and $X_{PL_{TPP}}$ are plotted against $[TPP]_{eq-O.D.}$ (from the optical density method). For the energy transfer extent (red curve), the behavior is very similar to the one from figure III.7 right. However, the evolution of the $X_{PL_{TPP}}$ extent is smoother, as it requires a higher porphyrin concentration to saturate. From the fitting function, the obtained values are K=0.52×10^6 for the reaction constant (ΔrG=-32.7 kJ.mol^{-1}) and h= 1.65 for the cooperativity. Hence, this measure provides a higher reaction Gibbs energy value (of around 1-2 kJ.mol^{-1}) and a lower cooperativity than the nanotubes features.

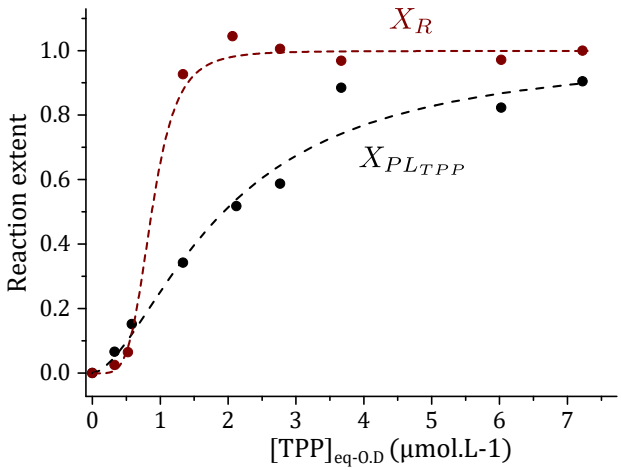

Figure III.8: Evolution of the reaction extent calculated from the porphyrin quenching $X_{PL_{TPP}}$ compared to X_R as a function of the equilibrium porphyrin concentration.

The first comment to these results is that all the methods to evaluate the reaction extent are not equivalent. From the discussion above, one knows that the h parameter is a probe of the microscopic reaction mechanism. As a consequence, measuring two different values of h is a proof of the complexity of the Nt/TPP interaction process. Secondly, there seems to be a large difference between the evolution of the nanotube spectroscopy features and the one from the porphyrins.

At this point, one can formulate the hypothesis that the nanotubes and the porphyrins spectroscopy features are not sensitive to the same physical effects. The nanotube spectroscopy may only be sensitive to effects occurring in the vicinity of the carbon layer. On the other hand, the porphyrin PL signal may depend on additional remote effects, such as the self-quenching between aggregates of molecules.

Evidence of a multilayer stacking process

To go further in the understanding of these processes, one can evaluate the non-normalized forms of the reaction extents: $\xi_{PL_{TPP}}$ and ξ_R. Their values correspond to the concentration of porphyrins involved in each process. The evaluation of these concentrations will bring a finer understanding of the complex stacking mechanism. For $\xi_{PL_{TPP}}$, it can be simply extracted from the formula:

$$\xi_{PL_{TPP}} = c_{tpp} - \frac{I_{PL_{TPP-NT}}}{\gamma_0} \tag{III.20}$$

The ξ_R value is more complicated to extract, as it comes from the nanotube spectroscopy. From the previous evaluation of the coverage, the global sites concentration

has been evaluated to $c_{site} = 3$ μmol.L^{-1}. When all these sites are occupied, the reaction extent is equal to $X_R = 1$. Thus the energy transfer extent can be calculated as $\xi_R = X_R \times c_{site}$.

The evolution of these two non-normalized reaction extents as a function of the equilibrium TPP concentration is displayed in figure III.9 left. The two curves increase with porphyrin concentration, as it was previously shown for the normalized extents. For small TPP concentrations ($[TPP]_{eq} < 2$ μmol.L^{-1}), the two curves take very similar values. However, at higher concentrations, the two extents evolve quite differently. While ξ_R saturates rapidly, the $\xi_{PL_{TPP}}$ extent increases slowly to reach an asymptotic value around 8 μmol.L^{-1}. Thus, the global behavior can be separated in two successive stages. At small TPP concentration, both the nanotubes and the porphyrin spectroscopic features are evolving, as a signature of their interaction. At higher concentrations, the nanotubes features reach an equilibrium, but the porphyrin ones are still showing evidences of the stacking process.

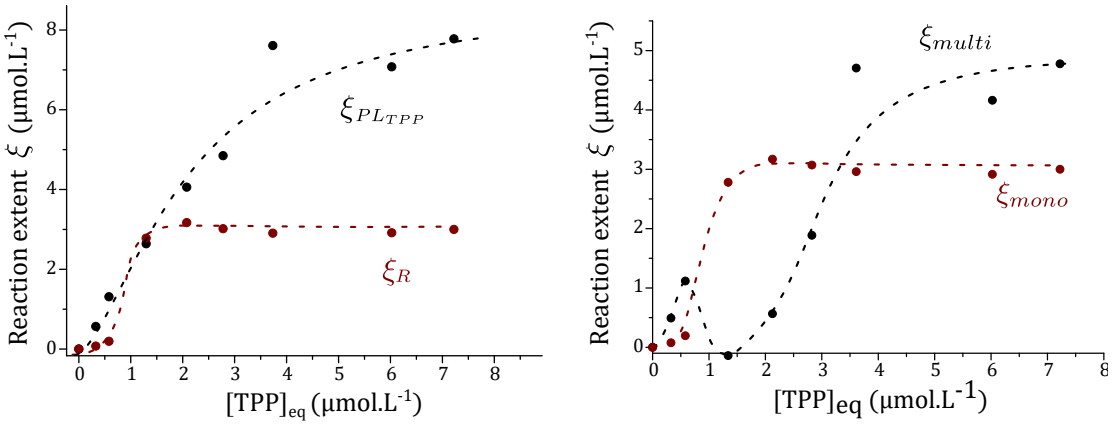

Figure III.9: Left: Evolution of the non normalized reaction extent calculated from the porphyrin quenching and the energy transfer ratio as a function of the equilibrium porphyrin concentration; Right: Evaluation of the monolayer and the multilayer reaction extents calculated from the porphyrin quenching and the energy transfer ratio extents.

The creation of multilayers of porphyrins around the tube could be responsible for such results (see figure III.10). Such hypothesis would explain the differences in reaction extents from the nanotube and the porphyrin points of view. In such perspective, the nanotube spectroscopic characteristics could be more sensitive to what occurs at the carbon surface (see figure III.9 right). They may only depend on the first monolayer of molecules that are actually π-stacked on the nanotube. On the other hand, the extent associated to the porphyrin features may still increase as multilayers of molecules are formed (see figure III.10). Going further with this

hypothesis, one can evaluate the separate extents of the monolayer and the multilayer processes using the values of $\xi_{PL_{TPP}}$ and ξ_R:

$$\xi_{mono} = \xi_R \quad ; \quad \xi_{multi} = \xi_{PL_{TPP}} - \xi_R \tag{III.21}$$

These two extents are plotted as a function of the equilibrium TPP concentration in figure III.9 right. At low porphyrin concentrations, the multilayer extent ξ_{multi} undergoes a small increase, followed by a return to zero at $[TPP]_{eq} \simeq 1.4$ μmol.L^{-1}, when the monolayer extent starts to grow. Even if its amplitude is within the error margin, one may try to interpret this effect. It occurs when the TPP concentration is too small to create the cooperative monolayer (ξ_{mono} is close to zero for these points). It could indicate the presence of a disorganized TPP phase that precedes the organization into 4 TPP structures. For larger $[TPP]_{eq}$ values, ξ_{multi} keeps rising to reach values around 5 μmol.L^{-1}. This process happens in parallel to the saturation of ξ_{mono} to 3 μmol.L^{-1}. Eventually, the multilayer process includes approximately twice as many molecules as the monolayer process. This could correspond to the creation of two additional porphyrin layers on top of the first monolayer. As a conclusion, this process can be seen as the creation of multilayers, once the first monolayer is totally packed.

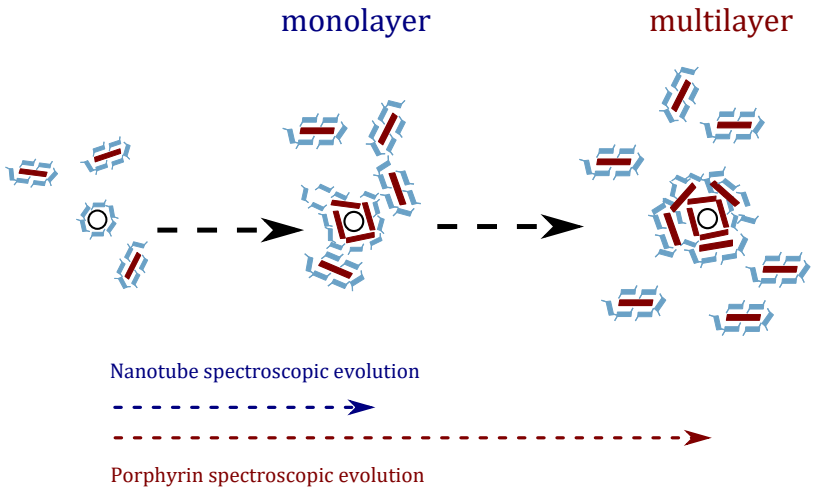

Figure III.10: Schematic view of the origin of the threshold differences between the nanotube and the porphyrin spectroscopy.

Even if one agrees to this multilayer hypothesis, it does not explain why the nanotube transfer resonance saturates at low TPP concentration, while the porphyrin quenching keeps increasing. In theory, these two processes are deeply connected: the energy received by the acceptor should be proportional to the one lost by the donor. As it was mentioned before, this supplementary loss of energy may be linked to the presence of molecular self aggregates in the nanotube remote environment. Such

TPP-TPP aggregation may create competitive relaxation pathways [116] that induce a significant loss of excitons, and will not lead to an energy transfer.

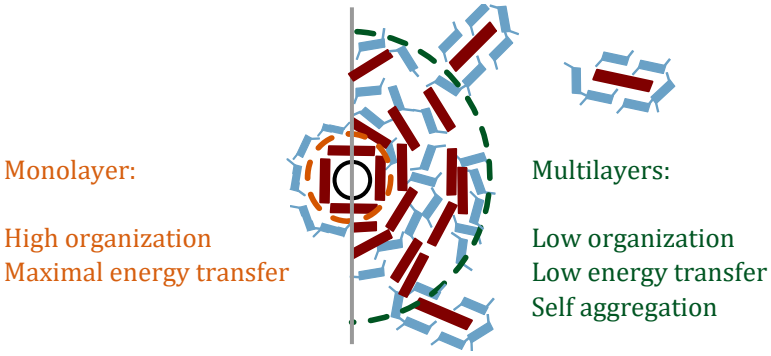

Figure III.11: Schematic view of the degree of organization in the monolayer and the multilayer configurations of TPP around a nanotube.

As displayed in figure III.11, the degree of organization may decrease as the number of layer raises. In the stacking process, the nanotube acts as a pattern for the molecules organization (see chapter 4 for more details on such a process). This effect may be very effective at the surface of the tube, leading to a very organized monolayer of porphyrins. This would explain why the energy transfer is maximal in the first layer of molecules.

Beyond the monolayer, the nanotube may still attract other molecules on a larger scale. However, as the distance between the porphyrins and the nanotube increases, the patterning effect may be less efficient. Thus, the porphyrins involved in the multilayer process might have a looser organization, with different orientations and the presence of TPP-TPP aggregates. Those self-aggregates are always present in a porphyrin suspension, but their proportion may be increased by the presence of the nanotube template. Other examples of template-induced aggregation [235, 236] or surfactant-induced aggregation can be found in litterature [116]. As a conclusion, the self aggregation and the patterning effect may explain why the energy transfer only depends on the first layer of porphyrin molecules.

Finally, the presence of this multilayer process brings some uncertainty on this thermodynamic study. Since the energetic values probed by the two different spectroscopic methods are different, one cannot define an absolute value for the Hill coefficient, or the reaction equilibrium constant. Nevertheless, it has been proven that the nanotube spectroscopic features are only affected by the monolayer process. They only evolve in the first part of the figure III.9 left, when the concentration of TPP is small and the proportion of multilayers is negligible. Thus, one can consider that the use of the nanotubes spectroscopic features gives accurate thermodynamic

results regarding the assembly of the first layer of porphyrins around the nanotube surface.

Study on a CoMoCat unsorted sample

The thermodynamic experiments was then adapted to an unsorted CoMoCat sample. This can help to test the reproducibility of the thermodynamic experiment, by repeating it in the same conditions than for the (6,5) sorted sample. A two phase mixing process has been used in a 2 w.t. % SC environment. The CoMoCat batch is not totally monochiral, and the nanotube concentration is much larger than for the previous sorted sample (with an optical density for the (6,5) S_{11} of 0.15).

The thermodynamic results are plotted in figure III.12. Both the reaction extent X_R from the energy transfer ratio R (black dots) and X_{PL} from the porphyrin quenching (red dots) are displayed. Both of them increase in the same fashion than for the (6,5) sorted sample in figure III.8.

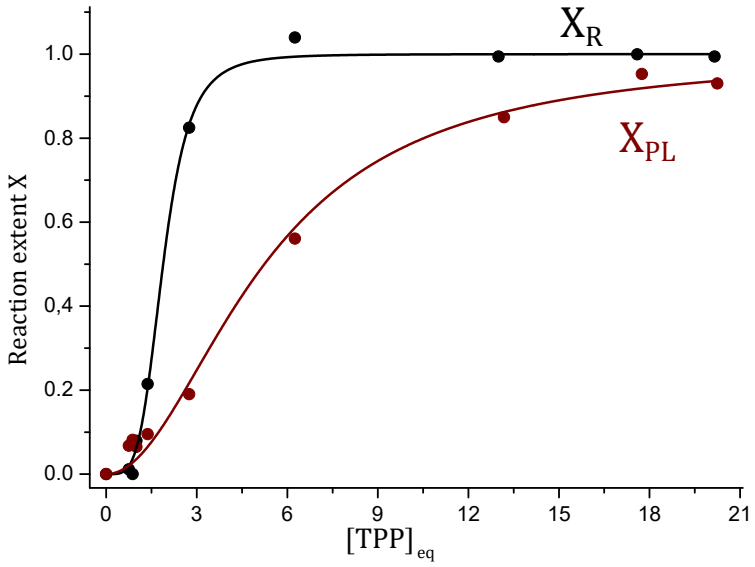

Figure III.12: Evolution of the extents X_R and X_{PL} as a function of $[TPP]_{eq}$ for the unsorted CoMoCat/TPP sample.

The Hill fitting from the nanotube spectroscopy has yielded results quite similar to the (6,5) sorted sample, with a reaction constant of 5.1×10^5 ($\Delta rG = -32.7$ kJ.mol^{-1}). The obtained Hill parameter h=4.5 is very close to the value for the (6,5) sorted sample from the previous section. The value of the equilibrium constant (from X_R) is here smaller than the previously obtained value (that was of K=1.0×10^6). This effect could be due to the higher nanotube concentration in the present sample. The TPP reaction extent (red dots) leads to an equilibrium constant of K=1.9×10^5 and a

cooperativity of h=1.98. Interestingly, this confirms the difference evidenced before between X_R and X_{PL}, with a smoother evolution of X_{PL} with respect to X_R.

1.5 Impact of the surfactant mixing

The previous chapter has highlighted the significant role of the surfactant environment in the reaction dynamics. Particularly, a modification of the micellar composition was proved to influence significantly the rate of the external diffusion. Here, the evolution of the equilibrium state will be monitored as a function of the nature of the surfactant environment with different proportions of SC and SDS.

To study the influence of the surfactant composition, the experiment was repeated with a 2 w.t.% CoMoCat sample and a porphyrin suspension in 2 w.t.% SDS, with a final ratio of r_{sds}=10%. The plot of the X_R extent (red dots in figure III.13 left) and the obtained Hill fitting function are very similar to the full SC sample, with K=5.0 10^5 ($\Delta rG = -32.7$ kJ.mol^{-1}) and h=4.0. Then, the same protocol was used with r_{sds}=50% and in full SDS sample (figure III.13 right). There, the results are quite different from the reference sample. In the mixed sample (red dots), the fitting parameters are K=3.2 10^5 ($\Delta rG = -31.6$ kJ.mol^{-1}) and h=1.8. Finally, the black dots correspond to the reaction scheme in full SDS samples. The reaction parameters are K=1.3 10^5 ($\Delta rG = -29.3$ kJ.mol^{-1}) and h=3.3.

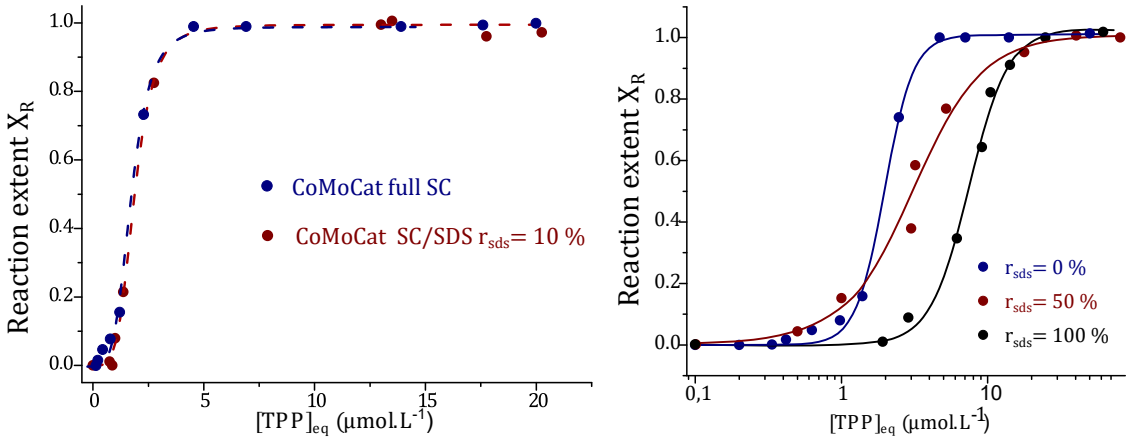

Figure III.13: Left: Hill diagram for a full SC (blue) and a SC/SDS sample with r_{sds}=10% (red); Right: Hill diagram for a full SC (blue), a full SDS (black) and a SC/SDS sample with r_{sds}=50% (red).

The results for the 10% ratio are quasi identical to those for a 100 % SC environment. At such a ratio, the SDS has a very small influence into the equilibrium state. However, for a 50 % ratio, the reaction equilibrium is less advanced than

for r_{sds}=10%, and the cooperativity is lower. The decrease of the equilibrium constant is amplified for the 100 % SDS environment, whereas the cooperativity is quasi recovered.

The present results exhibit an increase of the reaction Gibbs energy with the SDS proportion. From 100 % SC to 100 % SDS, this energy increases of around 3 kJ.mol^{-1}, proving that the reaction is less favored in the latter conditions. As discussed earlier, the surfactant environment plays an active role into the π-stacking process. Indeed, both the surfactant desorption and the porphyrin adsorption have to be performed for the Nt/TPP interaction to be complete. Many different physical effects could explain this increase of the reaction Gibbs energy when the SC is replaced by the SDS.

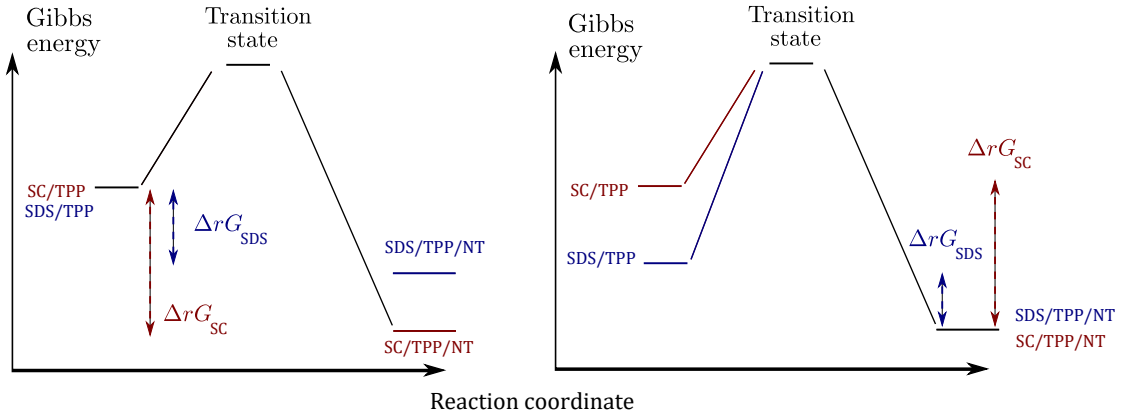

Figure III.14: Two possible explanations of the difference in reaction Gibbs energy in SC and in SDS. Left: A difference of the Gibbs energy in the final state; Right: A difference of the Gibbs energy in the initial state.

In absolute value $|\Delta rG_{SDS}|$ is smaller than $|\Delta rG_{SC}|$. This means that the difference in Gibbs energy between the initial and the final state is smaller in SDS than in SC. Two possible situations are highlighted in the figure III.14. First, this effect could be due to a higher Gibbs energy in the final state. For instance, the SDS/NT/TPP complexes may be less stable than the SC/NT/TPP ones. It may also be due to a larger stability of the initial state. Indeed, it has been shown in the previous chapter that SDS/TPP micellar structures were very stable (for ratios of 100 or 50 %). Thus the additional stability of the SDS/TPP structure with respect to the SC/TPP one may be at the origin of the increase of the reaction Gibbs energy.

Finally, one has to remember that SDS and SC form very different micelles, with totally different organizations. As the surfactant changes in the initial and the final state, the entropy associated to such states is likely to evolve. Thus, the observed difference of reaction Gibbs energy may have an entropic origin. As explained in

the previous chapter, this entropic effect may also come from the water environment surrounding the micelles.

1.6 Simulation of this two steps functionalization mechanism

At this point, an important amount of data has been collected on different parts of the reaction mechanism. The kinetic study revealed the presence of the porphyrin external diffusion step, while the thermodynamic data evidenced the cooperative behavior of the molecules during their π-stacking on the nanotube surface. However, the connection between those two steps remains unclear. To understand this connection, one can perform a kinetic simulation of the functionalization process. Some of the kinetic and the thermodynamic aspects of the reaction will be used to initialize this simulation. Then, this work will focus on reproducing every kinetic and thermodynamic characteristic results that have been evidenced on the samples with $r_{sds} = 10\%$:

- The cooperative behavior of the equilibrium state, with h=4 and K=0.5 10^5
- The global timescale of 60 minutes for reference concentrations
- The global dependence of the velocity with the porphyrins and the nanotubes concentrations
- The exponential dynamic behavior
- The incubation time before the exponential step

The starting point of this simulation is the modeling of the global mechanism as the succession of two separate steps: a micellar diffusion stage and a cooperative organization of the porphyrins around the nanotube (cut in adsorption sites). Both steps will be regarded as equilibrated, leading to a total of four kinetic constants: k_{in}, k_{out} for the TPP diffusion and k_{on} and k_{off} for the stacking. This leads to the following equations:

$$\mathrm{TPP}_{out} \underset{k_{out}}{\overset{k_{in}}{\rightleftharpoons}} \mathrm{TPP}_{in}$$

$$4\ \mathrm{TPP} + \mathrm{site} \underset{k_{off}}{\overset{k_{on}}{\rightleftharpoons}} \mathrm{TPP}_4/\mathrm{site} \tag{III.22}$$

To develop such a simulation, the SimBiology software from Matlab has been used to model the kinetic steps of the reaction. SimBiology uses ordinary differential equations methods (ODEs) and stochastic solvers to simulate the kinetics of chemical

reactions. The user has to provide the reactions parameters: the number of steps, the reactants partial orders, the reactions constants values.... For this purpose, one must fix certain parameters to be as close as possible from the experimental conditions.

First, one may quantify the concentrations of both reactants in the reference sample. During the kinetic studies, the reference sample was composed of c_{tpp}=20 μmol.L^{-1} and a (6,5) S_{11} optical density concentration of 0.15. At such TPP concentration, the thermodynamic study proved that the full nanotube coverage is achieved. This allows to quantify the concentration of adsorption site. From the equilibrium constant K=0.5 10^5, an evaluation of the adsorption sites concentration is deduced: $c_{site} \simeq 2.5$ μmol.L^{-1}. In the present model, each adsorption site can accept 4 molecules. Thus, the total concentration of porphyrins that may be attached to these sites is 4 times larger than c_{site}.

As a second step, a relationship can be found between the different kinetic constants. For instance, the ratio of k_{on} and k_{off} is linked to the value of K:

$$K^4 = \frac{k_{on}}{k_{off}} \quad ; \quad k_{on} = 6.25\ 10^{25} \times k_{off} \tag{III.23}$$

Here, it has been assumed that the first diffusion step does not play a significant role in the final equilibrium. The fourth power comes from the fact that the real reaction constant is $K' = K^4$, while K is the parameter used in the Hill formalism. It is a consequence of the cooperativity. Additionally, the diffusion rate of porphyrins can be assumed to be identical when they diffuse from and toward the nanotube micelle $k_{in} = k_{out}$. As a consequence, only two variable parameters remain: k_{in} and k_{on}. This will simplify the investigation.

Finally, the research can be restricted to the experimental timescale found in the kinetic study. For the reference sample of c_{tpp}=20 μmol.L^{-1}, a reaction rate of $1/\tau = 0.010$ min^{-1} has been evidenced. This value can be used to find the initial parameters of k_{in} and k_{on}. As k_{in} is directly expressed as a rate in min^{-1}, it can be initiated with the value:

$$k_{in-0} \simeq \frac{1}{\tau} = 0.010 \ \ \text{min}^{-1} \tag{III.24}$$

The evaluation of k_{on-0} is more complex, as this coefficient is expressed in min$^{-1}\mu$mol^{-4}.L^4. By transforming k_{on-0} into an effective rate k'_{on-0} (in min^{-1}), an arbitrary initial value of this rate can still be provided:

$$k'_{on-0} = k_{on-0} \times (c_{tpp}^4) \simeq \frac{1}{\tau} = 0.010 \ \ \text{min}^{-1}; \quad k_{on-0} \simeq 1.6\ 10^{-17} \text{min}^{-1}.\mu\text{mol}^{-4}.\text{L}^4 \tag{III.25}$$

Once the reaction constants and the reactants concentrations are fixed, the software provides the time evolution of the involved concentrations (see figure III.15). If

the simulation timescale is properly chosen, it allows to study carefully any part of the reaction: the initial reaction velocity V_0 (see previous chapter), or the equilibrium state of each reactants and products.

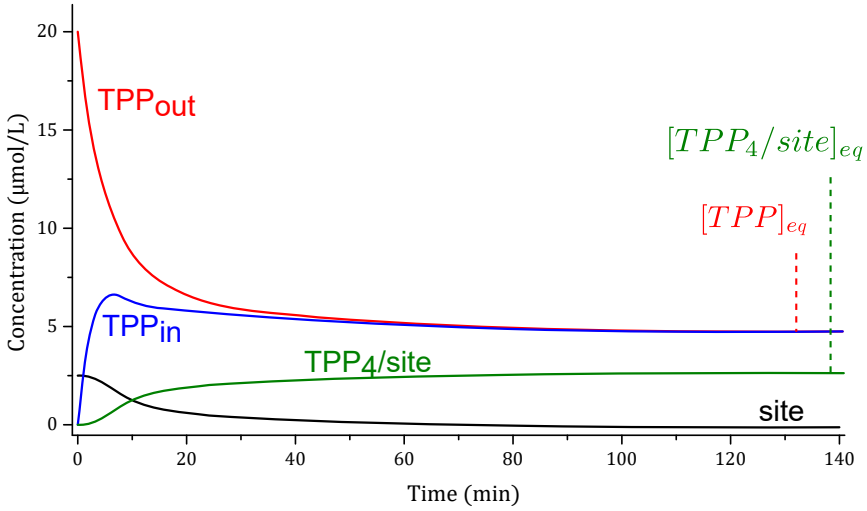

Figure III.15: Simulation of the reaction dynamics provided by the SimBiology sofwtare with $k_{in} = 0.17$ and $k_{on} = 3.12 \times 10^{-18} \mu\text{mol}^4.\text{L}^{-4}.\text{min}^{-1}$.

From this start, several parameters iterations have been performed in order to match with the time evolution of the optical density at r_{sds} =10%. The best match was found for $k_{in} = 0.17$ and $k_{on} = 3.12 \times 10^{-18} \mu\text{mol}^4.\text{L}^{-4}.\text{min}^{-1}$. The simulated line follows the experimental one with a nice agreement (see figure III.16 left). From the initial parameters presented above, one sees that the diffusion rate is one order of magnitude larger, while the stacking rate is one order of magnitude smaller. As a consequence, this simulation shows that the reaction dynamics is not only driven by the TPP diffusion but also by the TPP/nanotube interaction.

This is particularly visible in the initial part of the time evolution, where the model nicely reproduces the incubation stage of the experimental results. The figure III.17 brings more insight into the responsible mechanism. In the first minutes, the rise of $c_{TPP_4/site}$ seems to be limited by the low value of TPP_{in}. As mentioned earlier, the porphyrin partial order of 4 of the stacking reaction makes it very difficult and improbable. In this early stage of the reaction, the number of porphyrin that have penetrated the nanotube micelle is too low for the cooperative stacking to take place. Thus, this simulation brings an explanation to the non-linearity of the first part of the curve.

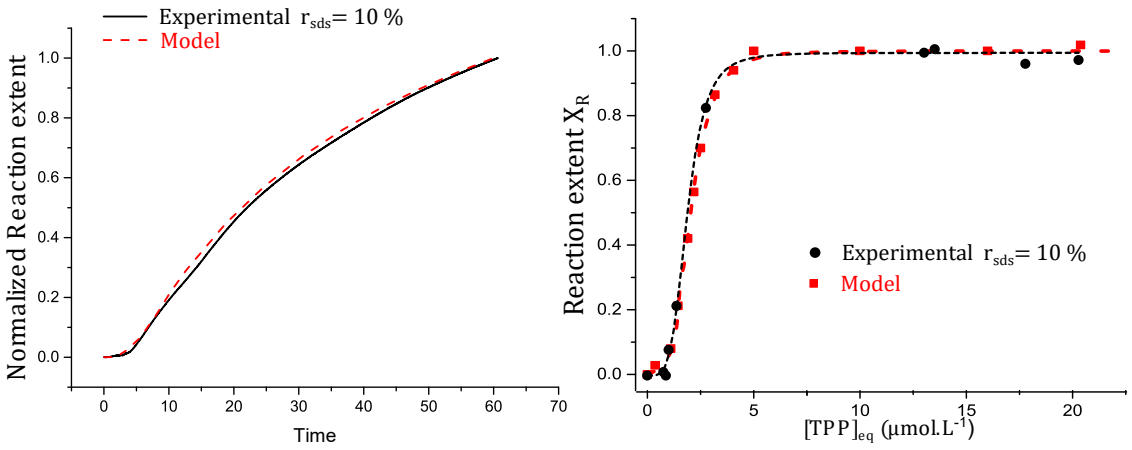

Figure III.16: Left: Time evolution of the optical density at 440 nm for the experimental sample (black) of r_{sds}=10%, c_{tpp}=20 μmol.L^{-1} and (6.5) S_{11} optical density concentration of 0.15, compared to the simulated optical density evolution (red) for similar concentrations for $k_{in} = 0.17$ and $k_{on} = 3.12 \times 10^{-18} \mu\text{mol}^4.\text{L}^{-4}.\text{min}^{-1}$; Right: Experimental Hill diagram for r_{sds}=10% (black) and its modeled equivalent (red).

This comprehension could not have been possible without considering such a two step mechanism. Later on, the speed of the stacking step increases significantly and the reaction begins to be limited by the porphyrin external diffusion. Here, we see that the simulation follows accurately the exponential evolution from the experimental curve after the incubation.

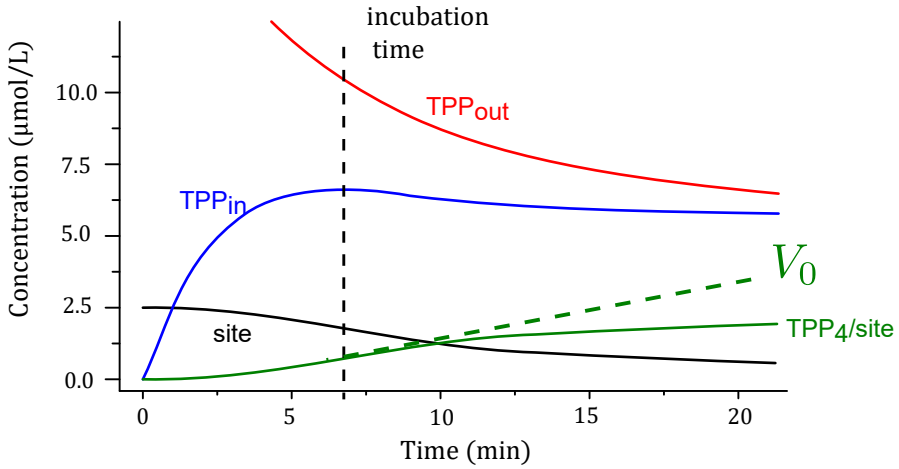

Figure III.17: Zoom on the incubation part of the reaction dynamics provided by the Simbiology sofwtare with $k_{in} = 0.17$ and $k_{on} = 3.12 \times 10^{-18} \mu\text{mol}^4.\text{L}^{-4}.\text{min}^{-1}$

In a second time, the modeled reaction may also be studied as a function of

reactants concentrations. The evolution of the reaction extent as a function of the TPP concentration is displayed in figure III.16 right (red). As the k_{on}/k_{off} ratio has been previously fixed, the purpose of this graph is to check that the simulation results respect the initial parameters. As shown on figure III.15, the value of $[\mathrm{TPP}]_{eq}$ is simply inferred from the final $[\mathrm{TPP}]_{out}$ value, while the reaction extent is calculated from:

$$X_{eq-model} = \frac{[\mathrm{TPP_4/site}]_{eq}}{c_{site}} \tag{III.26}$$

The Hill fitting parameters of the modeled curve are K=0.47 10^6 and h=4.2, which are in very good agreement with the experimental data. Such results are in agreement with the initial parameters of the simulation. Even though a diffusion stage has been introduced in the modeled mechanism, this indicates that it does not modify the final state of the reaction

Finally, the evolution of the initial velocity of the second phase is monitored as a function of the injected porphyrin and adsorption site concentration. The two diagrams are displayed in figure III.18. The simulated value of V_0 has been extracted as shown in figure III.17. Here, the experimental and modeled velocity have been both normalized between 0 and 1 over the chosen range of concentrations. Globally, the simulated curves follows the experimental trends, proving that the total behavior is a mix of the diffusion and the stacking stage dynamics.

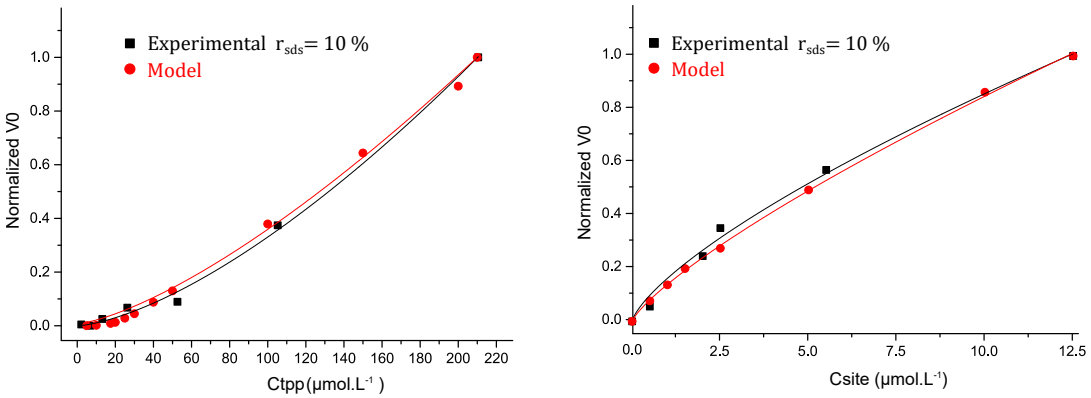

Figure III.18: Left: Experimental evolution of the velocity V_0 as a function of the porphyrin concentration (black) and its modeled equivalent (red); Right: Experimental evolution of the velocity V_0 as a function of the nanotube concentration (black) and its modeled equivalent (red).

As a conclusion, one can observe that a simple simulation is sufficient to provide a simplified view of the reaction mechanism. The experimental time evolution of the

reaction extent, as well as the dependence of the velocity on concentrations have been reproduced. It shows that the TPP diffusion step has no influence on the equilibrium π-stacking final state. On the other hand, it has been shown that the cooperative π-stacking was at the origin of the incubation mechanism that limits the kinetics at the beginning of the reaction. Under simple hypotheses, this simulation helped to quantify the reaction constants, and to understand the interplay between porphyrin diffusion and porphyrin/nanotube interaction. Finally, this simulation was able to describe the connection between the kinetic and the thermodynamic data.

2 Curvature dependence of the equilibrium

2.1 Evolution of the thermodynamics parameter as a function of the Nt diameter

The previous chapter evidenced kinetic variations over different nanotube chiralities. This behavior could be linked to the internal diffusion of the TPP towards the nanotube. Accordingly, one should expect to find similar effects with the thermodynamic experiments. Hence, several mixed HiPCO/TPP samples were prepared in full a 2 w.t.% SC medium, with a volume mixing ratio of 50 %. First, the equilibrium TPP concentration $[TPP]_{eq}$ is assessed by comparing the TPP Q band PL intensity to that of a reference TPP micellar suspension of known concentration (see figure III.19).

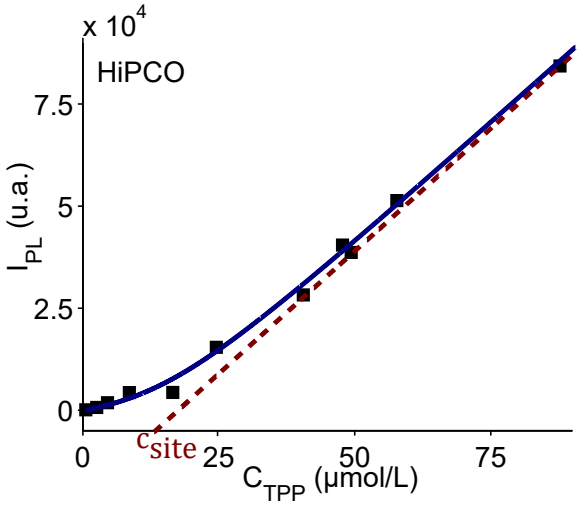

Figure III.19: PL intensity of the free TPP (black dots) integrated over the Q band region, in presence of HiPCo nanotubes (black), along with the proportionality slope (red) originated from the TPP alone, from [108, 189].

From the previous discussion, a method based on the nanotube spectroscopy was required to have a finer evaluation of the Nt/TPP interaction. For this purpose, PLE

maps have been performed (see III.20), to assess the reaction extent. Additionally, this 2D method has been chosen as it allows to single out the reaction extent of 16 chiral species in a single experiment. The reaction extent $X_{n,m}$ for each chiral species is evaluated through the nanotube PL intensities at the shifted and unshifted resonances of the 2D plot, corresponding respectively to the pristine and covered nanotubes (see III.20):

$$X_{n,m} = \frac{I_{shifted-n,m}}{I_{shifted-n,m} + I_{unshifted-n,m}} \tag{III.27}$$

The evolution of the reaction extent as a function of the equilibrium TPP concentration is presented in figure III.21. The displayed chiralities clearly require different amounts of TPP in order to be fully covered. The concentration threshold for (6,5) nanotubes is one order of magnitude larger ($[TPP]_{eq} \simeq 5\ 10^{-1}\ \mu$mol.L^{-1}) than for the (8,7) ($[TPP]_{eq} \simeq 6\ 10^{-2}\ \mu$mol.L^{-1}). The functionalization process is equilibrated for these three chiral species, but the reaction is thermodynamically more favored for (8,7) than for (6,5).

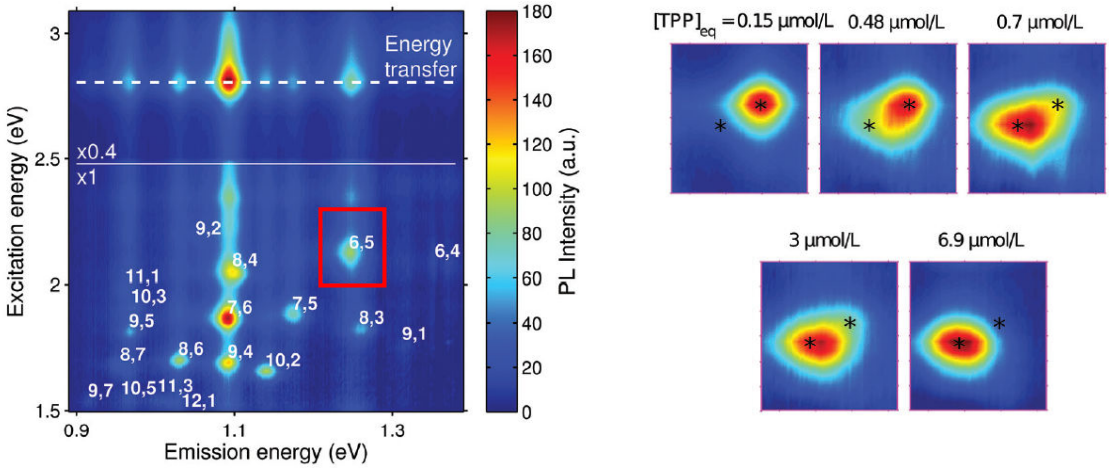

Figure III.20: Left: PLE map of a fully functionalized HiPCO solution; Right: Zoom on the region highlighted by a red rectangle in left for selected TPP concentrations illustrating the evolution of the coverage of the (6,5) species. The black stars point at the shifted (respectively unshifted) position of the lines for a fully functionalized (respectively unfunctionalized) sample, from [108, 189].

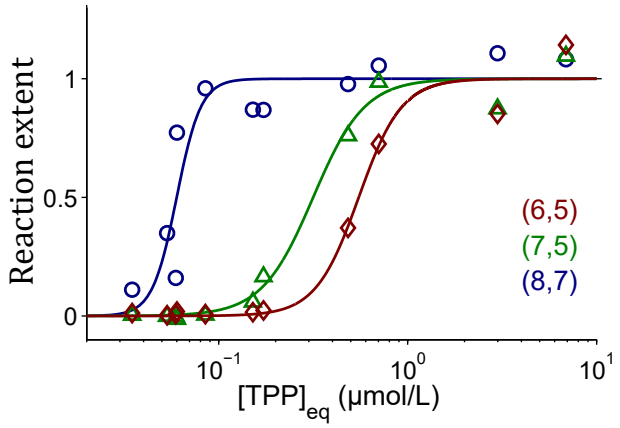

Figure III.21: Functionalization extent as a function the TPP equilibrium concentration (log scale) for selected species (symbols). Solid lines are fits of the Hill equation to these data, from [108, 189].

The Hill fitting of the experimental data gives the reaction constants $K_{n,m}$ and Hill coefficients $h_{n,m}$ for the 16 chiral species. The provided Hill coefficients displayed in figure III.22 left are always larger than one, proving the generality of the cooperative behavior. The corresponding reaction constants $K_{n,m}$ range between 2.10^6 and 2.10^7, in good agreement with reported values on monochiral functionalized compounds.

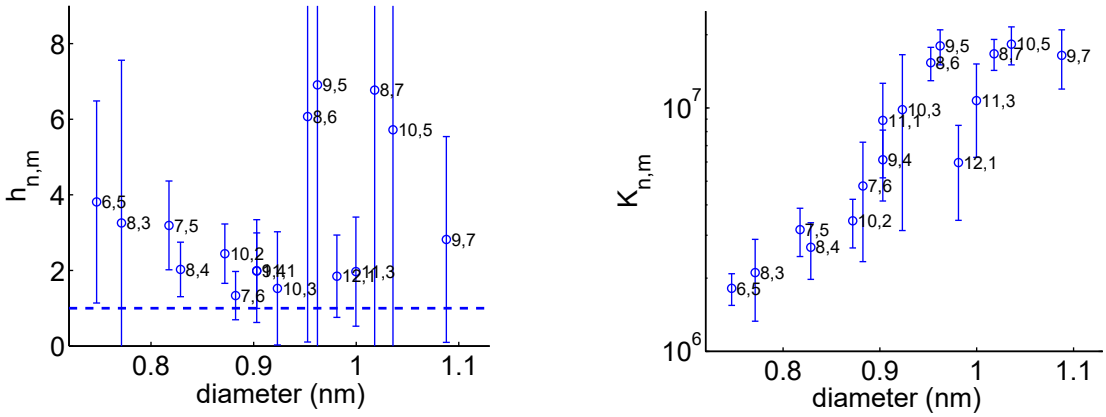

Figure III.22: Left: Hill coefficients for several (n,m) nanotube species as a function of the diameter as extracted from the fitting of the PLE data; Right: Corresponding reaction constant (log scale), from [108, 189].

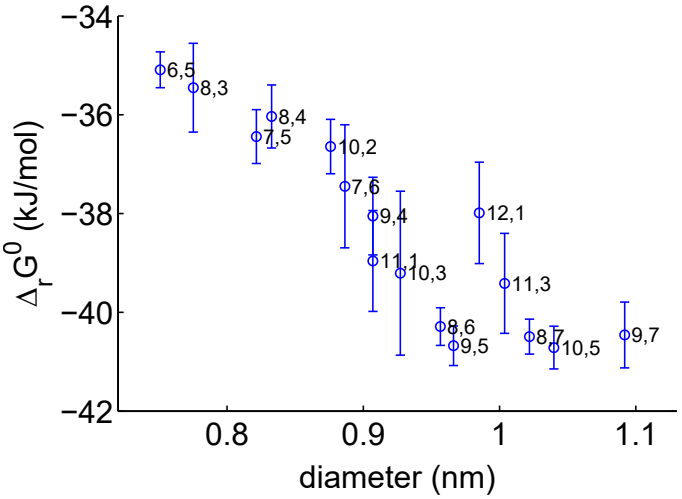

Figure III.23: Reaction Gibbs energy for several (n,m) nanotube species as a function of the diameter as extracted from the fitting of the data, from [108, 189].

To find a tendency, these constants may be plotted against the nanotubes diameter (see figure III.22 right). These reaction constants follow a monotonous increase with diameter. This means that the TPP will preferentially cover the large diameter nanotubes, as the TPP/NT interaction will be more favored. Correspondingly, the associated Gibbs energies for each chiral species present a decrease with increasing diameter (figure III.23). The obtained values range from -36 kJ.mol^{-1} for 0.75 nm diameters down to -41 kJ.mol^{-1} for 1.1 nm diameters.

2.2 Physical effects at the origin of the diameter dependence

At this point, the origin of such diameter evolution of the reaction remains unexplained. As described before, the studied mechanism corresponds to the replacement of the surfactant cover by a layer of porphyrins at the nanotube surface. This process includes many physical effects, that may all contribute to the measured Gibbs energy: TPP/ surfactant separation, desorption of the surfactant from the nanotube surface, adsorption of the TPP onto the tube... As an example, the previous sections showed that replacement of the surfactant from SC to SDS lead to an increase of the ΔrG value of 3 kJ.mol^{-1}.

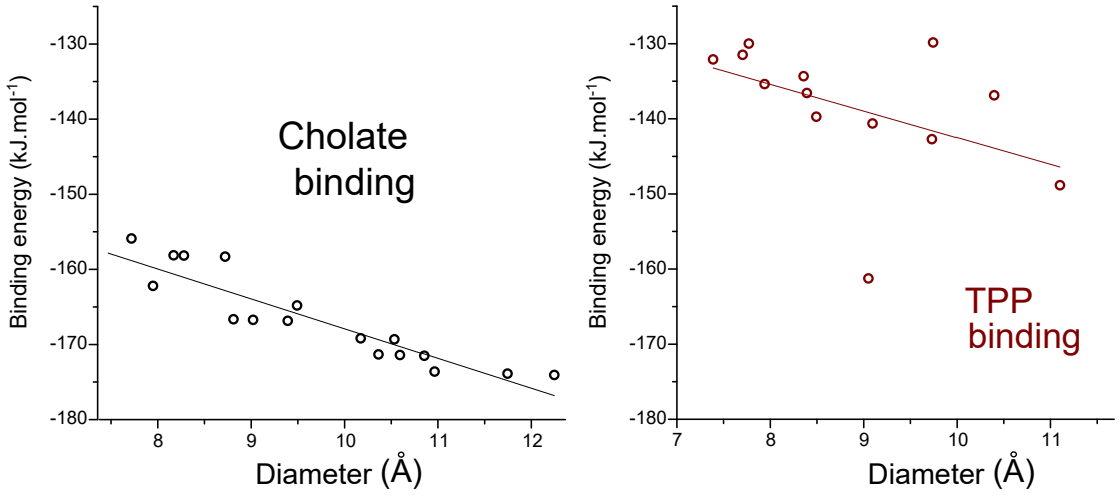

Figure III.24: Left: Calculated values of binding energies for the SC/Nt systems; Right: Calculated values of binding energies for the TPP/Nt system, respectively adapted from [237] and [238].

First, one can easily find estimations of the binding energies for SC/Nt and TPP/Nt systems in the literature. Carvalho and coworkers [237] used a molecular dynamics code to evaluate the binding energies for SC/nanotubes, as a function of diameter (figure III.24 left). They found values around - 170 kJ.mol^{-1}, with a binding energy decreasing with diameter. The slope of such drop is of - 3.95 kJ.mol^{-1}.Å^{-1}. On the figure III.24 right is plotted the results from a DFT work from Orellana *et al.* [238]. They have calculated the binding energy of a TPP onto different species of carbon nanotubes (neglecting the presence of the surfactant layer). They find a binding energy decreasing with diameter, with values around - 140 kJ.mol^{-1}. The slope of this curve is of - 3.5 kJ.mol^{-1}.Å^{-1}.

Therefore, the affinity of both TPP and SC rises with the increase of the host nanotube diameter. If one sets aside the absolute values of such binding energies, the diameter dependence of these estimations is comparable to the one of the experimental Gibbs energy.

As seen on figure III.25, the experimental slope of $\simeq$-2 kJ.mol^{-1}.Å^{-1} lies between the positive line corresponding to the cholate desorption ($\simeq$ +4 kJ.mol^{-1}.Å^{-1}) and the negative slope for the TPP adsorption ($\simeq$ -3.5 kJ.mol^{-1}.Å^{-1}). Between the two master curves, one can observe that the experimental data are much closer to the tendency of the TPP/Nt binding process. Thus, one can suppose that the diameter dependence of the reaction Gibbs energy is essentially related to the adsorption of the porphyrins on the carbon nanotube surface.

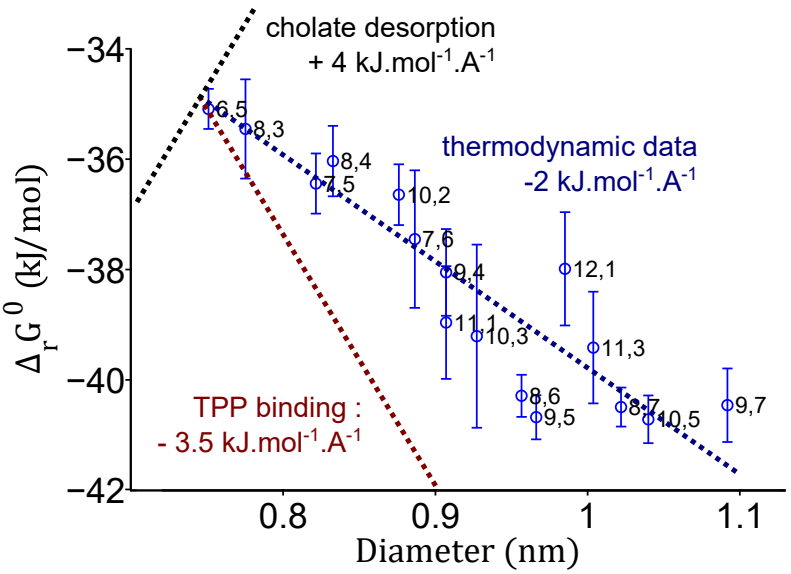

Figure III.25: Comparison of the slopes of the binding energies for the SC/Nt (black) and the TPP/Nt (red) systems with the experimental data (blue), respectively adapted from [233, 237, 238].

2.3 Discussion on the absolute value of the Gibbs energy

In this part, the absolute value of the simulated binding energies will be compared to experimental reaction Gibbs energy results. Even, if the precedent calculations have been made by different research groups, using different computing techniques, one can make here the assumption that they are quantitatively comparable. The two previous model provide very large values for the SC/Nt and the Nt/TPP binding energies. These values are one order of magnitude larger than the experimental value of ΔrG. In addition, the predicted binding energy for cholate is larger than the one for TPP: $E_{b-TPP} - E_{b-SC} \simeq +40$ kJ.mol^{-1}. If one considers only these two effects, the reaction becomes strongly unfavorable. This suggests that additional effects have to be invoked to account for the experimental negative value of the reaction Gibbs energy.

The unexplained negative value of the Gibbs energy may be a consequence of the cooperativity. Unfortunately, the calculations of the TPP/Nt binding energy presented above did not take account of the ability of porphyrin molecules to associate. Obviously, these cooperative effects are more complicated to compute than a simple molecule/Nt coupling. Nevertheless, Orellana has recently calculated this contribution for three chiralities in a recent article, including the (6,5) species [234]. In figure III.26, these cooperative binding energies per TPP are significantly lower, with values around -200 kJ.mol^{-1}. For the (6,5) chirality, this results in a negative

difference of energy $E_{b-TPP} - E_{b-SC} \simeq$ -30 kJ.mol^{-1}. This estimation is relatively close from the experimental value of the reaction Gibbs energy. As a consequence, the ability of porphyrins to cooperate may be the missing contribution to account for the experimental negative reaction Gibbs energy. Once again, a comprehensive simulation, taking account of all of the different physical effects, would be necessary to clarify the role of the porphyrin/porphyrin association in the global thermodynamics.

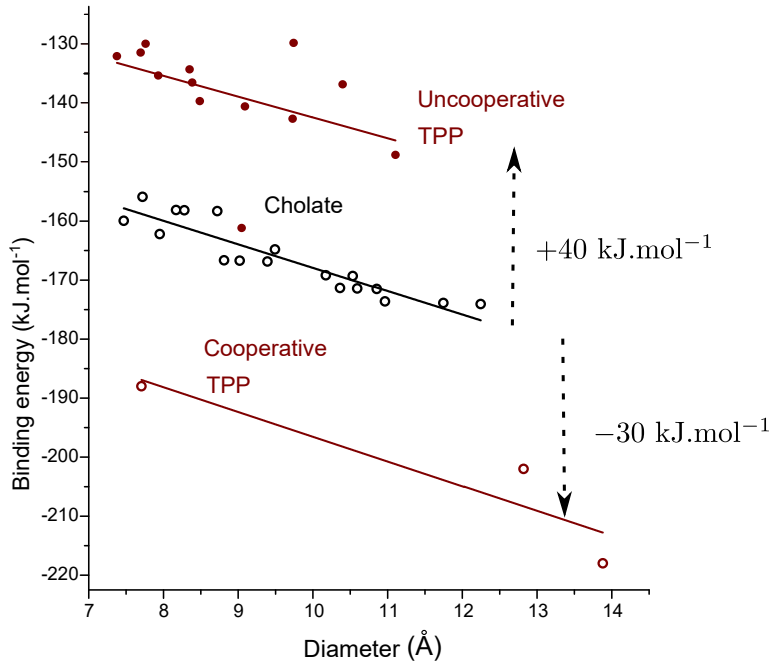

Figure III.26: Calculated values of binding energies for the SC/Nt systems (black) and the TPP/Nt system (red) with and without taking into account the cooperativity, respectively adapted from [237] and [234].

Until now, another important effect has not been taken into account: the entropy. Indeed, the organization of the porphyrin and the cholate molecules will undergo a massive evolution during the functionalization. In other words, the value of the entropy variation ΔrS is likely to be non negligible. However, there are very few data on this complicated topic in the literature.

To single out the enthalpy and the entropy contributions in the present experiments, the evolution of the reaction equilibrium as function of temperature has been studied. In principle, this study allows to evaluate the enthalpy contribution according to the Van't Hoff relation:

$$\frac{\mathrm{d}\ln(K)}{\mathrm{d}T} = -\frac{\Delta rH}{RT^2} \tag{III.28}$$

However, we did not observe any clear evolution of the extent with temperature. This effect can be the signature of athermic reaction ($\Delta rH = 0$), meaning that the functionalization would only be driven by disorder considerations: $\Delta rG \simeq= -T\Delta rS$. The value of the ΔrH is often connected to the binding energies. From this point of view, this result would imply that the sum of every involved binding energies (Sc/Nt, Nt/TPP,...) is null. This seems highly improbable from the energies values discussed above. Another explanation would be that the TPP diffusion step before the π-stacking is somehow irreversible preventing the porphyrin to leave the nanotube micelle. Thus, any attempt to modify the reaction extent by a temperature variation would be prevented. This last hypothesis is in agreement with the probable presence of multilayers of porhyrins around the carbon nanotubes. These multilayers may lead to irreversible porphyrins aggregates. As they are not visible through the nanotube spectroscopy, they prevent the measurement of an equilibrium displacement when the temperature is modified.

2.4 Sorting effects due to TPP/ nanotube density

As the environment of the nanotube changes, so does its density. Indeed, the concentration of surfactant molecules that can bind to the nanotube surface increases with its diameter. This principle has been used to sort different nanotube species [203]. Here, the close environment of functionalized nanotubes is composed of both cholate monomers and TPP molecules. Thus, their volumetric mass density is larger than the one of unfunctionalized nanotubes. As TPP monomers have a larger molar mass (614 g.mol^{-1} against 430 g.mol^{-1} for SC), this effect might be significant.

The work of this section intents to use this effect to sort the small diameters from the large ones. As shown earlier, the TPP π-stacking process exhibits a diameter dependence, leading to the preferential functionalization of the larger diameter NTs. In addition, the cooperative character of the reaction results in steep transitions when increasing the TPP concentration that may help to create a fine separation between nanotubes.

To test such a sorting effect, HiPCO nanotubes were functionalized with a limited TPP concentration to selectively target the larger diameter species. The partially functionalized solution is then centrifuged at 120 000g for 5 hours. Due to their larger density, the functionalized NTs, would in principle be sedimented at the bottom of the tube, leaving a supernatant enriched in the lower diameter species. Two mixed samples were created with TPP concentrations of c_{tpp} =1 μmol.L^{-1} and c_{tpp} =3 μmol.L^{-1}. Before and after ultracentrifugation, we performed a PLE map for each sample (see figure III.27). The color scale corresponds to the normalized PL intensity. On each map, the intensity of the highest signal has been set to 1 (dark red color), while the background level as been set to 0 (dark blue color).

Figures III.27 a. and b. corresponds to the 3 μmol.L^{-1} sample, respectively before and after ultracentrifugation. Between these two samples, one can see that the resonances of the (9,5), (7,6), (8,4) and (7,5) chiralities have experienced a loss of relative amplitude (inside the dotted black rectangle). On the contrary, the other chiralities have a nearly unchanged relative amplitude. The same experiments have been repeated for the 1 μmol.L^{-1} sample. Comparing figures c. and d., only the (9,5) and (7,6) chiralities have partially lost their PL signal amplitude.

Thus the nonfunctionalized species, having the smallest diameters (usually positioned at the right of each PL maps), are less affected by the centrifugation than the functionalized ones. Hence, the hypothesis of a higher density upon TPP addition is validated. Moreover, a closer look can be taken at the intermediary chiral species (between 1.1 and 1.2 eV of emission energies). These one are fully covered with TPP in the 3 μmol.L^{-1} sample, while they are practically unaffected in the 1μmol.L^{-1}.

As a consequence, the possibility to tune the centrifugation threshold by changing the amount of TPP is validated. To properly evaluate this effect, one may quantify the relative suppression of a given species by comparing the integrated PL intensity of this species in the PLE map before and after the sorting process. This is done by measuring the relative PL suppression $\rho_{PL}^{n,m}$:

$$\rho_{PL}^{n,m} = \alpha_{norm} \times \frac{PL_{\text{before}}^{n,m}}{PL_{\text{after}}^{n,m}} \quad ; \quad \alpha_{norm} = \frac{PL_{\text{after}}^{6,5}}{PL_{\text{before}}^{6,5}} \tag{III.29}$$

where $PL_{\text{before}}^{n,m}$ and $PL_{\text{before}}^{n,m}$ are the PL intensity of the the (n,m) species, respectively before and after the centrifugation. The α_{norm} is used to normalized this value to 1 for the (6,5), which is a chirality that is not functionalized in the current process. This coefficient helps to separate the contribution of the porphyrins during the centrifugation, from the usual behavior of Nts in a centrifugal field.

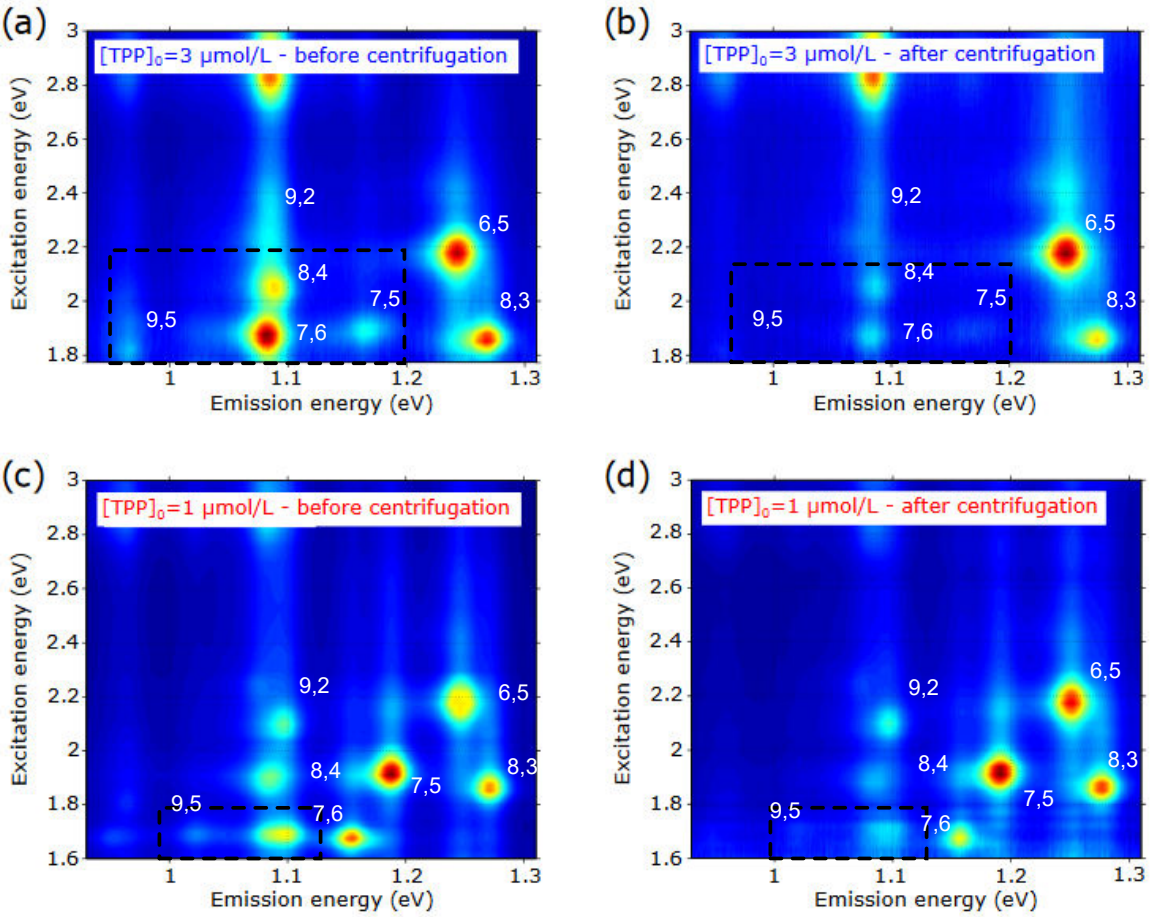

Figure III.27: Normalized PLE maps of partially functionalized HiPCO nanotubes with high (a,b) and low (c,d) TPP monomer concentrations, before (a,c) and after (b,d) the centrifugation process, from [189].

Figure III.28 shows a relative suppression of up to one order of magnitude for the species with a diameter larger than 0.82 ± 0.01 nm for an initial TPP concentration $c_{tpp} = 3\ \mu\text{mol.L}^{-1}$. The cut-off diameter is directly controlled by the initial TPP concentration. By tuning the initial TPP concentration to $[\text{TPP}]_0 = 1\ \mu\text{mol.L}^{-1}$the diameter edge is brought to 0.87 ± 0.01 nm.

As a conclusion, this work demonstrated the possibility to perform a short pass diameter filter for carbon nanotubes. One may note that the lower diameter nanotubes are not functionalized in the end of the process, which can be valuable for applications targeting pristine nanotubes. For the larger diameter fraction, the porphyrin monomers may be easily removed using a regular rinsing process on PTFE filters with organic solvent (DCM, acetone). Thus the pristine properties of carbon

nanotubes can be recovered.

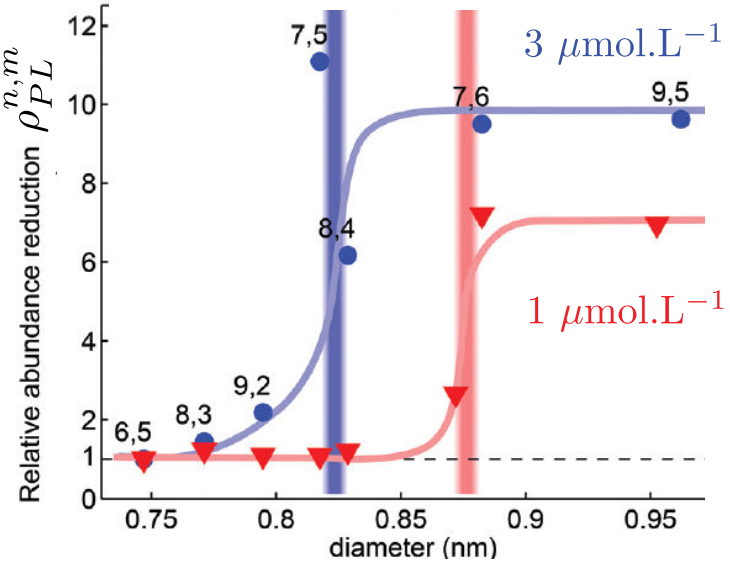

Figure III.28: Relative reduction of the resonant PL intensity of different species, between a stock HiPCO solution and the same solution after partial functionalization followed by a 5 hour centrifugation (120 kG). Two different monomers concentrations (1 μmol.L^{-1}, red or 3 μmol.L^{-1}, blue) give different diameter selectivity. The vertical lines highlight the cut-off diameter for each TPP concentration, from [189].

2.5 Equilibrium on graphene nanosheets

PL quenching and energy transfer

As it has been done for the kinetic studies, the purpose of this section is to compare the thermodynamics results on nanotubes with the one on graphene nanosheets. To do this, several samples were made by mixing graphene nanosheets with TPP suspensions of different concentrations. A full SC environment has been chosen and a 50/50 mixing ratio has been used. As for nanotubes samples, we performed PL experiments to evaluate the influence of graphene on the luminescence efficiency of the chromophores. The Q bands emission signal was monitored between 2.06 eV and 1.65 eV, for samples with and without graphene nanosheets. Figure III.29 represents the integrated photoluminescence signal of TPP samples, for a monochromatic light excitation at 2.95 eV, as a function of initial concentration c_{tpp}. In the presence of graphene sheets, the TPP PL intensity decreases significantly. This quenching of the molecule fluorescence is the signature of an energy transfer from the TPP to the graphene sheets. The proportion of quenching in a given sample can be written as:

$$\eta = 1 - \frac{I_{TPP/gr}}{I_{TPP_0}} \tag{III.30}$$

with $I_{TPP/gr}$ and I_{TPP_0} the emission intensity of the TPP in presence and in absence of graphene respectively. However, this proportion is just a lower limit of the energy transfer efficiency. Indeed, the presence of free porphyrins in solution limits the precision of such an estimation. On figure III.29, a quenching proportion of $\eta = 75\%$ is reached for an initial chromophore concentration c_{tpp} of 8 μmol.L^{-1}. From this global value of quenching, it is possible to deduce a finer evaluation of the actual energy transfer efficiency.

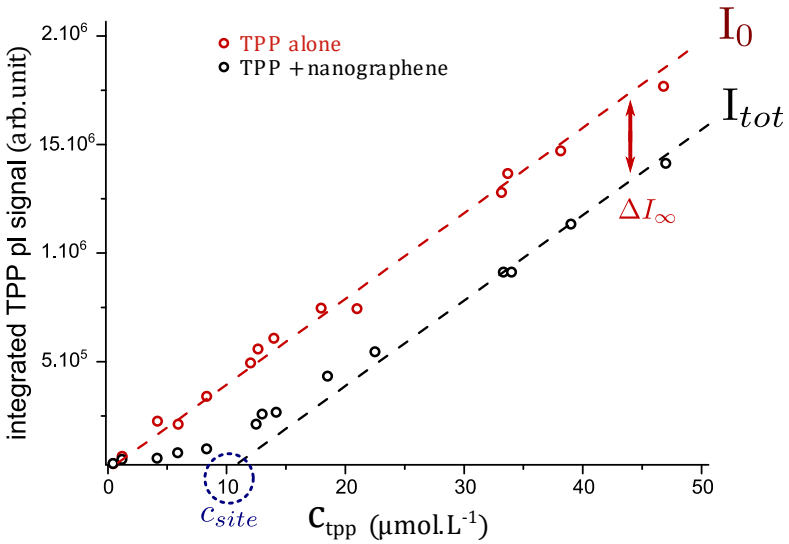

Figure III.29: PL signal from the porphyrin as a function of porphyrin concentration in absence (red) and in presence (black) of graphene nanosheets.

As it was shown in the previous chapter through an absorption spectrum, the final suspension of graphene/TPP contains both free and π-stacked porphyrins. Therefore, the black signal PL signal on figure III.29 (called I_{tot}) is the sum of two contributions: from the free porphyrin ($I_{TPP_{eq}}$) and the porphyrin stacked on graphene ($I_{TPP/gr}$):

$$I_{tot} = I_{TPP_{eq}} + I_{TPP/gr} \tag{III.31}$$

In order to quantify the transfer efficiency, the non interacting porphyrin contribution has to be removed to finally access the $I_{TPP/gr}$ value. From the absorption spectrum of the 8 μmol.L^{-1} reported in the previous chapter, the final proportion of free TPP can be estimated to be 30$\pm$5% of the total porphyrin concentration. Hence, one can deduce the free and interacting PL contributions within the TPP/graphene sample:

$$I_{TPP_{eq}} \simeq 0.3 \times I_{TPP_0} \quad ; \quad I_{TPP/gr} = I_{tot} - 0.3 \times I_{TPP_0} \tag{III.32}$$

From these formulae, $I_{TPP/gr}$ is estimated to be close to 1% of I_{TPP_0} in this 8 μmol.L^{-1} sample. Hence, we can estimate that the transfer efficiency from the stacked porphyrins to the graphene sheets is of $\eta_{transfer} = 99 \pm 5\%$. This near unity efficiency is comparable to the value presented earlier for nanotube/TPP samples for which a transfer efficiency of $1 - 10^{-5}$ was extracted [163]. A comparable value of $99 \pm 5\%$ was found for Xu *et al.* for ionic porphyrin on graphene oxide sheets [239]. One may also compare this result with the DFT calculation from Malic *et al.*, who predicted a transfer efficiency above 99 %, using a Förster energy transfer model for a 0.3 nm Nt/TPP distance [171].

Thermodynamical study on graphene

To monitor the equilibrium state of the reaction, the only option is to work with the TPP spectroscopic data, as no direct evidence of the energy transfer can be extracted from the graphene sheets with our optical techniques. Hence, both the optical density and PL quenching data from the porphyrin are used to monitor the evolution of the stacking process. As shown on figure III.29 (red), the PL signal of TPP molecules in the absence of graphene grows linearly with concentration, indicating that an increasing number of monomers are solubilized. In the presence of graphene, the PL signal follows a threshold behavior identical to the one presented for (6,5) nanotubes. For c_{tpp} <10 μmol.L^{-1}, the PL signal raises slowly, as an important fraction of monomers are quenched by their interaction with graphene. For concentrations above 10 μmol.L^{-1}, the slope of the PL signal progresses as the number of π-stacked TPP eventually saturates. As for carbon nanotubes samples, one may calculate the reaction extent as:

$$X = \frac{c_{tpp} - [TPP]_{eq}}{c_{site}} = \frac{[TPP/gr]}{c_{site}} \tag{III.33}$$

with c_{site} being the initial concentration of adsorption site. Given the ultraefficient quenching from graphene, the PL intensities are directly proportional to the concentrations of free porphyrin in each samples. Hence, the reaction extent X_{PL} can be expressed from the TPP point of view using the quantified quenching:

$$X_{PL} = \frac{I_{TPP_0} - I_{TPP_{eq}}}{\Delta I_\infty} \tag{III.34}$$

with ΔI_∞ being the difference of PL intensity between the two linear curves in figure III.29 at high concentrations. Figure III.30 displays the reaction extent X as a function of the free TPP concentration $[TPP]_{eq}$, extracted from the optical density measurement at 2.95 eV through the Beer-Lambert's Law. This plot yields a Hill

adsorption isotherm, with fitting parameters of $K = 1.3 \pm 1\ 10^6$ and $h = 1.3 \pm 0.3$. A free Gibbs energy of $\Delta rG \simeq -35$ kJ.mol^{-1} is extracted.

In the following, the values of this thermodynamic data will be discussed in regard of the values on carbon nanotubes. Indeed, it would be interesting to extend the diameter dependence of the Gibbs energy and see its consequences on the flat structure of graphene. However, a few precautions have to be taken, since the experimental methods are different. In particular, it was proven that the evaluation of the reaction extent through the TPP PL was not able to provide a precise information on the creation of the first monolayer of porphyrin (as seen in the previous chapter).

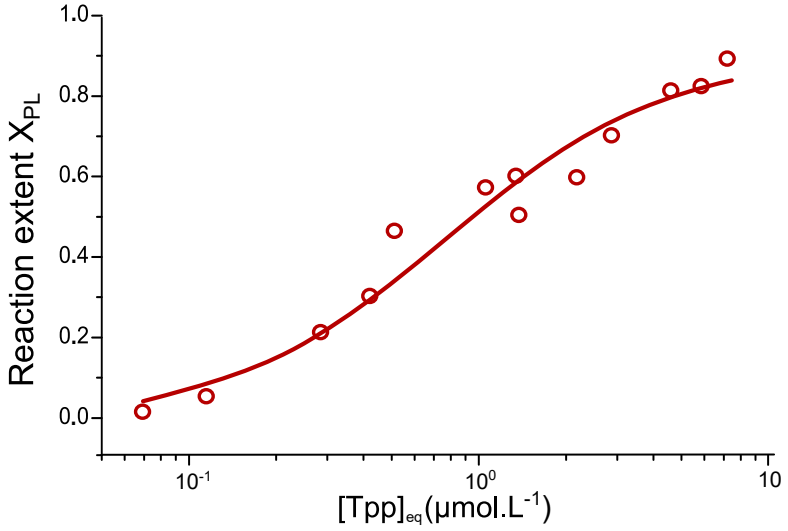

Figure III.30: Evolution of the reaction extent calculated from the TPP quenching as a function of TPP equilibrium concentration as well as the corresponding Hill fit.

Comparison between graphene and nanotubes thermodynamics

At this point, it could be valuable to compare the obtained thermodynamic values on graphene with the ones on carbon nanotubes. As graphene can be seen as the infinite diameter limit, it would be interesting to see if the graphene/TPP samples follow the diameter trend that has been evidenced in the Nt/TPP study. However, the evaluation of the reaction extent in NT/TPP samples was done using the nanotubes spectroscopy features. Therefore, the results of these two studies cannot be directly compared.

First, one must evaluate the probable influence of the multilayers of TPP in the graphene samples. To do this, the graphene/TPP thermodynamics values can be compared with the one extracted for TPP on sorted (6,5) nanotubes. Calculated with the TPP photoluminescence data, the Hill fitting values were of K=1.3 10^6

(ΔrG=-32.7 kJ.mol^{-1}) and h= 1.65 for this nanotubes sample. These values are very similar to the results on graphene/TPP samples, both for the Gibbs energy and for the cooperativity. In the nanotube case, the extent X_{PL} measured through the porphyrin spectroscopy was assumed to be sensitive to the creation of unregular porphyrin multilayers.

For the (6,5) nanotubes samples, the comparison of the X_{PL} extent with the one from the nanotube spectroscopy X_R led to a higher Gibbs energy of around 2 kJ.mol^{-1}. In the same comparison, the cooperativity was shown to be divided by a factor of 2.4. Thus, a measurement of the extent from the graphene point of view might have provided a larger estimation of the cooperativity, as well as a different Gibbs energy estimation. Nevertheless, one can still assume that the proportion of the multilayer process is similar on graphene and on nanotubes. There is no physical evidence to endorse such an assumption. Yet, it provides a simple estimation of the thermodynamic parameters corresponding to the creation of a porphyrin monolayer on the graphene surface:

$$\Delta rG_{mono} \simeq \Delta rG_{multi} - 2\text{kJ.mol}^{-1} \simeq -37 \text{ kJ.mol}^{-1} \quad ; \quad h_{mono} \simeq h_{multi} \times 2.4 \simeq 3.1 \tag{III.35}$$

Those values are very close from the one found on (6,5) nanotubes using the nanotube spectroscopy. In the previous section, it has been shown that the evolution of the reaction Gibbs energy with diameter has a similar slope to the one of the Nt/TPP binding energy calculated by Orellana *et al.* [238]. In other words, the relative evolution of these two physical parameters follows the same trend. It would be interesting to see if the case of graphene is consistent with this behavior, since graphene represents the infinite diameter limit. In this paper, Orellana has calculated a binding energy of $E_{b-gr} = 320$ kJ.mol^{-1} for the porphyrin on graphene, and a binding energy of $E_{b-(6,5)} = 130$ kJ.mol^{-1} for the porphyrin on (6,5) nanotubes. This corresponds to a variation in Gibbs energy of:

$$\frac{E_{b-gr} - E_{b-(6,5)}}{E_{b-(6,5)}} = 146\% \tag{III.36}$$

For the measured Gibbs energy, the same ratio yields:

$$\frac{\Delta rG_{mono-gr} - \Delta rG_{mono-(6,5)}}{\Delta rG_{mono-(6,5)}} = \frac{35 - 37}{37} = 5\% \tag{III.37}$$

which is significantly smaller than the predicted results. If the graphene case had followed the same trend as the calculated binding energy, the measured Gibbs energy would have been of the order of -140kJ.mol^{-1} and the reaction could have been considered total. As a consequence, one can observe that the diameter evolution of the reaction Gibbs energy cannot be adapted to graphene. Following the

precedent discussion, it is unclear how every physical effect involved in the SC/TPP replacement (SC desorption, TPP adsorption, cooperativity, entropy) changes when the carbon surface becomes flat.

Finally, one can wonder about the precision of the measure here with respect to the presence of porphyrin multilayers. For (6,5) nanotubes, it has been shown that that the multilayer process included approximately twice as many molecules as the monolayer process. For graphene, there is no way to evaluate the proportion of such multilayers. Due to the 2D, flat structure of graphene, the creation of these multilayers may be totally different from the nanotube case.

3 Tuning the porphyrin structure to modify the stacking ability

3.1 Adding substituent on the phenyl groups

In this chapter, the cooperative interaction between porphyrin molecules during the π-stacking step has been highlighted. In particular, DFT calculations from Orelanna and coworkers [233], show that cooperative effects could dramatically change the value of the Nt/TPP binding energies. As displayed in figure III.5 left (p. 97), they attributed this cooperative behavior to a stabilizing interaction between the phenyl groups of adjacent porphyrins. Indeed, these phenyl groups have π electrons that can lead to π-π interactions between close molecules. In this context, it has been decided to perform the functionalization process with modified porphyrins: 5,10,15,20-Tetra-p-tolyl-porphyrin (TpTP) and with the 5,10,15,20-(tetra-4-tert-butylphenyl)-porphyrin (TtbPP), having the following structure:

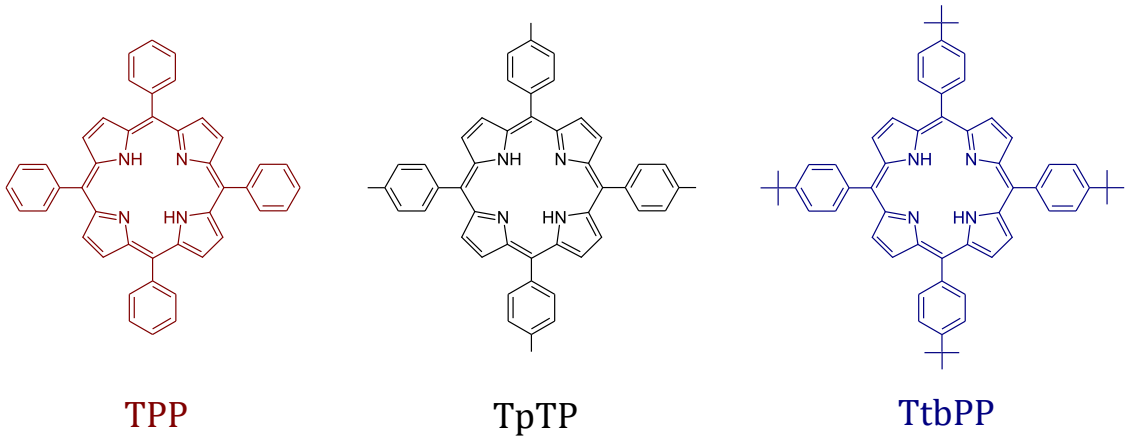

Figure III.31: Chemical representation of the three porphyrins compared in this section: 5,10,15,20-Tetraphenylporphyrin (red), 5,10,15,20-Tetra-p-tolyl-porphyrin (black) and 5,10,15,20-(tetra-4-tert-butylphenyl)-porphyrin (blue).

These two porphyrins have been chosen to present small substituents on the phenyl groups. The idea was to try to limit the phenyl-phenyl interaction and see if it has an impact of the functionalization ability. The experiment started by performing the single step micelle swelling method with these two molecules on a 2 w.t.% SC sample. Each sample contains a similar porphyrin concentration of 30 μmol.L^{-1}.

Figure III.32 presents the absorption measurements on the final samples. The final position of the nanotubes S_{11} transition reaches 1000 nm in presence of the TpTP (as for the TPP sample), while it is nearly unchanged for the TtbPP sample (994nm). As this shift is interpreted as a change in the surrounding environment of Nts, it would mean that the TpTP has successfully entered the SC/NT micelle, while the TtbPP has not. Hence, differences between the stacking behavior of the three molecules are starting to emerge.

This effect is confirmed by a close look on the optical density on the Soret band. First, the TtbPP exhibits a single band at 420 nm, which is totally unchanged in comparison with a sample without nanotube. This would confirm the absence of TbtTP/NT interaction. For the TpTP, the amplitude of the 420 nm line has decreased (as in regular TPP samples), but the red shifted line is very broad, with a maximum at 432 nm. Thus, the nice and regular band at 440 nm relative to the TPP is not observed here. Such a broad band at 430 nm is usually attributed to a large amount of disordered porphyrin aggregates [116].

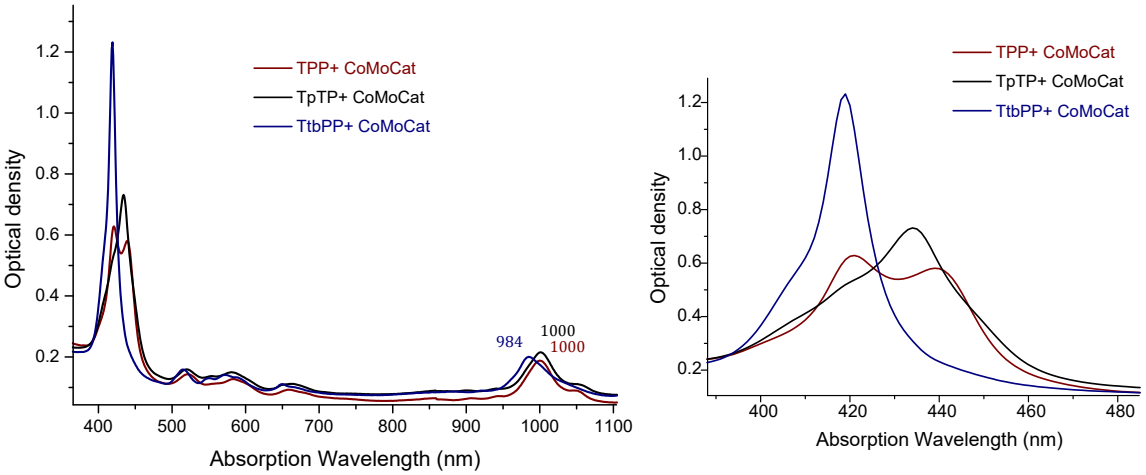

Figure III.32: Left: Optical absorption spectra samples of single step micelle swelling samples, in a 2 w.t. % SC environment, containing CoMoCat with TPP (red), TpTP (black) and TbtPP(blue); Right: Zoom on the Soret bands.

Then, PLE maps of these two samples were performed (see figure III.33). For the TpTP, one observes the red shifted regular resonance of the nanotube (λ_{ex}=580 nm

and λ_{ex}=1000 nm). Additionally, an energy transfer resonance at a larger excitation wavelength than for TPP is present (λ_{ex}=445 nm instead of 440nm). The observed small redshift may not be due to the nanotube but to the natural position of the regular Soret band for TpTP (422 nm) with respect of TPP (420 nm). If one now looks back at the corresponding absorption spectrum (black curve on figure III.32), a small shoulder is visible at 445/450 nm. This shoulder would correspond to the porphyrins that are transferring energy to the nanotube. For the TbtPP/Nt PLE map, the unshifted regular (6,5) resonance is present (λ_{ex}=570 nm / λ_{ex}=980 nm) while no evidence of the porphyrin/nanotube interaction is visible.

Therefore, the presence of small blocking substituents seems to have a dramatic effect on the porphyrin ability to couple with nanotubes. The larger terbutyl groups totally supress the interacting capacity, while the methyl (tolyl) have an intermediary behavior. They still allow a porphyrin coverage around the nanotube, leading to a high energy transfer. Yet, the absence of a proper resonance at 440 nm tends to indicate that molecules have a more disordered organization.

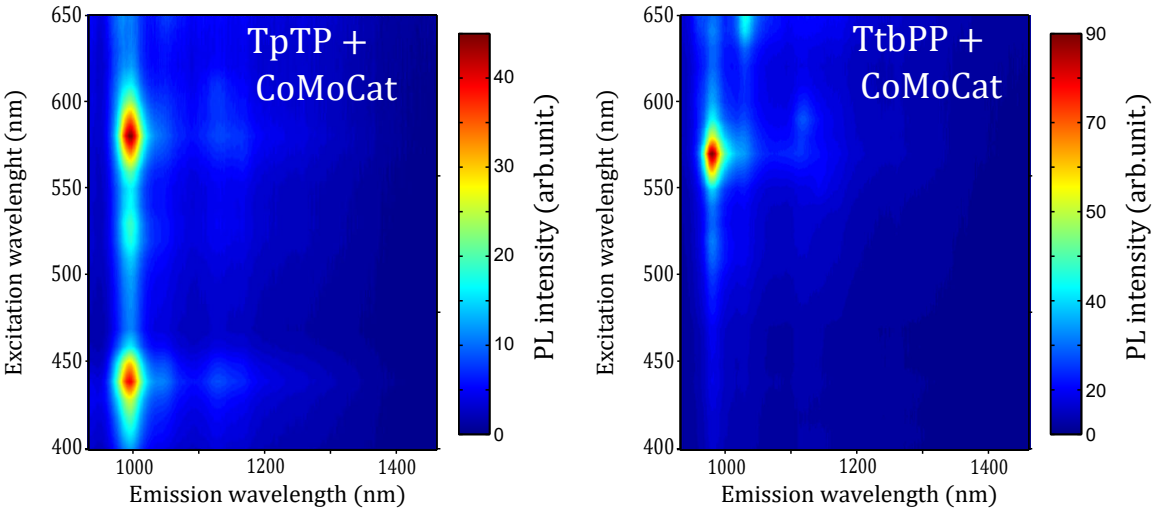

Figure III.33: PLE maps of single step micelle swelling samples of 2 w.t. % SC samples containing CoMoCat with TpTP (left) and TbtPP(right).

3.2 Kinetic and thermodynamic studies in different surfactants environments

There could be two explanations of the absence of organization for such molecules, both in connection with the additional substituents groups. On the one hand, it could be due to the progressive removal of the phenyl-phenyl interaction when the size of the substituent rises. On the other hand, all of these effects could be explained by a different degree of isolation of the molecules inside SC micelles. Indeed, Rharbi and coworkers have shown that the addition of subtituents on pyrene would change

the exchange dynamics of such molecules between micelles [204]. They attributed this effect to a different stability of the surfactant/pyrene micelles as a function of the added substituent.

To address this question the solubility of the TpTP molecule both in SC and in SDS has been tested. Following the method previously used for the TPP, the intensity of the $Q_y(1,0)$ band has been measured as a function of the maximal concentration for each surfactant. The results are displayed on figure III.34, in comparison with the TPP samples.

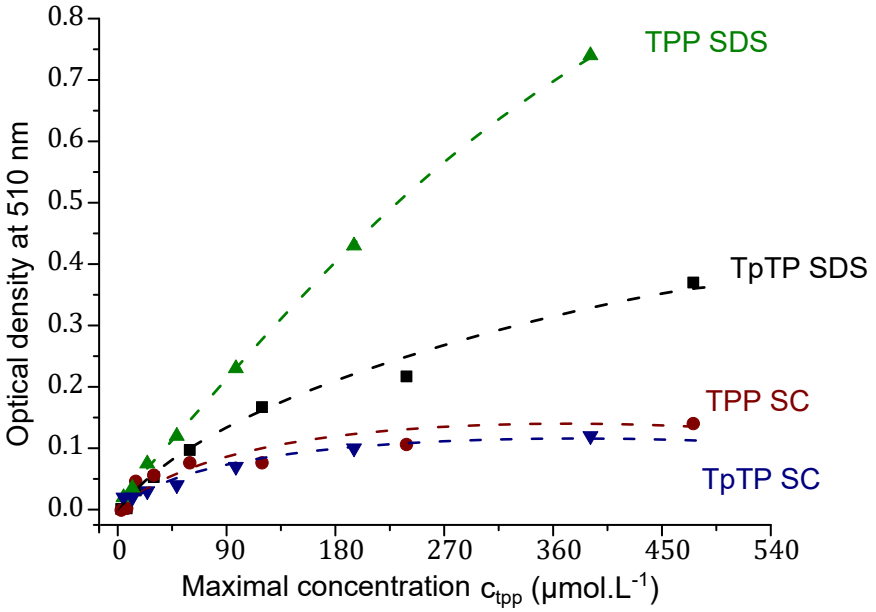

Figure III.34: Optical density of TPP and TpTP on the $Q_y(1,0)$ band in SC and in SDS, as a function of the maximal concentration of injected porphyrins.

For TpTP, the optical density in both surfactants increases with concentration and eventually reaches a saturation threshold. For SC (blue dots), the optical density reaches a threshold value for maximal concentrations above 100 μmol.L^{-1}. This value is relatively small, but this behavior is very similar to the one of TPP in SC (red dots), that presents a very similar threshold. However, the final absorption for TpTP is lower than for the TPP samples at the same concentration. This process can be explained by the poorer solubility of TpTP in SC, compared to TPP. This loss of solubility represents 30 % of the total absorption.

For TpTP in SDS (black curve), the threshold is reached at a much higher maximal concentration, above 400 μmol.L^{-1}. This proves the higher solubility of TpTP in SDS than in SC. A similar behavior was shown for TPP. As in SC, the final absorption of

TpTP in SDS is lower than for the TPP samples in SDS (green dots) for the the same concentration. Again, this can be explained by a poorer solubility of TpTP in SDS, compared to TPP. This loss of solubility represents 50 % of the total absorption. In conclusion, the TpTP is less soluble in surfactants than the classical TPP, but its solubility is better in SDS than in SC.

In order to get more information about the difference of functionalization between TPP and TpTP, a kinetic and a thermodynamic study of the process have been performed. A mix SDS/SC environment has been chosen, with r_{SDS}=50%. From the previous solubility study, such an important amount of SDS should allow to suspend a large quantity of TpTP in micelles. The figure III.35 displays the evolution of the transfer ratio for both samples as a function of time. Compared to the 14 days timescale of the TPP/CoMoCat sample, we see that the TpTP/CoMoCat requires a longer time (25 days) to reach the transfer peak saturation. This means that the kinetic process of transfer of the porphyrin to the nanotube surface is limited by the presence of the methyl groups. Quantitatively, this can be translated into a difference of activation Gibbs energy:

$$\Delta G_{a_{TpTP}} - \Delta G_{a_{TTP}} \simeq RT \ln(\frac{\tau_{TpTP}}{\tau_{TPP}}) = 1.1 \text{ kJ.mol}^{-1} \qquad \text{(III.38)}$$

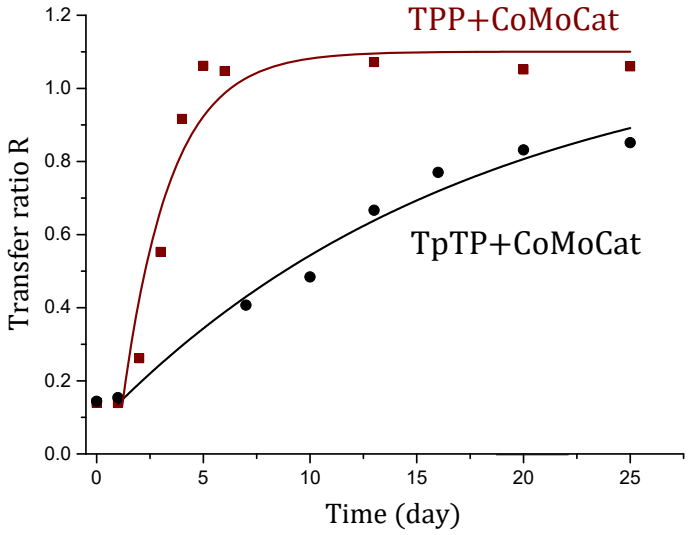

Figure III.35: Time evolution of the luminescence transfer ratio R for the mixed SDS/SC samples of CoMoCat with TPP (red) and TpTP (black).

In addition, an equilibrium study has also been performed. Figure III.36 displays the evolution of the transfer ratio X_R reaction extent as a function of the equilibrium porphyrin concentration. A very large amount ($c_{tptp} \simeq 200$ μmol.L^{-1}) of TpTp was

required to reach saturation, corresponding to $c_{tptp} \simeq 200$ μmol.L^{-1}, while only $c_{tpp} \simeq 30$ μmol.L^{-1} was enough to reach the full coverage.

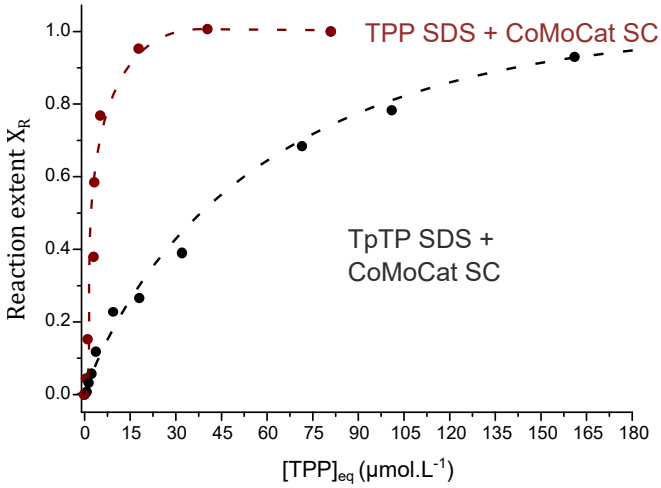

Figure III.36: Evolution of the reaction extent X_R calculated from luminescence transfer ratio R as a function of equilibrium porphyrin concentration, for the mixed SDS/SC samples of CoMoCat with TPP (red) and TpTP (black).

The Hill fitting figures are h=1.1 and K=2.6 10^4 ($\Delta rG = -25.3$ kJ.mol^{-1}). This data has to be compared to the values h=1.8 and K=3.2 10^5 ($\Delta rG = -31.6$ kJ.mol^{-1}) for the TPP in the same mixing conditions. This corresponds to an increase of the reaction Gibbs energy of 6 kJ.mol^{-1}. Thus, the reaction for TpTP has a very small reaction constant and is less cooperative. This could indicate that the presence of the methyl groups have hindered the cooperative interaction of porphyrins, leading to a very unfavorable reaction. However, it could also be due to the poorer solubility of TpTP in surfactants with respect to TPP.

As displayed in figure III.37 left, another consequence of the TpTP/NT interaction is an important redshift of the NT S_{11} transition. Compared to the 994 nm position for the TPP/NT for r_{SDS}=50 %, here the position can reach 1004 nm at very high TpTP concentrations ($c_{tpp} > 150$ μmol.L^{-1}). If this redshift is interpreted as a solvatochromism effect, this larger displacement may be due to a larger amount of TpTP around the tube than in the Nt/TPP case.

Finally, one may compare the reaction extent calculated from the S_{11} redshift $X_{S_{11}}$ and from the transfer ratio X_R. On figure III.37, one can see that the S_{11} position is shifted at very small TpTP concentration, while the energy transfer ratio requires a higher porphyrin amount. For the TPP, it has been shown before that both spectroscopic features follow the same evolution (and very similar reaction extents).

Here, the Hill fitting parameters for $X_{S_{11}}$ are K=1.36 10^5, $\Delta rG = -29.5$ kJ.mol^{-1} and h=1.3.

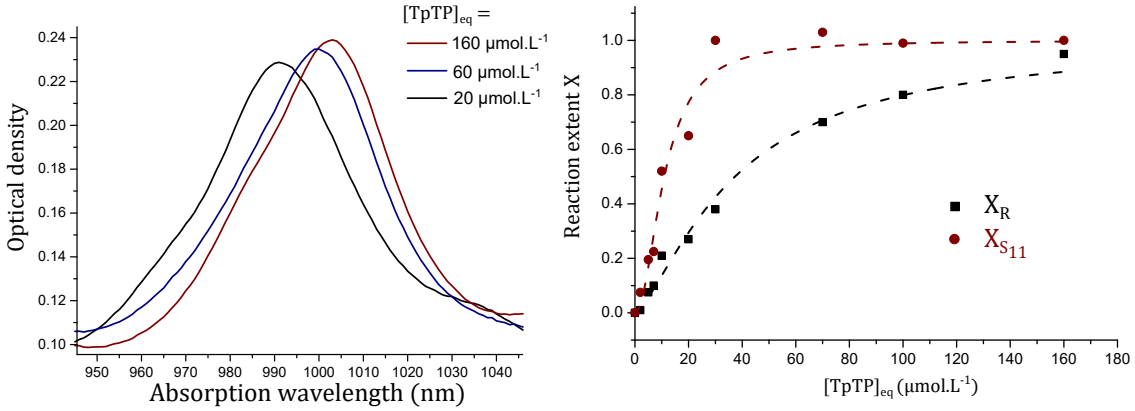

Figure III.37: Left: Evolution of the absorption spectrum corresponding to the (6,5) S_{11} transition in Nt/TpTP samples with increasing porphyrin concentrations; Right : Evolution of the reaction extent X_R (black) and $X_{S_{11}}$(red) as a function of equilibrium TpTP concentration, for the mixed SDS/SC samples of CoMoCat/TpTP samples.

This effect can be explained as a follows. At low concentration, the TpTP enters the nanotube micelle, but fails to create an organized monolayer of porphyrins around the nanotube. At higher TpTP concentration, a very large amount of porphyrins makes the nanotube's micelle swell, and eventually the porphyrins are forced to cover the nanotube surface.

Additionally, the organization of the porphyrins may also be involved in this process. Due to the intermolecular interaction, the energy transfer efficiency may depend on the degree of organization of the molecules, while the solvatochromism would not. This organization could be weak at low porphyrins coverage due to the substituted phenyl groups. When the coverage gets higher, those porphyrins may be forced to organize (at least at the very surface of the nanotube), leading to an important energy transfer.

In a nutshell, a transition behavior has been evidenced regarding the ability of TPP, TpTP and TbtPP to stack on carbon nanotubes. This transition is summarized in figure III.38. If the TPP is able to form a regular monolayer at the surface of the nanotubes, the TbtPP has almost no observed interaction with the nanotube.

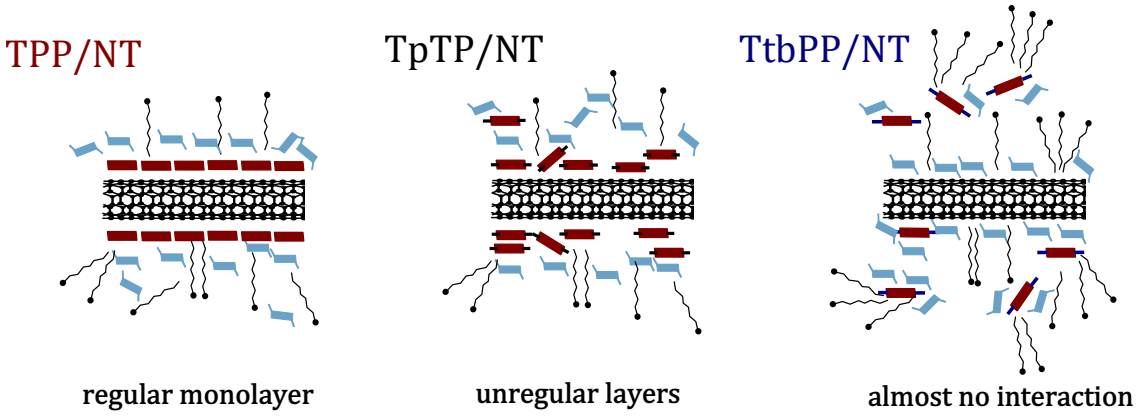

Figure III.38: Artistic view of the organization of TPP, TpTP and TbtPP inside a NT/SC/SDS structure.

One can speculate that the observed unfavorable reaction is due the decrease of the cooperativity of TpTP with respect to TPP. From Orelanna 's model [233], the contribution of the cooperativity could lead to a decrease of -70 kJ.mol^{-1} of the Nt/TPP binding energy (see figure III.39). Here, the experimental observed increase of 7 kJ.mol^{-1} would correspond to 10 % of this cooperativity energy contribution. This order of magnitude is not surprising, as the methyl groups on the TpTP are very small chemical functions, that would only have a limited effect on the global binding energy.

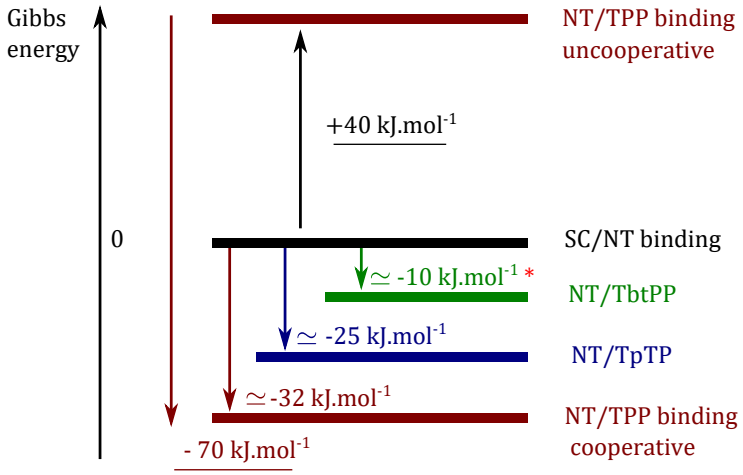

Figure III.39: Possible Gibbs energy diagram for the stacking of the TPP, the TpTP and the TbtPP on carbon nanotubes. The underlined values are extracted from binding energy theoretical calculations from [237] and [238]; the Nt/TbtPP reaction Gibbs energy (with the red asterisk) is a hypothetical value and not a measured one.

Yet, one can see that this effect creates large differences in the results of the thermodynamic experiments. The tertbutyl elements on the TbPP molecules are twice as long as the methyl groups. Leading to a smaller cooperativity, one could assume that they would lead to an even bigger increase of the reaction Gibbs energy, that would be closer to zero (see figure III.39). This increase would be sufficient to explain why their stacking on the nanotubes is not observed in the present reaction conditions: this reaction would be highly unfavorable.

However, it has also been evidenced that the TpTP has a poorer solubility in the SC and the SDS environments. It is also possible that the SDS/TpTP micelles are more stable than the SDS/TPP ones, due to the additional substituents [204]. Consequently, the surfactant/porphyrin interaction may also explain the differences between the Nt/TpTP and the Nt/TPP samples. For instance, if the SDS/TpTP structures were extremely stable (for $r_{SDS} = 50\%$), the reaction would be unfavorable. To study this hypothesis, the reaction will be tested for a very small r_{SDS} ratio to force the SDS micelles to break and release the TpTP (or the TbtPP).

Additional experiments are also planned to address this question: performing the reaction in different surfactant mixes (Triton, CTAB,..), or testing the ability of the TpTP and the TbtPP to stack on graphene nanosheets.

4 Conclusion

This chapter had focused on the study of the final state of the functionalization reaction. Through a careful monitoring of various spectroscopic features, we have looked at the porphyrin coverage around the nanotube surface. By modifying the porphyrin concentration, the study of the reaction equilibrium has been performed, giving access to the thermodynamical parameters of the reaction. Using a classical Hill model, this reaction was proven to be cooperative. For the (6,5) nanotubes, which represents one of the smallest diameter species, the reaction was proved to be the most limited, but with a significant cooperativity of 4. Differences in the fitting parameters were exhibited, depending on whether the nanotubes spectroscopy data or the porphyrin ones were employed. Such effects were attributed to two different, successive physical processes, that involved different amounts of porphyrins. The first of these processes was the Nt/TPP monolayer interaction, that can be measured trough the nanotube spectroscopy. The second process was the creation of unregular multilayers of porphyrins, that has an influence on the porphyrin spectroscopy.

Such effects were clearly linked to the diffusion processes studied in the previous chapter. To understand such connections, a thermodynamic study in various surfactant environments has been done. It has been shown that the TPP/surfactant stability could limit the functionalization extent. As a second step, a simulation of the kinetic and the thermodynamic data has helped to understand the link between the reaction dynamic and the final state. In particular, it has explained that the

incubation time was due to the difficulty to gather four TPP molecules, at an early time, to cover the nanotube surface.

Then, the thermodynamic study was performed in HiPCO nanotubes. For larger nanotubes, an increase of the reaction constant with diameter was exhibited, with a lower average cooperativity than for (6,5) nanotubes. Consequently, it has been proven that the Gibbs energy was decreasing with diameter, since the large nanotubes were the first to be covered. This dependency was proved to be very similar to the modeled evolution of the Nt/TPP binding energy with diameter. Various energetic (binding energies) and order elements (ordering of the different molecular layers) were evoked in order to understand the value of the experimental Gibbs energy value. It has been evidenced that the association ability of TPP was essential to break the SC/Nt binding energy threshold. This effect may be the key element to favor the global reaction. Finally, the study of substituted porphyrins has brought an insight into the stacking mechanism. Even small methyl groups were enough to limit the π-stacking of porphyrins. The final spectroscopic features of the TpTP/NT interaction proved the presence of molecular random aggregates, while the thermodynamic parameters have indicated that the reaction was uncooperative and more limited than for TPP. These effects may also be linked to the surfactant/porphyrin interaction. As a conclusion, this chapter has highlighted the ability of porphyrins to interact with each other to create a stable structure to surround the nanotube surface.

Chapter IV

Investigation into the self assembly of porphyrins on a sp^2 carbon surface

The three previous chapters have detailed every spectroscopic evidence of the coupling of porphyrin molecules with the nanotube. Many of them are relatively well understood, such as the energy transfer resonance, the shift of the nanotubes S_{22} and S_{11} transitions, or the molecule quenching. The evolution of the Soret band, with the creation of a redshifted component has also been widely mentioned in the previous discussions. However, the physical effects that lead to such redshift is still under debate. More precisely, there could be several effects that could induce such a spectroscopic modification.

The first section of this chapter will recall of the occurrences of such spectral shift for different samples. Then, every possible physical explanations of such spectroscopic shift will be described, in relation with the nanotube properties. Two main hypotheses will emerge: the molecule flattening and the molecule/molecule organization. For each case, a particular attention will be paid to predict the evolution of the two energy components of the Soret band (B_x,B_y). To get more information on such spectral effects, a polarized photoluminescence experiment will be detailed. This study will be first performed on isolated porphyrins samples. Then, it will be compared to the same experiments on Nt/porphyrins compounds by monitoring the nanotube's luminescence.

In a second part, the ability of porphyrins to self organize on a template will be discussed in regard of literature examples. Then, a model of dipole-dipole interaction between aggregated molecules will be developed. The example of the linear chain of molecules will be extensively detailed.

In a third part, this dipole coupling model will be adapted to the organization of TPP around a nanotube. Different geometries of aggregates will be studied. The effect of such organization will be confronted to experimental spectroscopy results.

The geometrical and electromagnetic influence of the nanotube will be discussed, in order to see if the experimental results are compatible with an ordering of porphyrins around carbon nanotubes.

Finally, two other types of aggregates, close to the Nt/TPP case, will be discussed. The first one is the organization of TPP on a graphene surface. An extensive study of optical absorption spectra of graphene/TPP samples will be performed. Then the dipole coupling model will be used to explore the possibility of organized multilayers of porphyrins on this carbon 2D template. The second one is the organization of diphenylporphyrins (DPP) on nanotubes. Molecular aggregates with slightly different geometries than in the Nt/TPP case will be evidenced.

1 Shifts and splittings of the Soret band

1.1 The Soret absorption band in carbon/TPP compounds

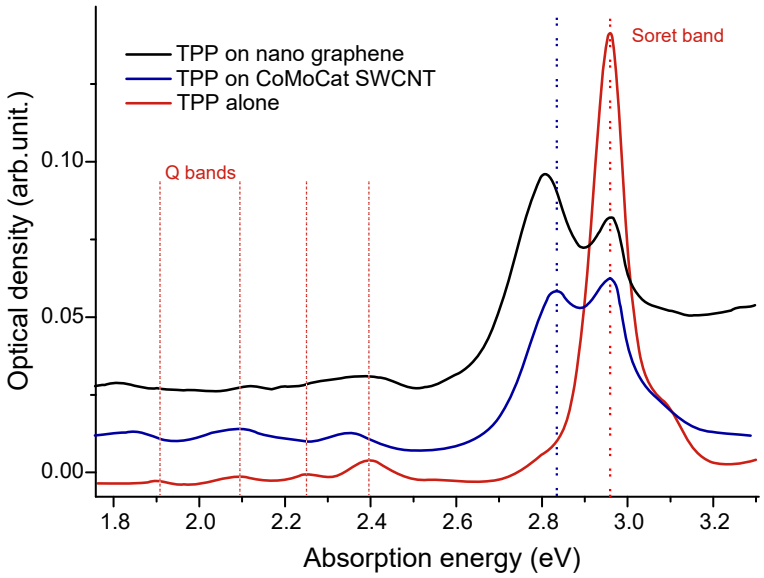

Figure IV.1: Comparison of optical absorption spectra of isolated TPP, graphene/TPP and CoMoCat SWCNT/TPP samples for similar concentrations in cholate. The scattering background has been subtracted to be able to point out the energy position of each transition.

During the three first chapters, the impact of the Nt/TPP interaction on the Soret Band has been presented as a low energy shift, visible on optical absorption spectra. Figure IV.1 is a summary of the main results related to this redshift effect. First, one can see this effect by comparing the TPP in cholate (red absorption curve) and

the (6,5) Nt/TPP compounds in cholate (blue curve). The center of the Soret is displayed of 18 nm (120 meV), from 420 nm (2.95 eV) to 438 nm (2.83 eV) for (6,5) sorted nanotubes samples.

The same absorption spectrum has been performed on graphene nanosheets/TPP compounds. The functionalization protocol is identical to the one presented in the two previous chapters. The absorption spectrum of a graphene/TPP sample (black curve is displayed in figure IV.1. On the three curves, the unshifted Soret contribution is centered approximately at the same energy of 2.95 eV and presents the same full width at half maximum of around 80 meV.

However, the structure of the shifted component is different. On the graphene nanosheets, the center position of the Shifted component is at 2.79 eV (445 nm), which represents a -40 meV redshift with respect to the case on CoMoCat sample (2.83 eV). The former Phd student Cyrielle Roquelet [168] monitored the position of the shifted Soret band upon adsorption of the porphyrin on different species of nanotubes (see IV.1). A decrease of the absorption energy of the low energy Soret band as a function of the nanotube mean diameter was found: for 2.83 eV to 2.80 eV when the average diameter changed from 0.8 to 1.2 nm. Graphene/TPP assemblies seem to follow this tendency, as a possible large diameter limit.

	CoMoCat	HiPCo	Laser ab.	Graphene
$< d >$(nm)	0.8	1	1.2	∞
$E_{stacked}$(eV)	2.83	2.82	2.8	2.79
$E_{stacked} - E_{free}$(meV)	-120	-130	-150	-160

Table IV.1: Evolution of the red shifted peak energy with mean curvature diameter in samples

Though significant differences have been evidenced between NT/TPP and graphene/TPP samples, the redshift seems to be a general feature of the π-stacking of porphyrins molecules on a carbon sp^2 surface.

1.2 Possible effects leading to a spectroscopic shift.

Nevertheless, the physical origin of the spectral shift of the Soret band remains unexplained. In the literature, the possible reasons to account for such effect are multiple. This section will list the main ones, and discuss their principal consequences.

At the moment of the Nt/TPP coupling, the electromagnetic environment of the nanotube changes leading to a solvatochromism effect. Consequently, the nanotube transitions are redshifted of around -20 meV. Reciprocally, it would be natural to think that the nanotube would have an electromagnetic influence on the porphyrins,

that may undergo a similar solvatochromism effect. However the amplitude of the observed Soret redshift in the present samples is 5 times larger than the one usually expected for such solvatochromic effects [239].

Thus, one may look for effects that can induce a larger redshift ($\simeq$ 100/200 meV). One situation that has been massively studied is the acidification of the porphyrin, when two inner hydrogens are added to the nitrogens. The obtained cation of the porphyrin has a redshifted Soret band centered at 2.82 eV [240], that could correspond to our observations. It would also lead to a four fold symmetry of the porphyrin molecules (as discussed in the first chapter). However, such effect is highly improbable due to the neutral borate buffer used in the samples to maintained the pH to 8, while the pKa of acidification of the porphyrin is located around 2.6 [119].

Flattening of the porphyrin on a surface

Several groups have reported important redshifts effects in the case of porphyrins molecules interacting with a flat surface. Among many examples, Xu *et al.* evidenced a 250 meV redshift effect when hydrosoluble porphyrins (called TMPYP) interact with anionic graphene oxide ([239], see figure IV.2 left). The authors attributed this effect to a flattening of the porphyrin molecules upon adsorption on the graphene surface.

Indeed, Chernia and coworkers [241] published a theoretical paper that studied the effect of the rotation of the phenyl groups. They affirmed that the flattening of the molecule would induce a progressive redshift of the Soret band (see figure IV.2 right). In a bulk state, they assumed that the phenyls of the porphyrin are forming an angle of 90 ° with respect to the macrocycle plane. Upon adsorption on a surface, these phenyls may acquire a smaller angle value, that depends on the intensity of the porphyrin coupling with the surface. As these phenyls enter progressively the porphyrin plane, their π electrons may couple to the macrocycle ones leading to higher conjugation. This additional conjugation can be at the origin of the observed redshifts.

As explained in the first chapter, the Soret band of the porphyrin is composed of two perpendicular components, B_x and the B_y. Within the flattening model, one can observe in figure IV.2 right that the B_x and the B_y band are both redshifted with nearly the same amplitude (the final splitting in energy is of 30 meV for an angle of 30 °). Indeed, on the experimental results from Xu *et al.* in figure IV.2 left, one can observe that no significant absorption contribution is observable around 400/410 nm, ruling out the presence of a blueshifted (or an unshifted) component within the Soret band.

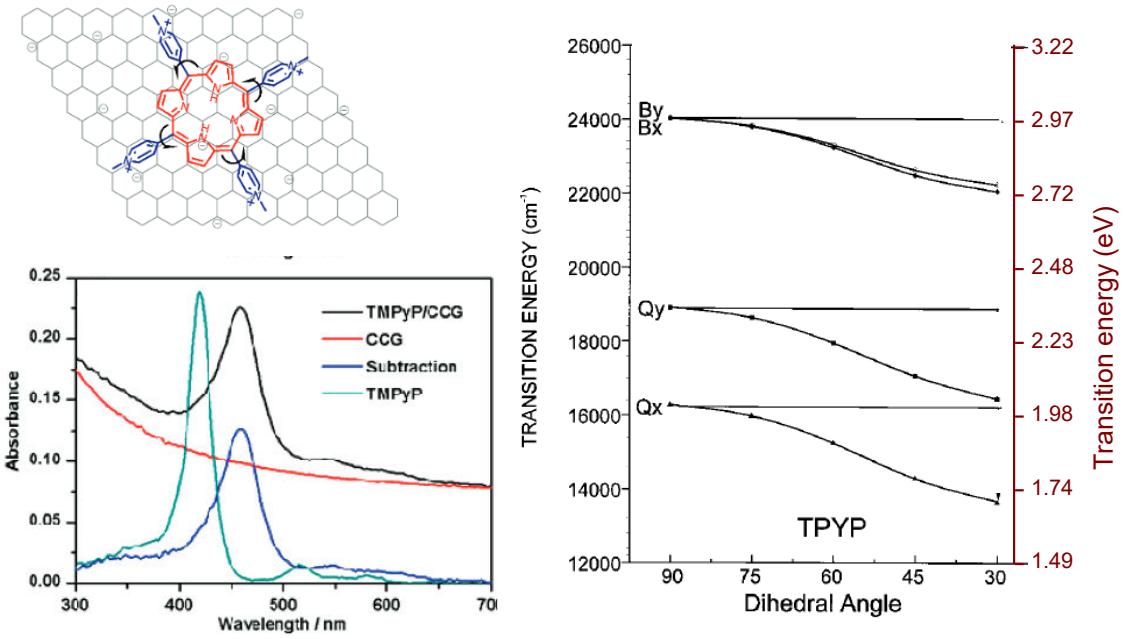

Figure IV.2: Left top: Artistic view of the TMPYP in interaction with the graphene oxide surface (CCG); Left bottom: Redshift of the porphyrin Soret band in presence of graphene with respect to the isolated molecule, from [239]; Right: Theoretical evolution of the energy positions of the principal TMPYP bands as a function of the phenyls angle with respect to the macrocycle, from [241].

Thus, to test this flattening hypothesis, one should look for the presence of this two perpendicular redshifted Soret components. In addition, this model shows that the Q bands undergo a significant shift of the similar amplitude to the Soret band.

This fact can be compared to the results on Nt/TPP samples, from figure IV.1. One can see that the first $Q_y(1,0)$ bands goes from 2.4 eV when it is free in micelle to 2.36 eV when it is stacked on the CoMoCat nanotubes. This redshift of $\simeq 40$ meV is three times smaller than the one of the Soret band. Such effect cannot be explained by this flattening model.

Self assembly of porphyrin molecules

The last physical effect that can explain such large shifts is the organization of the porphyrins into an ordered network of molecules. There are many experimental proofs that porphyrin molecules have the ability to self assemble in different configurations [242–244]. Anex and coworkers [245] have for instance studied in 1961

the properties of a tetraphenylporphyrin crystal by a polarized reflectometry experiment. As seen on figure IV.3 left, they exhibited the presence of a low energy and a high energy Soret components, with perpendicular crystal directions. Within one direction, the low energy component was redshifted of around -150 meV with respect to the Soret center position. One can observe that this shift has a comparable value to the ones obtained for the Nt/TPP samples. In the other direction, they exhibited a high energy component with a shift of around +100 meV. The energy difference between these two bands was around 250 meV.

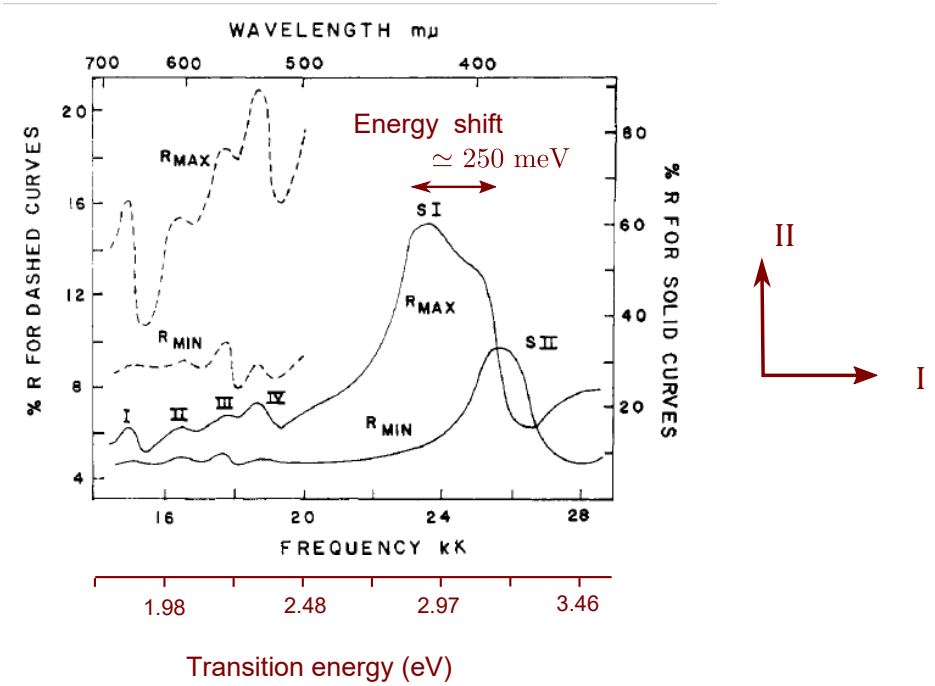

Figure IV.3: The reflectivity spectra obtained for the (010) face of tetraphenylporphine crystal, the incident light being polarized with its electric vector parallel to the "R_{max}" or to the "R_{min}" principal direction in that face. An expanded plot of the long wavelength spectra is included and the various bands labeled, from [245].

Indeed, one main characteristic of the coherent organization of molecular dyes is the presence of a spectral splitting. In such theory, the nanotube could be regarded as a template for the ordering of the porphyrin molecules. The differences of energy positions between the Soret band on graphene and on nanotubes could be explained by a different organization of molecules on a 1D and on a 2D template.

Another feature of this dipole-dipole coupling is that the value of the energy shift is proportional to the oscillator strength. Since the oscillator strength of the $Q_y(1,0)$ band is at least ten times smaller than the Soret band one [246], it should undergo

a smaller shift. As explained before, such effect has been observed in figure IV.1, though the factor of proportionality of ten is not observed.

One can see that the phenyl rotations and the molecular organization hypotheses may both explain the observe red shifts. One has to consider the possibility that these two effects may actually coexist. For instance, the organized ring structure suggested by Orelanna [233] also implies a modification of the phenyl angles. Nevertheless, the difference in shift between the Soret and the Q bands tends to validate the existence of an organization. In order to confirm this theory, one should design a experimental method to probe the energy position of the two components of the Soret band.

1.3 Experimental study of the energy splitting within the Soret band.

Study of intrinsic Soret energy bands in the TPP

Before discussing about the effect of the nanotubes on the porphyrins, it is important to know the structure of the Soret band in isolated porphyrins. For such purpose, polarized optical spectroscopy represents a suitable tool. Among theses optical techniques, some of them are based of the absorption of polarized light: such as linear dichroism [119]. However, this technique can only be used on samples in which every nano-object is aligned along the same direction. Otherwise, any polarization contribution would average to zero due to an isotropic distribution of all the molecules.

On the contrary, polarized PL experiments can be employed to study disorganized objects, as long as their motion is slow enough in comparison with their PL lifetime. This the reason why the PLE experiments that will be presented here have been performed on porphyrins in a DCM/castor oil organic phase. The castor oil is a viscous solvent that is employed here to slow the rotational dynamic of porphyrins, so that their rotation characteristic time becomes larger than their luminescence lifetime (12 ns, see first chapter). A 10-90% DCM-castor oil volume proportion has been chosen to achieve such effect, in consistence with literature [107].

Once the solution is prepared, an absorption spectrum is performed to rule out any spectral disturbance coming from the viscous solvent. As seen on figure IV.4, the amplitude and the width of the Soret and Q bands is similar to the one in a full DCM sample (presented in the first chapter). In particular the center of the Soret band at 2.97 eV (418 nm) is consistent with the expected value in dichloromethane, proving that the porphyrins are properly isolated in this solvent mix. One can note that the center of the Soret band in DCM is 20 meV higher in energy with respect to the results in cholate suspensions (2.95 eV). This is due to a different solvatochromic effect in these solvents. This effect will be considered when the result of this section will be compared to the one on Nt/porphyrins samples in cholate.

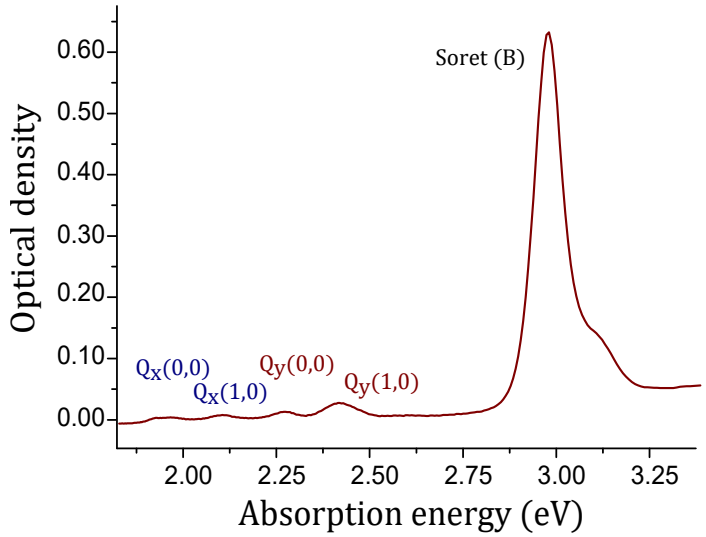

Figure IV.4: Optical absorption spectrum of the TPP inside the castor oil/ DCM mix.

In a second time, the nonpolarized PLE experiments has been performed (the grey curve in figure IV.5). This PLE line corresponds to the PL signal of the Q_x(0,0) band (1.91 eV) as a function of the excitation energy. This curve is very similar to the absorption diagram from figure IV.4. In particular, the Soret and the Q bands are all present at the same energy positions.

Then, two polarizers are added to the setup to perform the PLE experiment as a function of polarization. Four configurations are required to acquire the anisotropy diagram: VV, VH, HH, HV (cf chapter I). The two last components are measured to remove a polarization effect induced by the optical components (lenses, cuvette, diffraction gratings, optical filters, photodetectors...). Thus, the anisotropy r can be assessed through the formula:

$$r = \frac{I_{VV} - GI_{VH}}{I_{VV} + 2GI_{VH}} \tag{IV.1}$$

with $G = I_{HV}/I_{HH}$.

The extracted anisotropy (black) is superimposed to the unpolarized PLE spectrum (grey) in figure IV.5. As for the unpolarized PLE, the luminescence signal has been integrated over the Q_x(0,0) band. The anisotropy curve exhibits a complex behavior in consistence with the original study from Weigl [107]. Interestingly, the anisotropy curve presents a larger number of resonances than the unpolarized PLE

spectrum, proving the complex interplay between the Ox and Oy states upon high energy excitation of the porphyrin electrons.

As explained in the first chapter, coherence effects will induce different desexcitation pathways depending on the excitation polarization. The PL signal is always emitted from an O_x band. Consequently, the anisotropy is large and positive upon an excitation on the Ox oriented resonances. The maximum anisotropy of 0.17 is reached for an excitation on the $Q_x(0,0)$ transition at 2 eV, for the excitation and the emission practically on the same spectral region.

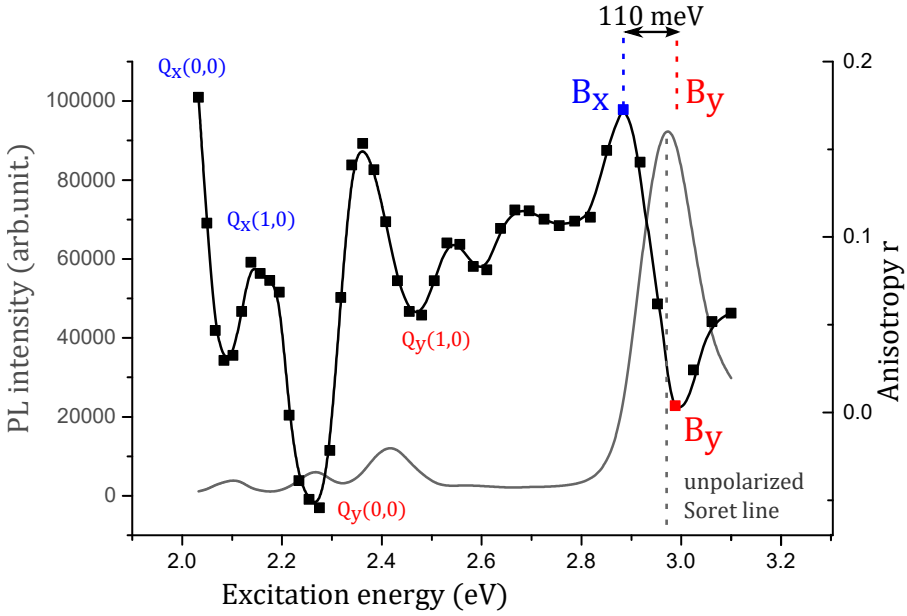

Figure IV.5: Grey: Unpolarized PLE spectrum of the TPP inside the castor oil/ DCM mix for a signal integrated over the $Q_x(0,0)$ band around 1.91 eV; Black: anisotropy measured in the same conditions with a polarized setup.

On the other hand, the anisotropy value is small or negative whenever the porphyrin is excited on a resonance oriented along Oy. The minimal value of -0.05 is reached upon excitation on the $Q_y(0,0)$ band at 2.28 eV. As it has been explained in the first chapter [107], the Soret band contains here two regions of anisotropy. The one at lower energies, centered at 2.88 eV, has a significant anisotropy of 0.17. The other one, centered at 2.99 eV presents an anisotropy close to zero. Thus, these two resonances are separated by around 110 meV, which is consistent with the value found by Weigl [107].

Then, the parallel and perpendicular intensity $I_{\parallel}$ and $I_{\perp}$ can be extracted from the formulae [117] detailed in the first chapter:

$$I_{\parallel}(\lambda) = \frac{r(\lambda) - r_{\perp}}{r_{\parallel} - r_{\perp}} I_T \quad ; \quad I_{\perp} = \frac{r_{\parallel} - r(\lambda)}{r_{\parallel} - r_{\perp}} I_T \tag{IV.2}$$

As explained in the first chapter, the previous anisotropy diagram allows to take $r_{\parallel} = r_{max} = 0.17$ and $r_{\perp} = -0.5 \times r_{\parallel} = -0.085$. The intensities $I_{\perp}$ and $I_{\parallel}$ are displayed in figure IV.6. One can observe the presence of the Ox and Oy bands (B_x, B_y, Q_x Q_y) that were discussed in the chapter one. In particular, the split of the Soret band is observable, with the low energy resonance B_x at 2.94 eV and the high energy B_y at 2.99 eV. This corresponds to a 50 meV energy difference between the center of these two resonances. This value is twice smaller than the one obtained from the anisotropy assignment of the bands positions from figure IV.5. Here, the $I_{\perp}$ and the $I_{\parallel}$ Soret components have very similar intensities.

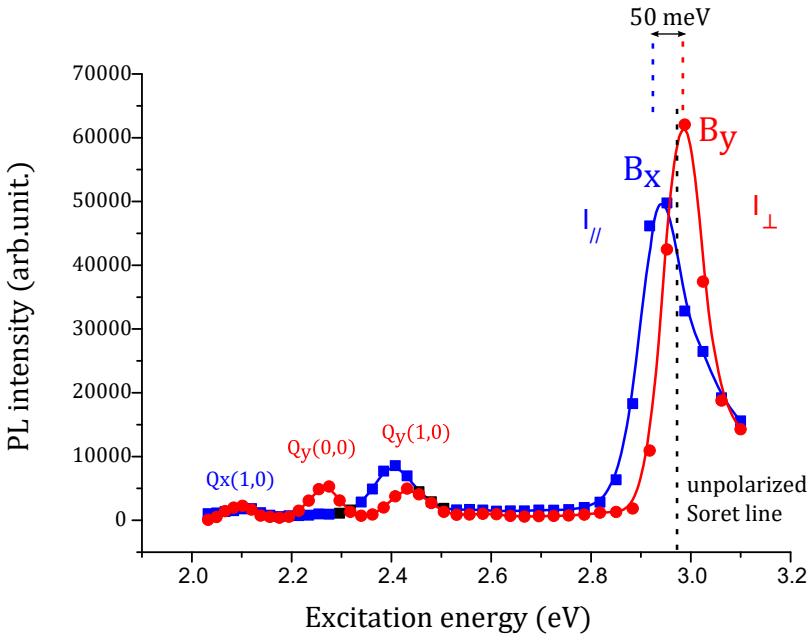

Figure IV.6: PLE parallel and perpendicular components of the photoluminescence of TPP molecules monitored on the $Q_x(0,0)$ band in a DCM/castor oil mix.

This representation is quite practical to visualize the parallel and the perpendicular spectral contributions. However, the method to obtain them is indirect and is based on a numerical correction. In order to point out the exact energy positions in $I_{\parallel}$ and $I_{\perp}$ a more complex fitting model would be required [247]. In many studies [115,248], this $I_{\parallel}/I_{\perp}$ representation is not employed and only the anisotropy values are discussed. In the following discussion, a value of 110 meV between the B_x and the B_y bands will be considered, as obtained from the anisotropy curve.

As a conclusion, the anisotropy diagram of the isolated TPP in a DCM/castor oil mix presents an intrinsic splitting behavior of the Soret band, with a low energy anisotropic component and a high energy isotropic one. This information is valuable and will be used as a reference in the next study on the Nt/TPP compounds.

Polarization resolved photoluminescence experiments on Nt/TPP samples

The previous section has proved that a spectral splitting exists within the Soret band in isolated porphyrins. The next step is to perform the same polarized PLE study on Nt/TPP samples, to look for a possible modification of the Soret energy components (redshift, blue shift, splitting,...). The energy transfer from the TPP to the nanotube will be monitored via polarized PLE experiments. In the present configuration, the rotational motion of the nanotube can be neglected during the timescale of the photoluminescence process.

The PLE map of a CoMoCat/TPP sample has been performed with an unpolarized setup. The corresponding PLE vertical cut for the (6,5) chirality is plotted in figure IV.7 left, for an emission energy of 1.24 eV. Among other features, this figure displays the regular nanotube resonance with the excitation on the S_{22} at 2.14 eV, and the Soret energy transfer resonance at an excitation energy around 2.83 eV.

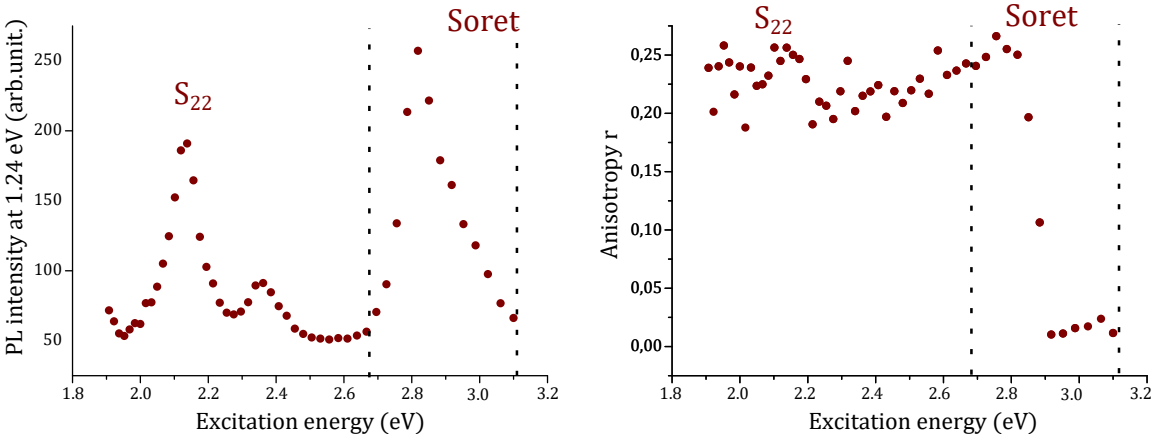

Figure IV.7: Left: PLE line for an 1.24 eV emission energy corresponding to the (6,5) nanotubes CoMoCat/TPP sample, with an unpolarized setup; Right: Corresponding anisotropy measurement for a 1.24 eV emission energy corresponding to the (6,5) nanotubes in Nt/TPP samples, from a polarized setup.

The plot of the anisotropy as a function of the excitation energy is displayed in figure IV.7 right. A maximal anisotropy value of 0.25 is found for the S_{22} excitation. Such value is similar, but slightly smaller than the one of 0.30 that can be found in litterature for nanotubes isolated in surfactants [117]. This result confirms

the strong anisotropy of the nanotube's photoluminescence. As explained in the first chapter, the anisotropy measured on a sample containing randomly oriented nanoobjects can reach values between 0.4 and -0.2, corresponding respectively to parallel and perpendicular absorption and emission dipoles.

However, the behavior of the Soret band is more complex, and presents two different energy bands. In its lower energy region ($E_{exc} \simeq 2.83$ eV), the value of the anisotropy is as high as the one from the regular S_{22} resonance. However, this value drops significantly at higher energies ($E_{exc} \simeq 2.98$ eV), reaching a zero value. As a consequence, the energy difference between the center of these two regions is around 160 meV.

The figure IV.7 right provides $r_{\parallel} = r_{max} = 0.25$ and $r_{\perp} = -0.5 \times r_{\parallel} = -0.125$. This allows to calculate the $I_{\parallel}$ and $I_{\perp}$ contributions for the (6,5) chirality (see figure IV.8 left). Two bands emerge, one that is parallel to the nanotube axis at 2.82 eV, and an isotropic one ($I_{\perp} \simeq I_{\parallel}$) at 2.98 eV. Similar results were found for other chiralities during experiments on HiPCO samples [108]. The example of the (8,6) chirality is shown in figure IV.8 right.

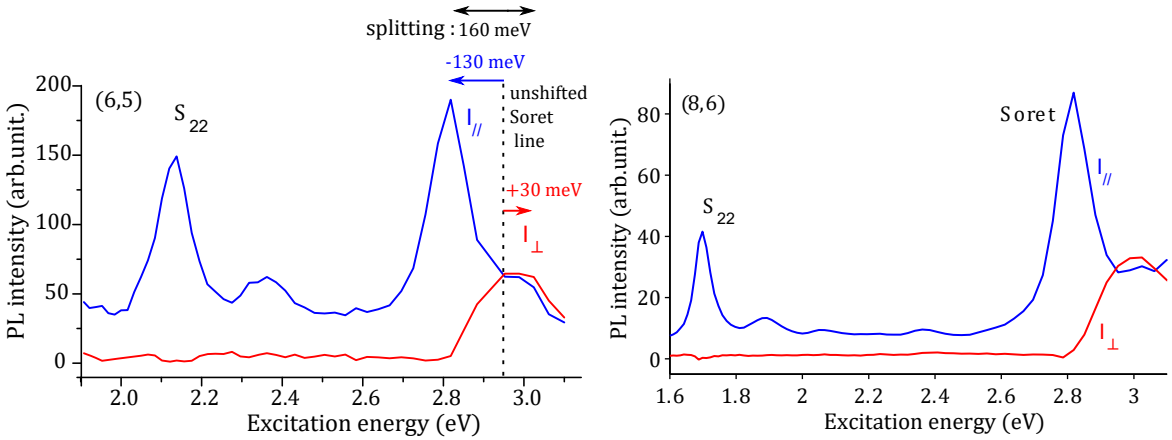

Figure IV.8: Left : PLE parralel and perpendicular components of a (6,5) from a CoMoCat sample; Right: PLE parralel and perpendicular components of a (8,6) nanotubes from a HiPCO suspended sample, from [108].

As a conclusion, the two transitions observed here have very different polarization behaviors. The low energy one is aligned with the nanotube axis while the high energy component is nearly isotropic (or slightly oriented toward the nanotube section). Interestingly, these two bands are very similar to the original B_x and B_y transitions in the isolated TPP. For instance, the low energy band in the Nt/TPP compounds and the B_x band in the isolated TPP both have a large positive anisotropy.

Consequently, one could conclude that the B_x band of each π-stacked is aligned with the tube axis. This is the first evidence of the alignment of the porphyrins on the carbon nanotube pattern. At this point, it is impossible to determine if this alignment is due to the Nt/TPP binding or the TPP/TPP interaction. These effects will be discussed in the next sections.

In these Nt/TPP compounds, the amplitude of the higher energy component is 4 times smaller than the one of the low energy band. This is a significant difference with the isolated TPP in which the B_x and B_y bands had similar amplitudes. Once again, these effects will be commented later.

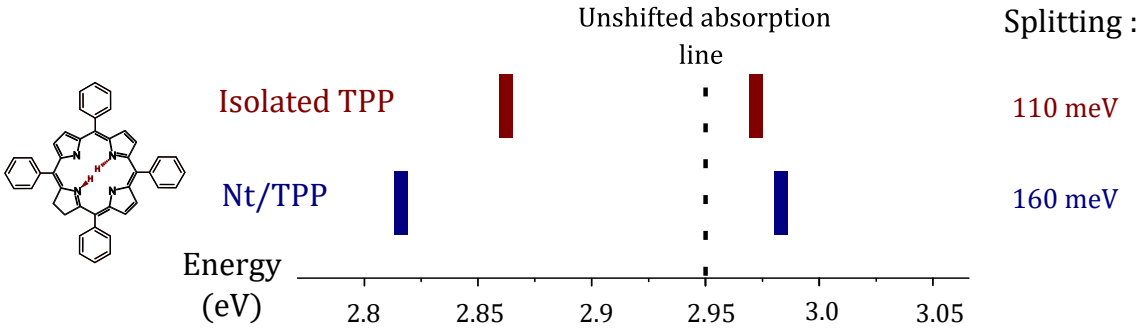

Figure IV.9: Energy position of the Soret components in isolated TPP and in Nt/TPP complexes obtained by polarized PLE experiments. A rigid shift of -20 meV has been applied to the energy positions from DCM/castor oil samples to account for the larger solvatochromism shift in cholate suspensions.

As a conclusion, the luminescence of the Nt/TPP compounds brings information on the inner structure of the Soret band of the π-stacked porphyrins. The interaction of the porphyrin with the nanotube seems to transform the spectroscopic features of the dye. In addition to the energy transfer, one sees that the two components of the Soret band are shifted in different energy directions. In other words, the intrinsic B_x/B_y splitting of the TPP seems to be amplified in the Nt/TPP compounds, going from 110 meV to 160 meV (see figure IV.9). Such increased splitting effect strongly supports the organization hypotheses, whereas a pure flattening effect would induce a redshift of the two components of the Soret band.

Polarization resolved microphotoluminescence experiments on single nanocompounds

In bulk samples, a very large number of Nt/TPP compounds are probed during a single experiment. Thus, the previous results are statistical mean characteristics, obtained by an indirect extraction method, that could deviate from the microscopic

physical effects. Consequently, it can be valuable to repeat the same polarization resolved experiments one nanotube at a time, using a microscopy setup.

The experiments were performed in the Pierre Aigrain laboratory, by the former Phd students Cyrielle Roquelet [168] and Fabien Vialla [108]. Using a confocal photoluminescence microscopy setup, the energy transfer and polarization data can be directly measured on isolated nanotubes [189]. The original nanotubes/porphyrins surfactant suspension is sprayed on a solid substrate, and cooled down to 4K. The results for several single nanotubes are reported on the figure IV.10. The unpolarized PLE lines for the (6,5) and (5,4) nanotubes present the same spectroscopic characteristics as the ensemble results: a pristine S_{22} and a Soret transfer resonance. In particular, the energy position of the maximum of the Soret band seems to be similar to ensembles (E_{Soret}=2.82 eV).

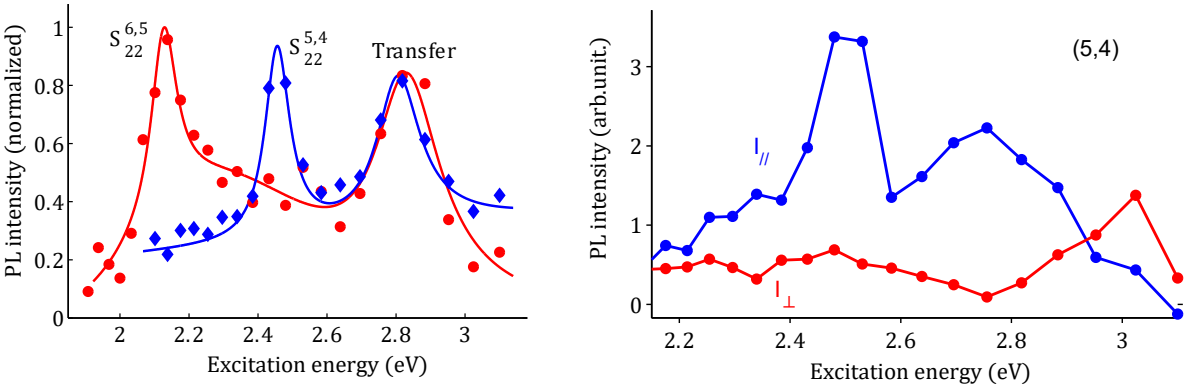

Figure IV.10: Left: PLE vertical lines relative to isolated (6,5) and (5,4) Nt/TPP compounds deposited on a solid substrate; Right: PLE parralel and perpendicular components of an isolated (5,4) nanotube deposited on a solid substrate, from [108].

Despite the low excitation power on this microscopy setup, the polarized PLE experiment has been performed on an isolated (5,4) nanotube. In figure IV.10 right, one can observe the presence of the split Soret band, similarly to the bulk samples. However, the two shifts are here slightly more important. The maximum of the parallel redshifted band is located at 2.78 eV.

As for the isotropic band, its maximum is at the higher energy 3.06 eV. To go further, the Xenon white lamp used for the excitation has been replaced by three laser sources at 3.06, 2.82 and 2.14 eV. The subsequent gain in excitation intensity allowed to perform a small scale statistical study on the polarization diagram of different isolated Nt/TPP compounds.

Upon excitation on the S_{22} resonance, the polarization diagram of every tested nanotube is very anisotropic. One can see an example for a (6,5) nanotube on

figure IV.11 left. This classical behavior, detailed in the first chapter, is explained by a maximal photoluminescence efficiency upon excitation and emission along the nanotube axis. Thus, this experiment allows to determine the direction of the probed nanotube axis (around 20° on figure IV.11 left).

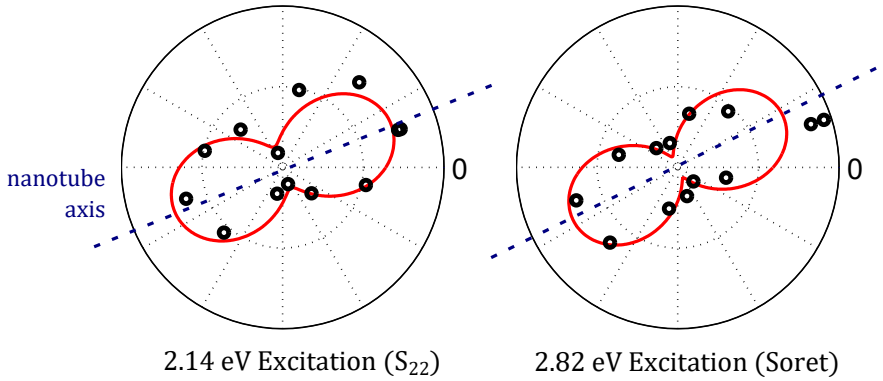

Figure IV.11: Evolution of the photoluminescence intensity (arb.unit.) of an isolated (6,5) Nt/TPP compound as a function of the excitation polarization angle for an excitation energy of 2.14 eV (left) and 2.82 eV (right), from [108].

When the experiment was repeated at the Soret energy of 2.82 eV, the diagram is very similar, with an anisotropic behavior and a maximal value for the same angle of 20°. Therefore, this transition is then aligned along the nanotube axis. Similar anisotropy features were found on other isolated nanotubes excited at the same energy. These results are consistent with the previous results presented for bulk samples.

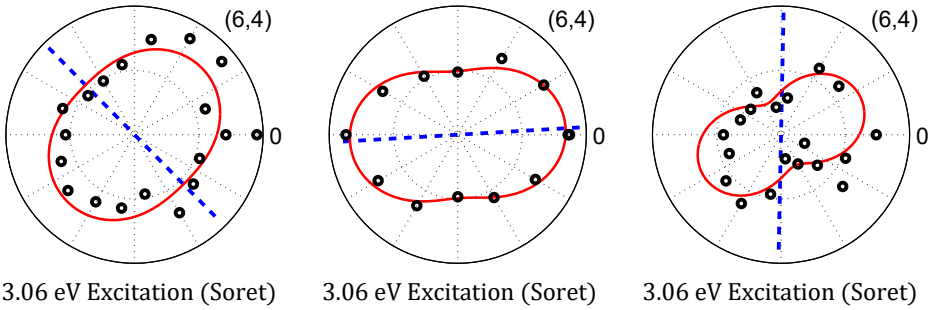

Figure IV.12: Evolution of the photoluminescence intensity (arb.unit.) of three isolated Nt/TPP compounds as a function of the excitation polarization angle for an excitation energy of 3.06 eV, from [108].

In a second time, a series of nanotubes have been studied with a polarized exci-

tation at 3.06 eV. Three examples of different excitation polarization diagrams are shown in figure IV.12. On each of them, the nanotube axis direction, obtained from the corresponding S_{22} polarization diagram, has been reported (blue dotted line). These diagram present a more isotropic behavior than the one presented above for excitation on the S_{22} or the redshifted Soret transition. On the first and the third one, the signal is maximal for a direction that is nearly perpendicular to the tube axis.

Once again, these microscopic results are consistent with the statistical spectroscopic features found for bulk samples. These experiments confirm the existence of a highly anisotropic Soret transition at low energy and a isotropic transition at high energy. Thus, the amplification of the energy splitting within the TPP Soret band upon adsorption on the nanotube pattern seems to be validated. The next step would be to confirm the hypothesis of an organization of the porphyrins.

2 Experimental evidences and modeling of the supramolecular organization process

2.1 Evidences of organization of porphyrins in the literature

The previous polarization resolved experiments proved the presence of an amplified energy splitting of the Soret band in Nt/TPP complexes. Before discussing the relationship between this splitting and a possible molecular organization, we will review two main examples in the literature that demonstrate the ability of TPP to self-assemble on a sp^2 carbon pattern. Then, a dipole-dipole model will be developed to see if such effect can account for the observed amplification of the energy splitting.

Orientation of porphyrins on a 2D surface

To begin, Bussetti and coworkers [249, 250] studied the organization of TPP on a highly oriented pyrolytic graphite (HOPG) surface. By means of STM measurement at room temperature they were able to prove that the porphyrins were all aligned along the axes of the graphite surface (see figure IV.13). The mean distance between the porphyrin molecules was of 1.65 nm. This distance can be seen as the sum of the lateral size of the molecule 1.25 nm and of a Van der Waals exclusion distance of 0.4 nm between two neighboring porphyrins.

This result constitutes a proof of the ability of porphyrins to coherently align over very long distances on a carbon surface. However, the alignment is here driven by strong coupling to the surface and is particularly sensitive to the orientation of the graphite lattice.

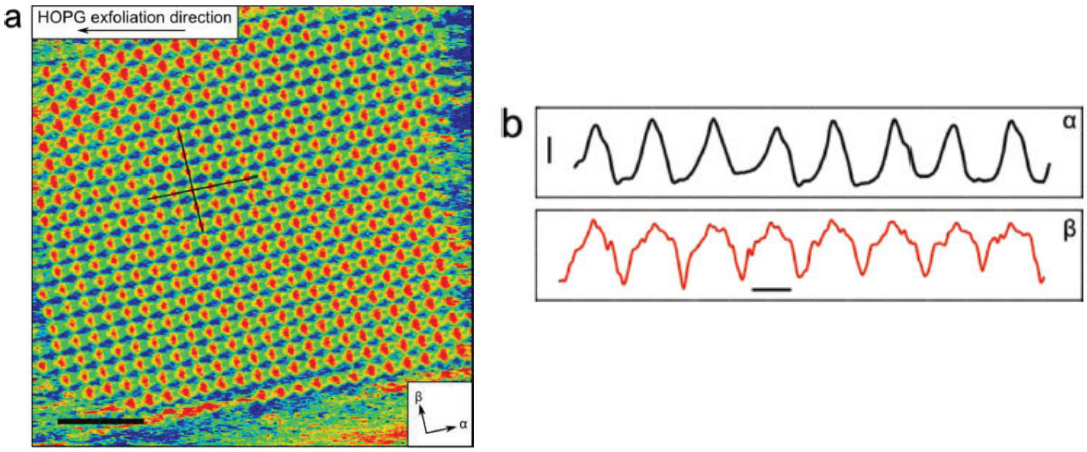

Figure IV.13: Left: Structure of a H_2TPP 2D domain on HOPG on a 36 nm × 36 nm STM image showing the arrangement of molecules in a square unit cell. The HOPG exfoliation direction is also indicated. The reported scale bar (bottom left) is 7 nm-long; Right: STM signal profiles acquired along the α and β directions, respectively. The vertical and the horizontal scale bars are 50 pm and 1 nm, respectively. The STM scan direction is nearly parallel with respect to the exfoliation one. Data have been acquired at RT, from [249].

A second example from Pham and coworkers [100], studies the ability of the TPP to organize into a monolayer on a graphene sheet. They placed a graphene layer on a gold surface, and then proceeded to the deposition of TPP through sublimation of a porphyrin powder.

Using a high resolution STM, they showed that the TPP molecules form a two-dimensional square-like lattice on pristine graphene at room temperature. They were able to observe a lattice of porphyrin molecules having the same orientation over around 100 nm^2 (see figure IV.14). At the opposite of the HOPG case, they observed that the porphyrin network do not follow the graphene pattern. Additionally, they were not able to monitor the presence of isolated porphyrins on the graphene surface, while it is a common situation when the graphene is replaced by a bare gold substrate [251]. These two facts indicate that the porphyrin/porphyrin interaction is significantly stronger than the TPP/graphene binding effect.

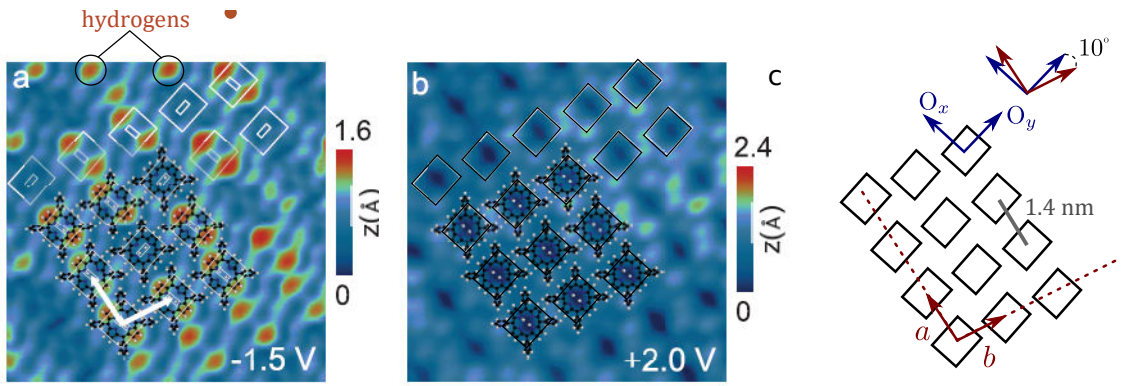

Figure IV.14: High-resolution STM images (8 x 8 nm^2) of a H_2TPP array on pristine graphene, recorded at (a) -1.5 V, 20 pA and (b) +2 V, 20 pA energies. The molecular models show the structure of the molecular lattice and mark the tautomer forms corresponding to the bright and dark molecules in (a), from [100]. (c) Geometric representation of the TPP aggregates with the lattice directions a and b and the molecules axes O_x and O_y.

This last statement is in contrast with the binding energies calculations performed by Orelanna [233], in the case of Nt/TPP complexes. In this model, the porphyrin/porphyrin interaction accounted for only 40% of the global Nt/TPP binding energy. The STM experiments tend to show that the graphene/TPP binding is here negligible with respect to the TPP/TPP interaction. Such a DFT model, adapted to nanotubes, cannot be directly transferred to the graphene/TPP situation. Nevertheless, these results are valuable regarding the importance of the cooperativity within the π-stacking process.

Then, they performed low temperature (4.6 K) and high resolution experiments. They were able to extract the geometrical characteristics of the porphyrin network (see figure IV.14 right). They found a 1.4 nm inter-molecule distance, which is significantly smaller than the one in HOPG samples, indicating the importance of the favorable porphyrin/porphyrin interaction in the π-stacking process. On the figure IV.14, the red spots are indicative of the presence of the inner hydrogens.

Thus, they were able to point out the O_x and O_y directions of each molecules. In figure IV.14, a majority of molecules can be observed with their O_x direction (and their hydrogens) along axis orientation (see a and b lattice directions in figure IV.14 right), while few of them are in the orthogonal b direction. Nevertheless, every molecule presents an angle of around 10 ° (respectively 100 °) between their O_x direction and the lattice directions (symbolized by the white arrows). Here, the porphyrins seem to present a natural tendency to align their O_x all along the same axis. This organization is created even though the interaction with the graphene

lattice is weak. These results are a strong evidence of the ability of the porphyrins to self assemble into an oriented network.

2.2 Modeling of the spectral consequences of the molecular organization

It has been established that the TPP have the ability to self-organize on a carbon surface. The next step will be to develop a dipole-dipole quantum model to predict the effect of such organization on the molecules spectroscopy. This will allow to simulate the energy positions of the molecules absorption bands inside these organized structures, to see if they are compatible with the experimental one from the polarized PLE experiments.

Theory of the dipole-dipole coupling in organized molecules

In order to understand the effect of the porphyrins organization, one can apply the theory of coherent molecular aggregates. The effects of aggregates on the molecules spectra were first evidenced by Davydov around 1940/1950, and called Davydov splitting afterwards [252]. In 1965, Kasha [192] developed a simplified formalism to account for such effects. It consists in treating the absorption transitions of two adjacent molecules as electromagnetic quantum dipoles.

To understand the results of this model, simplified situation can be considered. If one assumes the presence of two identical monomers (called 1 and 2), having each a single dipole $\overrightarrow{\mu_1}$ and $\overrightarrow{\mu_2}$ at the same energy E_{mono}. In the classical picture, the interaction between these two dipoles would induce a variation ΔE of the global energy according to the formula :

$$\Delta E = \frac{1}{4\pi\varepsilon_0}\frac{\overrightarrow{\mu_1}.\overrightarrow{\mu_2}}{r^3} - 3\frac{(\overrightarrow{\mu_1}.\overrightarrow{r})\,(\overrightarrow{\mu_2}.\overrightarrow{r})}{r^5} \tag{IV.3}$$

where ε_0 is the vacuum permittivity and r the distance between the two dipoles. In principle, those dipoles can take any independent direction of the space.

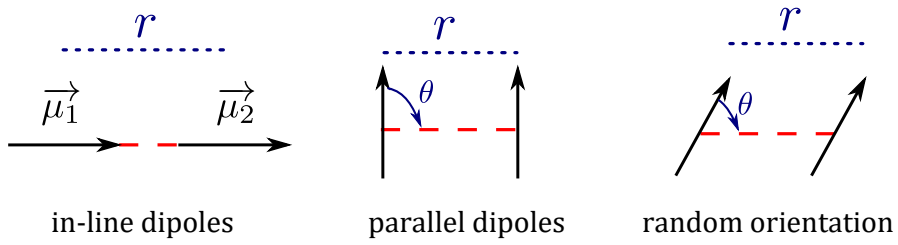

Figure IV.15: Three different configurations of dipoles that are parallel with each other.

In the following, the calculation will be restricted to the coupling of parallel dipoles (see figure IV.15), with the same dipole μ_{mono} and the same initial energy. This situation is quite representative of the experimental situations, in which aligned molecules have the same orientation. If the molecules have a fixed position, the value of the angle θ and the distance r between the dipoles are fixed. Therefore, one can easily calculate the value of the energy shift ΔE:

$$\Delta E = \frac{\mu_{mono}^2}{4\pi\varepsilon}\frac{1-3\cos^2(\theta)}{r^3} \tag{IV.4}$$

where θ is the angle between the dipole direction and the axis connecting the two dipoles (see figure IV.15).

In the quantum formalism, these two energy levels (and dipoles) correspond each to a given quantum state ϕ_1 and ϕ_2. In the following, ΔE will be regarded as a parameter in the calculation. For two degenerate quantum states of energies E_1=E_2=E_{mono}, Kasha and other groups have shown that this dipole-dipole coupling can be solved using the following matrix formalism [192, 253]:

$$\begin{array}{c} \\ \phi_1 \\ \phi_2 \end{array} \begin{array}{c} \begin{array}{cc} \phi_1 & \phi_2 \end{array} \\ \begin{pmatrix} E_{mono} & \Delta E \\ \Delta E & E_{mono} \end{pmatrix} \end{array} \tag{IV.5}$$

The two eigenvalues of this matrix corresponds to the energy of the two final states once the dipole-dipole coupling has been considered. At the end, this leads to a higher and a lower energy levels, very similarly to the bonding and anti-bonding states in a LCAO formalism in quantum chemistry [95]:

$$E^I = E_{mono} + \Delta E \quad ; \quad E^{II} = E_{mono} - \Delta E \tag{IV.6}$$

One can see that the amplitude of the splitting $2\Delta E$ between the two dipole states depends on the geometry (angles, distance), that has been included in the formula IV.4. Two eigenstates ψ^I and ψ^{II} can be assigned to these two energy levels. They will be made of a linear combination of the two uncoupled dipole states ϕ_1 and ϕ_2:

$$\psi^\alpha = C_1^\alpha \phi_1 + C_2^\alpha \phi_2 \quad ; \quad \alpha = I \text{ or } II \tag{IV.7}$$

with C^α being a real number between -1 and 1. As in the case of the bonding and anti-bonding states, the two eigenstates corresponding to the matrix IV.5 can be written as:

$$\psi^I = \frac{1}{\sqrt{2}}(\phi_1 + \phi_2) \quad ; \quad \psi^{II} = \frac{1}{\sqrt{2}}(\phi_1 - \phi_2) \tag{IV.8}$$

Now, the value of the resulting dipole must be evaluated. Before the coupling, the two initial dipoles $\overrightarrow{\mu_1}$ and $\overrightarrow{\mu_2}$ were parallel (see figure IV.15). Once the coupling is

considered, the final dipole $\overrightarrow{\mu^{\alpha}}$ will also be along the same direction, and its numerical value will be the sum of its two components:

$$\mu^{\alpha} = C_1^{\alpha}\mu_1 + C_2^{\alpha}\mu_2 = \mu_{mono}\,(C_1^{\alpha} + C_2^{\alpha}) \tag{IV.9}$$

Thus, the dipole-dipole coupling creates an amplified transition of dipole norm $\mu^I = \sqrt{2} \times \mu_{mono}$ and a forbidden one with $\mu^{II} = 0$. As it will be explained later, the oscillator strength of a given transition f^{α} is proportional to the square of the corresponding dipole norm μ^{α}. For the two final transitions, the model yields $f^I = 2 \times f_{mono}$ and $f^{II} = 0$, proving the conservation of the total oscillator strength.

J and H aggregates

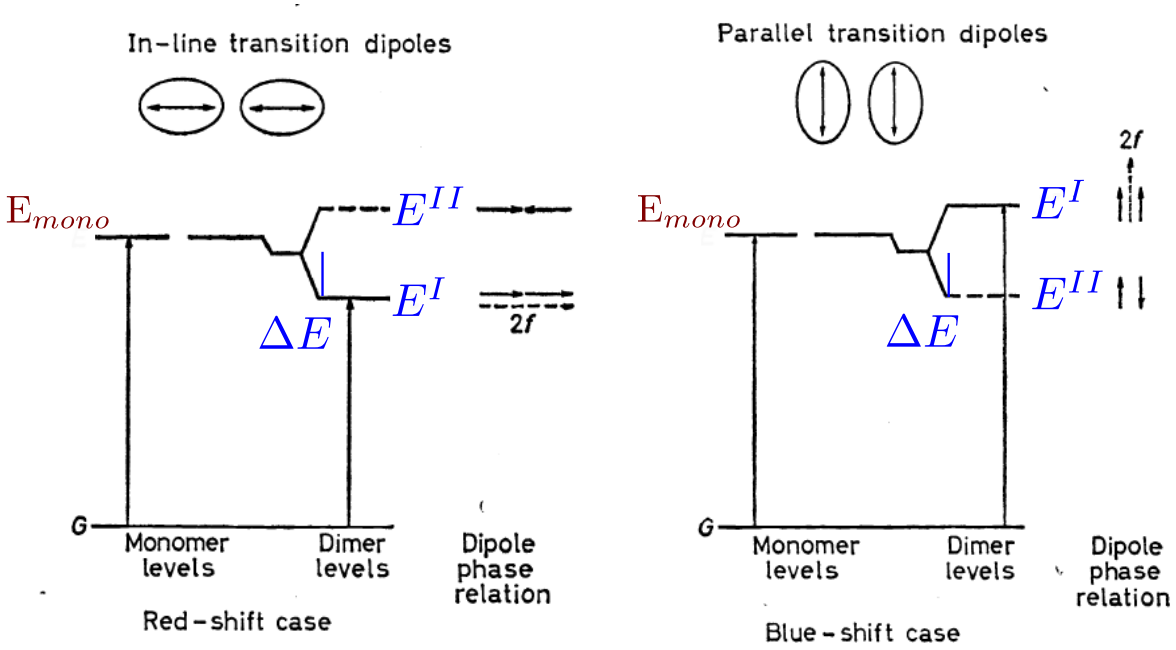

Figure IV.16: Exciton bands energy diagram for a molecular dimer, with in-line transition dipoles (left) and parallel transition dipoles (right), from [192].

The previous calculation applies for two aligned dipoles, regardless of the value of the angle θ between the dipoles and the line that connect them (see figure IV.15). In its original paper, Kasha detailed two particular situations: the in-line and the parallel case. For the in-line configuration, ΔE takes a negative value. Consequently, the low energy transition transition is allowed with a doubled oscillator strength (see figure IV.16 left), while the high energy one is forbidden. In the parallel configuration, ΔE takes a positive value, and only the high energy transition is allowed (see figure IV.16 right).

For real samples, this dipole coupling effect results in a redshifted absorption line when the molecules are assembled into an in-line configuration, and a blueshited absorption line in the parralel situation. These two cases are respectively called J-aggregates and H-aggregates. The result of such processes is displayed in figure IV.17, for hydrosoluble porphyrins H_2TPPS^{4-} in certain surfactant environments [116]. For in-lines dipoles the Soret transition is transferred to the low energies (figure IV.17 center) with respect to the uncoupled situation (figure IV.17 top). In the parallel case the Soret band is displaced to the high energies (figure IV.17 bottom).

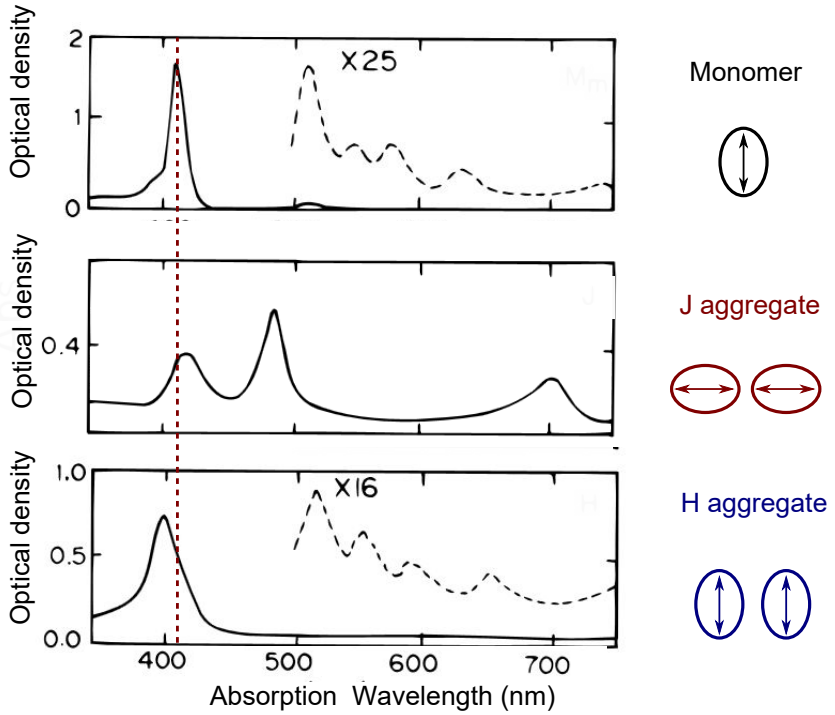

Figure IV.17: Absorption spectra for the different species of H_2TPPS^{4-}(10 μmol.L^{-1}); Top: the tetraanion (H_2TPPS^{4-}) at pH 8.1, Center: the J-aggregate with CTAB and H_2TPPS^{2-} and Bottom: the H-aggregate with CTAB and H_2TPPS^{2-}, from [116].

Calculation for a linear chain of dipoles

Finally, this matrix model can be adapted for any number N of aligned dipoles and for any geometry (i.e. different θ angles). In particular it can take into account different kind of dipoles interaction between different neighbors. In the general case, the coupling matrix M will be written as :

$$[M] = (M_{i,j})_{1 \leq i,j \leq N} \quad ; \quad M_{i,i} = E_{mono} \quad ; \quad M_{i,j} = \Delta E_{i,j} \quad j \neq i \tag{IV.10}$$

Apart from the diagonal terms, all the other coefficients depend on the corresponding dipole interactions. However, many of these coefficients vanish under the first neighbor approximation. For instance, this global model can be used to evaluate the energy positions of the bands in the case of a linear array of N molecules. This can be represented by the following matrix:

$$\begin{array}{c} \\ \phi_1 \\ \phi_2 \\ \phi_3 \\ \vdots \\ \phi_N \end{array} \begin{array}{c} \begin{array}{ccccc} \phi_1 & \phi_2 & \phi_3 & \cdots & \phi_N \end{array} \\ \begin{pmatrix} E_{mono} & \Delta E & 0 & \dots & 0 \\ \Delta E & E_{mono} & \Delta E & \dots & 0 \\ 0 & \Delta E & E_{mono} & \dots & 0 \\ \vdots & \vdots & \vdots & \ddots & \vdots \\ 0 & 0 & 0 & \dots & E_{mono} \end{pmatrix} \end{array} \tag{IV.11}$$

As the calculation starts with N ϕ dipoles states, the final result will provide a basis of N ψ eigenstates, with different corresponding dipole moment and eigenenergies. For each eigenstate ψ^i, the full calculation provides the energy value [253]:

$$E^i_{1\leq i\leq N} = E_{mono} + 2\Delta E \times \cos\left(\frac{i\times\pi}{N+1}\right) \tag{IV.12}$$

and the corresponding dipole moment is equal to [253] :

$$\mu^i_{1\leq i\leq N} = \mu_{mono}\sum_{1\leq j\leq N} C^i_j \;\;;\;\; C^i_j = \sqrt{\frac{2}{N+1}}\sin\left(\frac{i\times j\times\pi}{N+1}\right) \tag{IV.13}$$

One can take the example of an in-line J aggregate of 8 molecules, starting with the parameters $\Delta E = -32$ meV and E_{mono}=2.86 eV. The figure IV.18 displays the characteristics of the final dipole states in this case. It represents the square of the dipole norm $|\mu^i|^2$ for each eigenstate i as a function of its corresponding eigenenergy E^i. Due to symmetry in the formula IV.13, the $|\mu^i|^2$ value is strictly equal to zero whenever i is even.

For the odd values, they all have a very small contribution, except for i=1. For this particular state, the square dipole norm is close to the sum of the square norm of every non-coupled state : $8|\mu_{mono}|^2$ (see figure figure IV.18). The energy shift between E_{mono} and the lower energy level E^1 is of -60 meV, which is larger than the dimer shift of ΔE =-32 meV.

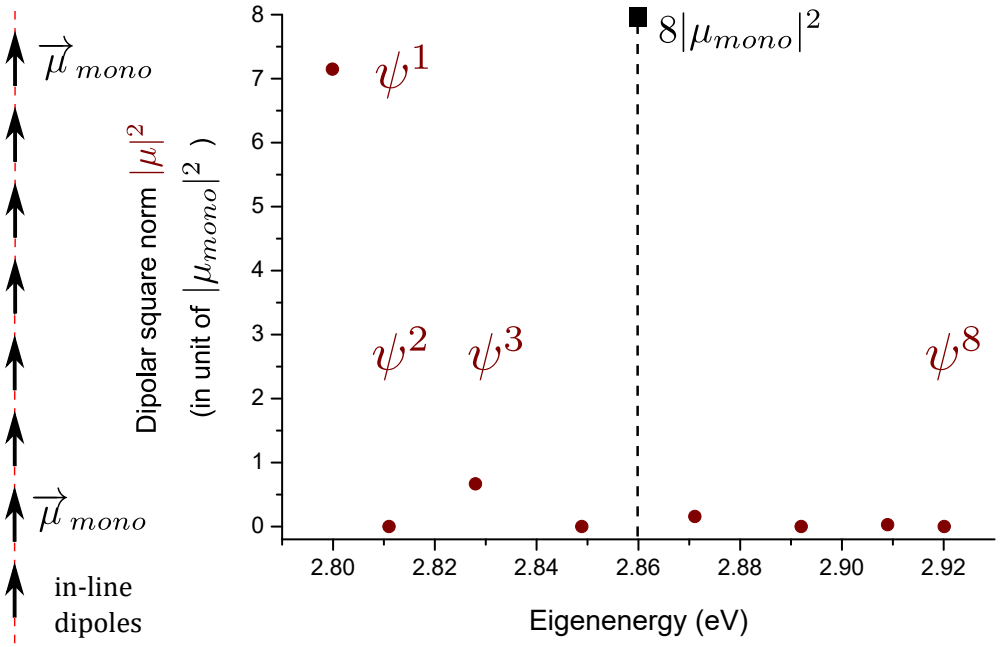

Figure IV.18: Results of the model for a in-line array of 8 dipoles. Red: The square of the dipole norm $|\mu^i|^2$ for each eigenstate i as a function of its corresponding eigenenergy E^i; Black: The non coupled situation with 8 degenerate dipoles.

This example illustrates a very common property of arrays of a linear chain of N aligned dipoles. Generally, only the i=1 state has a significant dipole norm, while the other have a negligible contribution [253]. In real arrays of N molecules, the only non zero transition is supposed to be located at the energy E^1:

$$E^1 = E_{mono} + 2\Delta E \times \cos\left(\frac{\pi}{N+1}\right) \underset{N\to+\infty}{\longrightarrow} E_{mono} + 2\Delta E \tag{IV.14}$$

One major result of this calculation is that the asymptotic energy shift for a large value of N is equal to twice the dimer value. Additionally, the value of the corresponding dipole moment and oscillator strength will be close to their maximal values:

$$\mu^1 \simeq \sqrt{N} \times \mu_{mono} \quad ; \quad f^1 \simeq N \times f_{mono} \tag{IV.15}$$

2.3 Dipole coupling model of a linear chain of porphyrins

Now that the model is set, it may be applied to evaluate the characteristics of a linear chain of TPP molecules. Before starting, one must calculate the oscillator strength and the dipole moment relative to the Soret band components. The figure IV.19 dis-

plays the molar extinction coefficient ε of TPP as a function of the energy (expressed in cm^{-1}).

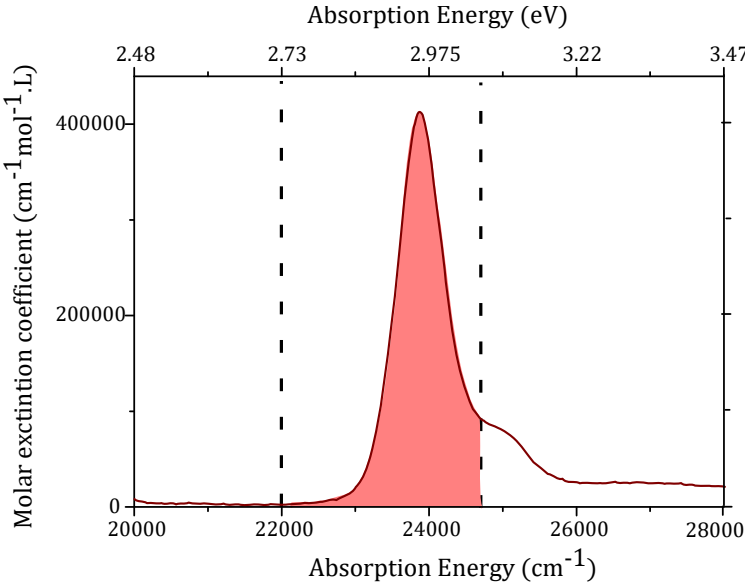

Figure IV.19: Graphical method to calculate the oscillator strentgh of the Soret transition of the TPP from the molar exctintion coefficient diagram, from [254]

The oscillator strength f can be extracted from the value of the molar extinction coefficient $\varepsilon(\nu)$ for each frequency ν included in the global transition, using the formula [255]:

$$f = \frac{1000\ln(10)}{N_A}\frac{m_e c^2}{\pi e^2}\int_{\text{transition}} \varepsilon(\nu)d\nu \tag{IV.16}$$

where m_e is the free electron mass and e is the electron elementary charge. When the extinction is plotted against the transition energy in cm^{-1}, this is simplified into the numerical formula [256]:

$$f = 4.319 \times 10^{-9}\int \varepsilon(\nu)d\nu \tag{IV.17}$$

From this formula, an oscillator strength of value f=1.58 is obtained for the whole Soret band, which is very close to the value reported in papers [257, 258]. From this value, one can evaluate the norm of the dipole moment associated to this transition [255]:

$$\mu^2 = \frac{3e^2\hbar}{4\pi m_e \nu_0} \times f \tag{IV.18}$$

where ν_0 is the central frequency of the transition. This yields the norm of the dipole moment: $\mu = 3.95 \times 10^{-29}$ Cm (in S.I. units) or 11.8 D (in Debye), which is once again similar to other published results [259, 260]. In order to use the previous dipole model, one has to determine the projections of the dipole moment on the two directions O_x or O_y. If one assumes an equal value in these two directions, it yields:

$$\mu_x = \mu_y = \frac{\mu}{\sqrt{2}} \tag{IV.19}$$

This corresponds to two degenerated dipoles of amplitude of 8.3 D in the O_x and O_y directions.

Now, one can study the case of two aligned porphyrins, and the coupling of two of their dipoles (two Bx or two By). The numerical value of the coupling term ΔE can be evaluated using the formula IV.4. At this point, one has to remember ΔE represents the difference in energy between the final optically allowed state and the initial state: $E_{allowed} = E_{mono} + \Delta E$.

One can consider the in-line dipole configuration (J case) first. Based on the experimental evidences (including the STM on graphene and HOPG), one can start by fixing the angle to $\theta = 0°$ and the distance between the two porphyrin to 1.4 nm. This gives a value of $\Delta E_J = -32$ meV for the shift of the new low energy transition with respect to the monomer transition. The parallel dipole configuration (H-case) can be directly inferred by taking $\theta = 90°$ and the same distance. This yields $\Delta E_H = +16$ meV.

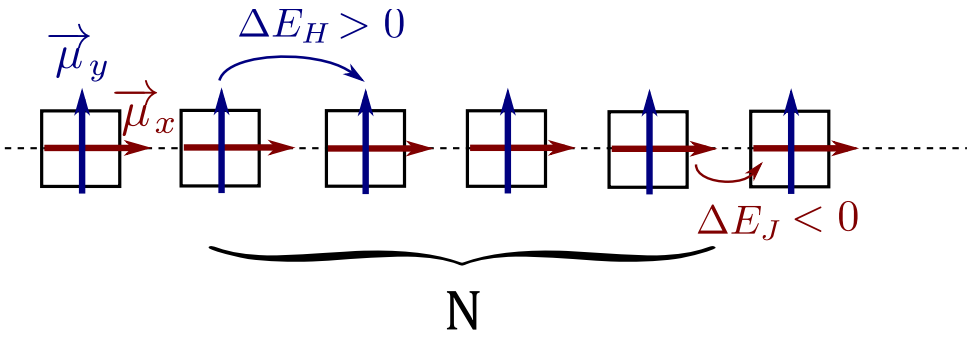

Figure IV.20: Schematic of an linear chain of N porphyrins, with their μ_x dipoles in the in-line configuration and the μ_y in the parallel configuration.

The geometric parameters that are deduced from the STM or theoretical contributions present a measurement uncertainty. Though they can be used in the present model, it would be useful to consider a variation of these parameters. Figure IV.21 studies the evolution of the ΔE_J coupling term as a function of the intermolecular

distance for an in-line dimer with an angle of $\theta = 0°$. As expected from the formula IV.4, this energy shift is proportional to the cube of the intermolecular distance.

When the distance between molecules is larger than 2 nm, the shift effect is negligible: $0 > \Delta E > -10$ meV. One has to remember that the porphyrin molecule has a lateral size of 1.25 nm. In the STM experiment on HOPG/TPP samples, Bussetti and coworkers [250] have found an intermolecular distance of 1.65 nm. This value could be explained as the superposition of the porphyrin diameter and of an additional Van Der Waals repulsion distance. For such value, the amplitude of the shift would be of -20 meV. If the Van Der Waals additional distance is reduced to zero (r=1.25 nm), the energy shift is of -45 meV. This could correspond to two molecules touching each other with interacting phenyls groups.

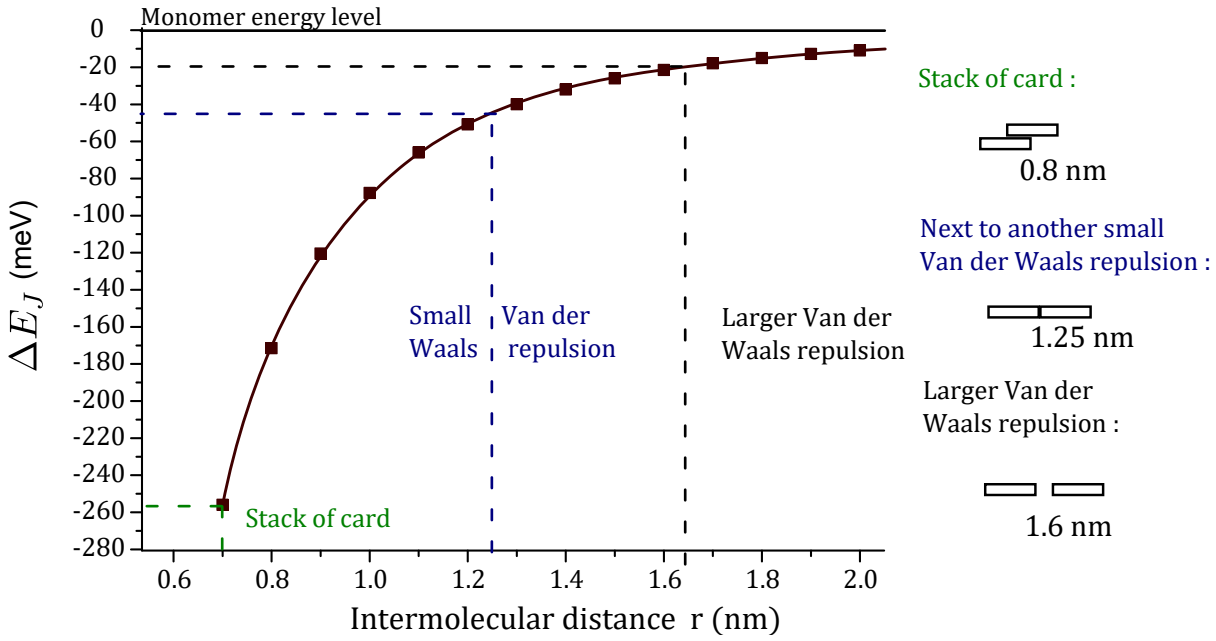

Figure IV.21: Simulation of the dipole coupling within an in-line porphyrin dimer, as a function of the porphyrins distance.

Finally, when hydrosoluble porphyrins are placed in a very acidic environment, they are able to form a stack of card structure (see figure IV.21). In this structure, the intermolecular distance can be smaller than the porphyrin diameter (as short as 0.7 nm), leading to energy shifts as large as $\simeq$-250 meV in a dimer. This study shows that the spectral magnitude induced by a dipole-dipole coupling can vary from tens of meV to hundreds of meV when the distance varies. These results can be easily transferred to the parallel case (H dimer), by multiplying all the value from figure IV.21 by a factor -0.5, according to the formula IV.4.

On a second hand, one can evaluate the progressive shift when the number of coupled molecules is larger than 2. Here, the distance has been kept to 1.4 nm and the angle to $\theta = 0$. The results from the equation IV.14 can be directly used. In figure IV.22, one can observe that both shifts gets larger as a function of N, with the asymptotic value of $2\Delta E$ (respectively -64 meV and +32 meV).

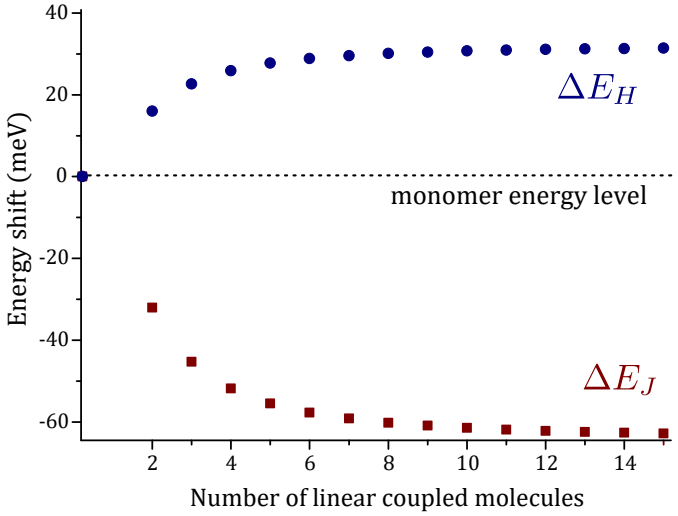

Figure IV.22: Evolution of the energy red and blue shifts as a function of the number of coupled monomers of porphyrins.

Now, that the model and the corresponding orders of magnitudes are obtained, one may confront them to the hypothesis of alignment of the porphyrins along the nanotube axis. In particular, an assumption has to be made regarding the orientation of the μ_y and μ_x with respect to the nanotube axis.

In the previous sections, the energy splitting between the two components of the Soret band was proved to be larger in the Nt/TPP samples than for the isolated TPP. In this discussion, it has been suggested to assume that every porphyrin molecules will align its μ_x dipole to the nanotube axis (see figure IV.23), with a negative coupling ΔE_J. Consequently, the μ_y dipoles will be orthogonal to the nanotube direction, with a positive coupling ΔE_H. This configuration would lead to a larger splitting, while any other situation would induce a smaller (or identical) energy difference. Nevertheless, the angle θ that is taken to zero in the figure IV.23, may vary slightly around this position without changing the mean result.

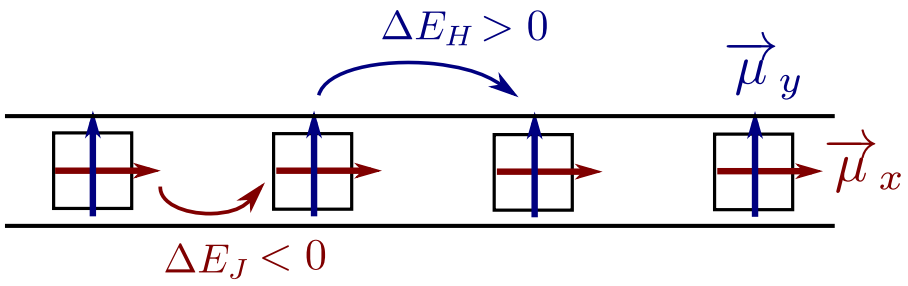

Figure IV.23: Schematic of an array of porphyrins at the surface of a carbon nanotube, with their B_x dipoles aligned to the nanotube axis.

In this configuration, the figure IV.24 displays the evolution of the two allowed transitions energies E_J and E_H, as a function of the number of coupled porphyrins for an intermolecular distance of 1.4 nm. In the isolated molecules, the energy splitting has been shown previously to be of 110 meV. For the dimer case, it is of $E_H - E_J = 158$ meV, with $E_J = 2.828$ eV and $E_H = 2.986$ eV. When an infinite number or porphyrins are coupled, this splitting reaches 200 meV, with $E_J = 2.799$ eV and $E_H = 3.002$ eV. One can observe that the order of magnitude of the obtained splittings is similar to the experimental values obtained with the polarized PLE study on NT/porphyrin complexes (170 meV).

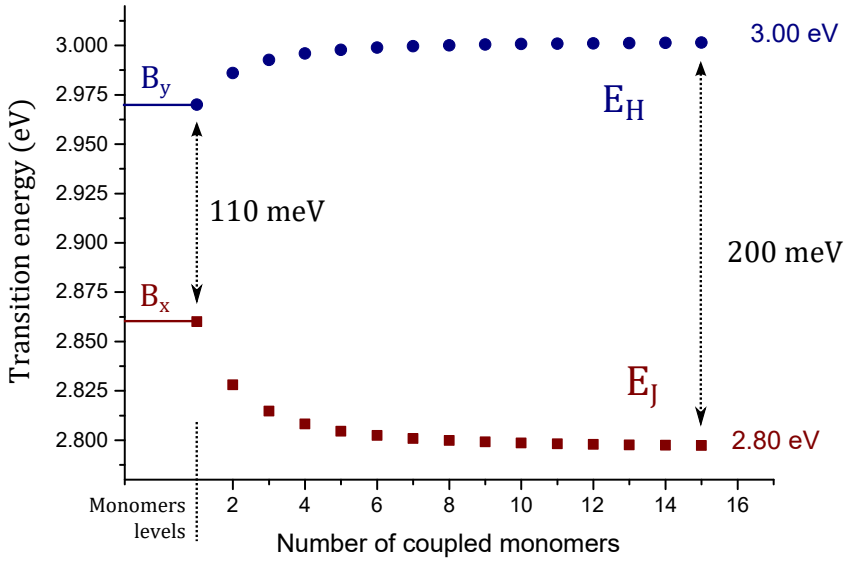

Figure IV.24: Evolution of the transition energy of the low energy E_J and the high energy E_H band as a function of the number of coupled porphyrin monomers. Only the allowed transitions are displayed in this graph.

As a conclusion, the dipole dipole coupling model for a linear chain of TPP is able to explain the amplification of the Soret energy splitting for Nt/TPP samples. However, this model should be modified to adapt to more realistic structures than the linear chain.

3 Possible organization of TPP around a nanotube

3.1 Geometrical characteristics from theoretical studies

To go further in the modeling of TPP aggregates around carbon nanotubes, articles in the literature can help to determine the most stable structures. Two independent studies have modeled the organization of tetraphenyl porphyrins on carbon nanotubes.

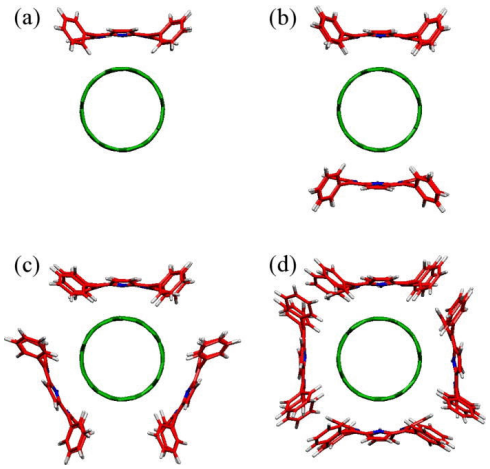

Figure IV.25: Front view of tetraphenylporphyrin molecules π-stacked on the (6,5) CNT surface in the equilibrium geometry. (a) (6,5)-1TPP, (b) (6,5)-2TPP, (c) (6,5)-3TPP, and (d) (6,5)-4TPP, from [233].

The first one has been already mentioned in the precedent chapter: the DFT model from Orellana [233]. It evidenced the organization of TPP molecules into 4 monomers rings at the surface of the nanotubes (see figure IV.25). It also predicted that the progressive coverage of the whole nanotube would occur through the interaction between these rings of porphyrins. These processes can lead to two favorable porphyrin superstructures: one where every TPP rings are aligned and one where the neighbor rings are tilted of a small angle. In the following, theses two structures will be referred as the ring and the spiral structures respectively.

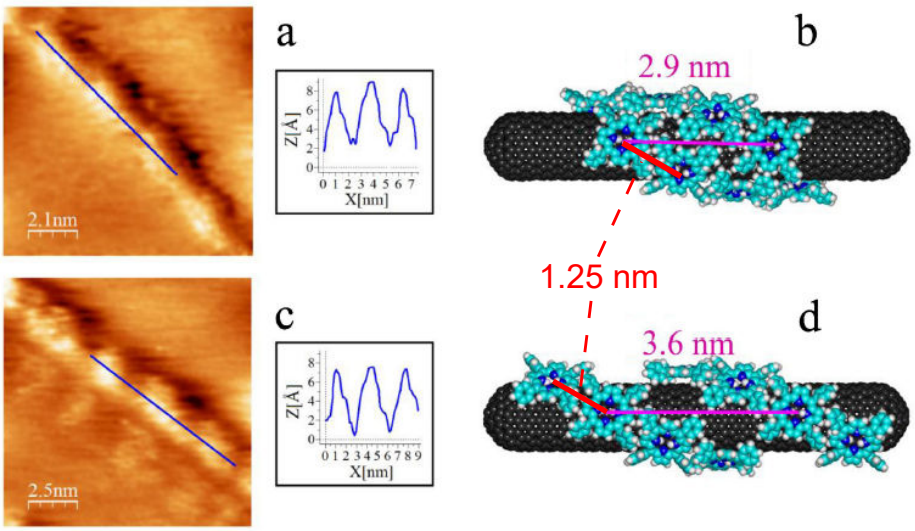

Figure IV.26: (a) and (c) STM topographic images of porphyrins on deposited carbon nanotubes; (b) and (d) The corresponding two geometries that allow to minimize the global system energy with molecular mechanic simulations, from [261].

On the other hand, Bassiouk and coworkers [261], used a molecular mechanic simulation to study the stacking of TPP on nanotubes. They showed that the most favorable configuration was the creation of spirals of porphyrin with intermolecular distances of 1.25 nm (see figure IV.26 right) between neighbor molecules and a distance of 2.9/3.6 nm between the two different rows of molecules. They confronted these calculations with STM measurements, where they were able to see the inter-row distance of 2.9/3.6 nm.

These two articles predict the creation of spirals of porphyrins. However, these two spirals structures start with different base elements. The former begins with the creation of 4 TPP rings, orthogonally to the nanotube axis. The latter is initiated by the coupling of porphyrins along the nanotube axis, while the interaction between porphyrin is very small orthogonally to the nanotube axis (see for instance figure IV.26 d). As it will be explained in the following model, this will have important consequences in the dipole-dipole coupling, and can be used to determine the actual organization in Nt/TPP samples.

3.2 Testing the ring structure on nanotubes

It is now possible to test the geometrical structures that have been suggested by the two theoretical contributions [233, 261]. In the two suggested structures, one can observe that the stable orientation of the TPP are practically the same (see figures IV.25 and IV.26). In each case, the phenyls of the TPP are at $\simeq 45°$ from

the nanotube axis, which means that the O_x (or O_y) direction of the TPP is aligned with the nanotube axis (see figure IV.27 a and b). As it was explained in the linear chain case, the only situation that would provide an amplified Soret splitting is when every TPP has its O_x direction along the nanotube axis. Consequently, only this configuration (see figure IV.27 b) will be studied in this section.

Interestingly, Basiouk *et al.* [261] choose to display this exact orientation in their spiral representation (without mentioning whether this is a consequence of their model or simply an artistic view). Indeed, one can observe that the white hydrogens spheres in each blue macrocycle are placed toward the nanotube axis in figure IV.26.

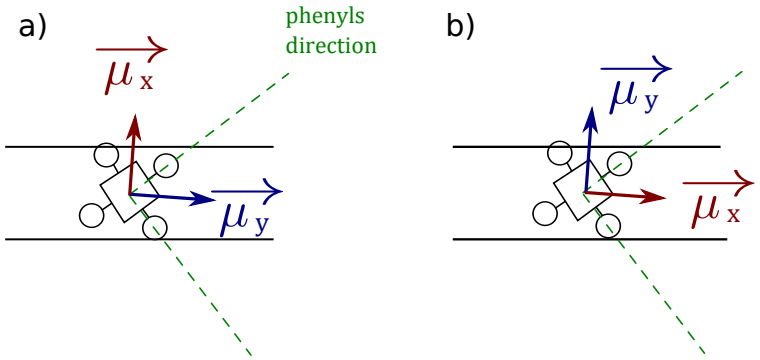

Figure IV.27: Schematic of the two possible orientations of a TPP with its two phenyls at 45° from the nanotube axis, adapted from the examples from [233, 261].

One can start with the ring structure from Orellana's work. For this purpose, the formalism of the previous section will be adapted as detailed on figure IV.28 and figure IV.29. For clarity, a number is assigned to each considered dipole μ_x and μ_y. The dipoles of the first ring are called μ_1, μ_2, μ_3 and μ_4, while the ones of the second ring will have a number between 5 and 8 (see figure IV.28).

Every TPP is placed at a distance of 0.3 nm from the carbon surface. The nanotube itself has a radius of 0.4 nm. According to the diagram IV.28 a), the distance between the two adjacent porphyrins is of 1 nm. This is significantly smaller than the intermolecular distance along the nanotube axis (1.4 nm, see figure IV.28c). As before, it will be assumed that the μ_x dipole of each porphyrin is aligned with the nanotube axis (see figure IV.29), while the μ_y one is orthogonal.

The situation of the μ_y dipoles can be considered first. Within the ring structure, one can observe that the two neighboring dipoles will be orthogonal to each other (as $\mu_{y,1}$ and $\mu_{y,2}$ in figure IV.28 b). Thus, they cannot be coupled to each other and would not be involved in the spectral shifts.

One can also consider the coupling between two dipoles at each side of the tube (see figure IV.28 b, between the $\mu_{y,i}$ and the $\mu_{y,i+2}$ dipoles). These two dipoles will be separated by 1.4 nm and will have a H coupling. Such coupling will create a blueshift of $\Delta E_H = +16$ meV of the B_y state. When the number of attached rings will increase, this effect will be constant as it only couples two molecules.

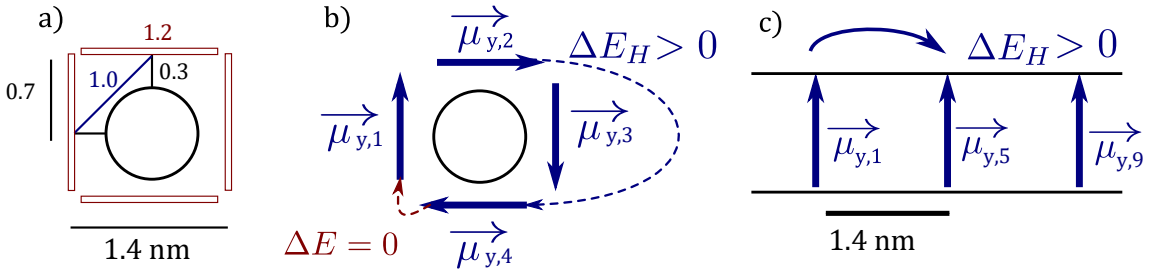

Figure IV.28: a) The ring geometry of 4 TPP around a (6,5) nanotube; b) The four orthogonal μ_y dipoles in the TPP rings; c) The array of μ_y dipoles along the nanotubes axis.

Then, the B_y states can be coupled along the nanotube axis (see figure IV.28 c, for the $\mu_{y,i}$ and the $\mu_{y,i+4}$ dipoles). This situation is identical to the linear chain of dipoles that has been studied earlier. There, the coupling will be different when the number of rings will change. Once again, it will lead to a blueshift, ranging from $\Delta E_H = +16$ meV to $2\Delta E_H = +32$ meV, respectively for 2 and N rings of TPP. For the B_y states, the result of these two blueshift effects are displayed in figure IV.30 (blue curve) and will be commented later.

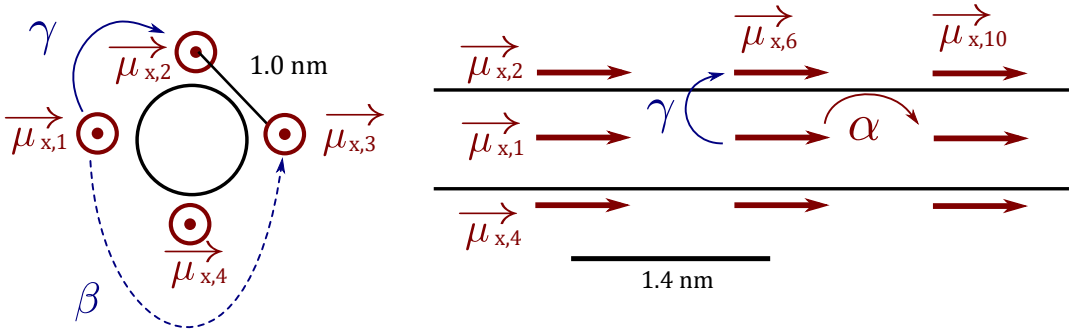

Figure IV.29: Left: The ring geometry with the four parallel μ_x dipoles in the TPP rings; Right: The array of μ_x dipoles along the nanotubes axis.

For the μ_x dipoles, the situation is more complex, as three kinds of interaction have to be considered. On the one hand, there are two kinds of parallel H coupling between the TPP of the same ring (see figure IV.29 left).

The first one is the coupling between the two first neighbors inside the ring, $\mu_{x,i}$ and the $\mu_{x,i+1}$. The energy shift ΔE associated to this coupling will be called γ for clarity. Since the intermolecular distance is here of around 1 nm, its value will be of $\gamma = +45$ meV.

On the second hand, one has to consider the dipoles at each side of the tube (between the $\mu_{x,i}$ and the $\mu_{x,i+2}$ dipoles). As for the μ_y case, it will lead to a H coupling with $\Delta E = +16$ meV. This coupling term will be here named β.

Finally, there is the classical in-line J coupling along the nanotube axis (see figure IV.29 right). As it was shown before, it will lead to a ΔE energy shift of -32 meV, here called α. Thus, every μ_x dipole can be coupled to five others, two along the nanotube axis and three within a TPP ring. The coupling matrix derived from this discussion is:

$$\begin{array}{c} \\ \phi_1 \\ \phi_2 \\ \phi_3 \\ \phi_4 \\ \phi_5 \\ \vdots \\ \phi_N \end{array} \begin{array}{c} \begin{array}{ccccccc} \phi_1 & \phi_2 & \phi_3 & \phi_4 & \phi_5 & \cdots & \phi_N \end{array} \\ \begin{pmatrix} E_x & \gamma & \beta & \gamma & \alpha & \cdots & 0 \\ \gamma & E_x & \gamma & \beta & 0 & \dots & 0 \\ \beta & \gamma & E_x & \gamma & 0 & \dots & 0 \\ \gamma & \beta & \gamma & E_x & 0 & \dots & 0 \\ \alpha & 0 & 0 & 0 & E_x & \dots & 0 \\ \vdots & \vdots & \vdots & \vdots & \vdots & \ddots & \vdots \\ 0 & 0 & 0 & 0 & 0 & \dots & E_x \end{pmatrix} \end{array} \tag{IV.20}$$

The evolution of the energy positions of the two bands (low and high energy) as a function of the number of coupled rings is displayed in figure IV.30. As expected, the high energy band (blue curve) is progressively moved to the higher energies, from 2.97 eV for a monomer to 3.018 eV for 4 rings and for longer aggregates (asymptotic value).

The evolution of the low energy band is more complex. Within a single ring, every μ_x dipole is coupled to the three other ones through a positive H term (γ or β), while there is no in-line coupling. This moves the energy position towards the higher energies to 2.96 eV. When several rings are axially coupled, the parallel coupling within the rings does not change.

However, the in-line coupling takes place, and gets larger with the number of rings. Nevertheless, since α is significantly smaller than γ, the amplitude of this J effect is not enough to fully compensate the H coupling. For an infinite number of rings, the final position of the low energy band will be of 2.90 eV, which is +40 meV above the initial value.

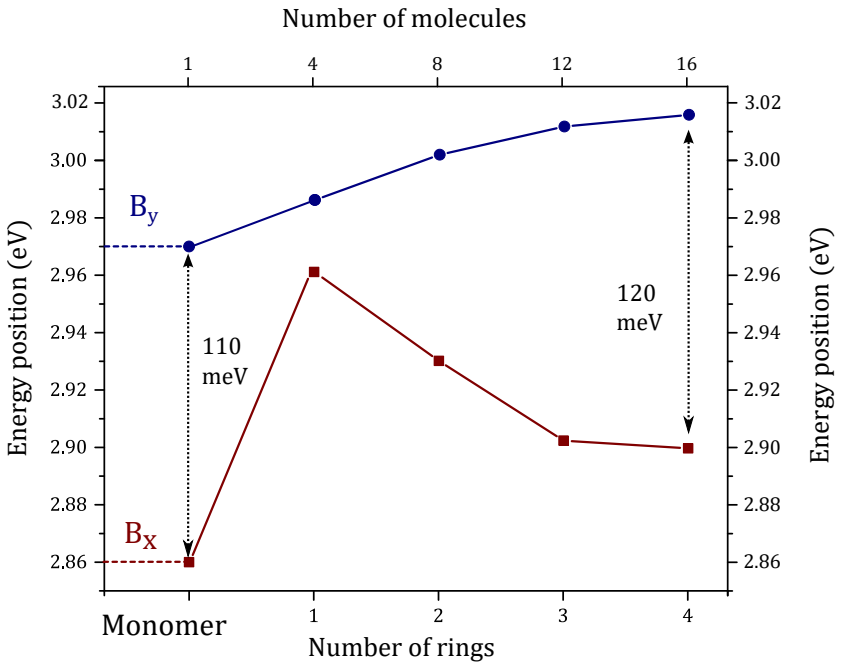

Figure IV.30: Effect of the ring geometry: Evolution of the transition energy of the low energy and the high energy band as a function of the number of rings of porphyrins (or of coupled porphyrin monomers).

Whatever the number of rings, the energy splitting between the two bands is never larger than 120 meV. Thus, this ring structure has an insignificant effect on the B_x/B_y splitting, that is originally of 110 meV. Moreover, the two Soret components are blueshifted in the process, which is not consistent with the experimental results. This effect comes from the strong H coupling of the dipoles inside the ring structure. As a conclusion, this ring structure does not reflect the experimental results: it cannot explain the shifts and the band splittings from the PLE experiments.

3.3 Testing the helix structure

The spiral structure can now be considered. It is simply an adaptation of the linear array geometry that has been studied before. From the model developed by Basiouk and coworkers [261], the angle θ of the spiral can be taken to 26°. Once again, the intermolecular distance will be taken to 1.4 nm. It will be assumed that the μ_x dipoles are still aligned towards the nanotube axis, while the μ_y ones are orthogonal. From the B_x transition, this will provide an energy shift of ΔE_J=-22.5 meV, while the corresponding shift will be of ΔE_H=+6.7 meV for the B_y transition. Both values are smaller than for the perfect in-line array with $\theta = 0$, due to the factor $(1 - 3\cos^2(\theta))$.

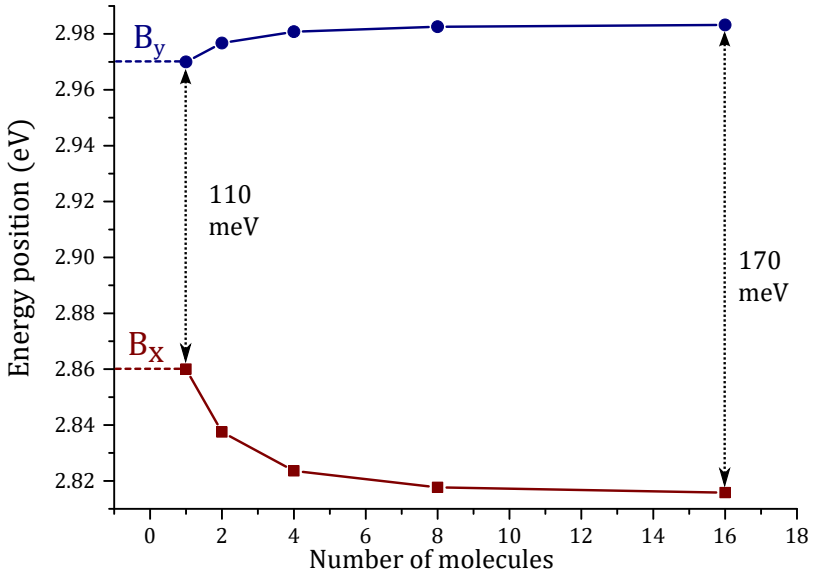

Figure IV.31: Effect of the spiral geometry: Evolution of the transition energy of the low energy and the high energy band as a function of the number of porphyrins in the spiral.

The evolution of the two energy bands for an increasing number of coupled monomers is displayed in figure IV.31. The high energy band is moved from 2.97 eV to 2.983 eV, between one and an infinite number of coupled μ_y dipoles. The low energy band starts at 2.86 eV and ends at 2.815 eV. Thus, this geometry provides a maximal band splitting of 170 meV for a very large number of coupled dipoles.

As a conclusion, this spiral structure, which is only a variation of the linear chain model, is compatible with the experimental results from the PLE experiments. In this configuration, both the splitting and the energy positions obtained for the H and J bands are in agreement with the experimental results on Nt/TPP structures. Additional experiments (such as STM) would be required to confirm this geometry. Nevertheless, this discussion shows that the dipole-dipole coupling model is a valuable tool to explain the amplification of the energy splitting of the Soret band in Nt/TPP complexes.

3.4 Effect of the nanotube on the organized porphyrins

Local field effect

Until now, this chapter has discussed about spectroscopic effects in NT/TPP compounds from the molecule's point of view. It has been evidenced that the dipole-dipole coupling model and the spiral geometry were able to explain the amplified energy splitting and the energy positions of the Soret components. However, the

nanotube has only been seen as a geometrical pattern and very little detail has been given on its physical influence.

In the polarized PLE experiments on the Nt/TPP compounds, it has been evidenced that the high energy Soret resonance (extracted from the $I_\perp$ intensity) has a much smaller amplitude than the low energy component (from $I_\parallel$). This result was in contrast with the situation in isolated TPP, where the B_x and the B_y transitions have a similar amplitude (see figure IV.34). This section will be dedicated to explain this effect, in connection with the electromagnetic influence of the nanotube.

First, it is important to understand how a carbon nanotube interacts with an incoming light beam. In such situation, a local field effect is created. This is one consequence of the antenna effect due to the 1D geometry of the nanotube. In presence of an incoming electric field $\overrightarrow{E_0}$, the nanotube will generate an additional electromagnetic contribution, called the depolarizing field. This will modify the amplitude of the global electric field $\overrightarrow{E}$ that will interact with the porphyrins at the surface of the nanotube. These effects have been well explained in previous doctoral manuscripts and a paper in the group [108, 118, 168].

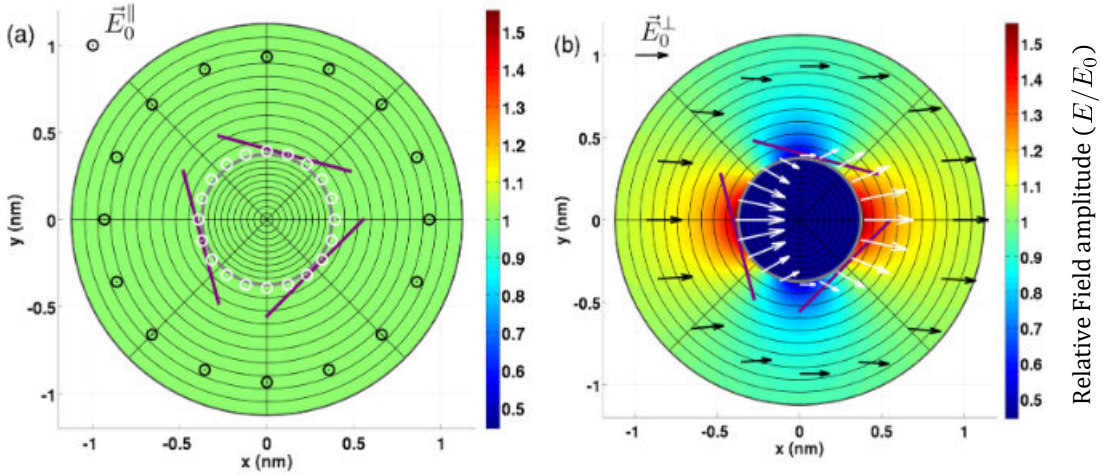

Figure IV.32: Left: Local electric field amplitude in the vicinity of a nanotube for an incoming field parallel to the tube axis calculated from the electromagnetic model; Right: Local electric field amplitude in the vicinity of a nanotube for a perpendicular incoming field. The diameter d has been taken to 0.75 nm. The arrows represent the electric field (amplitude and direction) on the outer tube surface (1.05 d/2, white arrows) and for a distance of 2.5 d/2 (black arrows). The field amplitude is in units of the incident field E_0 , from [118].

Through a simple electromagnetic model, the amplitude of the resulting field can be calculated as a function of the field orientation. When the electric field is aligned with the nanotube axis, the resulting field has an unchanged amplitude $E = E_0$ (see figure IV.32 left). This means that the effect of the nanotube on the electric field is negligible in this configuration.

On the other hand, when the field is perpendicular to the tube axis, its amplitude E depends strongly on the spatial coordinates (see figure IV.32 right). As a consequence, porphyrins that are placed at different locations will not interact with the same electromagnetic field. If the porphyrin is placed across the electric field direction (see figure IV.33 left), the electric field will have a larger amplitude than E_0. However in this configuration, the electric field is perpendicular to the porphyrin plane, which results in a zero absorption of incident photons by the porphyrin. Indeed, the out of plane porphyrin dipole moment is zero on the Soret and the Q bands.

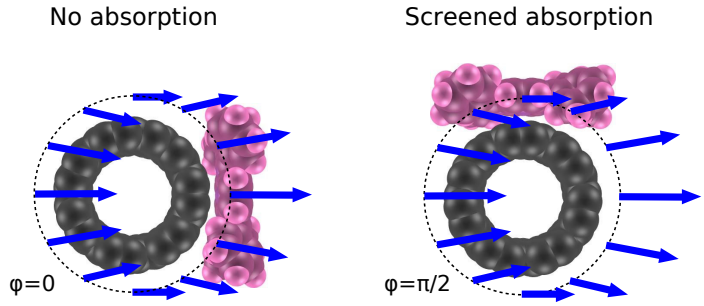

Figure IV.33: Artistic views of two possible positions of the porphyrin around the tube, in regard of the electric field axis, from [108].

If the porphyrin is placed at 90° from the field direction (see figure IV.33 right), it will interact with a screened electric field. At the very surface of the nanotube, the resulting field has an amplitude of 0.5 E_0 (and a square of the electric field norm $|E|^2=0.25|E_0|^2$).

As a conclusion, the effect of the nanotube will decrease the number of photons absorbed when the incident light is polarized perpendicular to the nanotube axis. At the opposite, it has been shown that the effect of the nanotube was negligible when the light was polarized along the nanotube axis. This study shows that local field corrections (or antenna effects) are essential in understanding the optical properties of the hybrid nanocompounds. In particular, the large polarizability at optical frequencies of the carbon nanotube allows to reshape drastically the absorption of the porphyrin (see figure IV.34).

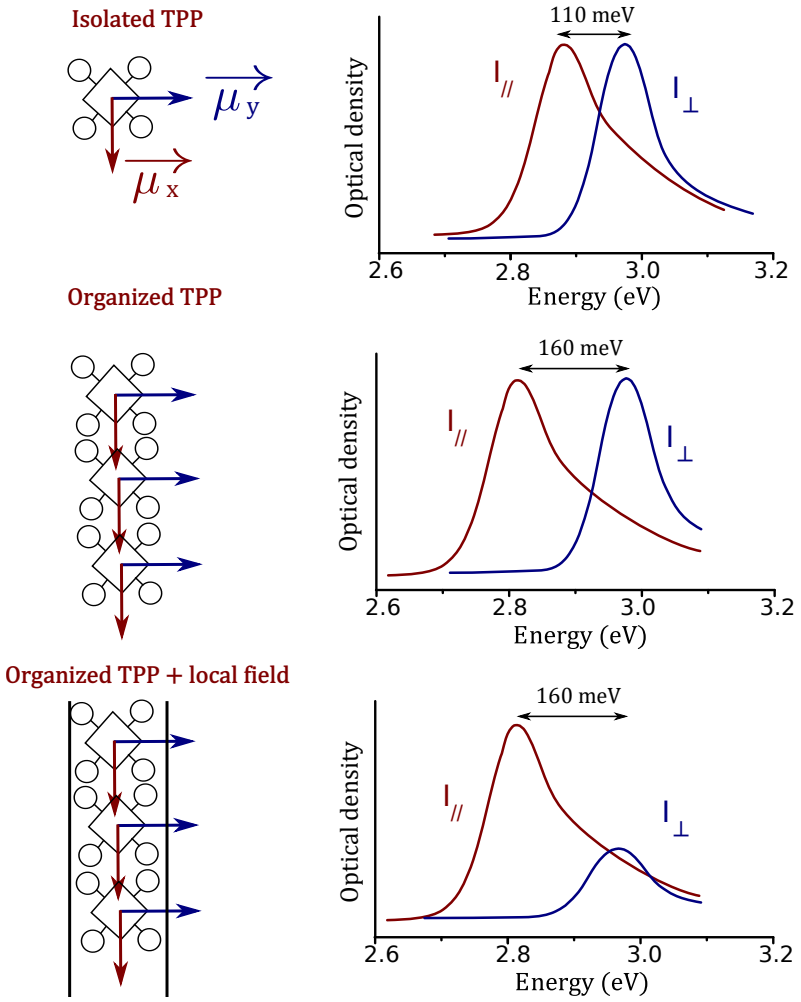

Figure IV.34: Schematic view of the influence of the nanotube local field effect on the Soret components of organized porphyrins in NT/TPP compounds.

Consequently, the local field effect is able to explain why the experimental high energy transition has a smaller intensity than the predicted one. From a simple electromagnetic calculation, the absorption intensity of a given transition can be proved to be proportional to the square of the interacting electric field norm. Therefore, one can observe that the local field effect would lead to a decrease of a factor four of the intensity of the transitions perpendicular to the nanotube axis. One can see this local field effect can quantitatively explain the decrease of a factor four of the amplitude of the high energy band (see figure IV.34).

Tautomerism blockade on surfaces

One aspect that has been neglected until now is the movement of the inner hydrogens atoms within the porphyrin. The structure of the porphyrin is quasi-isotropic, as it nearly possesses a four-fold symmetry. The only source of assymetry in such structure is the presence of the two central hydrogens. Consequently, these hydrogens have two symmetrical equilibrium positions. In a quantum characteristic behavior, these hydrogens are able to jump from one position to another, following a tautomerism process [262] with a fast rate of 10^{11} s^{-1}. This process can be seen as constant tunneling movement of the two protons from its respective pyrolle position to the neighbor one.

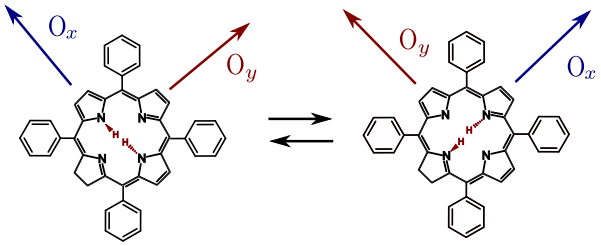

Figure IV.35: Representation of the tautomerism process.

This process has an important influence on the spectroscopy of the molecule. From the previous discussion, it has been assumed that every porphyrin would have its O_x direction toward the nanotube axis, its O_y direction being orthogonal. However, one should not neglect the tautomerism effect: the Ox and Oy axes are supposed to be constantly switching from one position to the other. Thus, even if one porphyrin has its B_x component along the nanotube axis at the moment t, it would in principle be replaced by the B_y component after the instant $t+\tau$, where τ is the switching characteristic time. Experimentally, the PLE signal would be integrated over a large number of porphyrins and over a time much larger than τ. Therefore, the spectroscopic splitting between the two energy Soret bands B_y and B_x could not be observable in polarized PLE experiments in Nt/TPP samples. Indeed, the measured signal would be the superimposition of the two situations, leading to an averaged signal with an anisotropy close to zero.

The only possibility for this spectroscopic splitting to persist is if the tautomerism effect is quenched. In other words, an additional physical effect may prevent the hydrogen from tunnelling between the two stable positions. Usually, such effects only exist at very low temperature [263], when the hydrogens do no have a sufficient energy pass through the energetic barrier. For instance, Pham and coworkers were able to observe stable tautomers of the TPP by STM experiments at very low temperature [100]. However, there are several examples in the literature of tautomerism blockade at higher temperature, especially if the molecules are in interaction with a surface.

One of these examples is the study presented earlier on a TPP monolayer on a HOPG substrate (see figure IV.36, [249]). In addition to STM measurements, the authors performed a polarized reflectometry experiment, to probe the Soret band of the adsorbed TPP. They showed that the B_x component (respectively the B_y) of every TPP were constantly aligned along the same graphitic direction (named either α or β in figure IV.36). Using an electromagnetic semi-empiric approach, they were able to extract the two spectroscopic components of the Soret band B_x and B_y (see figure IV.36 right bottom).

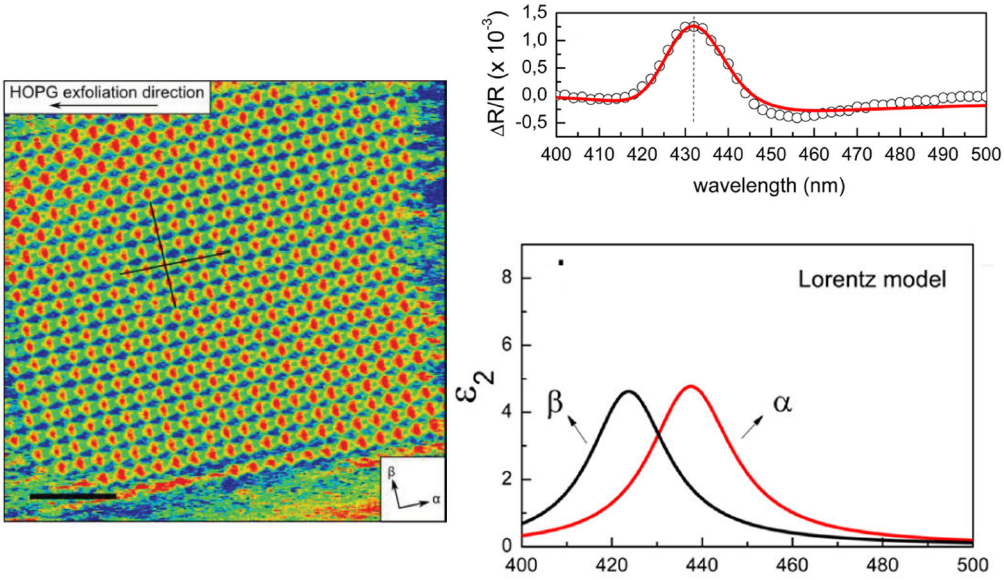

Figure IV.36: Left: Structure of a H_2TPP 2D domain on HOPG on a 36 nm x 36 nm STM image showing the arrangement of molecules in a square unit cell. The HOPG exfoliation direction is also indicated. The reported scale bar (bottom left) is 7 nm-long, from (ref); Right top: Experimental reflectance anisotropy spectroscopy spectrum of a pure 2D porphyrin layer obtained from a thin film, Right bottom: ε_2 dielectric coefficient corresponding to the two best fit Lorentz oscillators from the reflectance data, from [249].

These measurements were only possible due to an anisotropy of reflectance ΔR along the two axes α and β. They attributed this anisotropy to a tautomerism blockade induced by the graphite surface.

If such hydrogen blockade occurs on graphite at room temperature, it may also be present on graphene and on carbon nanotubes. In the case of the nanotube, it would mean that the two hydrogens are fixed in the direction of the nanotube axis, as if this position were more stable. If the reason of this effect is unknown, it would

explain why an energy splitting and a non-zero anisotropy is visible in the Nt/TPP samples.

4 Organization in other configurations

In the previous section, the combination of a dipole-dipole interaction and a local field effect were able to explain every features of the porphyrins spectroscopy in the Nt/TPP compounds. In this section, this dipole interaction model will be confronted to experimental results in two other situations. The first one will be the adsorption of TPP on graphene nanosheets. The second one will be the adsorption of diphenyl-porphyrins on carbon nanotubes.

4.1 Absorption characteristics of the porphyrin on carbon nanotubes and graphene

Due to the absence of a luminescence process from the graphene sheets, the polarized PLE experiments presented before cannot be used in this part. Therefore, only the absorption spectra of the graphene/TPP samples will be compared to the dipole-dipole interaction model.

At the beginning of this chapter, the absorption spectrum of a graphene/TPP sample has been compared to the one of a Nt/TPP samples. It was shown that the energy position of the Soret band of the π-stacked TPP was different in the two samples. At the end of the stacking process, the Soret peak of the porphyrins interacting with graphene was located at 2.79 eV, while it was only at 2.82/2.83 eV for Nt/TPP samples.

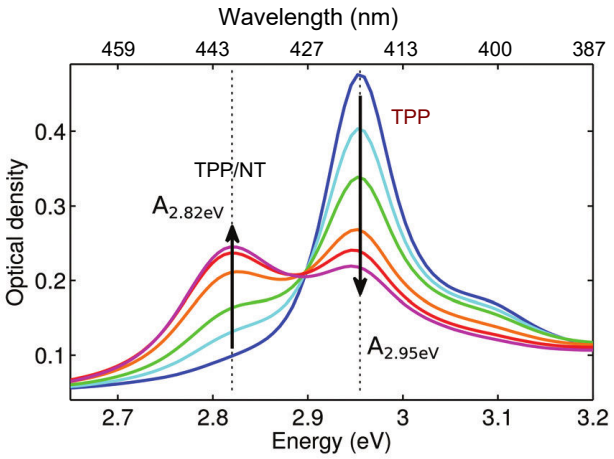

Figure IV.37: Evolution of the optical density of the Nt/TPP samples in the Soret region as a function of time after mixing the NT and the TPP suspension in cholate, from [189].

Another interesting difference between carbon nanotubes and graphene lies in the evolution of the redshifted Soret component during the functionalization process. As mentioned in the chapter II, an isosbestic process is taking place for the case of the Nt/TPP compounds. As seen in figure IV.37, the amplitude of the π-stacked porphyrins resonance is growing as a function of time. Yet, its position in energy remains practically the same during the process (though a multi-gaussian fitting process could evidence small differences). This isosbestic effect indicates that the porphyrins can only be in two states: either they are free in the solution or π-stacked at the nanotube surface.

The behavior is more complex for graphene/TPP samples. In figure IV.38, the evolution of the optical spectrum is displayed as a function of time for a porphyrin concentration of 8 μmol.L^{-1}. When the shifted Soret component appears after a few minutes, it is around 2.85-2.83 eV. Then, it undergoes a progressive additional redshift, to finally reach a value of 2.78 eV. Once again, a complex fitting process should be required to point out the exact center of the π-stacked porphyrin resonances. Nevertheless, this behavior is clearly not isosbestic: an additional redshift seems to occur once the porphyrin coverage on the graphene surface begins to be significant.

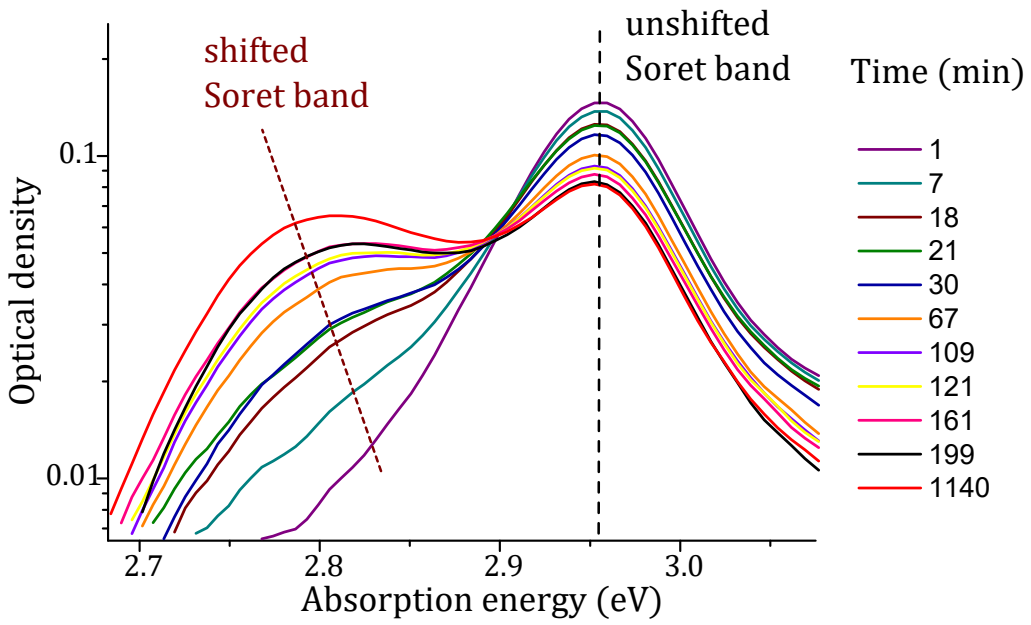

Figure IV.38: Evolution of the optical density of the graphene/TPP samples in the Soret region as a function of time after mixing for a porphyrin concentration of 8 μmol.L^{-1} in cholate.

Such an effect on graphene is even more visible by looking at samples contain-

ing different porphyrin concentrations. Figure IV.39 displays the absorption at the equilibrium state of samples containing TPP in concentrations between 1 and 25 μmol.L^{-1}. Once again, the progressive transition of the redshifted band between 2.83 and 2.77 eV is observed as the TPP concentration increases.

On the other hand, the absorption of the π-stacked Soret band for Nt/TPP samples was also studied upon an increase of the concentration of interacting porphyrins [168]. The position of the shifted Soret band was there independent of the quantity of porphyrins interacting with the nanotube.

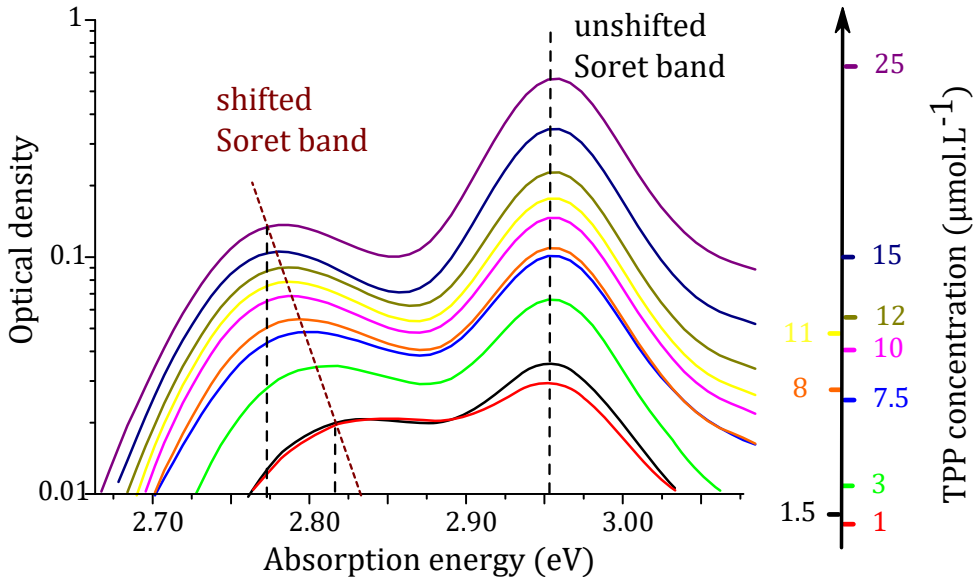

Figure IV.39: Evolution of the optical density once the equilibrium is reached for the graphene/TPP samples in the Soret region as a function of the total porphyrin concentration after mixing in cholate.

While the redshifts on nanotubes and graphene have comparable characteristics, there are significant differences between the two situations. In graphene/TPP samples, the redshift seems to be very sensitive to the molecular concentration. This behavior depends on the coverage proportion of the graphene surface by porphyrin molecules: it could be linked to the dipole-dipole coupling between the π-stacked porphyrins.

4.2 The organization of porphyrins on graphene

A monolayer of porphyrins

The next step would be to adapt the dipole-dipole coupling model to the graphene configuration, to see if the previous absorption behavior can be explained. The

geometry evidenced in STM by Pham *et al.* is good starting point for this model. The intermolecular distance r will be fixed to 1.4 nm and the tilt angle to $\theta = 10°$. To model the organization of porphyrins on graphene, it is easier to consider only squares or p×p=N porphyrins molecules. In the first line, the molecules will be tagged with a number from 1 to p, from p+1 to 2p for the second line... (see figure IV.40).

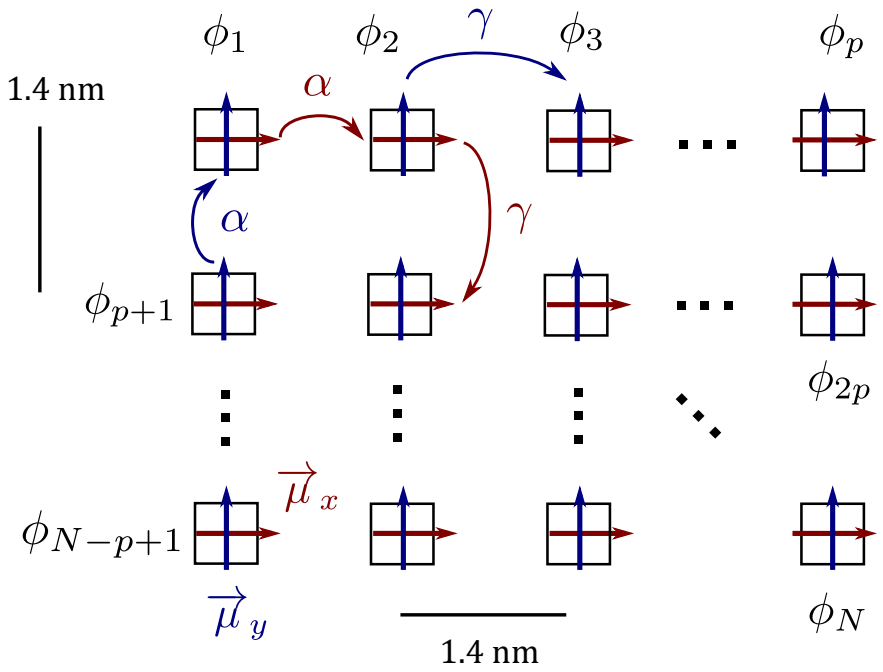

Figure IV.40: Representation of the square lattice of porphyrins on the graphene surface. In this schematic, the angle of $\theta = 10°$ has been omitted.

According to the formula IV.12, this will lead to two different terms of coupling. Between two in-line dipoles, the coupling term will be $\alpha = -30$ meV; while between two parallel dipoles, it will be of $\gamma = +14.4$ meV. Due to the planar symmetry, these two coupling terms apply both to the separate μ_x and μ_y lattices. For instance, it will lead to the following matrices when N=4 for the B_x and the B_y states:

$$M_x = \begin{array}{c} \\ \phi_1 \\ \phi_2 \\ \phi_3 \\ \phi_4 \end{array} \begin{array}{c} \begin{array}{cccc} \phi_1 & \phi_2 & \phi_3 & \phi_4 \end{array} \\ \begin{pmatrix} E_x & \alpha & \gamma & 0 \\ \alpha & E_x & 0 & \gamma \\ \gamma & 0 & E_x & \alpha \\ 0 & \gamma & \alpha & E_x \end{pmatrix} \end{array} \quad ; \quad M_y = \begin{array}{c} \\ \phi_1 \\ \phi_2 \\ \phi_3 \\ \phi_4 \end{array} \begin{array}{c} \begin{array}{cccc} \phi_1 & \phi_2 & \phi_3 & \phi_4 \end{array} \\ \begin{pmatrix} E_y & \gamma & \alpha & 0 \\ \gamma & E_y & 0 & \alpha \\ \alpha & 0 & E_y & \gamma \\ 0 & \alpha & \gamma & E_y \end{pmatrix} \end{array} \tag{IV.21}$$

Then, one can extract the eigenenergies and the corresponding dipole moments. As for the linear case, there is only one eigenstate having a significant dipole moment.

The evolution of the absorption lines positions when N increases is displayed in figure IV.41. Both bands undergo a redshift from -16 meV (for N=4) to -30 meV (for N=∞). For a very large number of molecules, the final energy positions are 2.83 and 2.94 eV, respectively for the low energy and the high energy band.

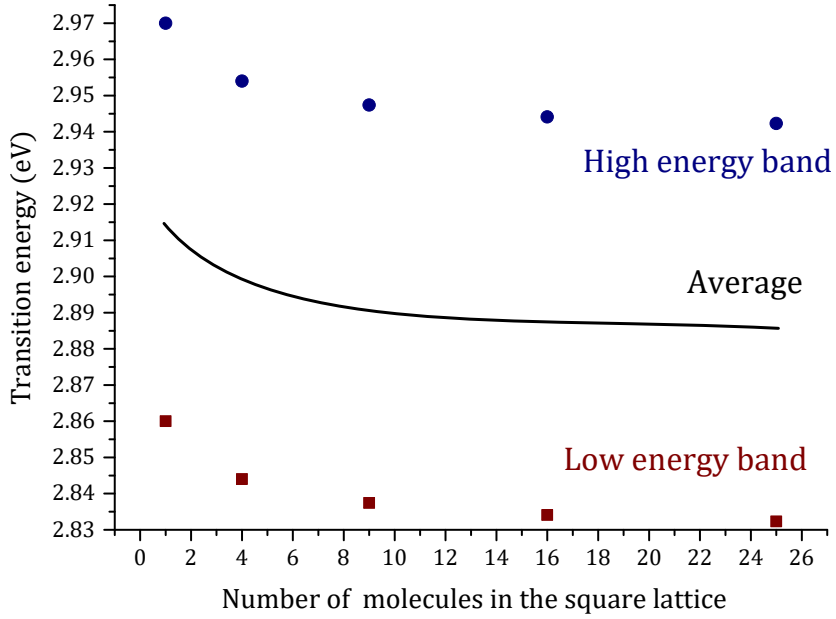

Figure IV.41: Evolution of the low energy and high energy bands within the graphene square lattice as a function of the number of coupled molecules.

Now, these figures can be compared to the Soret band of interacting porphyrins measured in optical absorption. In the previous results on graphene/TPP samples, the Soret band measured in absorption was centered at 2.82 eV at low TPP concentration, and moved to 2.79 eV at high porphyrins concentrations. In the present model, one can assume that the low energy and the high energy bands contribute equally to the optical absorption. Then the center of the band measured in absorption should theoretically be around the average of the two centers: $E_{\text{average}} = 0.5 \times (2.83 + 2.94) = 2.885$ eV (see figure IV.41). One can see that the experimental value is a 65 to 95 meV below the predicted center of the Soret band for graphene/TPP samples (that was of 2.79/2.78 eV).

This mismatch indicates that an additional physical phenomenon has to be taken into account. As graphene is a 2D flat surface, the contribution of the molecule flattening may be more important. Additionally, there is very little information about the effect of graphene regarding solvatochromism. When the porphyrins are at the surface of a graphene sheet, the induced redshift may be more important than for the nanotubes.

An example of porphyrins multilayers

At this point, it would valuable to look for the reason of this additional redshift in the literature. As it was shown before, this additional redshift was strongly dependent on the concentration of stacked porphyrins.

The work of Bussetti *et al.* on the stacking process of TPP molecules on HOPG has already been presented before [249]. A similar study from the same group [250] followed the evolution of the Soret band of TPP as a function of the amount of adsorbed molecules on the graphite surface (see figure IV.42). The authors used AFM images to probe the morphology of the sample after each adsorption process.

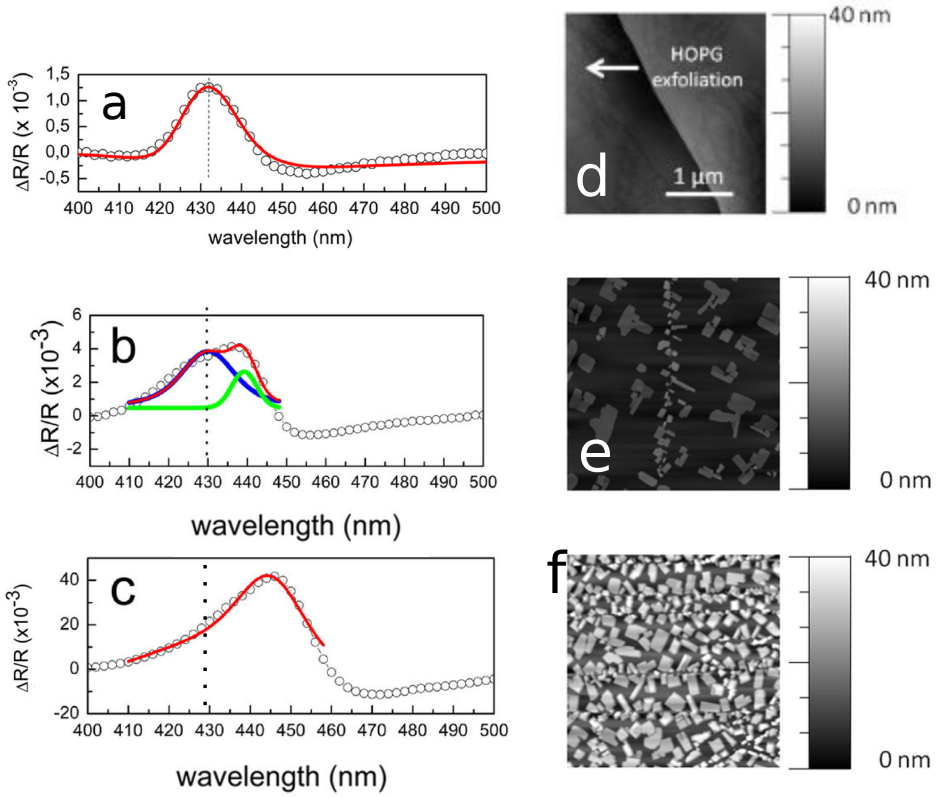

Figure IV.42: Left: Experimental polarized Reflectometry spectra of TPP thin films On a HOPG surface of (a) 0.05, (b) 1, and (c) 5 nm nominal porphyrin thickness; Right: The corresponding AFM images collected over 3×3 μm^2 wide regions.

In parallel to AFM experiments, they monitored the position of the maximum of the reflectance anisotropy, which lies in between the low energy and the high energy Soret band. For a monolayer of TPP (0.02 nm of thickness, figure IV.42 a. and d.), this center is as 430 nm (2.88 eV). This 2.88 eV value is very similar to the predicted

value from the previous dipoles coupling model. When the quantity of molecules is increased (until 5 nm of nominal thickness, figure IV.42 c. and f.), it progressively moves to 444 nm (2.79 eV). This last value is at the same position as the center of the Soret band that we measured in absorption for very concentrated graphene/TPP samples. When the authors performed AFM images of each of their samples, they observed the presence of large structures with an increasing size as a function of the amount of added porphyrins. These structures can cover up to 30 % of the surface, and are several times higher than the nominal thickness of the sample.

Interestingly, this proves the ability of the TPP to form very large, trimidimensional clusters, even on a flat template. Additional topographic experiments on graphene/TPP samples, such as AFM or STM, would allow to confirm such hypothesis.

Modeling the porphyrins multilayers on graphene

Nevertheless, the reason of this very large redshift when the porphyrins form the 3D aggregates is still unexplained. This effect can be the consequence of a very specific organization of the TPP multilayers. As seen in figure IV.43, one can imagine two possible organizations within a bilayer of TPP.

In the first one, the second layer of molecules would be placed vertically to the first layer. This would lead to positive dipole-dipole coupling and global blueshift of the B_x and the B_y bands. If one considers a small distance between the two layers ($\simeq$ 0.3/0.4 nm), the intensity of this blueshift can be of several hundreds of meV. Thus, this situation cannot reflect the experimental results.

On the other hand, a staggered structure is possible, in which the second layer is shifted in the two planar directions from the first (see figure IV.43). For instance, one can consider a situation in which the porphyrins of the second layers are shifted of 0.7 nm in both directions (while the intermolecular distance is of 1.4 nm). A TPP of the second layer would be placed in the middle of four TPP of the first layer. It would also lead to an angle between porphyrins of separate layers of around 45°. If one consider a distance of 0.4 nm between the two layers, it would lead to an intermolecular distance d of:

$$d = \sqrt{0.7^2 + 0.7^2 + 0.4^2} \simeq 1.1nm \tag{IV.22}$$

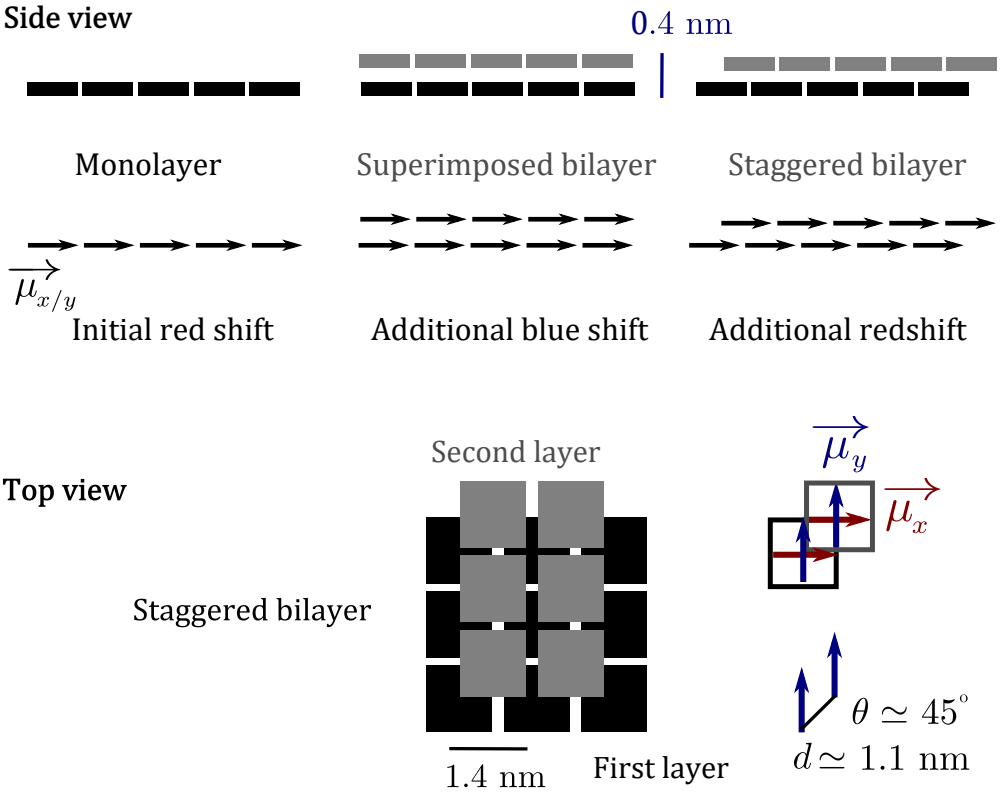

Figure IV.43: Possible organization of multilayers of porphyrins on a graphene/graphite surface.

In these conditions, the coupling term between two nearest neighbors of different layers would be of δ=-16 meV (both for the μ_x and for the μ_y dipoles). To estimate the effect of this bilayer structure, the example of two square layers of four TPP each can be taken. For only one of these square structures, the coupling matrix $M^{\text{monolayer}}$ was derived earlier (see the matrix IV.21). For the bilayer system, the corresponding matrix M_y^{bilayer} for the B_y band coupling, can be derived from $M_y^{\text{monolayer}}$:

$$M_y^{\text{bilayer}} = \begin{array}{c} \\ \text{Layer 1} \\ \text{Layer 2} \end{array} \begin{array}{c} \begin{array}{cc} \text{Layer 1} & \text{Layer 2} \end{array} \\ \begin{pmatrix} M_y^{\text{monolayer}} & \Delta^\dagger \\ \Delta & M_y^{\text{monolayer}} \end{pmatrix} \end{array} \tag{IV.23}$$

where Δ is 4×4 matrix that gathers the coupling terms δ between the two layers, and $\Delta^\dagger$ is the transpose of the matrix Δ.

The exact expression of the M_y^{bilayer} matrix is:

$$M_y^{\text{bilayer}} = \begin{array}{c} \\ \phi_1 \\ \phi_2 \\ \phi_3 \\ \phi_4 \\ \phi_5 \\ \phi_6 \\ \phi_7 \\ \phi_8 \end{array} \begin{array}{c} \begin{array}{cccccccc} \phi_1 & \phi_2 & \phi_3 & \phi_4 & \phi_5 & \phi_6 & \phi_7 & \phi_8 \end{array} \\ \begin{pmatrix} E_y & \gamma & \alpha & 0 & \delta & 0 & 0 & 0 \\ \gamma & E_y & 0 & \alpha & \delta & \delta & 0 & 0 \\ \alpha & 0 & E_y & \gamma & \delta & 0 & \delta & 0 \\ 0 & \alpha & \gamma & E_y & \delta & \delta & \delta & \delta \\ \delta & \delta & \delta & \delta & E_y & \gamma & \alpha & 0 \\ 0 & \delta & 0 & \delta & \gamma & E_y & 0 & \alpha \\ 0 & 0 & \delta & \delta & \alpha & 0 & E_y & \gamma \\ 0 & 0 & 0 & \delta & 0 & \alpha & \gamma & E_y \end{pmatrix} \end{array} \quad \text{(IV.24)}$$

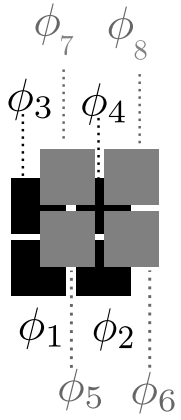

As usual, the diagonalization of this matrix provides only one eigenstate with a significant dipole norm. For the B_y band, its energy position is at 2.91 eV. For a single layer made of the 4×4 square lattice of four TPP, the diagonalization of $M_y^{\text{monolayer}}$ yielded a corresponding eigenenergy at 2.95 eV. Thus, the presence of a second layer on top of the first leads to a additional redshift of -40 meV. A similar result is found for the B_x band, proving that the two bands and the Soret center positions would be equally redshifted.

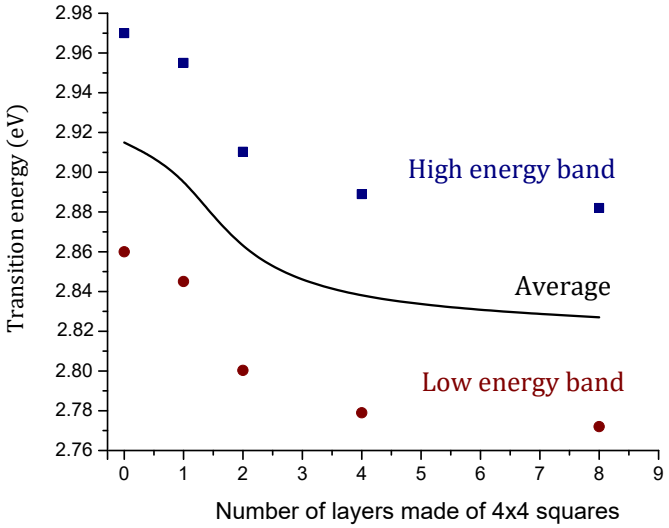

Figure IV.44: Evolution of the low energy and high energy band as a function of the number of layers, each one made of 4×4 square of TPP.

Then, the model can be easily adapted to several layers, each of them made of a 4×4 square of TPP. The energy positions found with this model are displayed

in figure IV.44, for a number of layers between 0 and 8. Both bands undergo a progressive redshift, that tends to saturate respectively at 2.88 eV and 2.77 eV. Thus, the additional redshift created by the multilayers structures saturates at -90 meV.

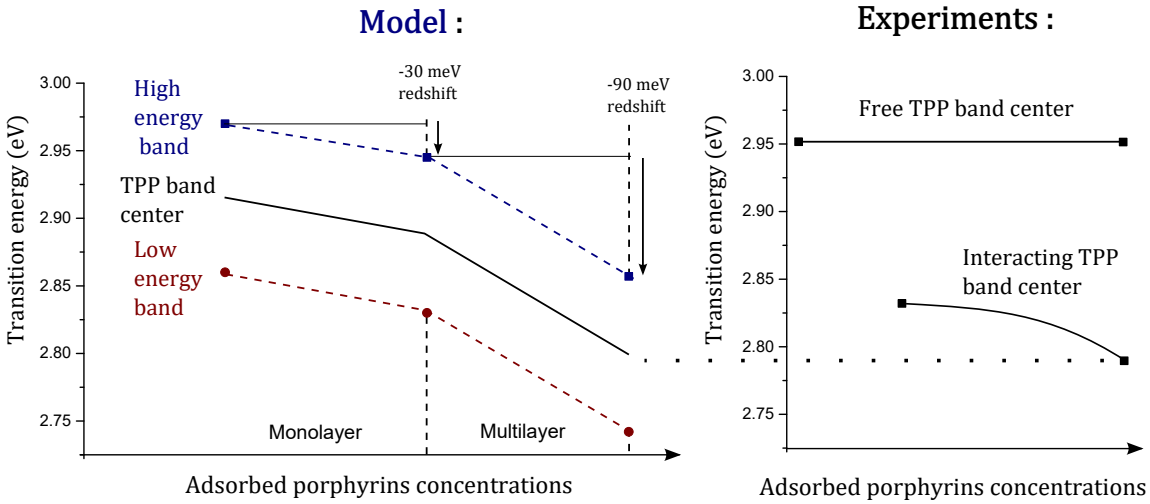

Figure IV.45: Comparison of the energy positions of the low and high energy bands from the multilayer dipole coupling model (Left) with the experimental center Soret positions found by optical absorption spectra (Right) for graphene/TPP samples. In the right panel, the black lines are not directly experimental curves. However, they are guides to the eyes that follow the tendency of the experimental results.

At this point of the discussion, the results from the mono/multilayer dipole coupling model have to be confronted with the absorption features from the experimental data (see figure IV.45). For a single 2D layer of porphyrin, the maximal shift of each component of the Soret band was of -30 meV. Then, through the multilayer process, an additional redshift of -90 meV is reached. When the two effects are combined, the center of the Soret band is predicted around 2.80 eV (see figure IV.45 left). This last value is very close to the position of 2.79 eV that was found by optical absorption for the Soret band in graphene/TPP samples with a large concentration of porphyrins.

As a conclusion, this multilayer hypothesis provides the good order of magnitude for the shift of the Soret band in graphene/TPP nano-assemblies. Moreover, the creation of a first monolayer and then of several multilayers would explain the non isosbestic behavior and the additional redshift effect. Once again, this discussion has proved that the organization of TPP on a carbon template could be understood thanks to a combination of optical spectroscopy, near field microscopy (STM,AFM) and a dipole-dipole coupling model.

4.3 Optical spectroscopy of diphenyl porphyrins on carbon nanotubes

In the previous chapter, a cooperative behavior of the π-stacking process of porphyrins on carbon nanotube has been unveiled. This process has been compared to a DFT study from Orellana [233] that attributed such associative behavior to the capacity of phenyl groups to couple between adjacent porphyrins. To test such effects, as well as to complete the TPP spectroscopic data, CoMoCat nanotubes have been coupled with 5,15-diphenylporphyrin (DPP).

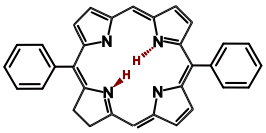

Figure IV.46: Chemical structure of the 5,15-diphenylporphyrin.

Figure IV.47 displays the absorption spectrum of the DPP in cholate. Its chemical structure does not have the two fold symmetry of the TPP (due to the phenyls removal), but its absorption spectrum possesses the same number of bands (Q bands, Soret,...). The main difference is that the Soret band is at a higher energy of 3.02 eV (410 nm) instead of 2.95 eV (420 nm) for TPP.

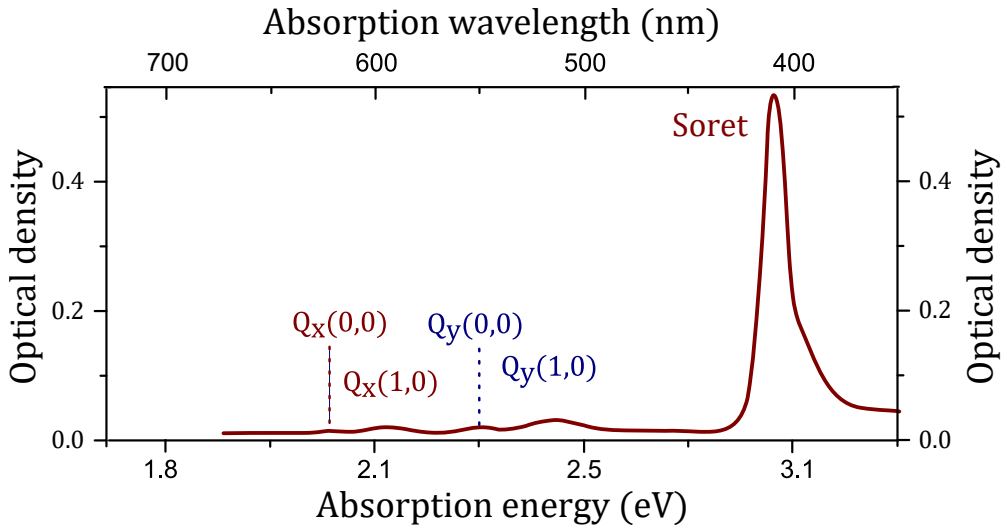

Figure IV.47: Absorption diagram of cholate suspensions containing diphenylporphyrin (DPP) alone.

Polarized PLE spectroscopy of isolated DPP

To start this discussion, polarized PLE experiments have been performed on the DPP molecules isolated in the DCM/castor oil mix. The figure IV.48 shows the unpolarized PLE diagram (red curve) for an emission recorded over the $Q_x(0,0)$ centered at 1.96 eV. This PLE exhibits a Soret band centered at 3.04 eV, at the same position as in a full DCM sample. Once again, this value is blueshifted of around 20 meV with respect to the value in cholate (3.02 eV). The anisotropy measurement on the same emission line at 3.04 eV is reported on the same graph. Surprisingly, the anisotropy is practically constant over the Soret band, for a value of around 0.12.

This value is significantly larger than the zero minimal value of the anisotropy for the TPP. Similarly to the TPP case, a steep change in anisotropy is present at a lower energy (around 2.9 eV), reaching an increased anisotropy of almost 0.20. Here, this steep change in anisotropy is shifted with respect to the Soret band of the DPP, while it was included inside the Soret band of the TPP. These results are remarkably similar to a previous study on metalated Zn diphenyl porphyrins, which exhibited an energy shift between maximal value of the anisotropy and absorption region of the Soret band [248]. Such effect is indicative of the complexity of the electronic structure within the Soret band, that includes several vibronic substates at low energy ($\simeq$ 100-200 meV below the Soret band center [109]).

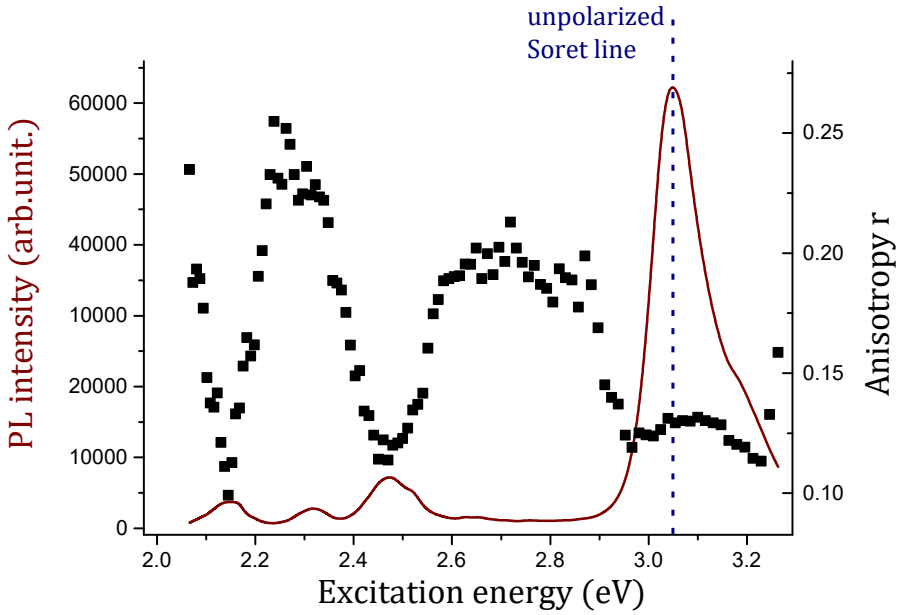

Figure IV.48: Red: PLE spectrum of the DPP inside the castor oil/ DCM mix for a signal integrated over the $Q_x(0,0)$ band around 1.96 eV; Black: anisotropy measured in the same conditions.

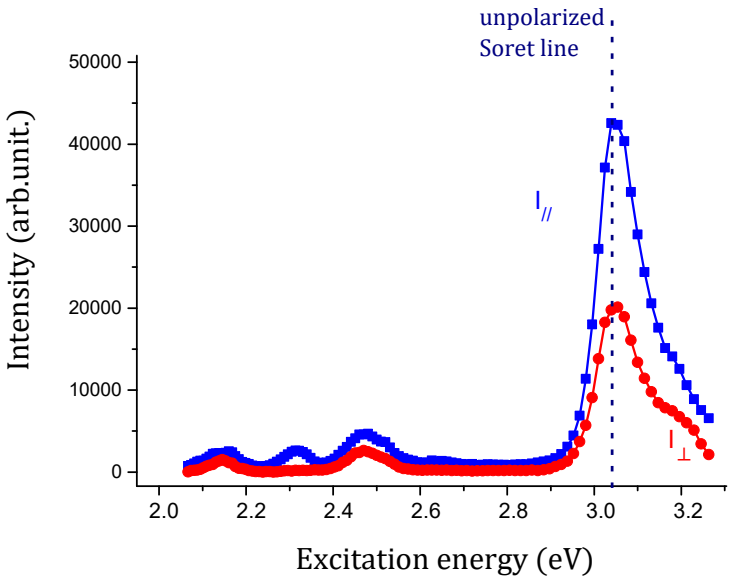

Figure IV.49: Red: PLE parralel and perpendicular components of the photoluminescence of the DPP molecules monitored on the $Q_x(0,0)$ band around 1.96 eV in a dcm/castor oil mix.

In figure IV.49 is plotted the PLE parallel and perpendicular components extracted from the DPP anisotropy. As the anisotropy value is positive, the parallel Soret component has a larger intensity than the perpendicular one in this spectral region. These two components are centered at the same energy of 3.04 eV, due to the absence of an anisotropy steep transition inside the Soret band. A a consequence, the two components of the Soret band are not split in energy. This result is significantly different from the same measurement on the TPP.

Spectroscopic characteristics of the Nt/ Diphenyl porphyrin compounds

In a second time, Nt/DPP samples have been synthesized in a SC environment. Figure IV.50 left displays the corresponding absorption diagram (blue line). The spectrum exhibits a split Soret band, with two components at 3.02 and 2.85 eV. The final behavior is close to the one of the TPP, even though the low energy component of the Soret band is at a higher energy position here (2.85 eV instead of 2.82 eV for TPP).

Simultaneously, the (6,5) S_{11} transition in figure IV.50 left undergoes a redshift. Its final position is 1.235 eV (1004 nm), which constitutes a larger shift than for the TPP (1.24 eV / 1000 nm). This effect could be the consequence of a larger molecular coverage, as the porphyrin lateral size decreases when two phenyls are removed. The figure IV.50 right shows the PLE maps from the Nt/DPP sample. An

energy transfer resonance is observed, with a maximum at an excitation wavelength of 435 nm (2.85 eV).

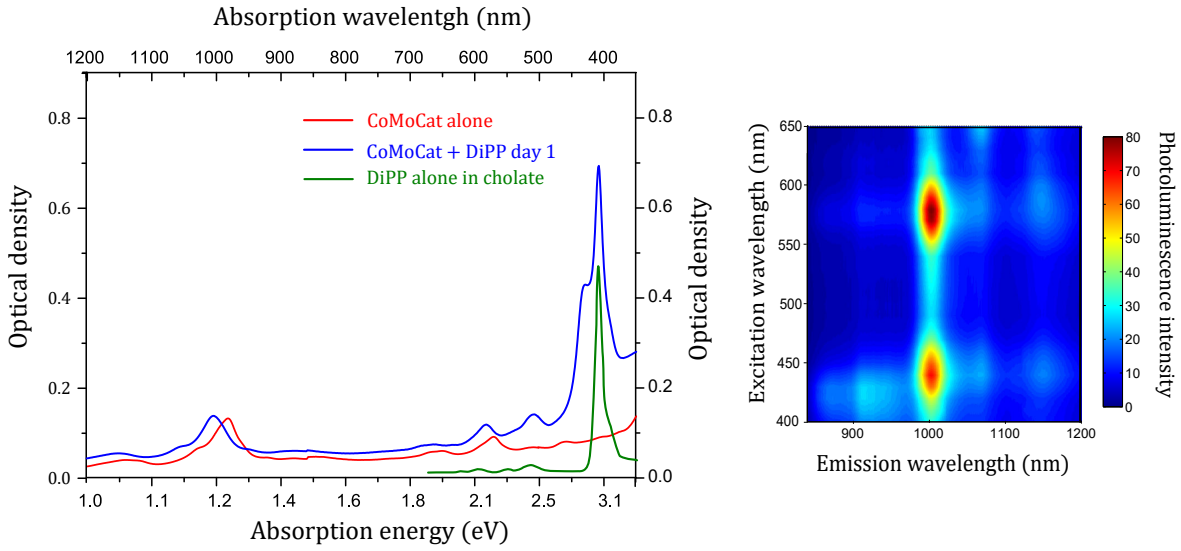

Figure IV.50: Left: Absorption diagram of cholate suspensions containing nanotubes alone (red), DPP alone (green) and Nt/DPP samples after the micelle swelling (blue); Right: PLE maps of the Nt/DPP sample after the swelling process.

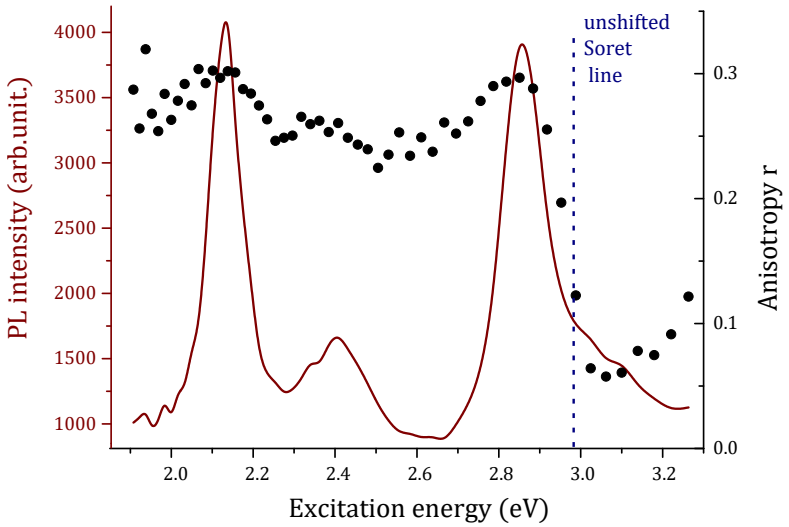

Figure IV.51: Red: Photoluminescence excitation spectrum of Nt/DPP samples; for a signal measured at 1.235 eV; Black: Corresponding anisotropy measurement at the same energy in a polarized setup.

The figure IV.51 left shows the anisotropy measurement as a function of the excitation energy, for an emission energy of 1.235 eV. This diagram presents similarities with the Nt/TPP one. A maximum anisotropy of 0.3 was evidenced, both for a S_{22} and a low energy Soret (2.85 eV) position. As for the Nt/TPP complexes, the anisotropy drops to nearly zero at higher energies (+ 0.05 at 3.05 eV), unveiling the presence of quasi isotropic contribution.

From this diagram the parallel and perpendicular intensities are calculated and displayed in figure IV.52. Once again this diagram is very similar the one of Nt/TPP complexes. The polarized low energy Soret component is centered at 2.85 eV, while the high energy component lies at 3.05 eV. The splitting is here of 200 meV, while it was of 160 meV for the Nt/Tpp compounds.

As a consequence, the spectroscopic features of coupling of the diphenylporphyrin on nanotubes are globally similar to the one of Nt/TPP complexes. Two major differences are the larger redshift of the S_{11} transition (1.235 eV instead of 1.24 eV) and the slightly larger splitting of the Soret band (of 200 meV instead of 160 meV).

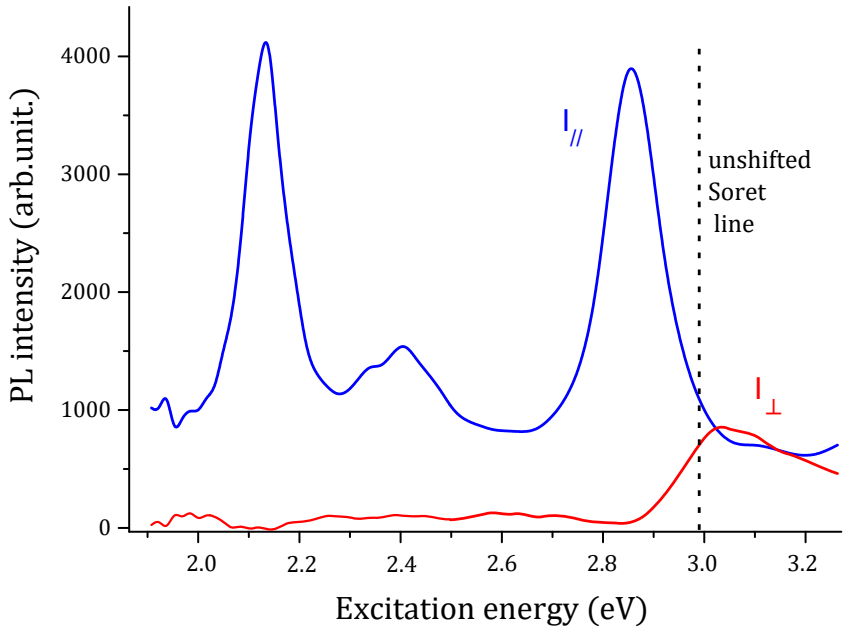

Figure IV.52: PLE parralel and perpendicular components of Nt/DPP complexes measured through the nanotube photoluminescence.

To compare the DPP and the TPP situations, the position of the O_x and O_y Soret bands in the porphyrins and the nanotube/porphyrins complexes are displayed in figure IV.53. This diagram highlights the important differences between the spec-

troscopy of the isolated TPP and DPP, while the Nt/TPP and the Nt/DPP complexes have very similar features.

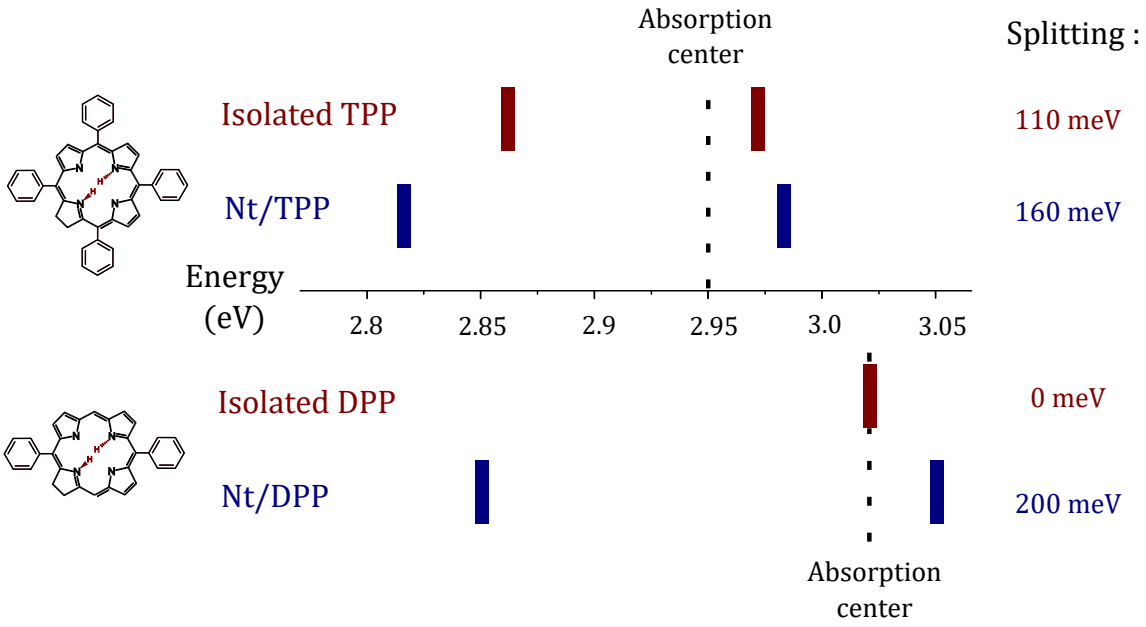

Figure IV.53: Energy position of the Soret components in isolated TPP and DPP and in Nt/TPP and Nt/DPP complexes obtained by polarized PLE experiments. A rigid shift of -20 meV has been applied to the energy positions from DCM/castor oil samples to account for the larger solvatochromism shift in cholate suspensions.

4.4 Modeling the organization of diphenylporphyrins

For the Nt/TPP complexes, the previous model was able to account for the 160 meV experimental shift. This shift could be explained as a superimposition of the pristine B_x/B_y energy separation of 110 meV and the additional splitting of 50 meV from the molecular spiral configuration.

In order to apply the same dipole model to the DPP, the extinction molar coefficient of the DPP was calculated experimentally. At the center of the Soret band, it was found to be of $\varepsilon = 370.000$ cm^{-1}.mol^{-1}.L, in agreement with literature [248,264]. This value is very similar to the one of TPP, which means that these two molecules have very similar oscillator strength and dipole moments.

From the previous discussion, the spiral/array structure was shown to induce a shift of the B_x band of around $\Delta E_J \in [-30, -60]$ meV and of the B_y band of $\Delta E_H \in [+20, +40]$ meV. Thus, this effect alone could account for a splitting between 50 and 100 meV. It was also evidenced earlier that no intrinsic splitting is present in

the polarized PLE diagram of the isolated DPP. Consequently, the spiral structure that was mentioned for the Nt/TPP compounds is not sufficient to account for the large 200 meV energy difference in Nt/DPP complexes.

To explain this difference, one must remember that the value of the energy splitting depends strongly on the intermolecular distance. Thus, this 200 meV splitting could be the consequence of a different geometry where the phenyl-phenyl interaction is not the driving effect (see figure IV.54 left). At this point, one has to observe that the origin of the $\overrightarrow{\mu}$ dipoles is located at the center the porphyrins macrocycles.

For instance, one could consider the creation of arrays of aligned DPP, that have their macrocycles next to another (see figure IV.54 right). In such structures, the intermolecular distance could take a value $r \in [0.8, 1.2]$ nm. This value is smaller than the size of 1.25 for the porphyrin molecules (from one phenyl to another). However, it is larger than the size of the macrocycle that is estimated to 0.7 nm [265].

For a distance of 1.1 nm between molecules, a redshift of $\Delta E_J \simeq$-65 meV could be reached. Simultaneously, the parallel coupling would create a blueshift of $\Delta E_H \simeq$ +33 meV. For N molecules, the maximal splitting obtained is of:

$$2\left(\Delta E_H - \Delta E_J\right) \simeq 200\text{meV} \tag{IV.25}$$

This value is in agreement with the experimental results in the Nt/DPP complexes presented above. One could also consider spiral alternatives of this macrocycle-coupling geometry in order to maximize the nanotube surface coverage.

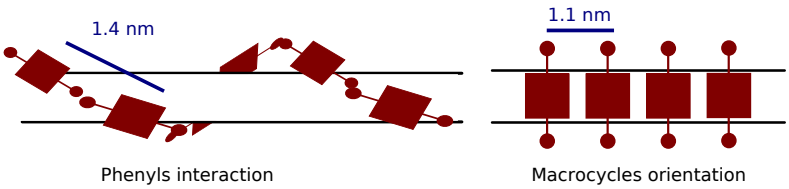

Figure IV.54: Representation of two possible organizations of the DPP on a carbon nanotube. Left: With the classical phenyl/phenyl interaction; Right: With adjacent macrocycles.

Though the energy splitting in the Nt/TPP and the NT/DPP samples have the same order of magnitude, they may arise from very different geometries of aggregates. In the Nt/DPP absorption spectrum presented in a previous section, the S_{11} nanotubes transition was at 1.235 eV (1004 nm), instead of 1.240 eV (1000 nm) for the Nt/TPP samples. This solvatochromic effect may be the consequence of a higher coverage of porphyrins at the surface of the nanotube. This effect would validate the

hypothesis of a smaller intermolecular distance within the DPP aggregates than in the TPP ones.

A DFT study of the ability of diphenylporphyrins to assemble at the surface of the nanotube would be an ideal complement to this study, in order validate the hypothesis of a macrocycles alignment instead of a phenyls coupling. A STM study of the deposition on diphenylporphyrins on nanotubes or graphene might also be helpful.

5 Conclusion

This chapter was dedicated to the comprehensive study of the energy shifts of the B_x and B_y components of the porphyrins Soret band upon adsorption. These effects are observed in many configurations: for tetraphenylporphyrins, for diphenylporphyrins, on carbon nanotubes or on graphene. In each configuration the final Soret band in absorption has different characteristics (position, amplitude, width) that provide valuable information on the π-stacking process.

A detailed study of the possible mechanisms that could create the observed energy shifts has been performed. Among them, the flattening of the molecule and the coherent organization of the molecules are the most probable. Many spectroscopic effects tend to validate the latter hypothesis.

By means of polarized PLE spectroscopy, the presence of an energy splitting of the Soret band has been evidenced. If this splitting exists in TPP molecules, it is not present in DPP. This effect also exists in Nt/porphyrins samples, but its value is significantly larger. In every sample, the polarization properties of the two Soret component was similar: the high energy band was quasi-isotropic while the low energy one was strongly anisotropic.

A review of valuable literature examples has proved that porphyrins have the ability of to self-assemble on a surface. Then, a dipole-dipole coupling model has been developed to predict the spectroscopic consequences upon cooperative aggregation. This study has shown that the structure of the porphyrins aggregates could be determined using the combined results from near field microscopy, optical spectroscopy and this dipole-dipole coupling model.

Indeed, this model has been adapted to the porphyrin characteristics, and several geometries have been tested. The case of the TPP and the DPP on nanotubes unveiled very different probable organizations, either driven by the phenyl-phenyl coupling or the macrocycles interaction. The configuration of TPP on graphene has also been studied under the hypothesis of the creation of multilayers. All of theses effects are valuable evidences of the ability of porphyrins to organize into very large layers at the surface of sp^2carbon materials.

Conclusion and perspectives

This thesis has been dedicated to the study of nanotube/porphyrins compounds with energy transfer properties. This work has demonstrated the remarkable properties of carbon based hybrid assemblies in the context of carbon-based thin films solar cells. The functionalization mechanism has been comprehensively studied from the organization of the surfactants to the self-assemblies of the porphyrins at the carbon surface.

Indeed, the active role of the surfactant, with its proper organization, has been unveiled. It was shown that the π-stacking reaction is actually starting by a diffusion step in which the TPP are evolving inside the surfactant environment. If it is not properly controlled, this environment can limit the efficiency of the functionalization process. It was also shown that the surfactant environment can influence the thermodynamics of the π-stacking mechanism.

Mixes of complementary surfactants were proved to be very efficient to control such reaction. By diluting strongly the SDS surfactant, a fast and controlled functionalization route was obtained. In such conditions, the final equilibrium was hardly disturbed by the surfactant mixed environment. These results may be applied to many nanoobjects usually suspended in surfactant environments: quantum dots, gold nanoparticles, polymers, biological elements,.. . In many situations, these objects need to be modified through a chemical reaction. In such case, this study proved that the experimentalist can influence the reaction dynamics by modifying the surfactant composition.

Additionally, the surfactant/porphyrin stability has been proved to be a limiting element for the reaction dynamics. Getting rid of the surfactant coverage around the dyes could represent a further improvement of the functionalization process. It would be interesting to test the functionalization process with carefully chosen hydrosoluble porphyrins, to see if the reaction dynamic can be accelerated. Indeed, these surfactant-free, ionic porphyrins may diffuse very rapidly through the SC/Nanotubes assemblies. In a recent article [173], Lutsyk *et al.* showed that cationic cyanin dyes could be mixed very easily with nanotubes in a anionic surfactant. As in the present work, the luminescence of the nanotubes was preserved and a strong energy transfer process was evidenced.

In addition, a comprehensive thermodynamic study of the nanotube/porphyrins compounds has been performed. A compact molecular coverage has been evidenced on different carbon nanotubes species and on graphene. The ability of porphyrins to form multilayers of porphyrins on a carbon template has also been investigated. A large affinity of porphyrins with large diameter nanotubes has been discovered, in a probable connection with the nanotube/porphyrin binding energy. This result could be used to perform a diameter sorting operation in a centrifugal field. Heavier porphyrins, such as metalated porphyrins could be used to amplify such effect.

On (6,5) nanotubes, the adsorption of porphyrin has been proved to be cooperative. In connection with a theoretical DFT model [233], this effect has been linked to the interaction of phenyl groups from adjacent molecules. By adding substituents of different sizes on such phenyls, the reaction equilibrium was shown to be less favored and the spectral features of the nanotube/porphyrin interaction were progressively lost.

Finally, many examples in literature proved that the self-assembly of porphyrins into organized layers is a general behavior. Based on absorption and polarized photoluminescence studies, the orientation of the molecules on the walls of the nanotubes and graphene has been discussed. The consequences of such cooperativity ability of the porphyrins on carbon surfaces has been modeled via a dipole coupling formalism. By using diphenylporphyrin molecules, it has been shown that the dyes organization depends on the molecular structure.

These results proves that the cooperativity is an important characteristic for the molecules to stack on the nanotube surfaces. For future researches, only molecules that have this ability should be selected, such as cyanins or perylenes derivatives. The candidates molecules should have a large oscillator strength to amplify the dipole-dipole coupling. The physics of J aggregates is very rich, especially when the molecules are very strongly coupled. It would be interesting to study the exciton dynamics inside coherent aggregates of dyes around carbon nanotubes.

It has been proved that the porphyrin organization depends on the carbon pattern dimensions. In nanotubes samples, the ring and spiral structures of porphyrins have been detailed. Only the spiral geometry was able to explain the experimental energy splittings. Spiral of porphyrins are remarkable structures, with very interesting geometric properties. In principle, they should have a particular chirality and a corresponding influence on a polarized incident light. Consequently, additional spectroscopy experiments on bulk or isolated nanotube/TPP compounds, would help to investigate into potential optical activity or Aimé Cotton effects in such hybrid compounds. Similar effect have been evidenced on nanotube wrapped with DNA branches [266].

On the other hand, a multilayer structure of porphyrins has been used to explain the spectroscopy of the graphene/TPP assemblies. The presence of multilayers of porphyrin around nanotubes has also been mentioned. This multilayers hypothesis could be investigated by near field experiments such as TEM or AFM on deposited hybrid compounds. If the results are similar to close examples in literature, these multilayers could have a dimension of several nanometers.

Such thick multilayers can be used as a protective shell around the carbon surface. It could lead to core-shell structure that may preserve the electronic and optical properties of the carbon objects. In the case of the nanotubes, it could lead to an improvement of the luminescence properties in terms of blinking or bleaching, that are often due to the disturbing influence of the environment. A great advantages of such multilayers is that they are fully reversible: a simple rinsing with an organic solvent remove the porphyrins molecules from the nanotubes [168]. If a very resistant coverage is required, porphyrins molecules can also be polymerized after stacking on the nanotube [151]. On the other hand, the diameter sorting effect evidenced in this manuscript should be considered in regard of this multilayer hypothesis. Indeed, nanotubes covered with such heavy multilayers of porphyrins would have a very high density.

This work opens new possibilities toward controlled aggregates of molecules on carbon nanotubes. The possibility to use align molecules with spin properties at the surface of carbon nanotube could be interesting [267]. Such effects have been demonstrated for iron porphyrins on a Cobalt surface [268]. Hybrid aggregates are also very promising, with an alternation of different complementary molecules (TPP, DPP, metalated porphyrins, cyanins). These molecules could be carefully selected to absorb efficiently in different parts of the optical spectrum. On a single nanotube, it would be possible to assemble complementary molecules, to efficiently absorb light on a broad spectrum and transfer it to the nanotube. This would be particularly valuable to create thin films solar cells. The possibility to stack two complementary molecules (A and B) in an organized structure could help to create a nanostructured coverage around the nanotube (for instance A-B-A-B or A-A-B-A-A). As for copolymers, it would be possible to tune the ratio between two adsorbent molecules. This could control and modulate many electrical and optical properties of the nanotubes: such as the energy transfer efficiency, or the solvatochromism effect, the diffusion or the extension length of excitons or phonons...

The work of this thesis has brought a better understanding of the interaction between the nanotubes and their physico-chemical environment. For nanotubes/porphyrins compounds, the remarkable intrinsic features of the nanotubes are preserved while environmental allows to introduce of new additional features. These hybrid structures made from carbon nano-objects present many promising properties that could be used for applications in chemistry, quantum physics or in optoelectronics.

Bibliography

[1] Anders Hagfeldt, Gerrit Boschloo, Licheng Sun, Lars Kloo, and Henrik Pettersson. Dye-sensitized solar cells. *Chemical reviews*, 110(11):6595–6663, 2010.

[2] Brian O'regan and M Graëtzel. A low-cost, high-efficiency solar cell based on dye-sensitized. *Nature*, 353(6346):737–740, 1991.

[3] Aswani Yella, Hsuan-Wei Lee, Hoi Nok Tsao, Chenyi Yi, Aravind Kumar Chandiran, Md Khaja Nazeeruddin, Eric Wei-Guang Diau, Chen-Yu Yeh, Shaik M Zakeeruddin, and Michael Grätzel. Porphyrin-sensitized solar cells with cobalt (ii/iii)–based redox electrolyte exceed 12 percent efficiency. *science*, 334(6056):629–634, 2011.

[4] Youngkyoo Kim, Steffan Cook, Sachetan M Tuladhar, Stelios A Choulis, Jenny Nelson, James R Durrant, Donal DC Bradley, Mark Giles, Iain McCulloch, Chang-Sik Ha, et al. A strong regioregularity effect in self-organizing conjugated polymer films and high-efficiency polythiophene: fullerene solar cells. *nature materials*, 5(3):197–203, 2006.

[5] Michael S Arnold, Jeramy D Zimmerman, Christopher K Renshaw, Xin Xu, Richard R Lunt, Christine M Austin, and Stephen R Forrest. Broad spectral response using carbon nanotube/organic semiconductor/c60 photodetectors. *Nano letters*, 9(9):3354–3358, 2009.

[6] Richard E Smalley. Discovering the fullerenes (nobel lecture). *Angewandte Chemie International Edition in English*, 36(15):1594–1601, 1997.

[7] Mildred S Dresselhaus and Paulo T Araujo. Perspectives on the 2010 nobel prize in physics for graphene. *ACS nano*, 4(11):6297–6302, 2010.

[8] A Paul Alivisatos. Semiconductor clusters, nanocrystals, and quantum dots. *Science*, 271(5251):933, 1996.

[9] Andre K Geim and Irina V Grigorieva. Van der waals heterostructures. *Nature*, 499(7459):419–425, 2013.

[10] Nam Joong Jeon, Jun Hong Noh, Young Chan Kim, Woon Seok Yang, Seungchan Ryu, and Sang Il Seok. Solvent engineering for high-performance

inorganic–organic hybrid perovskite solar cells. *Nature materials*, 13(9):897–903, 2014.

[11] Cyrielle Roquelet, Damien Garrot, Jean-Sébastien Lauret, Christophe Voisin, Valérie Alain-Rizzo, Ph Roussignol, JA Delaire, and Emmanuelle Deleporte. Quantum efficiency of energy transfer in noncovalent carbon nanotube/porphyrin compounds. *Applied Physics Letters*, 97(14):141918, 2010.

[12] RGJ Strens. The graphite deposit of seathwaite in borrowdale, cumberland. *Geological Magazine*, 102(05):393–406, 1965.

[13] Harold W Kroto, James R Heath, Sean C O'Brien, Robert F Curl, Richard E Smalley, et al. C 60: buckminsterfullerene. *Nature*, 318(6042):162–163, 1985.

[14] Sumio Iijima et al. Helical microtubules of graphitic carbon. *nature*, 354(6348):56–58, 1991.

[15] M Reibold, P Paufler, AA Levin, W Kochmann, N Pätzke, and DC Meyer. Materials: Carbon nanotubes in an ancient damascus sabre. *Nature*, 444(7117):286–286, 2006.

[16] Lunhui Guan, Kazu Suenaga, and Sumio Iijima. Smallest carbon nanotube assigned with atomic resolution accuracy. *Nano Letters*, 8(2):459–462, 2008.

[17] Mildred S Dresselhaus and Phaedon Avouris. Introduction to carbon materials research. In *Carbon Nanotubes*, pages 1–9. Springer, 2001.

[18] Jonathan N Coleman, Umar Khan, Werner J Blau, and Yurii K Gun'ko. Small but strong: a review of the mechanical properties of carbon nanotube–polymer composites. *Carbon*, 44(9):1624–1652, 2006.

[19] Ali Javey, Jing Guo, Qian Wang, Mark Lundstrom, and Hongjie Dai. Ballistic carbon nanotube field-effect transistors. *Nature*, 424(6949):654–657, 2003.

[20] Scott T Huxtable, David G Cahill, Sergei Shenogin, Liping Xue, Rahmi Ozisik, Paul Barone, Monica Usrey, Michael S Strano, Giles Siddons, Moonsub Shim, et al. Interfacial heat flow in carbon nanotube suspensions. *Nature materials*, 2(11):731–734, 2003.

[21] Phaedon Avouris, Marcus Freitag, and Vasili Perebeinos. Carbon-nanotube photonics and optoelectronics. *Nature photonics*, 2(6):341–350, 2008.

[22] Teri Wang Odom, Jin-Lin Huang, Philip Kim, and Charles M Lieber. Atomic structure and electronic properties of single-walled carbon nanotubes. *Nature*, 391(6662):62–64, 1998.

[23] Kostya S Novoselov, Andre K Geim, SV Morozov, D Jiang, Y_ Zhang, SV Dubonos, , IV Grigorieva, and AA Firsov. Electric field effect in atomically thin carbon films. *science*, 306(5696):666–669, 2004.

[24] Stephanie Reich, Christian Thomsen, and Janina Maultzsch. *Carbon nanotubes: basic concepts and physical properties*. John Wiley & Sons, 2008.

[25] R Saito, M Fujita, G Dresselhaus, and MS Dresselhaus. Electronic structure of chiral graphene tubules. *Applied physics letters*, 60(18):2204–2206, 1992.

[26] RA Jishi, MS Dresselhaus, and G Dresselhaus. Symmetry properties of chiral carbon nanotubes. *Physical Review B*, 47(24):16671, 1993.

[27] Michael S Strano. Carbon nanotubes: Sorting out left from right. *Nature nanotechnology*, 2(6):340–341, 2007.

[28] Xiaobin Peng, Naoki Komatsu, Sumanta Bhattacharya, Takanori Shimawaki, Shuji Aonuma, Takahide Kimura, and Atsuhiro Osuka. Optically active single-walled carbon nanotubes. *Nature Nanotechnology*, 2(6):361–365, 2007.

[29] Philip Richard Wallace. The band theory of graphite. *Physical Review*, 71(9):622, 1947.

[30] Stephanie Reich, Janina Maultzsch, Christian Thomsen, and Pablo Ordejon. Tight-binding description of graphene. *Physical Review B*, 66(3):035412, 2002.

[31] Jean-Christophe Charlier, Xavier Blase, and Stephan Roche. Electronic and transport properties of nanotubes. *Reviews of modern physics*, 79(2):677, 2007.

[32] H Lin, J Lagoute, V Repain, C Chacon, Y Girard, F Ducastelle, H Amara, A Loiseau, P Hermet, L Henrard, et al. Imaging the symmetry breaking of molecular orbitals in single-wall carbon nanotubes. *Physical Review B*, 81(23):235412, 2010.

[33] Xu Du, Ivan Skachko, Anthony Barker, and Eva Y Andrei. Approaching ballistic transport in suspended graphene. *Nature nanotechnology*, 3(8):491–495, 2008.

[34] KSA Novoselov, Andre K Geim, SVb Morozov, Da Jiang, MIc Katsnelson, IVa Grigorieva, SVb Dubonos, and AAb Firsov. Two-dimensional gas of massless dirac fermions in graphene. *nature*, 438(7065):197–200, 2005.

[35] KS Novoselov, Edward McCann, SV Morozov, Vladimir I Fal'ko, MI Katsnelson, U Zeitler, D Jiang, F Schedin, and AK Geim. Unconventional quantum hall effect and berry's phase of 2π in bilayer graphene. *Nature physics*, 2(3):177–180, 2006.

[36] A. H. Castro Neto, F. Guinea, N. M. R. Peres, K. S. Novoselov, and A. K. Geim. The electronic properties of graphene. *Rev. Mod. Phys.*, 81:109–162, Jan 2009.

[37] Riichiro Saito, G Dresselhaus, and MS Dresselhaus. Trigonal warping effect of carbon nanotubes. *Physical Review B*, 61(4):2981, 2000.

[38] JW Mintmire and CT White. Universal density of states for carbon nanotubes. *Physical Review Letters*, 81(12):2506, 1998.

[39] Léon Van Hove. The occurrence of singularities in the elastic frequency distribution of a crystal. *Physical Review*, 89(6):1189, 1953.

[40] Jeroen WG Wilder, Liesbeth C Venema, Andrew G Rinzler, Richard E Smalley, and Cees Dekker. Electronic structure of atomically resolved carbon nanotubes. *Nature*, 391(6662):59–62, 1998.

[41] Philip Kim, Teri W Odom, Jin-Lin Huang, and Charles M Lieber. Electronic density of states of atomically resolved single-walled carbon nanotubes: Van hove singularities and end states. *Physical review letters*, 82(6):1225, 1999.

[42] Claire Berger, Zhimin Song, Xuebin Li, Xiaosong Wu, Nate Brown, Cécile Naud, Didier Mayou, Tianbo Li, Joanna Hass, Alexei N Marchenkov, et al. Electronic confinement and coherence in patterned epitaxial graphene. *Science*, 312(5777):1191–1196, 2006.

[43] J Tersoff and DR Hamann. Theory of the scanning tunneling microscope. In *Scanning Tunneling Microscopy*, pages 59–67. Springer, 1985.

[44] Michel Le Bellac. *Physique quantique-Fondements: Fondements*, volume 1. EDP sciences, 2013.

[45] A Grüneis, R Saito, Ge G Samsonidze, T Kimura, MA Pimenta, A Jorio, AG Souza Filho, G Dresselhaus, and MS Dresselhaus. Inhomogeneous optical absorption around the k point in graphite and carbon nanotubes. *Physical Review B*, 67(16):165402, 2003.

[46] Ermin Malić, Matthias Hirtschulz, Frank Milde, Andreas Knorr, and Stephanie Reich. Analytical approach to optical absorption in carbon nanotubes. *Physical review B*, 74(19):195431, 2006.

[47] http://www.photon.t.u-tokyo.ac.jp/ maruyama/kataura/kataura.html.

[48] J Lefebvre and Paul Finnie. Polarized photoluminescence excitation spectroscopy of single-walled carbon nanotubes. *Physical review letters*, 98(16):167406, 2007.

[49] Seiji Uryu and Tsuneya Ando. Exciton absorption of perpendicularly polarized light in carbon nanotubes. *Physical Review B*, 74(15):155411, 2006.

[50] H Kataura, Y Kumazawa, Y Maniwa, I Umezu, S Suzuki, Yo Ohtsuka, and Y Achiba. Optical properties of single-wall carbon nanotubes. *Synthetic metals*, 103(1):2555–2558, 1999.

[51] Stéphane Berciaud, Vikram V Deshpande, Robert Caldwell, Yuhei Miyauchi, Christophe Voisin, Philip Kim, James Hone, and Tony F Heinz. All-optical structure assignment of individual single-walled carbon nanotubes from rayleigh and raman scattering measurements. *physica status solidi (b)*, 249(12):2436–2441, 2012.

[52] T Giamarchi. Quantum physics in one dimension oxford science publications. *New York*, 2004.

[53] Hongbo Zhao and Sumit Mazumdar. Electron-electron interaction effects on the optical excitations of semiconducting single-walled carbon nanotubes. *Physical review letters*, 93(15):157402, 2004.

[54] CL Kane and EJ Mele. Electron interactions and scaling relations for optical excitations in carbon nanotubes. *Physical review letters*, 93(19):197402, 2004.

[55] J Frenkel. On the transformation of light into heat in solids. i. *Physical Review*, 37(1):17, 1931.

[56] JK Kübler. The exciton binding energy of iii–v semiconductor compounds. *physica status solidi (b)*, 35(1):189–195, 1969.

[57] H Lin, J Lagoute, V Repain, C Chacon, Y Girard, J-S Lauret, F Ducastelle, A Loiseau, and S Rousset. Many-body effects in electronic bandgaps of carbon nanotubes measured by scanning tunnelling spectroscopy. *Nature materials*, 9(3):235–238, 2010.

[58] Andreas Thess, Roland Lee, Pavel Nikolaev, and Hongjie Dai. Crystalline ropes of metallic carbon nanotubes. *Science*, 273(5274):483, 1996.

[59] Alan M Cassell, Nathan R Franklin, Thomas W Tombler, Emory M Chan, Jie Han, and Hongjie Dai. Directed growth of free-standingsingle-walled carbon nanotubes. *Journal of the American Chemical Society*, 121(34):7975–7976, 1999.

[60] Jan Prasek, Jana Drbohlavova, Jana Chomoucka, Jaromir Hubalek, Ondrej Jasek, Vojtech Adam, and Rene Kizek. Methods for carbon nanotubes synthesis—review. *Journal of Materials Chemistry*, 21(40):15872–15884, 2011.

[61] Sulabha K Kulkarni. *Nanotechnology: principles and practices*. Springer, 2015.

[62] V Ardizzone, Y Chassagneux, F Vialla, G Delport, C Delcamp, N Belabas, E Deleporte, Ph Roussignol, I Robert-Philip, C Voisin, et al. Strong reduction of exciton-phonon coupling in single-wall carbon nanotubes of high crystalline quality: Insight into broadening mechanisms and exciton localization. *Physical Review B*, 91(12):121410, 2015.

[63] Jing Kong, Alan M Cassell, and Hongjie Dai. Chemical vapor deposition of methane for single-walled carbon nanotubes. *Chemical Physics Letters*, 292(4):567–574, 1998.

[64] J Lefebvre, Y Homma, and Paul Finnie. Bright band gap photoluminescence from unprocessed single-walled carbon nanotubes. *Physical review letters*, 90(21):217401, 2003.

[65] Pavel Nikolaev, Michael J Bronikowski, R Kelley Bradley, Frank Rohmund, Daniel T Colbert, KA Smith, and Richard E Smalley. Gas-phase catalytic growth of single-walled carbon nanotubes from carbon monoxide. *Chemical physics letters*, 313(1):91–97, 1999.

[66] Sergei M Bachilo, Leandro Balzano, Jose E Herrera, Francisco Pompeo, Daniel E Resasco, and R Bruce Weisman. Narrow (n, m)-distribution of single-walled carbon nanotubes grown using a solid supported catalyst. *Journal of the American Chemical Society*, 125(37):11186–11187, 2003.

[67] Michael S Arnold, Alexander A Green, James F Hulvat, Samuel I Stupp, and Mark C Hersam. Sorting carbon nanotubes by electronic structure using density differentiation. *Nature nanotechnology*, 1(1):60–65, 2006.

[68] Huaping Liu, Daisuke Nishide, Takeshi Tanaka, and Hiromichi Kataura. Large-scale single-chirality separation of single-wall carbon nanotubes by simple gel chromatography. *Nature communications*, 2:309, 2011.

[69] Jeffrey A. Fagan, Erik H. Hároz, Rachelle Ihly, Hui Gui, Jeffrey L. Blackburn, Jeffrey R. Simpson, Stephanie Lam, Angela R. Hight Walker, Stephen K. Doorn, and Ming Zheng. Isolation of 1 nm diameter single-wall carbon nanotube species using aqueous two-phase extraction. *ACS Nano*, 9(5):5377–5390, 2015. PMID: 25871430.

[70] Feng Yang, Xiao Wang, Daqi Zhang, Juan Yang, Da Luo, Ziwei Xu, Jiake Wei, Jian-Qiang Wang, Zhi Xu, Fei Peng, et al. Chirality-specific growth of single-walled carbon nanotubes on solid alloy catalysts. *Nature*, 510(7506):522–524, 2014.

[71] Juan Ramon Sanchez-Valencia, Thomas Dienel, Oliver Gröning, Ivan Shorubalko, Andreas Mueller, Martin Jansen, Konstantin Amsharov, Pascal Ruffieux, and Roman Fasel. Controlled synthesis of single-chirality carbon nanotubes. *Nature*, 512(7512):61–64, 2014.

[72] Marceli Nencki and N Sieber. Über das hämatoporphyrin. *Naunyn-Schmiedeberg's Archives of Pharmacology*, 24(6):430–446, 1888.

[73] Arthur Gamgee. On the relations of turacin and turacoporphyrin to the colouring matter of the blood. *Proceedings of the Royal Society of London*, 59(353-358):339–342, 1895.

[74] Claude Rimington. A reinvestigation of turacin, the copper porphyrin pigment of certain birds belonging to the musophagidae. *Proceedings of the Royal Society of London. Series B, Biological Sciences*, pages 106–120, 1939.

[75] GR Agarwal, OP Agarwal, et al. *Text book of Biochemistry*. Krishna Prakashan Media, 2007.

[76] Raymond Bonnett. Photosensitizers of the porphyrin and phthalocyanine series for photodynamic therapy. *Chemical Society Reviews*, 24(1):19–33, 1995.

[77] Simon Mathew, Aswani Yella, Peng Gao, Robin Humphry-Baker, Basile FE Curchod, Negar Ashari-Astani, Ivano Tavernelli, Ursula Rothlisberger, Md Khaja Nazeeruddin, and Michael Grätzel. Dye-sensitized solar cells with 13% efficiency achieved through the molecular engineering of porphyrin sensitizers. *Nature chemistry*, 6(3):242–247, 2014.

[78] Engelbert Weis and Joseph A Berry. Quantum efficiency of photosystem ii in relation to 'energy'-dependent quenching of chlorophyll fluorescence. *Biochimica et Biophysica Acta (BBA)-Bioenergetics*, 894(2):198–208, 1987.

[79] Jennifer L Herek, Wendel Wohlleben, Richard J Cogdell, Dirk Zeidler, and Marcus Motzkus. Quantum control of energy flow in light harvesting. *Nature*, 417(6888):533–535, 2002.

[80] Yasuhiro Tachibana, Lionel Vayssieres, and James R Durrant. Artificial photosynthesis for solar water-splitting. *Nature Photonics*, 6(8):511–518, 2012.

[81] Devens Gust and Thomas A Moore. Mimicking photosynthesis. *Science*, 244(4900):35–41, 1989.

[82] Michael R Wasielewski. Photoinduced electron transfer in supramolecular systems for artificial photosynthesis. *Chemical Reviews*, 92(3):435–461, 1992.

[83] Paul Rothemund and Amel R Menotti. Porphyrin studies. iv. 1 the synthesis of α, β, γ, δ-tetraphenylporphine. *Journal of the American Chemical Society*, 63(1):267–270, 1941.

[84] SS Eaton and GR Eaton. Rotation of phenyl rings in metal complexes of substituted tetraphenylporphyrins. *Journal of the American Chemical Society*, 97(13):3660–3666, 1975.

[85] Maximiliane S Boeckl, Ariana L Bramblett, Kip D Hauch, Tomikazu Sasaki, Buddy D Ratner, and JW Rogers. Self-assembly of tetraphenylporphyrin monolayers on gold substrates. *Langmuir*, 16(13):5644–5653, 2000.

[86] Willi Auwärter, David Écija, Florian Klappenberger, and Johannes V Barth. Porphyrins at interfaces. *Nature Chemistry*, 7(2):105–120, 2015.

[87] Robert F Pasternack, Esther J Gibbs, Peter J Collings, Julio C dePaula, L Christine Turzo, and Antonio Terracina. A nonconventional approach to supramolecular formation dynamics. the kinetics of assembly of dna-bound porphyrins. *Journal of the American Chemical Society*, 120(24):5873–5878, 1998.

[88] G Alan Schick, Irwin C Schreiman, Richard W Wagner, Jonathan S Lindsey, and David F Bocian. Spectroscopic characterization of porphyrin monolayer assemblies. *Journal of the American Chemical Society*, 111(4):1344–1350, 1989.

[89] Johannes M Kroon, Ernst JR Sudhoelter, Albertus PHJ Schenning, and Roeland JM Nolte. Self-organization of amphiphilic porphyrins at the air-water interface. *Langmuir*, 11(1):214–220, 1995.

[90] Roald Hoffmann. An extended hückel theory. i. hydrocarbons. *The Journal of Chemical Physics*, 39(6):1397–1412, 1963.

[91] William T Simpson. On the theory of the π-electron system in porphines. *The Journal of Chemical Physics*, 17(12):1218–1221, 1949.

[92] HC Longuet-Higgins, CW Rector, and JR Platt. Molecular orbital calculations on porphine and tetrahydroporphine. *The Journal of Chemical Physics*, 18(9):1174–1181, 1950.

[93] Karl M Kadish, Kevin M Smith, and Roger Guilard. Handbook of porphyrin science. *World Scientific: Singapore*, 2014:1–35, 2010.

[94] Ulf Norinder, Olof Wennerström, and Hakan Wennerström. Hückel theory applied to large linear and cyclic conjugated π-systems. *Tetrahedron*, 41(4):713–726, 1985.

[95] Sheldon L Matlow. An lcao mo study of the structure of chlorophyll prototypes. *The Journal of Chemical Physics*, 23(4):673–680, 1955.

[96] Kimio Ohno, Yukito Tanabe, and Fukashi Sasaki. Simple molecular orbital calculations on the electronic structure of iron-porphyrin complexes. *Theoretica chimica acta*, 1(4):378–392, 1963.

[97] Inan Chen. Pi-electron conjugation in porphyrins. *Journal of Molecular Spectroscopy*, 23(2):144–148, 1967.

[98] EJ Baerends, G Ricciardi, A Rosa, and SJA Van Gisbergen. A dft/tddft interpretation of the ground and excited states of porphyrin and porphyrazine complexes. *Coordination chemistry reviews*, 230(1):5–27, 2002.

[99] Maurizia Palummo, Conor Hogan, Francesco Sottile, Paolo Bagalá, and Angel Rubio. Ab initio electronic and optical spectra of free-base porphyrins: The role of electronic correlation. *The Journal of chemical physics*, 131(8):084102, 2009.

[100] Van Dong Pham, Jérôme Lagoute, Ouafi Mouhoub, Frédéric Joucken, Vincent Repain, Cyril Chacon, Amandine Bellec, Yann Girard, and Sylvie Rousset. Electronic interaction between nitrogen-doped graphene and porphyrin molecules. *ACS nano*, 8(9):9403–9409, 2014.

[101] Martin Gouterman. Study of the effects of substitution on the absorption spectra of porphin. *The journal of chemical physics*, 30(5):1139–1161, 1959.

[102] JR Platt and A Hollaender. Radiation biology, vol. *IIIMcGraw-Hill, New York*, page 71, 1956.

[103] Marilyn H Perrin, Martin Gouterman, and Charles L Perrin. Vibronic coupling. vi. vibronic borrowing in cyclic polyenes and porphyrin. *The Journal of Chemical Physics*, 50(10):4137–4150, 1969.

[104] Jeanette G Grasselli and William M Ritchey. Crc atlas of spectral data and physical constants for organic compounds. 1975.

[105] Martin Gouterman. Spectra of porphyrins. *Journal of Molecular Spectroscopy*, 6:138–163, 1961.

[106] Taru Nikkonen et al. Structure-property relationships and self-assembly of chlorophyll derivatives in development of light-harvesting structures and materials. 2015.

[107] John W Weigl. The polarization of the fluorescence of tetraphenylporphine. *Journal of Molecular Spectroscopy*, 1(1):133–138, 1957.

[108] Fabien Vialla. *Interaction between carbon nanotubes and their physico-chemical environment : towards the control of the optical properties*. Theses, Université Pierre et Marie Curie - Paris VI, March 2014.

[109] J Spencer Baskin, Hua-Zhong Yu, and Ahmed H Zewail. Ultrafast dynamics of porphyrins in the condensed phase: I. free base tetraphenylporphyrin. *The Journal of Physical Chemistry A*, 106(42):9837–9844, 2002.

[110] GRADYUSH. AT and MP Tsvirko. Probabilities of intercombination transitions in porphyrin and metalloporphyrin molecules. *OPTICS AND SPECTROSCOPY-USSR*, 31(4):291, 1971.

[111] Koichi Kikuchi, Yutaka Kurabayashi, Hiroshi Kokubun, Youkoh Kaizu, and Hiroshi Kobayashi. Triplet yields of some tetraphenylporphyrins and octaethylporphyrins. *Journal of Photochemistry and Photobiology A: Chemistry*, 45(2):261–263, 1988.

[112] Paul G Seybold and Martin Gouterman. Porphyrins: Xiii: fluorescence spectra and quantum yields. *Journal of Molecular Spectroscopy*, 31(1):1–13, 1969.

[113] Joseph R Lakowicz. *Principles of fluorescence spectroscopy*. Springer Science & Business Media, 2013.

[114] Wang Zhang Yuan, Ping Lu, Shuming Chen, Jacky WY Lam, Zhiming Wang, Yang Liu, Hoi Sing Kwok, Yuguang Ma, and Ben Zhong Tang. Changing the behavior of chromophores from aggregation-caused quenching to aggregation-induced emission: Development of highly efficient light emitters in the solid state. *Advanced materials*, 22(19):2159–2163, 2010.

[115] Joseph R Lakowicz, Henryk Szmacinski, Kazimierz Nowaczyk, Klaus W Berndt, and Michael Johnson. Fluorescence lifetime imaging. *Analytical biochemistry*, 202(2):316–330, 1992.

[116] Nakul C Maiti, Shyamalava Mazumdar, and N Periasamy. J-and h-aggregates of porphyrin-surfactant complexes: time-resolved fluorescence and other spectroscopic studies. *The Journal of Physical Chemistry B*, 102(9):1528–1538, 1998.

[117] Yuhei Miyauchi, Mototeru Oba, and Shigeo Maruyama. Cross-polarized optical absorption of single-walled nanotubes by polarized photoluminescence excitation spectroscopy. *Physical Review B*, 74(20):205440, 2006.

[118] Cyrielle Roquelet, Fabien Vialla, Carole Diederichs, Philippe Roussignol, Claude Delalande, Emmanuelle Deleporte, Jean-Sébastien Lauret, and Christophe Voisin. Local field effects in the energy transfer between a chromophore and a carbon nanotube: A single-nanocompound investigation. *ACS nano*, 6(10):8796–8802, 2012.

[119] Osamu Ohno, Youkoh Kaizu, and Hiroshi Kobayashi. J-aggregate formation of a water-soluble porphyrin in acidic aqueous media. *The Journal of chemical physics*, 99(5):4128–4139, 1993.

[120] Nakul C Maiti, Shyamalava Mazumdar, and N Periasamy. Dynamics of porphyrin molecules in micelles. picosecond time-resolved fluorescence anisotropy studies. *The Journal of Physical Chemistry*, 99(27):10708–10715, 1995.

[121] DM Kehl. Observations et journal sur la physique, de chimie et d'histoire naturelle et des arts, 1793.

[122] A Dabrowski. Adsorption—from theory to practice. *Advances in colloid and interface science*, 93(1):135–224, 2001.

[123] FE Bartell and EJ Miller. Adsorption by activated sugar charcoal. i1. *Journal of the American Chemical Society*, 44(9):1866–1880, 1922.

[124] Robert W Coughlin and Fouad S Ezra. Role of surface acidity in the adsorption of organic pollutants on the surface of carbon. *Environmental Science & Technology*, 2(4):291–297, 1968.

[125] A Dierichs and L Jaehn. Adsorption of polyvalent phenols from industrial waste water. *Chem. Tech.(Germany)*, 10:576, 1958.

[126] C Namasivayam and Dyes Kavitha. Removal of congo red from water by adsorption onto activated carbon prepared from coir pith, an agricultural solid waste. *Dyes and pigments*, 54(1):47–58, 2002.

[127] Romain Mailler, Johnny Gasperi, Yves Coquet, Fabrice Nauleau, Olivier Rousselot, and Vincent Rocher. Traitement des eaux résiduaires urbaines par charbon actif en poudre - étude du procédé carboplus® pour les polluants prioritaires et émergents. In *Journées Information Eaux 2014*, Poitiers, France, November 2014. Apten and ENSI Poitiers.

[128] Duncan Smith. Fuelling the future: Solid phase hydrogen storage. *Education in Chemistry*, 44(6):176, 2007.

[129] Ekaterina E Romanova, Rana Akiel, Franklin H Cho, and Susumu Takahashi. Grafting nitroxide radicals on nanodiamond surface using click chemistry. *The Journal of Physical Chemistry A*, 117(46):11933–11939, 2013.

[130] Kei Ohkubo, Paul A Karr, Shunichi Fukuzumi, Francis D'Souza, et al. A 'two-point'bound zinc porphyrin–zinc phthalocyanine–fullerene supramolecular triad for sequential energy and electron transfer. *Chemical Communications*, 49(69):7614–7616, 2013.

[131] Michael J O'connell, Sergei M Bachilo, Chad B Huffman, Valerie C Moore, Michael S Strano, Erik H Haroz, Kristy L Rialon, Peter J Boul, William H Noon, Carter Kittrell, et al. Band gap fluorescence from individual single-walled carbon nanotubes. *Science*, 297(5581):593–596, 2002.

[132] Vadym N Mochalin, Olga Shenderova, Dean Ho, and Yury Gogotsi. The properties and applications of nanodiamonds. *Nature nanotechnology*, 7(1):11–23, 2012.

[133] Arno S Rettenbacher, Bevan Elliott, Joan S Hudson, Armen Amirkhanian, and Luis Echegoyen. Preparation and functionalization of multilayer fullerenes (carbon nano-onions). *Chemistry–A European Journal*, 12(2):376–387, 2006.

[134] Maurizio Prato. [60] fullerene chemistry for materials science applications. *Journal of Materials Chemistry*, 7(7):1097–1109, 1997.

[135] Yuan-Zhi Tan, Bo Yang, Khaled Parvez, Akimitsu Narita, Silvio Osella, David Beljonne, Xinliang Feng, and Klaus Müllen. Atomically precise edge chlorination of nanographenes and its application in graphene nanoribbons. *Nature communications*, 4, 2013.

[136] Kannan Balasubramanian and Marko Burghard. Chemically functionalized carbon nanotubes. *Small*, 1(2):180–192, 2005.

[137] Jian Chen, Mark A Hamon, Hui Hu, Yongsheng Chen, Apparao M Rao, Peter C Eklund, and Robert C Haddon. Solution properties of single-walled carbon nanotubes. *Science*, 282(5386):95–98, 1998.

[138] Christopher A Dyke and James M Tour. Overcoming the insolubility of carbon nanotubes through high degrees of sidewall functionalization. *Chemistry–A European Journal*, 10(4):812–817, 2004.

[139] Anup K Deb and Charles C Chusuei. *Aqueous Solution Surface Chemistry of Carbon Nanotubes*. INTECH Open Access Publisher, 2013.

[140] Thomas Palacin, Hung Le Khanh, Bruno Jousselme, Pascale Jegou, Arianna Filoramo, Christian Ehli, Dirk M Guldi, and Stéphane Campidelli. Efficient functionalization of carbon nanotubes with porphyrin dendrons via click chemistry. *Journal of the American Chemical Society*, 131(42):15394–15402, 2009.

[141] Michael S Strano, Christopher A Dyke, Monica L Usrey, Paul W Barone, Mathew J Allen, Hongwei Shan, Carter Kittrell, Robert H Hauge, James M Tour, and Richard E Smalley. Electronic structure control of single-walled carbon nanotube functionalization. *Science*, 301(5639):1519–1522, 2003.

[142] Yanmei Piao, Brendan Meany, Lyndsey R Powell, Nicholas Valley, Hyejin Kwon, George C Schatz, and YuHuang Wang. Brightening of carbon nanotube photoluminescence through the incorporation of sp3 defects. *Nature chemistry*, 5(10):840–845, 2013.

[143] Xuedan Ma, Nicolai F Hartmann, Jon KS Baldwin, Stephen K Doorn, and Han Htoon. Room-temperature single-photon generation from solitary dopants of carbon nanotubes. *Nature nanotechnology*, 10(8):671–675, 2015.

[144] Chelsea R Martinez and Brent L Iverson. Rethinking the term "pi-stacking". *Chemical Science*, 3(7):2191–2201, 2012.

[145] Xiaomin Tu, Suresh Manohar, Anand Jagota, and Ming Zheng. Dna sequence motifs for structure-specific recognition and separation of carbon nanotubes. *Nature*, 460(7252):250–253, 2009.

[146] Friederike Ernst, Timm Heek, Antonio Setaro, Rainer Haag, and Stephanie Reich. Excitation characteristics of different energy transfer in nanotube-perylene complexes. *Applied Physics Letters*, 102(23):233105, 2013.

[147] Adrian Nish, Jeong-Yuan Hwang, James Doig, and Robin J Nicholas. Direct spectroscopic evidence of energy transfer from photo-excited semiconducting polymers to single-walled carbon nanotubes. *Nanotechnology*, 19(9):095603, 2008.

[148] SG Chou, HB Ribeiro, EB Barros, AP Santos, D Nezich, Ge G Samsonidze, C Fantini, MA Pimenta, A Jorio, F Plentz Filho, et al. Optical characterization of dna-wrapped carbon nanotube hybrids. *Chemical physics letters*, 397(4):296–301, 2004.

[149] Davide Pantarotto, Ravi Singh, David McCarthy, Mathieu Erhardt, Jean-Paul Briand, Maurizio Prato, Kostas Kostarelos, and Alberto Bianco. Functionalized carbon nanotubes for plasmid dna gene delivery. *Angewandte Chemie*, 116(39):5354–5358, 2004.

[150] Konstantin Iakoubovskii, Nobutsugu Minami, Yeji Kim, Kanae Miyashita, Said Kazaoui, and Balakrishnan Nalini. Midgap luminescence centers in single-wall carbon nanotubes created by ultraviolet illumination. *Applied physics letters*, 89(17):173108, 2006.

[151] Guillaume Clavé, Géraud Delport, Cyrielle Roquelet, Jean-Sébastien Lauret, Emmanuelle Deleporte, Fabien Vialla, Benjamin Langlois, Romain Parret, Christophe Voisin, Philippe Roussignol, et al. Functionalization of carbon nanotubes through polymerization in micelles: A bridge between the covalent and noncovalent methods. *Chemistry of Materials*, 25(13):2700–2707, 2013.

[152] J Campo, Y Piao, S Lam, CM Stafford, JK Streit, JR Simpson, AR Hight Walker, and JA Fagan. Enhancing single-wall carbon nanotube properties through controlled endohedral filling. *Nanoscale Horizons*, 2016.

[153] DJ Hornbaker, S-J Kahng, S Misra, BW Smith, AT Johnson, EJ Mele, DE Luzzi, and A Yazdani. Mapping the one-dimensional electronic states of nanotube peapod structures. *Science*, 295(5556):828–831, 2002.

[154] Wim Wenseleers, Sofie Cambré, Jelena Čulin, August Bouwen, and Etienne Goovaerts. Effect of water filling on the electronic and vibrational resonances of carbon nanotubes: Characterizing tube opening by raman spectroscopy. *Advanced Materials*, 19(17):2274–2278, 2007.

[155] E Gaufrès, NY-Wa Tang, F Lapointe, J Cabana, M-A Nadon, N Cottenye, F Raymond, T Szkopek, and R Martel. Giant raman scattering from j-aggregated dyes inside carbon nanotubes for multispectral imaging. *Nature Photonics*, 8(1):72–78, 2014.

[156] Sofie Cambré, Jochen Campo, Charlie Beirnaert, Christof Verlackt, Pegie Cool, and Wim Wenseleers. Asymmetric dyes align inside carbon nanotubes to yield a large nonlinear optical response. *Nature nanotechnology*, 10(3):248–252, 2015.

[157] Kevin D Ausman, Richard Piner, Oleg Lourie, Rodney S Ruoff, and Mikhail Korobov. Organic solvent dispersions of single-walled carbon nanotubes: toward solutions of pristine nanotubes. *The Journal of Physical Chemistry B*, 104(38):8911–8915, 2000.

[158] Michael J O'Connell, Peter Boul, Lars M Ericson, Chad Huffman, Yuhuang Wang, Erik Haroz, Cynthia Kuper, Jim Tour, Kevin D Ausman, and Richard E Smalley. Reversible water-solubilization of single-walled carbon nanotubes by polymer wrapping. *Chemical physics letters*, 342(3):265–271, 2001.

[159] Sergei M Bachilo, Michael S Strano, Carter Kittrell, Robert H Hauge, Richard E Smalley, and R Bruce Weisman. Structure-assigned optical spectra of single-walled carbon nanotubes. *Science*, 298(5602):2361–2366, 2002.

[160] Alexander A Green and Mark C Hersam. Processing and properties of highly enriched double-wall carbon nanotubes. *Nature Nanotechnology*, 4(1):64–70, 2009.

[161] Cyrille Richard, Fabrice Balavoine, Patrick Schultz, Thomas W Ebbesen, and Charles Mioskowski. Supramolecular self-assembly of lipid derivatives on carbon nanotubes. *Science*, 300(5620):775–778, 2003.

[162] Antoine Lucas, Cécile Zakri, Maryse Maugey, Matteo Pasquali, Paul van der Schoot, and Philippe Poulin. Kinetics of nanotube and microfiber scission under sonication. *The Journal of Physical Chemistry C*, 113(48):20599–20605, 2009.

[163] Cyrielle Roquelet, Damien Garrot, Jean-Sébastien Lauret, C. Voisin, Valérie Alain-Rizzo, Philippe Roussignol, Jacques A. Delaire, and Emmanuelle Deleporte. Quantum efficiency of energy transfer in noncovalent carbon nanotube/porphyrin compounds. *Applied Physics Letters*, 97(14):141918, 2010.

[164] Jinyu Chen and C Patrick Collier. Noncovalent functionalization of single-walled carbon nanotubes with water-soluble porphyrins. *The Journal of Physical Chemistry B*, 109(16):7605–7609, 2005.

[165] Hiroto Murakami, Takuro Nomura, and Naotoshi Nakashima. Noncovalent porphyrin-functionalized single-walled carbon nanotubes in solution and the formation of porphyrin–nanotube nanocomposites. *Chemical Physics Letters*, 378(5):481–485, 2003.

[166] Gurvan Magadur, Jean-Sébastien Lauret, Valérie Alain-Rizzo, Christophe Voisin, Philippe Roussignol, Emmanuelle Deleporte, and Jacques A Delaire. Excitation transfer in functionalized carbon nanotubes. *ChemPhysChem*, 9(9):1250–1253, 2008.

[167] John P Casey, Sergei M Bachilo, and R Bruce Weisman. Efficient photosensitized energy transfer and near-ir fluorescence from porphyrin–swnt complexes. *Journal of Materials Chemistry*, 18(13):1510–1516, 2008.

[168] Cyrielle Roquelet. *Transfert d'énergie dans des composés nanotube de carbone/porphyrine*. PhD thesis, École normale supérieure de Cachan-ENS Cachan, 2012.

[169] Randy K Wang, Wei-Chiang Chen, Daisy K Campos, and Kirk J Ziegler. Swelling the micelle core surrounding single-walled carbon nanotubes with water-immiscible organic solvents. *Journal of the American Chemical Society*, 130(48):16330–16337, 2008.

[170] Carlos A Silvera-Batista, Randy K Wang, Philip Weinberg, and Kirk J Ziegler. Solvatochromic shifts of single-walled carbon nanotubes in nonpolar microenvironments. *Physical Chemistry Chemical Physics*, 12(26):6990–6998, 2010.

[171] Ermin Malic, Heiko Appel, Oliver T Hofmann, and Angel Rubio. Förster-induced energy transfer in functionalized graphene. *The Journal of Physical Chemistry C*, 118(17):9283–9289, 2014.

[172] Friederike Ernst, Sebastian Heeg, Timm Heek, Antonio Setaro, Rainer Haag, and Stephanie Reich. Selective interaction between nanotubes and perylene-based surfactant. *physica status solidi (RRL)-Rapid Research Letters*, 7(8):546–549, 2013.

[173] Petro Lutsyk, Raz Arif, Jan Hruby, Anatolii Bukivskyi, Olexander Vinijchuk, Mykola Shandura, Viktor Yakubovskyi, Yuri Kovtun, Graham A Rance, Michael Fay, et al. A sensing mechanism for the detection of carbon nanotubes using selective photoluminescent probes based on ionic complexes with organic dyes. *Light: Science & Applications*, 5(2):e16028, 2016.

[174] Yusuke Tsutsumi, Tsuyohiko Fujigaya, and Naotoshi Nakashima. Polymer synthesis inside a nanospace of a surfactant–micelle on carbon nanotubes: creation of highly-stable individual nanotubes/ultrathin cross-linked polymer hybrids. *RSC Advances*, 4(12):6318–6323, 2014.

[175] Jeffrey L Blackburn, Timothy J McDonald, Wyatt K Metzger, Chaiwat Engtrakul, Garry Rumbles, and Michael J Heben. Protonation effects on the branching ratio in photoexcited single-walled carbon nanotube dispersions. *Nano letters*, 8(4):1047–1054, 2008.

[176] Andrew J Hilmer, Thomas P McNicholas, Shangchao Lin, Jingqing Zhang, Qing Hua Wang, Jonathan D Mendenhall, Changsik Song, Daniel A Heller, Paul W Barone, Daniel Blankschtein, et al. Role of adsorbed surfactant in the reaction of aryl diazonium salts with single-walled carbon nanotubes. *Langmuir*, 28(2):1309–1321, 2012.

[177] E Ruckenstein and R Nagarajan. Critical micelle concentration. transition point for micellar size distribution. *The Journal of Physical Chemistry*, 79(24):2622–2626, 1975.

[178] Juan P Marcolongo and Martín Mirenda. Thermodynamics of sodium dodecyl sulfate (sds) micellization: an undergraduate laboratory experiment. *Journal of Chemical Education*, 88(5):629–633, 2011.

[179] Tharwat F Tadros. Physical chemistry of surfactant solutions. *Colloids in Agrochemicals: Colloids and Interface Science, Volume 5*, pages 19–40, 2005.

[180] SJ Marrink, DP Tieleman, and AE Mark. Molecular dynamics simulation of the kinetics of spontaneous micelle formation. *The Journal of Physical Chemistry B*, 104(51):12165–12173, 2000.

[181] Alexander Patist, SG Oh, R Leung, and DO Shah. Kinetics of micellization: its significance to technological processes. *Colloids and Surfaces A: Physicochemical and Engineering Aspects*, 176(1):3–16, 2001.

[182] E. A. G. Aniansson, S. N. Wall, M. Almgren, H. Hoffmann, I. Kielmann, W. Ulbricht, R. Zana, J. Lang, and C. Tondre. Theory of the kinetics of micellar equilibria and quantitative interpretation of chemical relaxation studies of micellar solutions of ionic surfactants. *The Journal of Physical Chemistry*, 80(9):905–922, 1976.

[183] J Lang, C Tondre, R Zana, R Bauer, H Hoffmann, and W Ulbricht. Chemical relaxation studies of micellar equilibriums. *The Journal of Physical Chemistry*, 79(3):276–283, 1975.

[184] EAG Aniansson, SN Wall, M Almgren, H Hoffmann, I Kielmann, W Ulbricht, R Zana, J Lang, and C Tondre. Theory of the kinetics of micellar equilibria and quantitative interpretation of chemical relaxation studies of micellar solutions of ionic surfactants. *The Journal of Physical Chemistry*, 80(9):905–922, 1976.

[185] Seong-Geun Oh, Scott Paul Klein, and DO Shah. Effect of micellar life-time on the bubble dynamics in sodium dodecyl sulfate solutions. *AIChE journal*, 38(1):149–152, 1992.

[186] Jan van Stam, Serge Creutz, Frans C De Schryver, and Robert Jérôme. Tuning of the exchange dynamics of unimers between block copolymer micelles with temperature, cosolvents, and cosurfactants. *Macromolecules*, 33(17):6388–6395, 2000.

[187] Jan Alsins and Mats Almgren. Quenching dynamics and diffusion of small hydrophobic molecules in long rodlike micelles. *Journal of Physical Chemistry*, 94(7):3062–3069, 1990.

[188] C Bohne, R Konuk, and JC Scaiano. Dynamics of the redistribution of 1-dodecylpyrene aggregates in micellar solution. *Chemical physics letters*, 152(2):156–159, 1988.

[189] F Vialla, G Delport, Y Chassagneux, Ph Roussignol, Jean-Sébastien Lauret, and C Voisin. Diameter-selective non-covalent functionalization of carbon nanotubes with porphyrin monomers. *Nanoscale*, 2016.

[190] Feng Bai, Zaicheng Sun, Huimeng Wu, Raid E Haddad, Eric N Coker, Jian Yu Huang, Mark A Rodriguez, and Hongyou Fan. Porous one-dimensional nanostructures through confined cooperative self-assembly. *Nano letters*, 11(12):5196–5200, 2011.

[191] Peipei Guo, Guangyao Zhao, Penglei Chen, Bin Lei, Lang Jiang, Hantang Zhang, Wenping Hu, and Minghua Liu. Porphyrin nanoassemblies via surfactant-assisted assembly and single nanofiber nanoelectronic sensors for high-performance h2o2 vapor sensing. *ACS nano*, 8(4):3402–3411, 2014.

[192] M Kasha, HR Rawls, and M Ashraf El-Bayoumi. The exciton model in molecular spectroscopy. *Pure and Applied Chemistry*, 11(3-4):371–392, 1965.

[193] George Wypych. *Handbook of solvents*. ChemTec Publishing, 2001.

[194] Wim Wenseleers, Igor I Vlasov, Etienne Goovaerts, Elena D Obraztsova, Anatolii S Lobach, and August Bouwen. Efficient isolation and solubilization of pristine single-walled nanotubes in bile salt micelles. *Advanced Functional Materials*, 14(11):1105–1112, 2004.

[195] KR Hall, LC Eagleton, Andreas Acrivos, and Theodore Vermeulen. Pore-and solid-diffusion kinetics in fixed-bed adsorption under constant-pattern conditions. *Industrial & Engineering Chemistry Fundamentals*, 5(2):212–223, 1966.

[196] Raweewan Klaewkla, Matthias Arend, and Wolfgang F Hoelderich. *A review of mass transfer controlling the reaction rate in heterogeneous catalytic systems*, volume 5. INTECH Open Access Publisher, 2011.

[197] Irving Langmuir. The adsorption of gases on plane surfaces of glass, mica and platinum. *Journal of the American Chemical society*, 40(9):1361–1403, 1918.

[198] Weijie Huang, Yi Lin, Shelby Taylor, Jay Gaillard, Apparao M Rao, and Ya-Ping Sun. Sonication-assisted functionalization and solubilization of carbon nanotubes. *Nano Letters*, 2(3):231–234, 2002.

[199] Laura Oudjedi, A Nicholas G Parra-Vasquez, Antoine G Godin, Laurent Cognet, and Brahim Lounis. Metrological investigation of the (6, 5) carbon nanotube absorption cross section. *The journal of physical chemistry letters*, 4(9):1460–1464, 2013.

[200] Fabien Vialla, Cyrielle Roquelet, Benjamin Langlois, Géraud Delport, Silvia Morim Santos, Emmanuelle Deleporte, Philippe Roussignol, Claude Delalande, Christophe Voisin, and Jean-Sébastien Lauret. Chirality dependence of the absorption cross section of carbon nanotubes. *Physical review letters*, 111(13):137402, 2013.

[201] Balázs Jójárt, Mihalj Poša, Béla Fiser, Milán Szőri, Zita Farkaš, and Béla Viskolcz. Mixed micelles of sodium cholate and sodium dodecylsulphate 1: 1 binary mixture at different temperatures–experimental and theoretical investigations. *PloS one*, 9(7):e102114, 2014.

[202] Pei Zhao, Erik Einarsson, Georgia Lagoudas, Junichiro Shiomi, Shohei Chiashi, and Shigeo Maruyama. Mechanism behind separation of single-walled carbon nanotubes via density gradient ultracentrifugation using co-surfactant dispersions.

[203] Michael S Arnold, Jin Suntivich, Samuel I Stupp, and Mark C Hersam. Hydrodynamic characterization of surfactant encapsulated carbon nanotubes using an analytical ultracentrifuge. *ACS nano*, 2(11):2291–2300, 2008.

[204] Yahya Rharbi, Mei Li, Mitchell A Winnik, and Kenneth G Hahn. Temperature dependence of fusion and fragmentation kinetics of triton x-100 micelles. *Journal of the American Chemical Society*, 122(26):6242–6251, 2000.

[205] Yahya Rharbi and Mitchell A Winnik. Salt effects on solute exchange and micelle fission in sodium dodecyl sulfate micelles below the micelle-to-rod transition. *The Journal of Physical Chemistry B*, 107(7):1491–1501, 2003.

[206] Robert M Weinheimer, D Fennell Evans, and EL Cussler. Diffusion in surfactant solutions. *Journal of Colloid and Interface Science*, 80(2):357–368, 1981.

[207] Robert F Pasternack, Cavan Fleming, Stephanie Herring, Peter J Collings, Gerard DeCastro, Esther J Gibbs, et al. Aggregation kinetics of extended porphyrin and cyanine dye assemblies. *Biophysical journal*, 79(1):550–560, 2000.

[208] Nicholas J Turro and Ahmad Yekta. Luminescent probes for detergent solutions. a simple procedure for determination of the mean aggregation number of micelles. *Journal of the American Chemical Society*, 100(18):5951–5952, 1978.

[209] K Motomura, M Yamanaka, and Makoto Aratono. Thermodynamic consideration of the mixed micelle of surfactants. *Colloid and Polymer Science*, 262(12):948–955, 1984.

[210] Nakul C Maiti, Shyamalava Mazumdar, and N Periasamy. Dynamics of porphyrin molecules in micelles. picosecond time-resolved fluorescence anisotropy studies. *The Journal of Physical Chemistry*, 99(27):10708–10715, 1995.

[211] Richard I Masel. *Principles of adsorption and reaction on solid surfaces*, volume 3. John Wiley & Sons, 1996.

[212] Frank K Brunecker, Friedrich Schöppler, and Tobias Hertel. Interaction of polymers with single-wall carbon nanotubes. *The Journal of Physical Chemistry C*, 120(18):10094–10103, 2016.

[213] Wen-Che Hou, Somayeh BeigzadehMilani, Chad T Jafvert, and Richard G Zepp. Photoreactivity of unfunctionalized single-wall carbon nanotubes involving hydroxyl radical: chiral dependency and surface coating effect. *Environmental science & technology*, 48(7):3875–3882, 2014.

[214] Timothy J McDonald, Chaiwat Engtrakul, Marcus Jones, Garry Rumbles, and Michael J Heben. Kinetics of pl quenching during single-walled carbon nanotube rebundling and diameter-dependent surfactant interactions. *The Journal of Physical Chemistry B*, 110(50):25339–25346, 2006.

[215] Timothy J McDonald, Jeffrey L Blackburn, Wyatt K Metzger, Garry Rumbles, and Michael J Heben. Chiral-selective protection of single-walled carbon nanotube photoluminescence by surfactant selection. *The Journal of Physical Chemistry C*, 111(48):17894–17900, 2007.

[216] Margaret Robson Wright. *Introduction to Chemical Kinetics*. John Wiley & Sons, 2005.

[217] TR Waite. Theoretical treatment of the kinetics of diffusion-limited reactions. *Physical review*, 107(2):463, 1957.

[218] Julio Casado, M Arturo Lopez-Quintela, and Francisco M Lorenzo-Barral. The initial rate method in chemical kinetics: Evaluation and experimental illustration. *J. Chem. Educ*, 63(5):450, 1986.

[219] Shangchao Lin and Daniel Blankschtein. Role of the bile salt surfactant sodium cholate in enhancing the aqueous dispersion stability of single-walled carbon nanotubes: a molecular dynamics simulation study. *The Journal of Physical Chemistry B*, 114(47):15616–15625, 2010.

[220] private communication with nanointegris.

[221] http://www.nanointegris.com/en/puresheets.

[222] Dong Wang, Shi-Yuan Gou, and Daniel Axelrod. Reaction rate enhancement by surface diffusion of adsorbates. *Biophysical chemistry*, 43(2):117–137, 1992.

[223] Jozsef Toth. *Adsorption*. CRC Press, 2002.

[224] Stephen Brunauer, Lola S Deming, W Edwards Deming, and Edward Teller. On a theory of the van der waals adsorption of gases. *Journal of the American Chemical society*, 62(7):1723–1732, 1940.

[225] Aydin Akgerman and Minoo Zardkoohi. Adsorption of phenolic compounds on fly ash. *Journal of Chemical & Engineering Data*, 41(2):185–187, 1996.

[226] G_ S_ Adair et al. The hemoglobin system vi. the oxygen dissociation curve of hemoglobin. *Journal of Biological Chemistry*, 63(2):529–545, 1925.

[227] Terrell L Hill. Statistical mechanics of multimolecular adsorption ii. localized and mobile adsorption and absorption. *The Journal of Chemical Physics*, 14(7):441–453, 1946.

[228] Henry d'A Heck. Statistical theory of cooperative binding to proteins. hill equation and the binding potential. *Journal of the American Chemical Society*, 93(1):23–29, 1971.

[229] James N Weiss. The hill equation revisited: uses and misuses. *The FASEB Journal*, 11(11):835–841, 1997.

[230] Maumita Mandal, Mark Lee, Jeffrey E Barrick, Zasha Weinberg, Gail Mitchell Emilsson, Walter L Ruzzo, and Ronald R Breaker. A glycine-dependent riboswitch that uses cooperative binding to control gene expression. *Science*, 306(5694):275–279, 2004.

[231] John H Viles, Fred E Cohen, Stanley B Prusiner, David B Goodin, Peter E Wright, and H Jane Dyson. Copper binding to the prion protein: structural implications of four identical cooperative binding sites. *Proceedings of the National Academy of Sciences*, 96(5):2042–2047, 1999.

[232] Tamás Turányi and Alison S Tomlin. Reaction kinetics basics. In *Analysis of Kinetic Reaction Mechanisms*, pages 5–37. Springer, 2014.

[233] Walter Orellana. Strong π-π interaction of porphyrins on (6, 5) carbon nanotubes with full surface coverage: Ab-initio calculations. *Applied Physics Letters*, 105(2):023110, 2014.

[234] Walter Orellana. Single-and double-wall carbon nanotubes fully covered with tetraphenylporphyrins: Stability and optoelectronic properties from ab initio calculations. *Chemical Physics Letters*, 634:47–52, 2015.

[235] Rosaria Lauceri, Antonio Raudino, Luigi Monsù Scolaro, Norberto Micali, and Roberto Purrello. From achiral porphyrins to template-imprinted chiral aggregates and further. self-replication of chiral memory from scratch. *Journal of the American Chemical Society*, 124(6):894–895, 2002.

[236] Peipei Guo, Penglei Chen, and Minghua Liu. One-dimensional porphyrin nanoassemblies assisted via graphene oxide: Sheetlike functional surfactant and enhanced photocatalytic behaviors. *ACS applied materials & interfaces*, 5(11):5336–5345, 2013.

[237] Elton JF Carvalho and Maria Cristina dos Santos. Role of surfactants in carbon nanotubes density gradient separation. *ACS nano*, 4(2):765–770, 2010.

[238] Walter Orellana and Julián D Correa. Noncovalent functionalization of carbon nanotubes and graphene with tetraphenylporphyrins: stability and optical

properties from ab initio calculations. *Journal of Materials Science*, 50(2):898–905, 2015.

[239] Yuxi Xu, Lu Zhao, Hua Bai, Wenjing Hong, Chun Li, and Gaoquan Shi. Chemically converted graphene induced molecular flattening of 5, 10, 15, 20-tetrakis (1-methyl-4-pyridinio) porphyrin and its application for optical detection of cadmium (ii) ions. *Journal of the American Chemical Society*, 131(37):13490–13497, 2009.

[240] James R Weinkauf, Sharon W Cooper, Aaron Schweiger, and Carl C Wamser. Substituent and solvent effects on the hyperporphyrin spectra of diprotonated tetraphenylporphyrins. *The Journal of Physical Chemistry A*, 107(18):3486–3496, 2003.

[241] Z Chernia and D Gill. Flattening of tmpyp adsorbed on laponite. evidence in observed and calculated uv-vis spectra. *Langmuir*, 15(5):1625–1633, 1999.

[242] MM El-Nahass, HM Zeyada, MS Aziz, and MM Makhlouf. Optical absorption of tetraphenylporphyrin thin films in uv–vis-nir region. *Spectrochimica Acta Part A: Molecular and Biomolecular Spectroscopy*, 61(13):3026–3031, 2005.

[243] SM Vlaming, R Augulis, MCA Stuart, J Knoester, and PHM Van Loosdrecht. Exciton spectra and the microscopic structure of self-assembled porphyrin nanotubes. *The Journal of Physical Chemistry B*, 113(8):2273–2283, 2009.

[244] Esther J Gibbs, Ignacio Tinoco, Marcos F Maestre, Panayiotis A Ellinas, and Robert F Pasternack. Self-assembly of porphyrins on nucleic acid templates. *Biochemical and biophysical research communications*, 157(1):350–358, 1988.

[245] Basil G Anex and Robert S Umans. The absolute assignment of the electronic transitions of α, β, γ, δ-tetraphenylporphine. *Journal of the American Chemical Society*, 86(22):5026–5027, 1964.

[246] GD Dorough, JR Miller, and Frank M Huennekens. Spectra of the metalloderivatives of α, β, γ, δ-tetraphenylporphine. *Journal of the American Chemical Society*, 73(9):4315–4320, 1951.

[247] SF Shkirman, KN Solov'ev, TF Kachura, SA Arabei, and ED Skakovskii. Interpretation of the soret band of porphyrins based on the polarization spectrum of n-methyltetraphenylporphin fluorescence. *Journal of applied spectroscopy*, 66(1):68–75, 1999.

[248] Yong Hee Kim, Hyun Sun Cho, Dongho Kim, Seong Keun Kim, Naoya Yoshida, and Atsuhiro Osuka. Photophysical properties of meso, meso-linked porphyrin arrays: steady-state and time-resolved fluorescence polarization. *Synthetic metals*, 117(1):183–187, 2001.

[249] Gianlorenzo Bussetti, Marcello Campione, Michele Riva, Andrea Picone, Luisa Raimondo, Lorenzo Ferraro, Conor Hogan, Maurizia Palummo, Alberto Brambilla, Marco Finazzi, et al. Stable alignment of tautomers at room temperature in porphyrin 2d layers. *Advanced Functional Materials*, 24(7):958–963, 2014.

[250] G Bussetti, M Campione, L Ferraro, L Raimondo, B Bonanni, C Goletti, M Palummo, C Hogan, L Duò, M Finazzi, et al. Probing two-dimensional vs three-dimensional molecular aggregation in metal-free tetraphenylporphyrin thin films by optical anisotropy. *The Journal of Physical Chemistry C*, 118(29):15649–15655, 2014.

[251] Van Dong Pham, Vincent Repain, Cyril Chacon, Amandine Bellec, Yann Girard, Sylvie Rousset, Alexander Smogunov, Yannick J Dappe, and Jerome Lagoute. Control of molecule–metal interaction by hydrogen manipulation in an organic molecule. *The journal of physical chemistry letters*, 7(8):1416–1421, 2016.

[252] AS Davydov. *Theory of absorption spectra of molecular crystals*. Department of Chemistry, University of California, 1949.

[253] Jai Parkash, John H Robblee, John Agnew, Esther Gibbs, Peter Collings, Robert F Pasternack, and Julio C de Paula. Depolarized resonance light scattering by porphyrin and chlorophyll a aggregates. *Biophysical journal*, 74(4):2089–2099, 1998.

[254] http://omlc.org/spectra/photochemcad/html/099.html.

[255] Markus Sauer, Johan Hofkens, and Jörg Enderlein. *Handbook of fluorescence spectroscopy and imaging: from ensemble to single molecules*. John Wiley & Sons, 2010.

[256] Nicholas J Turro. *Modern molecular photochemistry*. University science books, 1991.

[257] Jean B Kim, John J Leonard, and Frederick R Longo. Mechanistic study of the synthesis and spectral properties of meso-tetraarylporphyrins. *Journal of the American Chemical Society*, 94(11):3986–3992, 1972.

[258] Wen Li and Carl C Wamser. Synthesis and characterization of interfacially polymerized films of tetraphenylporphyrin derivatives. *Langmuir*, 11(10):4061–4071, 1995.

[259] Yonbon Arai and Hiroshi Segawa. J-aggregation of protonated meso-tetrakis (sulfonatothienyl) porphyrin isomers: Morphological selection of self-assembled nanostructures from structurally similar zwitterionic porphyrins. *Chemical communications*, 46(24):4279–4281, 2010.

[260] Myong Yong Choi, Jennifer A Pollard, M Adam Webb, and Jeanne L McHale. Counterion-dependent excitonic spectra of tetra (p-carboxyphenyl) porphyrin aggregates in acidic aqueous solution. *Journal of the American Chemical Society*, 125(3):810–820, 2003.

[261] María Bassiouk, Vladimir A Basiuk, Elena V Basiuk, Edgar Álvarez-Zauco, Melchor Martínez-Herrera, Aaron Rojas-Aguilar, and Iván Puente-Lee. Non-covalent functionalization of single-walled carbon nanotubes with porphyrins. *Applied Surface Science*, 275:168–177, 2013.

[262] Bernd Wehrle, Hans-Heinrich Limbach, Matthias Köcher, Otto Ermer, and Emanuel Vogel. 15n-cpmas-nmr study of the problem of nh tautomerism in crystalline porphine and porphycene. *Angewandte Chemie International Edition in English*, 26(9):934–936, 1987.

[263] Willi Auwärter, Knud Seufert, Felix Bischoff, David Ecija, Saranyan Vijayaraghavan, Sushobhan Joshi, Florian Klappenberger, Niveditha Samudrala, and Johannes V Barth. A surface-anchored molecular four-level conductance switch based on single proton transfer. *Nature nanotechnology*, 7(1):41–46, 2012.

[264] Raymond P Briñas and Christian Brückner. Synthesis of 5, 10-diphenylporphyrin. *Tetrahedron*, 58(22):4375–4381, 2002.

[265] Peter L Marek. *Biomimetic dye aggregate solar cells*. Springer Science & Business Media, 2013.

[266] Gordana Dukovic, Milan Balaz, Peter Doak, Nina D Berova, Ming Zheng, Robert S Mclean, and Louis E Brus. Racemic single-walled carbon nanotubes exhibit circular dichroism when wrapped with dna. *Journal of the American Chemical Society*, 128(28):9004–9005, 2006.

[267] Kaushik Bairagi, Olga Iasco, Amandine Bellec, Alexey Kartsev, Dongzhe Li, Jérôme Lagoute, Cyril Chacon, Yann Girard, Sylvie Rousset, Frédéric Miserque, et al. Molecular-scale dynamics of light-induced spin cross-over in a two-dimensional layer. *Nature Communications*, 7, 2016.

[268] H Wende, M Bernien, J Luo, C Sorg, N Ponpandian, J Kurde, J Miguel, M Piantek, X Xu, Ph Eckhold, et al. Substrate-induced magnetic ordering and switching of iron porphyrin molecules. *Nature materials*, 6(7):516–520, 2007.

Résumé de la thèse

Ce manuscrit présente une étude expérimentale sur le processus de recouvrement de nanotubes de carbone monoparois en suspension micellaire par des molécules de colorants organiques appelées tetraphenylporphyrines. Ces nanocomposés nanotubes/porphyrines présentent un phénomène de transfert d'énergie ultra efficace de la molécule de porphyrine (donneur) vers le nanotube (accepteur). Ce type de propriétés est particulièrement intéressante pour des applications telles que les cellules solaires en couche mince ou la bioimagerie. En raison des propriétés électroniques exceptionnelles et de la structure chimique carbonée de ces nanotubes, une modification de leur environnement physico-chimique a une grande influence sur leurs propriétés optoélectroniques. Les conséquences de cette fonctionnalisation de surface sont ici étudiées par des techniques de spectroscopie optique. Le procédé de fonctionnalisation non covalente de nanotubes par des molécules de porphyrines en milieu micellaire est détaillé selon trois axes de recherches complémentaires.

Dans un premier temps, les aspects cinétiques de ce processus réactionnel seront discutés. En particulier, le rôle de l'organisation de l'environnement micellaire est mis en évidence. La solubilité de la molécule de porphyrins dans différents surfactant a été préalablement étudiée. De plus, nous avons montré que le caractère ionique des surfactants communément utilisés joue un rôle central dans la cinétique de fonctionnalisation des nanotubes par les porphyrines. Cela peut rendre le processus extrêmement lent, avec des temps caractéristiques de plusieurs jours. De manière à contourner ce problème, nous avons développé une nouvelle méthode de fonctionnalisation que nous avons appliquée ici au couple nanotubes de carbone / molécules de porphyrines. En passant la concentration du surfactant solubilisant les molécules sous sa concentration micellaire critique à l'aide d'une dilution, il est possible de contourner la stabilité des surfactants ioniques tout en conservant leur pouvoir de solubilisation. Cette méthode permet de contrôler finement la réaction et de moduler son temps caractéristique sur plusieurs ordres de grandeurs.

Ensuite, une étude thermodynamique de l'interaction nanotube/porphyrines a été réalisée. Le formalisme d'adsorption de Hill a été utilisé pour modéliser le processus de couverture du nanotubes par les molécules. Cela a permis de mettre en évidence que l'environnement micellaire a une influence sur l'énergie de Gibbs de la réaction. Cela a aussi démontré le comportement associatif des porphyrines au cours de leur interaction avec le nanotube. Dans un second, temps, un modèle cinétique a été développé pour comprendre comment l'étape de diffusion externe et l'étape d'adsorption sur les nanotubes étaient imbriquées. De plus, il a été prouvé que les porphyrines ont une affinité plus grande avec les nanotubes de grand diamètre. L'étude de l'adsorption des molécules de porphyrines sur des nanofeuillets de graphène en milieu micellaire a aussi été réalisée, en suivant une méthode similaire.

Dans un troisième chapitre, les caractéristiques spectrales de la porphyrine isolée et lorsqu'elle est adsorbée sur la surface de carbone seront comparées. Pour ce faire une expérience d'excitation de la photoluminescence résolue en polarisation a été mise en place. Cela a permis de révéler la présence de deux composantes internes à la bande de Soret des porphyrines. De plus, au cours de l'adsorption des porphyrines sur le nanotube, ces deux composantes subissent une amplification de leur écart en énergie. Un modèle de couplage dipôle-dipôle a été développé pour comprendre cet effet. De plus, ce modèle permet de mettre en évidence que les molécules s'auto-organisent sur le substrat carboné (nanotube ou graphène). Pour mieux comprendre ce phénomène, plusieurs exemples d'effets similaires issus de la littérature sont discutés, démontrant que la molécule de porphyrine a une capacité naturelle à s'organiser sur différents substrats. Dans le cas des nanotubes, la création de spirales de molécules, entourant toute la surface du nanotube, semble être l'hypothèse la plus probable. L'effet de champ local du nanotube a aussi été invoqué pour expliquer les amplitudes distinctes des composantes de Soret des molécules adsorbées sur les nanotubes.

université PARIS-SACLAY | ÉCOLE DOCTORALE Ondes et Matière (EDOM)

Titre : Fonctionnalisation non covalente de nanotubes de carbone.
De l'organisation des micelles à l'auto-assemblage des porphyrines

Mots –clés : Carbone, Optique, Spectroscopie, Transfer d'énergie, Nanomatériaux
Résumé :

Ce manuscrit présente une étude expérimentale sur le processus de recouvrement de nanotubes de carbone monoparois en suspension micellaire par des molécules de colorants organiques. En raison des propriétés électroniques exceptionnelles et de la structure chimique carbonée de ces nanotubes, une modification de leur environnement physico-chimique a une grande influence sur leurs propriétés optoélectroniques. Les conséquences de cette fonctionnalisation de surface sont étudiées par des techniques de spectroscopie optique.
Le procédé de fonctionnalisation non covalente de nanotubes par des molécules de porphyrines est détaillé selon trois axes de recherches complémentaires. Dans un premier temps, les aspects cinétiques de ce processus réactionnel seront discutés. En particulier, le rôle de l'organisation de l'environnement micellaire est mis en évidence. Cela permet de comprendre et de contrôler la durée de la réaction. Une étude thermodynamique de l'interaction nanotube/porphyrines sera ensuite menée. Le comportement associatif des porphyrines au cours de leur interaction avec le nanotube sera démontré. Dans un troisième chapitre, les caractéristiques spectrales de la porphyrine lorsqu'elle est adsorbée sur la surface de carbone sont discutées. Un modèle de couplage dipôle-dipôle est développé pour comprendre ces effets, en lien avec une tendance des molécules à s'aligner et s'auto-assembler sur une couche de carbone.

Title: Non-convalent functionalization of carbon nanotubes.
From the organization of surfactants to the self-assembly of porphyrins.

Keywords : Carbon, Optics, Spectroscopy, Energy transfer, Nanomaterials
Abstract:

This manuscript presents an experimental study on the process of coverage of single-wall carbon nanotubes by organic dyes molecules. Due to the exceptional electronic properties and the monolayer carbon structures of such nanotubes, a modification of their physico-chemical environment has a great influence on their optoelectronic properties. The consequences of this surface functionalization are studied by means of optical spectroscopy.
The process of non covalent functionalization of surfactant suspended nanotubes by porphyrin molecules is studied in three complementary aspects. The first one details the kinetic aspects of this reaction process. In particular, the role of the organization of the surfactant environment will be highlighted. This allows to understand and control the reaction timescale. On the second hand, a comprehensive thermodynamic study of the nanotube/porphyrins interaction is performed. The associative behavior of the porphyrin during the interaction with the nanotube is evidenced. Then, the spectral characteristics of the porphyrin when it is adsorbed on a carbon surface is discussed. A dipole-dipole coupling model is developed to understand such effects, in relation with a tendency of the molecules to self-align and organize on the carbon template.